COMPUTATIONAL FLUID DYNAMIC OF SINGLE AND TWO PHASE FLOW IN MICROCHANNELS

A thesis submitted for the degree of Doctor of Philosophy

By

Amirah Mohamad Sahar

College of Engineering, Design and Physical Sciences
Brunel University London
Uxbridge, UB8 3PH, UK

DECEMBER 2019

ABSTRACT

A numerical study of single and two-phase fluid flow and heat transfer in single microchannels was conducted using the computational software package ANSYS Fluent. The geometry construction and mesh generation were performed using the hexa meshing option in the ICEM mesh-generator. In the single-phase flow simulations, two different configurations were studied: (1) a single channel with a hydraulic diameter of 0.561 mm and (2) a multichannel with inlet and outlet manifolds, comprising 25 channels with a hydraulic diameter of 0.409 mm. In the single channel simulations, the effect of axial conduction and geometrical parameters, i.e. aspect ratio and hydraulic diameter, on the fluid flow and heat transfer were investigated. Four numerical models, using 2D thin-wall, 3D thin-wall (heated from the bottom), 3D thin-wall (three-side heated) and 3D fully conjugated geometries were employed in order to study the effect of axial conditions on heat transfer rate. The simulations were conducted for Reynolds numbers ranging from Re = 100 to Re=3000 and water was used as the working fluid. The setup of the 3D thin-wall model simulation used thermal boundary conditions that were very similar to those assumed in the accompanying experiments (uniform heat flux), resulting in the numerical friction factor and heat transfer results showing an excellent agreement with the existing experimental data. In contrast. On the contrary, the results of the 3D fully conjugated model demonstrated that there is a significant deviation (more than 50%) when compared to the 3D thin-wall and the experimental data. The results of the 3D fully conjugated model indicated that there is a significant conjugate effect and the heat flux is not uniformly distributed along the channel.

The effect of aspect ratio and hydraulic diameter on fluid flow and heat transfer in a single microchannel was investigated by using the 3D thin-wall approach to avoid conjugate heat transfer effects. Two sets of simulations were conducted, where in the first set of simulation, the effect of hydraulic diameter was studied by varying the channel width and depth while keeping the aspect ratio constant. The range of

hydraulic diameters was 0.1–1 mm and the aspect ratio was fixed at 1. In the second set of simulations, the aspect ratio ranged from 0.39 to 10, while the hydraulic diameter was kept constant at 0.56 mm. The simulations were conducted for a range of Reynolds numbers, Re = 100–2000, and water was used as the working fluid. The friction factor was found to decrease slightly with aspect ratio up to AR ≈ 2, after which it increased with increasing aspect ratio. The results demonstrated that the slope of the velocity profile at the channel wall changes significantly with aspect ratio for AR > 2. The effect of the aspect ratio and hydraulic diameter on the dimensionless hydrodynamic entry length is not significant. Also, the aspect ratio does not affect the heat transfer coefficient, while the dimensionless Nusselt number as well as the friction factor were found to increases with increasing hydraulic diameter.

In the multichannel configuration, the flow distribution inside the twenty-five parallel channels, including the effect of conjugate heat transfer, was studied. The numerical study was carried out using R134a as a working fluid. The obtained friction factor is in agreement with experimental data provided by Fayyadh et al. (2015), while the value is under-predicted compared to Shah and London (1978) in the laminar region and Philips (1987) in the turbulent region. For the heat transfer results, the numerical Nusselt number results differed significantly from the experimental results by Fayyadh et al.(2015) as well as the correlation provided by Shah and London (1978). In addition, based on the average velocity and temperature of the fluid inside the twenty-five channels, the flow was uniformly distributed only at the channel located in the centre region. This could be due to the occurrence of flow recirculation because of the the sharp edges in the inlet manifold leading to a reduction of flow rate in the channels located at the lateral edges of the parallel microchannels. Therefore, the under-prediction of numerical heat transfer results could be attributed to the conjugate effects and flow mal-distribution. Subsequently, the effect of various parameters such as, inlet/outlet area manifold, inlet/outlet flow arrangement and number of channels (N=9, 13, 17, 25, 33) on the flow distribution inside channels was examined. The dimensionless channel flow ratio and flow maldistribution factor were introduced to quantify the flow distribution inside individual channels and the uniformity of this flow distribution. A uniform flow distribution is achieved when the MF value approaches 0. In the present study, the area of the inlet and outlet manifolds

were varied by varying the length of manifolds while the width of the manifold remained constant. The inlet and outlet manifold areas were showing a significant effect on flow distribution, where longer inlet and outlet manifolds were observed to have a better flow distribution. In addition, three different types of flow arrangements, namely, U-type, I-type and Z-type flow arrangements with two different inlet and outlet manifold areas were used. Based on the flow distribution results, the Z-type flow arrangement was showing the worst flow uniformity compared to the other flow arrangement types, irrespective of the inlet and outlet manifold area used. However, in the study of the effect of the number of channels on the flow distribution, two different phenomena were observed as the number of channel increases. Firstly, if the number of channels is less than twenty, the maldistribution value was found to increase as the number of channels increases. In contrast, if the number of channels exceeds twenty, the maldistribution value reduces with increasing number of channels. Finally, a newly design for the inlet manifold was proposed in this study, where edges with a curved shape were suggested in order to reduce the occurrence of flow recirculation at the sharp edges. This resulted in a better flow distribution over the parallel channels.

In the two-phase study, a 1 mm circular microchannel with a vertical orientation was used. The setup of these numerical simulations, using R134a vapour-liquid as a working fluid, had two purposes. The first aim was to develop a numerical flow regime map in order to identify the slug flow boundaries and the dependence on the annular nozzle configuration. In these simulations two dimensional, axi-symmetry was assumed in order to save computational time and effort. The second aim was to study the topology of the hydrodynamic flow and heat transfer distribution of slug flow using three-dimensional flow simulations and related these to the operational condition, i.e. the gas superficial velocity. Based on the numerical flow pattern maps developed in this study, four basic flow patterns, including bubbly flow, slug flow, slug-annular, annular flow, were observed. The present results were verified through comparison with the visualization results reported in the experiments of Chen et al. (2006) and were shown to agree well. The study also showed that Computational Fluid Dynamic can be used to obtain a reliable two-phase flow pattern map.

The slug formation in the R134a vapour-liquid, using the annular (concentric) nozzles configuration of Shao, et al. (2008), was studied. A three dimensional computational domain of 1 mm vertical circular channels was used. A mechanism that consist of expanding, contracting and necking processes was found to occur at the lower end of the bubble. Close to the nozzle, as similar pattern of behaviour as shown by Shao et al. (2008) was observed. In addition, slug cells with a dry zone and irregular shapes were obtained in the present 3-D numerical work. Previously, most researchers assumed the flow to remain axisymmetric in order to save computational time. This assumption lead to identical bubble slugs. However, the process of bubble generation using the axisymmetric assumption is not realistic and a fully three dimensional simulation is required. Asadolahi et al. (2011). In Gupta et al. (2010) concluded that dry-out is one of the problems in numerical work in and it can be avoided by properly constructing numerical grids and algorithms However, Talimi et al. (2012) suggested that the appearance of a dry-out condition, in numerical work is not because of a poor mesh resolution, which could leads to nonphysical results. To settle this dispute, further study of this phenomenon is needed. Therefore, several individual cells with different behaviours and shapes were carefully selected in order to understand the characteristics of the hydrodynamic and thermal behaviour.

In the final part of the two-phase flow study, the effect of superficial gas velocity (with constant superficial liquid velocity) on two phase slug flow was studied. Three different superficial gas velocities were employed in this study. As the mixture velocity increases, the void fraction, β, the capillary number, Ca, and the Reynolds number, Re, are also increasing. In addition, changes in bubble shape, bubble length, liquid film thickness, velocity and temperature profile, pressure drop and heat transfer at different operations were discussed.

DECLARATION

This research is the original work of the author except where otherwise specified, or where acknowledgements are made by references. This research was conducted at the College of Engineering, Design and Physical Sciences, Brunel University London, under the supervision of Prof. T. G. Karayiannis and Dr. Jan G. Wissink.

The work has not been submitted for another degree or award to any other institution.

ACKNOWLEDGEMENT

Firstly, I would like to express my sincere gratitude to my supervisors Professor T.G. Karayiannis and Dr. Jan G. Wissink for all their guidance and patience during this work. Their comments at research meetings encouraged me to accomplish this work.

I am grateful to Dr. M.M. Mahmoud for offering me his help even during his intensive working hours.

I would also like to thank to the Dr Shaiful M. Ishak valuable guidance and support.

I would like to acknowledge the Majlis Amanah Rakyat (MARA) and Univerisiti Kuala Lumpur, (UniKL) for granting me a fully funded scholarship during my study.

To my parents and my family, there are no any proper words to express my gratitude for their incomparable support and encourage me to success. Without their love and support.

I am thankful to the amazing support and friendship of all my friends especially Dr Syakira and family, Dr Fathullah and family.

Finally, I would like to thank my lovely husband, Haidee Che Rizmin deeply for his patience and encouragement all the time. Without his support, this work would not have been possible.

Love HASNA AZZAHRA, AAIRA HUMAIRA, ALFIE ADLEE

TABLE OF CONTENTS

ABSTRACT ..... **II**

DECLARATION ..... **VI**

ACKNOWLEDGEMENT ..... **VII**

LIST OF FIGURES ..... **XIII**

LIST OF TABLES ..... **XXII**

NOMENCLATURE ..... **XXIV**

1 INTRODUCTION **1**

1.1 Research Background 1

1.2 Research Motivation 2

1.3 Research Objectives 5

1.4 Thesis Structure 6

2 LITERATURE REVIEW **8**

2.1 Microchannel 8

2.2 Single Phase Fluid Flow and Heat Transfer in Microchannels 10

2.3 Single Phase Pressure drop 10

2.3.1 Friction factor and comparison with conventional theory results 12

2.3.2 Friction factor not in agreement with conventional theory 16

2.4 Single Phase Heat transfer 20

2.4.1 Nusselt number was agree with conventional theory 21

2.4.2 Nusselt number not in agreement with conventional theory 22

2.5 Effect of geometrical parameter on fluid flow and heat transfer 24

2.6 Effect of axial conduction on heat transfer 27

2.7 Single Phase Fluid Flow and Heat Transfer in Multi-Microchannel 33

2.7.1 Effect of Inlet/Outlet Configuration on Flow Distribution 36

2.7.2 Effect of Manifold Design on Flow Distribution 43

2.7.3 Effect of Channel Dimensions and Number of Channel on Flow Distribution 50

2.8 Conclusions 53

2.9 Two Phase Fluid Flow and Heat Transfer in Mircochannel 54

2.9.1 Dimensionless numbers 54

2.9.2 Adiabatic flow patterns 56

2.9.3 Slug Flow in Microchannel without Phase Change 63

2.10 Conclusions 82

2.11 Summary 83

3 CFD MODELLING OF SINGLE PHASE FLUID FLOW IN RECTANGULAR SINGLE MICROCHANNEL 94

3.1 Introduction 94

3.2 Effect of axial conduction on heat transfer 95

3.2.1 Model descriptions 95

3.2.2 Numerical Method 98

3.2.3 Data analysis 102

3.2.4 Discussion of the results 103

3.3 Effect of aspect ratio and hydraulic diameter on fluid flow and heat transfer..... 110

3.3.1 Model descriptions 110

3.3.2 Effect of Aspect Ratio 112

3.3.3 Effect of Hydraulic Diameter 129

3.3.4 Effect of channel geometry on entry/exit losses 140

3.3.5 Thermal Performance Index (TPI) 143

3.4 Summary 146

4 CFD MODELLING OF SINGLE PHASE FLUID FLOW IN A RECTANGULAR MICRO MULTICHANNEL..... 148

4.1 Introduction 148

4.2 Model Descriptions 148

4.2.1 Numerical Method 150

4.2.2 Results validation 152

4.2.3 Results discussions..... 156

4.2.4 Effect of Various Parameters on Flow Distribution..... 158

4.2.5 Proposed manifold design 186

4.3 Summary 192

5 CFD MODELLING OF TWO PHASE FLUID FLOW AND HEAT TRANSFER IN MICROCHANNEL 193

5.1 Introduction 193

5.2 Two phase flow pattern in 1 mm circular microchannel 193

5.2.1 Model description..... 193

5.2.2 Governing equations 196

5.2.3 Flow solver..... 197

5.2.4 Results and discussion 198

5.3 Two phase slug flow without phase change in 1 mm circular microchannel..... 216

5.3.1 Model description..... 216

5.3.2 Results and discussion 217

5.4 Effect on superficial velocity on hydrodynamic and heat transfer on two phase flow patterns..... 235

5.4.1 Bubbles development..... 236

5.4.2 Bubble length 240

5.4.3 Velocity and thermal profile 241

5.4.4 Void fraction 250

5.4.5 Film thickness 251

5.4.6 Pressure drop..... 252

5.4.7 Heat transfer..... 254

5.5 Summary 256

6 CONCLUSIONS AND RECOMMENDATIONS..... 258

6.1 Conclusions..... 258

6.1.1 CFD Modelling of Single Phase Fluid Flow in a Rectangular Single Microchannel..... 259

6.1.2 CFD Modelling of Single Phase Fluid Flow in a Rectangular Micro Multichannel Microchannel 261

6.1.3 Two phase flow in 1 mm circular microchannel..... 262

6.2 Recommendations..... 265

REFERENCES..... 267

PUBLICATIONS 294

LIST OF FIGURES

Figure 2-1 : Schematic of (a) thin wall model and (b) conjugate model. *29*

Figure 2-2 : Schematic of parallel multichannel with various inlet configuration. (a) I-arrangement (b) Z-arrangement (c)]-arrangement (d) L- arrangement (e) ***Γ****- arrangement, Lu and Wang (2006).* *38*

Figure 2-3 : Geometric configurations of (a) I- type (b) C-type (c) V- type (d) U-type (e) Z-type microchannel heat sinks, Kumaran et al.(2013). *40*

Figure 2-4 : Schematic of D-, N-, I-, U-, V- and S-type of microchannel heat sinks, Chein and Chen (2009). *40*

Figure 2-5 : (a) Conventional inlet/outlet arrangement with rectangular headers (b) Proposed inlet/outlet arrangement with rectangular headers, Kumar and Singh (2019). *43*

Figure 2-6 : Top views of all shapes of model were used in Amiri (2019), (a) Rectangular (b) Triangle 90 (c) Trapezoidal (d) Triangle *49*

Figure 2-7 : Two phase flow patterns in the 1.097 mm diameter circular (a) bubbly; (b) slug; (c) churn; (d) slug-annular; (e) annular, Triplett et al. (1999). *57*

Figure 2-8 : Schematic flow patterns of two-phase flow in vertical channels (a) bubbly flow (b) slug flow (c) annular flow (d) dispersed flow, Dziubinski et al. (2004). *58*

Figure 2-9 : Flow pattern in microchannel for AR=0.92 (a) bubble (b) slug bubble (c) elongated bubble (d) liquid ring flow, Choi et al. (2011). *61*

Figure 2-10 : Flow pattern in vertical circular micro-channel with 0.53 mm diameter, Saisorn and Wongwises (2015). *63*

Figure 2-11 : Mechanism of bubble break-off in T-junction (a) Ca =8.75 × 10^{-4} (b) Ca= 1.4 × $^{10-2}$, Guo and Chen, (2009). *66*

Figure 2-12 : The slug formation in annular/ concentric nozzels, Shao et al. (2008). *67*

Figure 2-13 : Bubble shape and flow field of slug flow by Kurimoto et al. (2018). .. *70*

Figure 2-14 : Temperature iso-contours in the break-up zone of the slug flow, Lakehal et al. (2008). *80*

Figure 4-1 : 2D computational domain of a single microchannel system (Model 1). *95*

Figure 4-2 : Computational domain of single microchannel system (Thin-wall Models 2 and 3). *96*

Figure 4-3 : 3D fully conjugated computational model of single microchannel system (Model 4). *97*

Figure 4-4: Schematic and computational meshes of geometrical model. *101*

Figure 4-5 : Comparison of predicted friction factor with existing experimental results and existing correlations. *104*

Figure 4-6 : Comparison of predicted average Nusselt number with experimental data and correlations. *105*

Figure 4-7 : Prediction local heat flux distribution for bottom and side wall along the channel length (Model 4). *106*

Figure 4-8 : Axial temperature variation of fluid and bottom wall along the channel at Re=216 (Thin wall analysis). *107*

Figure 4-9 : Comparison of an axial temperature variation of fluid and bottom wall along the channel single channel system at Re=216 with existing experimental data by Mirmanto et al. (2012). *108*

Figure 4-10 : Variation of local Nusselt number along the channel. *109*

Figure 4-11: Hydrodynamic entry length identification, (a) maximum velocity attains 99 % of the fully developed value for D_h = 0.1 mm, (b) development of the velocity profile for Re = 181, D_h = 0.56 mm and AR = 0.39. ..... *113*

Figure 4-12 : Velocity and temperature contour at (a) AR=10 and (b) AR=0.39 along the channel. *116*

Figure 4-13 : Comparison of numerical dimensionless entrance length and existing correlations Ahmad and Hassan (2010) and Galvis et al. (2012) at different channel aspect ratios (0.39 < AR <10) with D_h = 0.56 mm. *118*

Figure 4-14 : Vena contracta effects produced by sharp edge corner at the microchannel inlet..... 119

Figure 4-15 : Velocity contour and streamline at inlet channel..... 120

Figure 4-16: (a) Comparison between predicted friction factor and existing correlations (b) Variation of friction factor with varying channel aspect ratio..... 121

Figure 4-17 : Fully developed velocity profile against (a) channel width and (b) channel height for AR=0.39, 2 and 10 at Re ≈ 500. 123

Figure 4-18 : Effect of Reynolds number and aspect ratio on Poiseuille number... 124

Figure 4-19 : The friction factor versus aspect ratio compared to the results of Xing et al. (2013). 125

Figure 4-20 : Comparison between predicted Nusselt number and existing correlations, Shah and London (1978) and Bejan (2004). 127

Figure 4-21 : Variation of Nusselt with varying channel aspect ratio. 128

Figure 4-22 : Comparison of wall temperature (solid line) and fluid temperature (dotted line) for tested aspect ratio at (a) Re≈500 (b) Re≈1500 ; [red] AR=0.39;[green] AR=10. 129

Figure 4-23 : Comparison of obtained dimensionless entrance length at different channel hydraulic diameter (0.1< D_h (mm) <1) with existing correlations. 130

Figure 4-24 : Comparison between predicted friction factor and existing correlations 131

Figure 4-25 : Variation of friction factor with varying channel hydraulic diameter, D_h. 132

Figure 4-26 : Fully developed velocity profile against channel (a) height and (b) width for Dh =0.1 mm, 0.5 mm and 1 mm at Re ≈ 500. 133

Figure 4-27 : Fully developed velocity profile against channel (a) height and (b) width for D_h =0.1 mm , 0.5 mm and 1 mm at Re ≈ 1500. 134

Figure 4-28 : Comparison between numerical Nusselt number predictions and the correlation of Bejan (2004). (solid lines: [orange] 1 mm ;[black] 0.9 mm ; [purple]

0.7 mm ; [blue] 0.5 mm; [red] 0.3 mm; [green] 0.1 mm) with varying channel hydraulic diameter. 135

Figure 4-29 : Variation of Nusselt number with varying hydraulic diameter. 136

Figure 4-30 : Comparison of wall temperature (solid line) and fluid temperature (dotted line) for the tested aspect ratio at (a) Re≈500 (b) Re≈1500 ; [red] D_h =1 mm ;[green] D_h =0.1 mm. 137

Figure 4-31 : Axial heat transfer coefficient and Nusselt number at Re=1500 (a,b) and Re 500 (c,d). 140

Figure 4-32 : The total pressure along the test section for Re = 578, $\boldsymbol{Dh}$ = 0.56 mm , AR = 1.52. 141

Figure 4-33 : Variation of thermal performance index against Re at different (a) AR and (b) $\boldsymbol{Dh}$ 145

Figure 5-1 : 3D fully conjugated computational model of multi-microchannel system. 149

Figure 5-2 : Channel cross-section domain 150

Figure 5-3 : Effect of grid size on average velocity in microchannels in multichannel system. 153

Figure 5-4 : Comparison of predicted friction factor with experimental results and correlations. 155

Figure 5-5 : Comparison of predicted Nusselt with experimental results and correlations. 155

Figure 5-6 : Axial temperature variation of fluid and bottom wall along the channel for multichannel system at Re=585 (3D fully conjugated analysis). 156

Figure 5-7 : Average velocity in each channel at various Reynolds numbers 157

Figure 5-8 : Average temperature in each channel at various Reynolds numbers. 157

Figure 5-9 : Schematic diagram of rectangular manifold. 158

Figure 5-10 : Flow ratio in each channel of microchannel heat sinks with various inlet/outlet manifold area; (a) V_{in}=0.030 m/s (b) V_{in}=0.0645 m/s (c) Vin=0.1133 m/s. 162

Figure 5-11 : Velocity streamlines of microchannel heat sink. 163

Figure 5-12 : Velocity contours of inlet manifold for various area (a) Type D-1, D-4, D-5 (b) Type D-2, D-6 (c) Type D-3, D-7. 164

Figure 5-13 : Influence of inlet/outlet condition area on flow distribution/ maldistribution under different inlet velocity conditions. 166

Figure 5-14 : Schematic of 25 channels multichannel heat sinks. 167

Figure 5-15 : Comparison of velocity streamlines of (a(i)) I-type , (b(i)) U-type , (c(i)) Z-type for microchannel heat sink Type D-1 and (a(ii)) I-type , (b(ii)) U-type , (c(ii)) Z-type for microchannel heat sink Type D-2. 169

Figure 5-16 : Flow ratio of the rectangular header, (a) Type D-1 and (b) Type D-2 for I-Type flow 171

Figure 5-17 : Comparison of secondary flow behaviour at the inlet manifold at V_i = 0.1915 m/s (left-hand side) and V_i = 0.7971 m/s (right-hand side) for I-type flow . 171

Figure 5-18 : Flow ratio of the rectangular header, (a) Type D-1 and (b) Type D-2 for U-Type flow. 173

Figure 5-19 : Comparison of secondary flow behaviour in the inlet manifold at V_i = 0.1915 m/s (left-hand side) and V_i = 0.7971 m/s (right-hand side) for U-type flow. 173

Figure 5-20 : Flow ratio of the rectangular header, (a) Type D-1 and (b) Type D-2 for Z-Type flow 174

Figure 5-21 : Influences of the inlet/outlet flow arrangement on flow maldistribution under different inlet velocity conditions. 177

Figure 5-22 : Surface velocity contour for (a) N=9, (b) N=13, (c) N=17, (d) N=25, (e) N=33. 181

Figure 5-23 : Comparison of normalized velocity distribution profile within channels for (a)V_i =0.03m/s, (b)V_i =0.0645 m/s and (c) V_i =0.1133m/s 183

Figure 5-24 : Maldistribution factor of (a) N=9, (b) N=13, (c) N=17, (d) N=25, (e) N=33 at different velocity inlet conditions. 186

Figure 5-25 : Schematic diagram of (a) Trapezoid manifold (b) Rectangular manifold (c) Proposed manifold..... 187

Figure 5-26 : Normalized velocity in each channel of (a) Trapezoid manifold (b) Rectangular manifold (c) Proposed manifold at different inlet conditions ; (a) V_{in}=0.030 m/s (b) V_{in}=0.0645 m/s (c) Vin=0.1133 m/s. 189

Figure 5-27 : Maldistribution factor for different inlet manifolds at various inlet velocity conditions..... 190

Figure 5-28 : Velocity contour in the inlet manifold (a) Trapezoid manifold (b) Rectangular manifold (c) Proposed manifold..... 191

Figure 6-1 : Schematic representation of the geometry and boundary condition used in simulations. 194

Figure 6-2 : The computational mesh used in the simulations. The mesh is refined near the wall (top of figure) to capture liquid film. 195

Figure 6-3 : Velocity profile for different mesh. 195

Figure 6-4 : Numerical simulation conditions cases for model validation on the flow pattern map of Chen et al. (2006). 200

Figure 6-5 : The flow patterns of obtained in the numerical simulation validation runs: (a) bubbly flow; (b)-(c) slug flow; (d) slug-annular; and (d) annular flow. .. 203

Figure 6-6 : Bubble flow patterns for R134a in 1mm circular microchannel 205

Figure 6-7 : Slug-flow patterns for R134a in 1 mm circular microchannel 206

Figure 6-8 : Slug–annular flow pattern for R134a in 1 mm microchannel. 207

Figure 6-9 : Annular flow pattern for R134a in 1 mm microchannel..... 208

Figure 6-10 : Flow regime map for R134a (●-Bubble, ○-Bubble-Slug, ■- Slug, ▲ - Slug-Annular, △-Annular) 209

Figure 6-11 : Bubble-slug transition flow pattern for R134a in 1 mm microchannel. 210

Figure 6-12 : Comparison of the present numerical results with the flow regimes maps of Chen et al. (2006) -solid line. *212*

Figure 6-13 : Comparison of present numerical results with flow regimes maps of Chung and Kawaji (2004)-dotted line Triplett et al. (1999)-solid line. *213*

Figure 6-14 : Comparison of present numerical results with flow regimes maps of Hassan et al. (2005) for different orientations (Horizontal line-dotted line; Vertical - solid line). *214*

Figure 6-15 : Comparison of present numerical results with flow regimes maps of Wei et al. (2017). *215*

Figure 6-16 : Schematic representation of the geometry and boundary conditions used in the simulation. *216*

Figure 6-17 : Cross sectional contours showing slug flow formation and evolution for $\boldsymbol{UGs = 0.23}$ *and* $\boldsymbol{ULs = 0.12}$ *red: gas phase, blue: liquid phase.* *218*

Figure 6-18 : Measurement of each gas (red) and liquid (blue) slug. *219*

Figure 6-19 : Comparison of bubble length obtained in present simulation with existing correlation. *220*

Figure 6-20 : Three dimensional visualisation identifying the gas bubbles. *221*

Figure 6-21 : Comparison of present simulation work with the study conducted by Chen et al. (2006). *222*

Figure 6-22 : (a) Pressure surface contour (b) temperature surface contour and (c) velocity vector at breakup region (Zone 1) at t =4.8 ms. The boundaries of the cells are identified by colours lines ; Red (gas phase) , Blue (liquid phase), Yellow-green (gas-liq liquid interface). *224*

Figure 6-23 : (a) Velocity vector and (b) temperature contour of 3rd cell ; (c) velocity profiles and (d) temperature profiles at selected locations of 3^{rd} *cell.* *226*

Figure 6-24 : (a) Velocity vector and (b) temperature contour of the 4th cell ; (c) velocity profile and (d) temperature profile of selected location on the 4th cell. *228*

Figure 6-25 : (a) Velocity vector and (b) temperature contour of 5th unit cell ; (c) velocity profile and (d) temperature profile of selected location on 5th unit cell. *230*

Figure 6-26 : Bubble shape as obtained in CFD simulations at three different time. *230*

Figure 6-27 : Variation of wall pressure and axial pressure distribution at t=4.8 ms. *232*

Figure 6-28 : Bulk temperature variation and wall temperature in the axial direction at a time t=4.8ms obtained from Ansys Fluent. *233*

Figure 6-29 : Local Nusselt number at 4.8e-2s in axial direction. *234*

Figure 6-30 : Nusselt number at single location on tail and nose of the bubble slug. *235*

Figure 6-31 : Variation of time of bubble formation at three different superficial gas velocity, $\boldsymbol{UGS}$*= (a) 0.14 m/s (b) 0.22 m/s and (c) 0.29 m/s.* *237*

Figure 6-32 : Gas superficial velocity effect on the development of the two phase flow pattern; $\boldsymbol{UGS} =$ *(a) 0.14 m/s (b) 0.22 m/s and (c) 0.29 m/s.* *240*

Figure 6-33 : (a) Velocity vector and (b) temperature contour of a unit cell of $UGS = 0.14\ m/s$*; (c) velocity profile and (d) temperature profile of selected location on a unit cell for* $UGS = 0.14\ m/s$**.** *The boundaries of the cells are identified by colours lines; Red (gas phase), Blue (liquid phase), Yellow-green (gas-liquid interface).* .. *243*

Figure 6-34 : (a) Velocity vector and (b) temperature contour of a unit cell of $UGS = 0.22\ m/s$*; (c) velocity profile and (d) temperature profile of selected location on a unit cell for* $UGS = 0.22\ m/s$*. The boundaries of the cells are identified by colours lines; Red(gas phase) , Blue (liquid phase), Yellow-green (gas-liquid interface).* . *245*

Figure 6-35 : (a) Velocity vector and (b) temperature contour of a unit cell of $UGS = 0.29\ m/s$*; (c) velocity profile and (d) temperature profile of selected location on a unit cell for* $UGS = 0.29\ m/s$*. The boundaries of the cells are identified by colours lines; Red (gas phase), Blue (liquid phase), Yellow-green (gas-liquid interface).* .. *247*

Figure 6-36 : Comparison of normalized (a) velocity profile and (b) temperature profile of liquid slug at different superficial velocity. *249*

Figure 6-37 : Pressure distribution of unit cell at certain location. *253*

Figure 6-38 : Comparison of (a) Wall temperature (Tw), (b) fluid temperature (Tf), and Nusselt number (Nu) at y_k location of unit cell for all cases i.e; $UGS = 0.14\ m/s$, $UGS = 0.22\ m/s$, $UGS = 0.29\ m/s$ 256

LIST OF TABLES

Table 2-1 : Channel classification by Mehendale et al. (2000) and Kandlikar (2002). *8*

Table 2-2 : Conventional correlations from the literature for the prediction of channel heat transfer..... *20*

Table 2-3 : Film thickness correlations in literature. *73*

Table 2-4 Review of numerical work in single phase microchannel *84*

Table 2-5 Review of numerical work in single phase flow and heat transfer in multichannel..... *87*

Table 2-6 Review of numerical work in two phase flow in microchannel. *89*

Table 3-1 Percentage difference predicted friction factors for each of the different grids considered. *102*

Table 3-2 : Channel dimensions used for the numerical simulations in the present study, $\boldsymbol{Lch = 62}$ *mm.*..... *111*

Table 3-3: Entry and exit pressure losses..... *141*

Table 4-1 : Various inlet and outlet manifold parameters for numerical study. *159*

Table 4-2 : Comparison of non maldsitribution factor (MF). *165*

Table 4-3 : Inlet and outlet information for U-, Z-, I- Type...... *167*

Table 4-4 : Comparison of the maldistribution factor (MF) for Type D-1 and Type D-2 for I-,U-,Z- flow arrangement under different inlet velocity...... *175*

Table 4-5 : Structure dimension of fin thickness microchannel heat sinks..... *178*

Table 4-6 : Comparison of maldistribution factor (MF) for trapezoid, rectangular and proposed manifold..... *184*

Table 5-1 : Properties of gas and liquid used in simulations. *194*

Table 5-2 : Flow operating conditions of numerical simulation study for model verification *198*

Table 5-3 : Summary of operating conditions and corresponding dimensionless numbers. *236*

Table 5-4 : Simulated bubble length under different gas superficial velocities. *241*

Table 5-5 : Percentage difference between simulation ***UBUTP*** *value with existing correlations.* *248*

Table 5-6 : Percentage difference between simulation void fraction value with existing correlations. *250*

Table 5-7 : Percentage difference between simulation film thickness value with existing correlations. *252*

Table 5-8 : Percentage difference between simulation pressure drop across single bubble value with existing correlations. *254*

NOMENCLATURE

AR	Aspect ratio, [-]
$\overline{AR}$	Area ratio, [-]
A_{ch}	Channel cross sectional area, [m^2]
A_p	Plenum cross section area, [m^2]
A_{ht}	Heated area, [m^2]
β_k	Dimensionless channel flow ratio, [-]
Bo	Bond number, [-]
C'	Constant in Eq. (2.5)
Ca	Capillary number, [-]
c_f	Fanning friction factor [-]
c_p	Specific heat, [J/kg K]
D	Diameter, [m]
D_p	Plenum diameter, [m]
D_h	Hydraulic diameter, [m]
E	Energy, [kgm^2/s^2]
$\vec{F}$	External body force, [N/m^3]
f	Darcy friction factor [-]
f_{app}	Apparent friction factor [-]
G	Mass flux, [kg/sm]
g	Gravity, [m/s^2]
H_{ch}	Channel height, [m]
H_m	Manifold height, [m]
H_p	Plenum height, [m]
h	Heat transfer coefficient, [W/m^2K]
$h\ (x)$	Local heat transfer coefficient, [W/m^2K]
h_{av}	Average Heat transfer coefficient, [W/m^2K]
$K(\infty)$	Dimensionless incremental pressure drop number, [-]
K_c	Contraction loss coefficient, [-]
k	Channel number, [-]

k_{eff}	Effective conductivity, $k + k_t$, [W/m K]
k_f	Fluid thermal conductivity, [W/m K]
k_s	Wall thermal conductivity, [W/m K]
k_t	Turbulent thermal conductivity, [W/m K]
L	Length, [m]
L_B	Bubble length, [m]
L_{ch}	Channel length, [m]
L_e	Entrance length, [m]
L_s^*	Dimensionless liquid slug length, [-]
$\dot{m}$	Mass flow rate, [kg/s]
$\dot{m}_{pq}$	Mass transfer rate from phase p to phase q, [kg/s]
$\dot{m}_{pq}$	Mass transfer rate from phase q to phase p, [kg/s]
N	Number of channel, [-]
Nu	Nusselt number. [-]
Nu_{av}	Average Nusselt number,$\frac{h_{av}D_h}{k_f}$ [-]
n	Normal vector, [-]
$P_{ch,in}$	Pressure inlet, [pa]
$P_{ch,out}$	Pressure outlet, [pa]
ΔP_{ch}	Channel pressure drop, [pa]
ΔP_{ex}	Sudden expansion loss, [Pa]
ΔP_c	Sudden contraction loss, [Pa]
p	Pressure, [pa]
P_o	Pressure outlet, [Pa]
Pr	Prandtl number, [-]
Po	Poiseuille number, *fRe* [-]
Q_k	Volume flow rate of channel k, [m^3/s]
Q_{total}	Total volume flow rate, [m^3/s]
q''	Heat flux, [W/ m^2]
R_{eqv}	Non-dimensional equivalent sphere radius, [-]

Re	Reynolds number, $\frac{\rho_f V D_h}{\mu_f}$ [-]
Ra	Average roughness, [m]
T_w	Wall temperature [K]
T_f	Fluid temperature, [K]
$T_{f,av}$	Average fluid temperature, [K]
$T_{w,av}$	Average wall temperature. [K]
T_i	Fluid inlet temperature, [K]
T_o	Fluid outlet temperature, [K]
U_B	Velocity bubble, [m/s]
U_{Gs}	Superficial gas velocity, [m/s]
U_{Ls}	Superficial liquid velocity, [m/s]
U_{TP}	Mixture velocity, U_{Gs} + U_{Ls} , [m/s]
V_p	Velocity in the manifold, [m/s]
V_i	Velocity inlet, [m/s]
V_{ch}	Velocity inside the channel, [m/s]
V_{max}	Maximum velocity, [m/s]
$\vec{V}$	Velocity, [m/s]
$\bar{V}$	Average velocity, [m/s]
V_P	Velocity in the plenum, [m/s]
v_f	Fluid specific volume, [m^3/kg]
W	Width, [m]
W_{ch}	Channel width, [m]
We	Weber number, [-]
x,y,z	Cartesian coordinates, [m]

Greek symbols

α	Void fraction, [-]
β	Homogenous void fraction, [-]
β_k	Dimensionless channel flow ratio, [-]
δ	Liquid film thickness, [-]

ε_g	Void fraction of unit cell volume, [-]
κ	Interface curvature, [-]
μ	Viscosity, [kg/m s]
μ_f	Fluid viscosity, [kg/m s]
ρ	Density, [kg/m^3]
ρ_f	Fluid density, [kg/m^3]
σ	Surface tension, [N/m]
$\bar{\sigma}$	Mean flow rate, [m^3/s]
σ_k	Channel flow rate, [m^3/s]
τ	Shear stress, [Pa]

Subscripts

av	Average
Gs	Superficial gas
i	Inlet
in	Inlet
Ls	Superficial liquid
Man	Manifold
num	Numerical
out	Outlet
TP	Two phase

Abbreviations

CSF	Continuum surface force
exp	Exponential
MF	Maldistribution factor
VOF	Volume of Fluid

1 INTRODUCTION

1.1 Research Background

Recently, microchannel flow has found application in compact heat exchangers, electronic cooling, bioengineering and biotechnology, aerospace, Micro-Electro-Mechanical Systems (MEMS), material processing and thin film deposition technologies. Microchannels have characteristics dimensions ranging from 10-1000 μm, Morini (2004); Qu *et al*. (2006) ; Bandara *et al*. (2015) and serve as flow passages for cooling liquid. Microchannel heat sinks are a reliable cooling technology due to their superior heat carrying capability. They combine a very high surface area to volume ratio, a large convective heat transfer coefficient, a small mass and volume, and a small fluid inventory. Typically, they are fabricated from high-thermal-conductivity solid substrates such copper or silicon. Microchannel heat sinks contain a series of parallel microchannels that serve as flow passages for the liquid coolant. Because of advances in microfabrication techniques, it is possible to build microchannels with micrometer dimensions. Several manufacturing techniques for the fabrication of microchannel have been used by researchers, such as milling, sawing, anisotropic wet chemical etching, dry plasma etching, surface micromachining and laser cutting. Microchannels act as a heat sink that is attached to the surface of an electronic device. The heat generated by the electronic device is transferred by conduction to the microchannels through the solid substrate of the heat sink, and carried away from the heat sink by liquid flowing through the microchannels, Qu and Mudawar (2002); Qu *et al*. (2006); Pan *et al*. (2008). Microchannel heat sink studies started with Tuckerman and Pease`s (1981) pioneering work in which they studied the heat transfer capability of water flowing under single phase laminar conditions through silicon wafer microchannels. They suggested that the heat transfer coefficient of

working fluid increases with decreasing hydraulic diameter of microchannel. Heat flux values of 790 W/cm^2 was achieved so that the chip temperature was maintained below 110 °C. Their pioneering work has motivated many researchers to focus on this topic and microchannel flow has been recognised as a high performance heat removal tool.

Microchannel heat sinks are classified into single phase and two phase according to whether boiling of liquid occurs inside the microchannels. Both topics have been extensively studied by numerous researchers in past decades. Single phase flow in microchannel relies on a sensible heat rise to achieve cooling. The large streamwise temperature gradient designed for high flux situations results in a high pressure drop, Mudawar (2011). Compared to single-phase microchannel flow, two-phase flow offers the following important additional benefits: a higher convective heat transfer coefficient, a better axial temperature uniformity, and smaller coolant flow rates, Qu and Mudawar (2003)

1.2 Research Motivation

The rapid development of small, mini and microfluidic devices is driving the demand for a comprehensive understanding of the underlying transport mechanisms. Most of the microchannel flow studies reported in open literature were concerned with understanding the fundamentals of microchannel flow, the validity of conventional theories to microchannels and the reasons of the deviations. However, there are still numerous open questions to be answered before reliable design tools are available in the form of correlating equations for heat transfer and pressure drop. The comparative analysis by Kadam and Kumar (2014) showed that available single phase and two phase correlations are inconsistence and a large variation is observed among these correlations for the same channel geometry, fluid and operating conditions. Furthermore, the discrepancies reported in the past studies can be due to measurement uncertainties and scaling effects as reported by Rosa *et al*. (2009). They concluded that

macro scale theory and correlations are valid at micro scale if the measurement uncertainty and scaling effects were carefully considered. However, a consistent model description of fluid flow and heat transfer on the microscale is still needed.

Currently, parallel microchannel are widely used in micro heat exchangers due to their large contact area with the liquid and the availability of a large mass of fluid to carry away heat. Requirements for such heat exchangers are a high heat dissipation rate combined with a low junction temperature. The geometrical structure of the manifold and the microchannels play an important role in the flow distribution between microchannels, it might affect the heat and mass transfer efficiency and even the performance of the micro heat exchanger. However, along with their high thermal power, these exchangers are associated with higher pressure drops. Most literature studies focus on optimising the design of the microchannel heat sink. Most studies were limited and only studied one single cell without considering the flow distribution over multiple channels, Fedorov and Viskanta, (2000); Qu and Mudawar, (2002). This simplification used in previous studies, led to under or over-prediction of the microchannel heat sink performance and inconsistent results in the open literature. However, in experimental studies, it is difficult to employ conventional measurement techniques for microchannel heat sinks with which to extract localised flow and temperature data needed to characterise the fluid flow and heat transfer. Therefore, the practical design of exchangers basically involves the selection of an optimized solution, keeping an optimal balance between gain in heat transfer and the associated pressure drop penalty, Dixit and Ghosh (2015).

Flow boiling provides a very effective means of heat transfer compared to a single-phase flow due to the large latent heat transfer at a constant temperature in a liquid, Kandlikar *et al*. (2013). The key design issue in two phase flow boiling are the variation in flow regimes, the occurrence of a dry-out condition, flow instabilities, and understanding of the heat transfer coefficient and vapour quality, Sardeshpande and Ranade (2013). However, in view of the great complexities and instability of the flow boiling, non-boiling two phase segmented flows are still being considered favourably Bandara *et al.* (2015). Prior to the heat transfer investigation for the two phase non-boiling flow, two phase flows under adiabatic conditions have been investigated by

many researchers. In spite of extensive research, large deviation of the reported results still exists, especially for the observed flow patterns and heat transfer coefficients.

The study of flow regimes is important because the pressure drop and heat transfer characteristics cannot be predicted accurately in the absence of comprehensive information about the difference types of flow regime present, Kadam and Kumar (2014). Two phase flows have been studied widely over the last decades, flow patterns have been identified and boundaries between flow patterns have been defined by visual observations. The main issue occurs due to the variety in flow pattern definitions used by different authors, and also due to difficulties involved in the identification of transition flows, McQuillan and Whalley, (1985). Knowledge of flow regime and flow regime transition paths is essential for the development of predictive tools for the design and performance assessment of two phase flows in microchannels. Furthermore, recently transport phenomena in the slug flow regime for gas-liquid flows in microchannels have received significant attention due to enhanced mixing and heat transfer resulting from the internal recirculating inside liquid slug due to the presence of a gas bubble, He *et al*. (2010);Kumari *et al*. (2019). Because of the enhanced mixing, the slug flow regime is employed in a wide range of applications i.e microreaction technologies for mass transfer operations and reactions processes (with or without catalyst involved), Yue *et al*. (2008);Yao *et al*. (2019), electronics cooling, Zhao and Bi, (2001), compact heat exchanger, Bao *et al*. (2000). Many studies has been conducted extensively using both experimental, Walsh *et al*., (2010); Lim *et al*. (2013); Yao *et al*. (2019) and numerical techniques, He *et al*. (2010); Asadolahi *et al*. (2011); Kumari *et al*. (2019). However, most of studies have been neglecting heat transfer in slug flow, Choi *et al*. (2010); Kurimoto *et al*. (2018).

Performing experiments with microchannels can be very costly in both time and money. To reduce the number of experiments that need to be performed researchers employ Computational Fluid Dynamics (CFD) as a tool for heat transfer analysis. CFD can be used when setting up experiments as a tool to predict the flow parameters and boundary conditions. Application of computational methods can significantly shorten the design cycle and thereby reduce experimental costs. In CFD solutions to the Navier-Stokes equation, derived from Newton's second law of motion,

are approximated using numerical methods. The Navier-Stokes equations describe the flow of a Newtonian fluid using a continuum assumption. The equations are then solved by a CFD solver to approximate flow variables throughout the computational domain. CFD simulations have been used to study many different aspects of microchannels, Tullius *et al*. (2011). Examples of CFD applications in the chemical process industry include drying, combustion, separation, heat exchange, mass transfer, pipeline flow, reaction, mixing, multiphase systems and material processing. Validation of CFD models is often required to assess the accuracy of the computational model. This assessment can assist in the development of reliable CFD models. Analyses based on the Navier-Stokes and energy equations would be expected to model the phenomena observed adequately, as long as the experimental conditions and measurements are identified and simulated correctly, Sobhan and Garimella (2001). Validation is achieved by comparing CFD results with available experimental, theoretical, or analytical data. Validated models become established as reliable, while those that fail the validation test need to be modified and revalidated.

1.3 Research Objectives

The numerical research presented in this thesis aims to employ the Fluent CFD solver to investigate flow and heat transfer in micro channel configurations. The following objectives are identified:

- Perform numerical simulations of single phase flow in single and multichannel micro heat exchangers.
- Compare numerical results with standard theory and correlations and assess the effect of size on flow and heat transfer.
- Examine the effect of conjugate heat on fluid flow and heat transfer.

- Examine the effect of geometry including shape of manifolds and number of channels on flow distributions, pressure drop and heat transfer rates in multichannel systems.
- Study of the flow patterns map of adiabatic two-phase flow in circular microchannels.
- Study the fluid flow and heat transfer of slug flow in circular microchannels without phase changes.

1.4 Thesis Structure

Chapter 1 gives an introduction of the project work, including the definition of a microchannel, the application of CFD to solve flow and heat transfer in microchannels, discussions of single-phase and two-phase flow issues, presenting the research objectives, and providing an outline of the thesis. In **Chapter 2** an extensive literature survey is presented providing an overview of both experimental and theoretical research related to single and two-phase flow as well as heat transfer in micro channels. In the theoretical survey, the emphasis is mostly on literature presenting results obtained using computational fluid dynamics (CFD). **Chapter 3** presents the relevant equations that are employed to model single phase and two-phase flow in a micro channel. These model equations include the continuity equation, the momentum equations and the energy equation. **Chapter 4** presents the results obtained simulating single-phase fluid flow in a single rectangular micro channel for both the laminar and the turbulent regime. In this section, the effects of conjugate heat, hydraulic diameter and aspect ratio are discussed. **Chapter 5** presents results obtained in simulations of single phase fluid flow in a multichannel configuration, consisting of a series of rectangular micro channels in parallel. Geometric effects related to the manifold design and the number of channels on the flow distribution inside the parallel micro channels are studied. In **Chapter 6** two phase flow in a single circular microchannel is studied and the design of numerical works pursued two aims. The first aims were to developed

numerical flow regime maps in order to identify the slug flow boundaries in dependence on annular nozzles configurations and on liquid properties. In this work, the flow field has been calculated using a two dimensional, axisymmetric geometry due to save computational time and effort. Secondly, a three dimensional work was carried out to examined the topology of hydrodynamic flow and heat transfer distribution of slug flow. Furthermore, was to related those to the operation condition, i.e; gas superficial velocity. **Chapter 7** present the overall conclusion and future recommendations, respectively.

2 LITERATURE REVIEW

A comprehensive literature review of previous work on single phase and two phase flow in microchannels is presented in this chapter. Detailed predictions/experimental results on the friction factor and heat transfer values and probable reason for discrepancies are discussed. The capability of CFD methods to be used in the study of single and two-phase flows in microchannels is reviewed. The literature review on microchannel revealed that there are many important factors that need to be considered while evaluating the fluid flow and heat transfer. These are presented and discussed in the chapter.

2.1 Microchannel

The word 'micro' was embraced enthusiastically with the opening of its newest branch in microscale heat transfer. The details of the channel size to distinguish between macroscale channel and microchannel were proposed by Mehendale *et al*. (2000) and Kandlikar (2002) (see Table 2-1). Mehendale *et al*. (2000) defining heat exchangers in term of hydraulic diameter, while Kandlikar (2002) have classified the channels based on engineering application areas.

Table 2-1 : Channel classification by Mehendale *et al*. (2000) and Kandlikar (2002).

Mehendale *et al*. (2000)		Kandlikar (2002)	
Micro heat exchanger	D_h =1-100 µm	Microchannels	D_h =10 -200 µm
Meso heat exchanger	D_h =100 µm - 1mm	Minichannels	D_h =200 µm – 3 mm

Compact/macro heat exchanger	D_h =1 – 6 mm	Conventional channels	D_h > 3 mm
Conventional heat exchanger	D_h > 6 mm		

The next range under this classification, termed as microchannel, is influenced by the rarefaction effects for gases, as described by the Knudsen number, Kn:

$$Kn = \frac{\lambda}{D_h} \tag{2.1}$$

where λ is the mean free path for the gas calculated from the following equation:

$$\lambda = \frac{\mu\sqrt{\pi}}{\rho\sqrt{2RT}} \tag{2.2}$$

where R is gas constant, μ is dynamic viscosity, ρ is density, and T is absolute temperature. The microchannel range, covering 10 μm to 200 μm, is generally affected by the rarefaction effects for many gases. The continuum approach with no wall slip is modified in these channels; this approach being valid for $0.1>Kn>0.001$, the region identified as the slip region. Below 10 μm, depending on the gas and the pressure, the transitional region is encountered, where rarefaction effects are more severe and approach the molecular flow. The range $10 \geq Kn \geq 0.1$ is referred to as the transitional region. Although the above criteria are developed mainly from gas flow considerations, they are recommended for both liquid as well as two-phase flow applications to provide a uniformity in channel classification.

2.2 Single Phase Fluid Flow and Heat Transfer in Microchannels

A comprehensive study on convective heat transfer and pressure drop in microchannels have been extensively conducted in last past decade due to high heat transfer coefficients and low to moderate pressure drops when compared to conventional cooling systems for small scale devices. Past reports were reviewed and summarized by a few researchers to identify the heat transfer mechanisms and pressure drop in microchannel. Dixit and Ghosh (2015) reviewed over 200 past works on micro- and minichannels for single phase fluids. In this paper they pointed out that the discrepancies of past papers on the application of conventional theory to determine the friction factor and heat transfer values of micro- and minichannels was still a questionable issue, and it needed to clarification with the intention of giving direction to researchers regarding the applicability of conventional theory in mini- and microchannels or news ideas need to be applied. Asadi *et al*. (2014) noted that most researchers derived correlations for predicting pressure drop and heat transfer coefficient in microscale by assuming macroscale behaviour. They claimed, this is one of the reason of inconsistencies between published results and conventional predictions either in laminar and turbulent region. However, Rosa *et al*. (2009) recommended that conventional correlations are reliable for microchannels if the scaling effects are considered carefully.

2.3 Single Phase Pressure drop

In conventional laminar flow, the Re number is independent on Poiseuille number (*Po*). It has a constant value of 64 for circular pipe using Darcy friction factor, *f*. Poiseuille number is represent the fully developed laminar flow friction data for conventional size ("macroscale") channels as shown in Eq. (2.3).

$$Po = fRe \tag{2.3}$$

In fluid flow analysis, the friction coefficient or Fanning friction factor (C_f) are commonly used, where $f = 4C_f$. The Fanning friction factor is defined as the ratio of the wall shear stress to the flow kinetic energy per unit volume as shown in Eq. (2.4) and the friction factor in terms of the pressure drop, Δp and mass flux, G is given in Eq. (2.5).

$$C_f = \frac{\tau}{0.5\rho\bar{V}^2} \tag{2.4}$$

where, τ is the wall shear stress, ρ is the fluid density, and $\bar{V}$ is the average velocity

$$f = \frac{\Delta p D_h \rho}{2LG^2} \tag{2.5}$$

where, D_h is the hydraulic diameter and L is the channel length.

For non-circular channel, Shah and London (1978) determined a Poiseuille number for fully developed laminar flow and developing flow in a function of aspect ratio as shown in Eq. (2.6) and (2.7), respectively. This correlation is valid for aspect ratio less than one.

$$fRe = 24[1 - 1.3553AR + 1.9467AR^2 - 1.7012\,AR^3 + 0.9564AR^4 - 0.2537AR^5] \tag{2.6}$$

$$f_{app}Re = \frac{3.44}{\sqrt{x^+}} + \frac{(fRe)_{fd} + \frac{K(\infty)}{4x^+} - \frac{3.44}{\sqrt{x^+}}}{1 + \frac{C\prime}{(x^+)^{0.2}}} \tag{2.7}$$

where

$$K(\infty) = 0.6611 + 1.182\,AR + 2.1758\,AR^2 - 5.8322\,AR^3 + 4.4683\,AR^4 - 1.1553\,AR^5 \quad (2.8)$$

and

$$x^+ = \frac{x}{ReD_h}$$

In fully developed turbulent flow, the Blasius correlation (Eq. 2.8) is used for conventional smooth tubes in both circular and non-circular channel. However, for the developing turbulent flow, the friction factor was developed by Phillips (1987) in Eq. (2.9)

$$f = \frac{0.0791}{Re^{-0.25}} \quad (2.9)$$

$$f_{app} = \left(0.0929 + \frac{1\,01612}{L/D_h}\right) Re^{*\left(-0.268 - \frac{0.3293}{L/D_h}\right)} \quad (2.10)$$

where

$$Re^* = Re\left(\frac{2}{3} + \frac{11}{24AR}\left(2 - \frac{1}{AR}\right)\right) \quad (2.11)$$

2.3.1 Friction factor and comparison with conventional theory results

In last few years, several studies on microchannel friction factor were reported. Some authors addressed a validity conventional theory to describe fluid flow in single phase in microchannel. In the early 1990s, Rahman and Gui (1993) conducted an experiment to investigate forced convection using water in trapezoidal cross section channels made with silicon with D_h ranging between 175 to 325 μm. Their experimental friction factors values showed good agreement with the convectional theory. Later, the **s**ame conclusion was drawn by Harm *et al*. (1999) based on their

experiment in deep rectangular microchannels for single and multiple configurations with hydraulic diameter of the channels were 1923 μm and 404 μm, respectively. However, the flow transition occurred at *Re* =1500, which is earlier that the expected value for conventional tubes, at Re from 2300 to 3000. Controversial phenomena between two different microchannel heat sinks made of aluminium and silicon were found by Xu *et al*. (2000) where the friction factor was smaller than the prediction of conventional theory, occurred in aluminium plate for D_h less than 100 μm. However, the friction factor in the silicon microchannel was in good agreement with the prediction from conventional theory. They attributted the differences observed in the aluminium channels compared to the silicon channels to deviations in the channel cross sectional area resulting from the difference in the manufacturing method and test section sealing. The aluminium channels were manufactured by machining on aluminium substrate and sealed by a top cover which might create a small gap at the top of the channel. The silicon channels were fabricated by the etching method which is more accurate than machining and the top cover sealed the test section using an anodic bonding technique. Additionally, the onset of transition from laminar to turbulent flow in the aluminium channels occurred at *Re* = 1500. Yang and Lin (2007) summarized that the friction factors predicted by the conventional correlations is applicable in microtubes applications. They carried out their experimental study in both laminar and turbulent region in a stainless steel microtube and water was used as the working fluid. There was no significant deviation in measured friction factors of water flow in tested tubes with conventional theories (f=16/Re). Celata *et al*. (2002) investigated the flow characteristics and forced convection heat transfer of R114 flowing through six microtubes with hydraulic diameter of 0.130 mm and in 90 mm length. The microchannel was fabricated from stainless steel. The experimental tests are carried out in a wide range of *Re* between 100-8000. The measured friction factor is in good agreement with Poiseuille theory in laminar flow regime for *Re* < 585. They found the transition occurs at range of *Re* from1880 to 2480.

Agostini *et al*. (2006) conducted an experimental study to investigate liquid flow friction and heat transfer coefficient in three different cross section shape; rectangular, circular and square, by using refrigerant R134a. The hyraulic diameter ranged from 0.77-2.01 mm. The presented results show, that transition occurred at

1400 < *Re* < 2000 , which is closed to the accepted value for conventional theory. Additionally, the measured friction factor is in good agreement with the macroscale theory if the pressure losses were take into account. Mokrani *et al*. (2009) study the characterization of fluid flow and heat transfer in rectangular cross-section channels in the fully developed region. The transition region between laminar and turbulent occurred at *Re* between 2000 to 3000 for all tested channels. They concluded that the conventional laws and correlations are applicable to microchannels with $D_h \geq 0.1$ mm. They noted that the descripancies in literature were due to entrance effect.

Some researchers investigated the effect of fluid properties, channel material and channel geometry on fluid flow in microchannels. However, they claimed no evidence to suggest the significant influences of parameter, such as Judy *et al*. (2002) conducted an experimental study to measure the single phase pressure drop in circular and square microchannels. The microchannels were fabricated from two different materials namely fused silica and stainless steel. The hydraulic diameter and length of the channels ranged from 0.015 to 0.15 mm and 36 to 300 mm, respectively. All channels were tested using three fluids; distilled water, isopropanol and methanol. No difference in behaviour was found for circular and square channel geometries and the Poiseuille number (*Po*) was nearly independent of Re for all diameter ranges in the laminar regime. The measured friction factor was in good agreement with the conventional laminar flow theory, without early transition and no significant influences of fluid properties were detected. Han and Kedzierski (2008) designed an experimental setup to using three tubes made of three different materials. Fused silica, polyetheretherketone and stainless steel were used to study the effect of surface condition on pressure drop. They used three ionic concentrations of water; distilled water, tap water and deionized water to study the effect of fluid ionic composition on pressure drop. In addition, there was no early transition observed and this region occurred approximately at *Re* ≈ 2000. Silverio and Moreira (2008) conducted an experiment to measure a pressure drop for three different working fluids; distilled water, methoxy-nonafluorobutane and methanol in circular and square channels. The friction factor results obeyed conventional theory for hydraulic diameter range between 200 and 500 μm at *Re* number more than 100.

Zhang *et al*. (2014) studied experimentally the effect of hydraulic diameter and aspect ratio on fluid flow and heat transfer of water in aluminium multiport microchannel flat tubes. The hydraulic diameter was varied from 0.48 mm to 0.84 mm while the aspect ratio was nearly constant (AR = 0.83 – 0.88) and the aspect ratio was varied from 0.45 to 0.88 while the hydraulic diameter was almost constant (D_h = 0.6 – 0.63 mm). The relative roughness of all tested samples ranged from 0.29 % to 1.06 %. The experiments were performed for Reynolds number ranging from 120 to 3750. They reported that the friction factor for all test samples agrees well with the correlation of Shah and London (1978) for fully developed laminar flow and thus they concluded that the effect of entry region is negligible for $L/D_h > 179$. The transition from laminar to turbulent flow was found to occur at Re = 1200 – 1600 without an evidence on the correlation between aspect ratio and the early transition from laminar to turbulent flow.

In numerical work, Fedorov and Viskanta (2000) developed the three-dimensional model to investigate flow and conjugate heat transfer in presence of surface chemical interactions. The approximation of fully developed flow was eliminated. Predicted Poiseuille friction law are linearly proportional to the Reynolds number and had a well agreement with conventional theory. Gao *et al*. (2002) investigated single phase flow of water in rectangular microchannels etched in a silicon wafer with a channel height range 0.1 – 1 mm and a fixed width of 25 mm (AR = 0.003 – 0.04 and D_h = 0.008 – 0.077 mm). The surface roughness was less than 0.1 µm. The results demonstrated that channel height does not have a significant effect on the Poiseuille number in the laminar region where the value was almost constant at about 24 (the fully developed value). Also, the length of the entry region was found to be equal to $0.1ReD_h$. It is worth mentioning that the transition was found to occur at Re = 3500 – 4000.

Later, Baviere *et al*. (2006) also pointed out the insignificant effect of geometrical parameter. They performed further experiments and numerical simulation in a test-section similar to Gao *et al*. (2002). The presented results of friction factor were in a good agreement with the laminar theory. The observed value of the critical Re numbers were found to vary from 3500 to 4500. They pointed out that the validity

of the conventional theory may be extended to small microchannel tested in this study. Qu and Mudawar (2002) conducted both an experimental and numerical study to predict the pressure drop in rectangular microchannel heat sink, which was fabricated from oxygen-free copper. Water was used as working fluid. There was no early transition reported by these authors. The authors have suggested the applicability of conventional Navier–Stokes and energy equations to predict fluid flow and heat transfer in microchannels. Lelea *et al*. (2004) conducted an experimental and numerical study to investigate heat transfer and fluid flow in microtubes. The diameters of the microtubes were 0.1, 0.3, and 0.5 mm and flow regime was laminar *Re* range up to 800. The working fluid was distilled water and material was stainless steel. Based on the results, the fRe will be constant if the total length of the tube is heated, while the value of fRe will be lower than the conventional for partial heating (total length heated $\neq$ total length). However, no early transition occured in their results.

Kim (2016) conducted an empirical study on fully developed laminar flow on FC770 and water through rectangular microchannel. They concluded that laminar friction factor were agree well with the conventional Poiseuille flow theory.

2.3.2 Friction factor not in agreement with conventional theory

In this section, reports on single phase frictional characteristics that are not in agreement with conventional correlations reported in the literature are discussed. The significant influence of geometric configurations on microchannel flow behaviour was reported by Peng *et al*. (1995a). They investigated experimentally flow characteristics of water flowing through rectangular microchannels having a hydraulic diameter range of 0.113 – 0.367 mm, an aspect ratio range of 0.333 – 1 and a relative average roughness (Ra/D_h) range of 0.6 – 1 %. The friction factor was found to deviate significantly from the conventional laminar flow theory. They proposed a new empirical correlation in which the friction factor was proportional to $Re^{-1.98}$ in the

laminar region, while for turbulent it is $Re^{-1.72}$. It is worth mentioning that the different flow regimes (laminar, transitional and turbulent) were identified from changes in the slope of the friction factor plotted against *Re*. In addition, the early transition occurred at Re number ranging from 200 to 700 was reported by them. They attributed this early transition to the significant effect of the channel wall, which influences the intensity of the velocity fluctuations due to inertia and viscous forces. However, the reported unusual phenomena at *AR* of approximately 0.5 where the friction factors lower than conventional theory. They indicated that *AR* of approximately 0.5 is an optimum parameter in designing the microchannel heat exchanger devices. Pfund *et al*. (2000) conducted an experimental study to measure the pressure drop directly across a microchannel excluding entrance and exit losses. The test section was designed such that flow visualization was possible in order to detect different flow regimes (laminar, transition and turbulent). The channel width and length were kept constant at 10 mm and 100 mm, respectively, while the channel height was varied from 0.128 to 1.05 mm (AR = 0.0128 – 0.105 and D_h = 0.025 – 0.19 mm). The surface roughness of the examined chanenls ranged from 0.16 μm to 1.9 μm . The local pressure was measured at eleven equidistance locations along the channel. Water was used as the working fluid. The onset of laminar-to-turbulent flow transition was found to occurr at a *Re* range of 1500 – 2200, where the lower value corresponds to the smaller channel depth. The Poiseuille number (*Po*) was found to be significantly higher than the theoretical value for fully developed laminar flow as predicted by Eq. (2.4) given by Shah and London (1978). The deviation was found to increase with either decreasing the channel height for the same surface roughness (0.16 μm average roughness) or increasing the surface roughness for the same channel height (1.9 μm average roughness). However, they reported that it is difficult to conclude which parameter (channel geometry or surface roughness) has the strongest effect on the Poiseuille number (*Po*) due to the experimental uncertainty of their experiment

A similar conclusion was reached by Mala and Li (1999) in their experimental work of water flow in different types of microtubes; fused silica and stainless steel. The hydraulic diameter ranges between 50 - 254 μm. A significant deviation from conventional theory was observed based on their friction factor results for small diameters, while for large diameter tubes, the experimental results are in good

agreement with the classical theory. The measured pressure drop and friction factor were higher than the predicted conventional for D_h less than 150 and at *Re* greater than 500. They noted that the deviation from the conventional Poiseuille flow theory was significantly affected by the surface roughness of the channel. In addition, they also suggested that the higher value of friction factor is due to the early transition that may occur in smaller microtubes. They reported the transition region started in the Reynolds number range of 300 to 900. In addition, a pressure gradient in a fused silica microtube is higher than in a stainless steel microtube for identical flow rate and channel diameter size. The obtained result indicated material dependence of the flow behaviour. Later, similar work also was conducted by Li *et al*. (2007) However they observed the measured friction factor was in agreement with conventional theory, for smooth fused silica microtubes, while, for stainless steel tubes showed a significant deviation from conventional friction factor when the relative surface roughness larger than 1.5%. Pressure measurements were carried out by Ergu *et al*. (2009) with distilled water in rectangular microchannel having width, height and length, 3.70 mm, 0.107 mm and 35 mm, respectively. The experiment friction factors values were slightly higher than those calculated with the theoretical correlation and the deviation increased with increasing Reynolds number. They indicted this can be attributed to the roughness of the surface. However, the effect of surface roughness on friction factor can be neglected at low Reynolds numbers. They also indicated that the classical laminar flow equations can also be used for the calculation of friction factor in microchannel in the range of the presented channel dimension on flow conditions.

Contrary to the above that some of researchers reported that frictional factor was found lower than that given by the conventional theory. For example, a smaller value of friction factor, as compared to conventional theory was observed by Choi *et al*. (1991). They performed experimental investigations on nitrogen gas through micro-tubes with diameter between 3 to 81μm and *Re* up to 20,000. They proposed a friction factor correlation given by Eq. (2.12)

$$f = \frac{53}{Re} \tag{2.12}$$

However, they indicated that the surface roughness had no significant effect on the friction factor. Later**,** Yu *et al*. (1995) continued the work by Choi *et al*. (1991) in an experiment with nitrogen and water flow in micro-tubes for Reynolds number ranging from 250 to over 20,000. Similar observations were also made by them, i.e. the friction factor for both water and nitrogen was less than the theoretical value in laminar and turbulent region. The also recommended relation, f=50.13/Re at Re less than 2000, while in turbulent flow can be expressed as, f=0.302/$Re^{0.25}$. Peng and Peterson, (1996) single-phase forced convective heat transfer and flow characteristics in rectangular channels with having hydraulic diameters of 0.133 to 0.367 mm. Water was used as working fluid. They observed the friction factor in fully developed turbulent flow was smaller than the predicted friction factor from conventional correlation.

Gamrat *et al*. (2005) performed a 2D and 3D numerical study on the conduction and entrance effects on laminar flow heat transfer of water in rectangular microchannels. They modeled the geometry of the test section used in the experiments conducted by Gao *et al*. (2002) mentioned above for a *Re* number range 200 – 3000. The numerical Poiseuille number results was found to be significantly smaller than that predicted by Eq. (2.5) below given by Shah and London (1978) for developing laminar flow. The value of the constants $K(\infty)$ and C' in Eq. (2.5) depend on the channel aspect ratio and the values are given in Shah and Sekulic (2003). They attributted this deviation to the boundary layer characteristics at the channel entrance which were not considered in the model of Shah and London (1978) who assumed a uniform velocity profile at the channel inlet. Furthermore, the numerical results revealed no significant size effects on heat transfer in the microchannel heat sink down to the smallest size considered in their paper (0.1 × 25 mm).

2.4 Single Phase Heat transfer

The common non-dimensional parameter used in order to represent the heat transfer of micro heat exchanger device is Nusselt number. The Nusselt number for fully developed flow in circular ducts in conventional sizes channel, the Nusselt number is constant 4.36 for uniform heat flux boundary condition and 3.66 for uniform wall temperature boundary condition. In non-circular ducts with aspect ratio of 1, the Nusselt number for constant heat flux and constant uniform temperature, is constant 3.61 and 2.98, respectively, Incropera *et al*. (2006). In addition, heat transfer correlations for laminar and turbulent flows in channels have been widely employed in the literature for comparison against experimental results for microchannels are shown in Table 2-2.

Table 2-2 : Conventional correlations from the literature for the prediction of channel heat transfer.

Dittus–Boelter (1930)	Dittus–Boelter correlation: $$Nu = 0.023Re^{0.8}Pr^{1/8}$$	(2.13)
Sieder and Tate (1936)	Sieder–Tate correlation: $$Nu = 1.86\,(\frac{RePrD}{L})^{1/3}\left(\frac{\mu_f}{\mu_w}\right)^{0.14}$$	(2.14)
Gnielinski (1976)	Gnielinski's correlation: $$Nu = \frac{\left(f/8\right)(Re-1000)Pr}{1+12.7\left(f/8\right)^{0.5}(Pr^{\frac{2}{3}}-1)}$$ where	(2.15)

	$f = \frac{1}{(1.82\ln(Re) - 1.64)^2}$	
Shah and London (1978)	$Nu = 1.953\ (RePr\,{}^{D}/_{L})^{1/3}$ for, $RePr\,{}^{D}/_{L} \geq 33.3$ $Nu = 4.364 + 0.0722RePr\,{}^{D}/_{L}$ for, $RePr\,{}^{D}/_{L} < 33.3$	(2.16) (2.17)

2.4.1 Nusselt number was agree with conventional theory

Single phase heat transfer research in microchannels has been extensively conducted in past decade. Some authors observed that the heat transfer characteristics were in agreement with conventional theory; see Harms *et al*. (1999); Lelea *et al*. (2004); Owhaib and Palm (2004); Qu and Mudawar (2002); Lee and Garimella (2006). Harms *et al*. (1999) and Lelea *et al*. (2004) suggested that the local Nusselt number is in a good agreement with the conventional theory, if entrance effects were considered. Later, Lee and Garimella (2006) investigated laminar convective heat transfer in the entrance region of microchannels of rectangular cross-section. The generalized correlations proposed by authors for predicting Nusselt numbers were compared with conventional correlations proposed by Chandrupatla and Sastri (1977) and Perkins *et al*. (1973) and with available experimental data, and found to be in very good agreement. Owhaib and Palm (2004) investigated the heat transfer in forced convective single-phase flow of R134a through circular microchannels with having inner diameter of 1.7, 1.2, and 0.8 mm Based on the comparison of the obtained Nusselts numbers with both the conventional correlations developed for macroscale channels, Dittus–Boelter (1930), Gnielinski (1976), and Petukhov (1970), they indicated the applicability of the classical correlations at fully developed turbulent flow on

microchannel. Furthermore, observed the insignificant effect of diameter tube on Nusselt number.

2.4.2 Nusselt number not in agreement with conventional theory

Many studies on turbulent regime have been reported and found significant deviation of microscale heat transfer characteristics from conventional theory. Yu *et al*. (1995) concluded that in the heat transfer is much higher than macro-scale conventional theory turbulent regime. They studied the fluid flow and heat transfer characteristics of dry nitrogen and water flow in a circular channel with a diameter of 19, 52, and 102 μm. They recommended a new correlation for heat transfer based on their experimental results as shown in Eq. (2.18)

$$Nu = 0.007Re^{1.2}Pr^{0.2} \qquad 6000 < Re < 20{,}000 \qquad (2.18)$$

Higher value of heat transfer coefficient in turbulent region was also found in experimental work conducted by Choi *et al*. (1991) and they concluded that this might be due to the suppression of turbulent eddy motion in the radial direction in small diameter channel. There was no significant effect found of surface roughness on heat transfer coefficient. In addition, Wang and Peng, (1994) indicated that the single phase heat transfer in turbulent flow could be predicted using the macroscale, Dittus-Bottler's equation, by adjusting the Dittus-Boelter constant coefficient from 0.023 to 0.00805. They claimed that liquid temperature, flow velocity and microchanne size have a great significant effect on both transition and laminar flow heat transfer characteristics. Later, Adam *et al* (1998) also proposed a modification of another existing conventional correlation, the Gnielinski correlation. They performed experiments to investigate the heat transfer characteristics of water flow through circular microchannels (0.76 mm < Di < 1.09 mm) in turbulent region, Re > 3200. They attributed the occurrence of experimentally observed higher values of Nusselt number, as compared to Gnielinski correlation due to reduction of channel size.

The experimentally obtained heat transferred coefficient by Rahman and Gui (1993) and Rahman (2000) showed larger value than corresponding analytical predicted values for developing laminar flow. They studied the heat characteristics of water through rectangular microchannels with the hydraulic diameters in the range of 176 –325 μm. They concluded that the reason for the higher value was the breakage of the velocity boundary layer by surface roughness. Unfortunately, the detail surface roughness was not reported by them. In contrast, Qu *et al*. (2000) found that the experimentally determined Nusselt number is much lower than the prediction of the conventional heat transfer theory in their experimental work on water flowing through silicon trapezoidal microchannels, with a hydraulic diameter ranging from 62 to 169 μm. However, similar conclusion has been drawn by them, which the deviation of Nusselt number value and the prediction of the conventional heat transfer is may be due to the presence of surface roughness. They concluded that the presence of surface roughness will reduced the velocity gradient near the wall and lead to reducing of temperature gradient near the wall and therefore, the convective heat transfer is reduced. The effect of surface roughness on heat transfer in a compact copper heat sink was highlighted by Shen *et al*. (2006) and the obtained results were compared with that of the conventional theory. They investigated the single phase convective heat transfer for deionized water flowing through the microchannels rectangular microchannels of 300 μm width and 800 μm depth. They concluded that that both the local and the average Nusselt numbers are significantly lower than the conventional theory predictions. Besides, they also claimed that this differences were attributed to another factor, i.e. is the cross-sectional aspect ratio. Similar opinion about the inclusion of the geometrical effect in the microchannel heat transfer has been suggested by Wu and Cheng (2003). The significant influence of the geometrical parameters; hydraulic diameter and aspect ratio will be discussed in the next section (Section 2.5)

2.5 Effect of geometrical parameter on fluid flow and heat transfer

Several researchers investigated single phase flow and heat transfer in microchannels and reported significant deviations compared to the conventional flow theory and they claimed that this is due to the effect of geometrical parameters. For example, Peng *et al*. (1995) found that the Poiseuille number (*Po*) increases with increasing aspect ratio, which is contrary to the behaviour in conventional large-diameter channels. However, they reported that it is difficult to explain the effect of aspect ratio due to the narrow range of aspect ratios examined in their study (few experimental data). Futhermore, the critical Reynolds number for the onset of transition from laminar to turbulent flow was found to depend on the channel hydraulic diameter. Transition occurred at $Re = 200$ for $D_h \leq 0.2$ mm and at $Re = 700$ for $D_h \geq$ 0.2 mm. Peng and Peterson (1995) investigated the effect of channel size on single phase flow and heat transfer characteristics in microchannels using water and methanol as the test fluids. The channel height was kept constant at 0.7 mm while the channel width was varied from 0.2 to 0.8 mm ($AR = H_{ch}/W_{ch} = 0.875 – 3.5$). These dimensions gave a hydraulic diameter range of 0.155 – 0.747 mm. Their experimental results demonstrated that the start of the laminar-to-turbulent flow transition occurs at $Re \approx$ 300, while a fully developed turbulent flow regime was first obtained at $Re \approx 1000$. Additionally, the heat transfer coefficient in the channel with aspect ratio 1.75 was found to be much higher than the one obtained in other channels. They did not explain why the heat transfer coefficient is high in this channel compared to the other investigated channels. They also indicated that microchannel size play an important role to improve heat transfer performance. Peng and Peterson (1996) investigated the effect of geometric parameter, aspect ratio, and ratio of hydraulic diameter to distance between center to center of microchannel, on water flow in a stainless steel microchannel. The test models have the range hydraulic diameter, D_h = 0.133-0.367 mm, aspect ratio, AR =0.5-3 and length, 45 mm. They proposed two correlations for predicting Nusselt number in laminar and turbulent region.(see eq. 2.16 and 2.17 below) However, they reported that the effect of D_h /W_c on heat transfer and fluid flow in microchannels was not clear in their work and required further investigation.

$$Nu = 0.1165 \left(\frac{D_h}{W_c}\right)^{0.81} \left(\frac{H}{W}\right)^{-0.79} Re^{0.62} Pr^{1/3} \quad (2.19)$$

$$Nu = 0.072 \left(\frac{D_h}{W_c}\right)^{1.15} [1 - 2.421(Z - 0.5)^2] Re^{0.8} Pr^{1/3} \quad (2.20)$$

$$Z = \frac{\min(H.W)}{\max(H,W)}$$

(Gao, et al., 2002) observed that the Nusselt number decreases with decreasing channel height for a channel height less than 0.4 mm. However, the dimensional heat transfer coefficient plotted against channel height indicated an opposite effect where the coefficient increased with decreasing channel height, i.e decreasing D_h. They attributted this behaviour to: (1) possible inappropriateness of using the hydraulic diameter to represent the phenomena at micro scale, (2) electrokinetic effects and (3) the presence of a thin layer of air trapped next to the wall. However, they concluded that there is no satisfactory explanation for the results presented in their study.

In numrical work, Lee and Garimella (2006) conducted three dimensional numerical simulation for laminar thermally developing flow in microchannels under uniform wall temperature and uniform wall heat flux thermal boundary condition. The width and length of the channel in their present study were held constant at 200 µm and 120 mm, respectively, while the height was varied, between 200 and 2000 µm. The tested rectangular ducts having a hydraulic diameter range of 200 - 364 µm and aspect ratio between 1 to 10. The presented local and average Nusselt number was obtained as a function of axial distance $x^*=x/RePrD_h$ and aspect ratio. The Nusselt number was increased as the aspect ratio increase. Gunnasegaran *et al*. (2010) studied the effect of channel shape on water flow and heat transfer in multi-microchannel configuations for Re = 100 - 1000. They studied three different geometrical shapes namely; rectangular, trapezoidal and triangular. For the rectangular geometry, three cases were investigated with hydraulic diameter 0.259 – 0.385 mm and and aspect ratio (H_{ch}/W_{ch}) range 1.03 – 2.56. They reported that the rectangular channel with the

smallest hydraulic diameter has the highest heat transfer coefficient. Also, the heat transfer coefficient and the Poiseuille number were higher compared to the other examined geometries. It was also found that the Poiseuille number increases as the aspect ratio increases. Wang *et al*. (2016) conducted a similar numerical study investigating the effect of channel shape on fluid flow and heat transfer in multi-microchannel configurations. A microchannel heat sinks with rectangular channels having hydraulic diameter ranging 0.172 – 0.406 mm and aspect ratio range 1.03 – 20.33 were investigated. The overall thermal resistance and pumping power were used as evaluation parameters. They reported that the rectangular geometry achieved the best performance for aspect ratio range 8.904 – 11.442 and the rectangular geometry achieved the lowest thermal resisrtance compared to the tringular and trapezoidal geomteries. On the other hand, the pressure drop was found to increase with *Re* and *AR*. This means that increases in Re or *AR* will raise pumping power consumption. Therefore, they suggested that a smaller D_h combined with a larger wetted perimeter and convective heat exchange area in a rectangular microchannel is beneficial for improving the cooling performance of microchannel heat sinks.

Dharaiya and Kandlikar (2012) conducted numerical investigations of heat transfer in rectangular microchannels under uniform circumferential and axial heat flux boundary conditions in fully developed and developing flow. The aspect ratio was varied from 0.1 to 10 and the length of channel was 100 mm . Five different cases were simulated under uniform wall heat flux; (1) four sides heated, (2) three sides heated, (3) two sides heated (opposing walls), (4) two sides heated (adjacent walls), (5) one side heated. The effect of the inlet plenum was studied through simulating a channel with a plenum that has an abrupt decrease in the cross sectional area and another plenum with a gradual decrease in cross sectional area. It was found that the entrance effects on *Nu* in the entry region of the developing flow are insignificant. Also, in the fully developed region, *Nu* was found to reach an asymptotic value and increases with increasing aspect ratio for the four and three sides heated boundary conditions. For the one side and two sides heated boundary conditions *Nu* was found to decrease with aspect ratio. Additionally, the thermal entrance length was found to increase as the aspect ratio increases. Zhao and Lu (2002) conducted an analytic solution and numerical simulation on heat transfer in microchannel heat sink. They effect of

channel aspect ratio was investigated where the Nusselt number increase as aspect ratio increases.

Contrary to the above studies, some reported insignificant influence of geometrical on fluid flow and heat transfer. For example, Zhang *et al*. (2014) observed an insignificant effect of aspect ratio on heat transfer rate and the reported heat transfer enhancements in their study was attributted to the effect of surface roughness and the entry region. Mokrani *et al*. (2009) designed an experimental device and investigated fluid flow and convective heat transfer in low aspect ratio (AR < 0.1) rectangular microchannels by varying the channel height from 0.05 to 0.5 mm and the hydraulic diameter from 0.1 to 1 mm. It was also observed that the microchannel hydraulic diameter has no effect on the Nusselt number.

Rosa *et al*. (2009) investigated the scalling effects on single phase flow in microchannels. They concluded that macro scale theory and correlations are valid at micro scale if measurement uncertainty and scaling effects were carefully considered. These scaling effects include: entrance effects, viscous heating, conjugate heat transfer, electric double layer effects, surface roughness, and properties dependent on temperature, compressibility and rarefactions (for gas flow only).

2.6 Effect of axial conduction on heat transfer

In conventional sized channels, under fully developed flow conditions, a constant heat flux boundary condition at the solid-fluid interface leads to maximum heat transfer coefficient. In general, the channel thickness is very small compared to hydraulic diameter of the conventional channel; hence the axial heat conduction in channel wall for conventional size channels can be neglected because the wall thickness is usually very small compared to the channel diameter, Guo and Li (2003). However, in microchannels, the wall thickness can be equal in size or larger than hydraulic diameter of the channels. Therefore, the heat transferred in the wall by conduction cannot be neglected for the case of convective liquid flow in microchannels

and the heat transfer mechanism becomes conjugate, Cole and Cetin, (2011). An axial heat conduction along the solid walls of heat exchangers involving microchannels is quiet often overlooked during the design / analysis stage and interpretation of experimental data to estimate the heat transfer coefficient. This is the reason of of erroneous conclusions and inconsistencies in interpretation of data, Moharana *et al*. (2012); Maranzana *et al*. (2004).

Practically, most research on convective heat transfer coefficient and Nusselt number in microchannel was based on fluid temperature of inlet and outlet rather than bulk fluid temperature. It must be noted that the experiments in microchannels are extremely difficult to get accurate data, due to the small size of the test sections. Moreover, there is also no direct measurement of heat flux at the fluid-solid interface in published studies. Furthermore, wall temperature measurements are performed at some distance away from this interface. As a result, it is difficult to directly deduce the Nusselt number from the measurements so that the experimental data must be carefully interpreted. Several assumptions are usually made to infer unknown quantities from the measured ones. Among them, the wall heat flux assumed in most studies to be uniformly distributions over the fluid/solid surface when the heat source is supplied electrically, which may be far from the actual boundary conditions. Hence it is not reasonable to compare the experimental results with analytical counterparts.

The experimental estimation of convective heat transfer coefficient requires the use of a heat conduction model for the wall because direct measurements of temperature and the wall heat flux at the interface between fluid and solid and direct local measurement of the bulk temperature of fluid are very difficult to implement – need a Computational Fluid Dynamics model. Until now, the research community working in the micro-scale applied the valid model in macro-scale to measure the heat transfer coefficient (one-dimensional heat conduction in wall –perpendicular to the flow). So the wall heat flux is considered to be uniform along the channel. The local temperature difference between the wall and the fluid is calculated, either by choosing a linear variation for the bulk temperature of the fluid, Qu *et al*. (2006) or by considering an extrapolation of the parallel flow heat exchanger modelling and by choosing the logarithmic mean temperature difference.

Nowadays, numerous work has been done using Computational Fluid Dynamics software packages to predict the flow and heat transfer characteristics in microchannels. In Ansys Fluent, there are two approaches for dealing with the wall boundary. The first approach is called the *full conjugate model* in which the solid and fluid zones are meshed and the energy equation is solved in both zones. Thus, the heat conduction in all directions is accounted for through solving the energy equation in the solid and the fluid. The second approach is a simplified approach called the *thin-wall model*. Here the solid zone heat transfer is modeled by a constant heat flux at the outer surface of the walls of the fluid zone. As there is no need to calculate heat transfer in the solid zone the numerical calculation time is reduced. Figure 1 depicts the difference between the two approaches. The *thin wall model* approach is illustrated in Figure 2-1(a) while Figure 2-1(b) shows the *fully conjugate model* that includes the entire substrate. Numerical modelling of fluid flow associated heat transfer may be a very helpful tool to interpret experimental data and to test these assumptions, Qu *et al*. (2006). It may be very useful to evaluate the relative importance of the physical phenomena possibly involved in microchannel heat transfer, Gamrat *et al*. (2005).

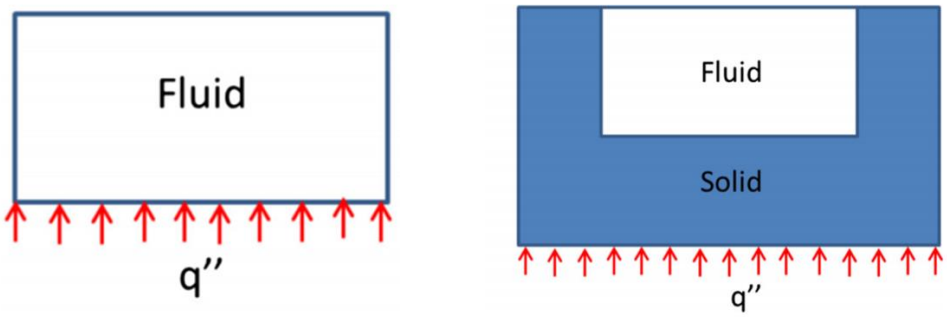

(a) (b)

Figure 2-1 : Schematic of (a) thin wall model and (b) conjugate model.

Fedorov and Viskanta (2000) noted that the concept of the local heat transfer coefficient and Nusselt number is meaningless in strongly conjugate problem. The temperature distributions showed a complex heat flow pattern in the channel combined

convection-conduction heat transfer. They observed the local heat flux from the solid to the fluid region was higher at the early leading edge and decreasing along the longitudinal direction. This is due to the average convective heat transfer at the inlet region and also because the highly conducting channel support the redistribution from the downstream to upstream region of the channel. They recommended that possible failure of the cooling system was due to the thermal stress induced by the extremely large temperature gradient at the entrance channels. However, there no detailed comparison between experimental results and numerical predictions was provided in this paper to validate the numerical results.

Tiselj *et al*. (2004) performed an experiment and numerical analysis to evaluate heat transfer characteristics of water through triangular silicon microchannels, seventeen parallel microchannels were etched in the silicon substrate. Each cross section of this channels have a dimension of 160 μm in hydraulic diameter and 10 mm in length. The obtained axial bulk and heated wall temperature do not change linearly along the channel. The non-monotonous behaviour of water and wall temperature is due to high values of axial heat fluxes in the silicon substrate. The temperature distribution obtained in the experimental work also showed similar behaviour. They noted that, the axial heat flux affects the temperature of the heated wall and bulk temperature distribution along the flow direction. They also indicated that the Nusselt number along the channel has a singular point.

Maranzana *et al*. (2004) analysed fluid flow and heat transfer and proposed analytical models of channel flow heat transfer between two parallel plates. They noted that the axial conduction effect leads to very large bias in measured heat transfer coefficient, especially for small Reynolds number. They introduced an axial conduction number, *M* (heat flux conduction / heat flux convection) to compare axial heat transfer by conduction in the wall and convective heat transfer in the flow. They stated that the number *M* is usually very low in the case of macro-channels. This implies that conductive heat transfer in walls is nearly one-dimensional and perpendicular to the fluid flow for these macroscopic cases. They noticed that the axial conduction can be neglected as soon as the *M* number get lower than 0.01, since the coupling between convection in microchannels and conduction in walls is weak. The

coupling between wall and bulk fluid temperatures is important for low hydraulic diameter because the heat transfer coefficient is extremely high. The consequence is that the axial conductive heat transfer in the wall cannot be neglected and that, the wall heat flux density cannot stay uniform.

Lee *et al*. (2005) conducted experimental and numerical studies to investigate the validity of the classical laminar flow theory at micro scale level. The investigated channels were made of copper and had a rectangular cross sectional area and a hydraulic diameter range of 0.318 – 0.903 mm and a length of 24.5 mm. They evaluated two numerical models, namely a *fully conjugate model (*similar as shown in Figure 2-1*(b))* and a *thin-wall model(*similar idea as shown in Figure 2-1*(a))*. In the *fully conjugate model*, both convection in the channel and conduction in the substrate were taken into account. The substrate thickness of 1.5 mm was included in this model and a uniform heat-flux was applied at the bottom surface, simulating the heat flow from the catridge heaters. For a thin wall analysis, a thin and highly conductive wall without axial conduction was employed in this model. Utilizing symmetry conditions, only a quarter domain was modeled. Their results showed that there is no significant difference between the predictions made by the two models and the experimental data, i.e. insignificant conjugate effects. Thus, they concluded that the *thin-wall model* can be used as a computationally economical alternative to the *fully 3D conjugate* analysis. The insignificant conjugate effects reported by Lee *et al*. (2005) could be attributted to the fact that the substrate thickness used in their *3D full conjugate* model was 1.5 mm which is very small. Liu *et al*. (2007) conducted a numerical investigation for water fluid flow and heat transfer in microchannel cooling passages. Two- dimensional simulation was performed at Reynolds numbers ranging from 10 to 200 in 100 μm single tube. They stated that non-uniform heating conditions are another important factor in the practical operation of microchannel devices in term of both space and time scales. It was usually assumed, as either isothermal or uniform heat flux.

Moharana and Khandekar (2012) conducted a numerical study on axial wall heat conduction in hydrodynamically and thermally simultaneously developing flow in rectangular microchannels using water at *Re* =100. They conducted four sets of simulations which are summarized as follows: (1) varying the channel aspect ratio

while keeping the channel cross-sectional area constant, (2) varying the channel aspect ratio but keeping the heated perimeter constant, (3) varying the channel aspect ratio but keeping the channel width constant and (4) varying the channel aspect ratio while keeping the channel height constant. The channel aspect ratio was varied from 0.25 to 2.22 and the hydraulic diameter varied from 0.16 to 0.203 mm. A constant heat flux boundary condition was applied at the bottom of the channel substrate while all other surfaces were considered adiabatic. They found that the average Nusselt number decreases with increasing aspect ratio (*W/H*) until $AR \approx 2$ after which it starts to increase with aspect ratio for constant cross sectional area and heating perimeter of the channel. The authors did not give an explanation to this phenomenon. Accordingly, they suggested using channels of $AR > 2$ for better heat transfer performance and ease of manufacture, compared to channels of low aspect ratio.

Mansoor *et al*. (2012) performed 3D simulations for flow in a rectangular microchannel incorporating both conduction in the copper substrate and convection by the channel fluid. The microchannel had dimensions of 0.194 mm, 0.884 mm, and 25.4 mm for width, height, and length, respectively. De-ionized water served as the working fluid under laminar conditions with ranging Re number between 500 to 2000. High heat fluxes ranging from 45 W/cm^2 to 130 W/cm^2 were included to investigate microchannel thermal characteristics. The simulations were carried out using the Fluent CFD code and were validated by comparison with existing experimental data in Lee *et al*. (2005) and numerical results having similar microchannel dimensions and conventional correlations. Validations results were found to be in good agreement with an average deviation of less than 4.2%. The predicted Nusselt number was observed to increase with an increase in applied heat flux. They also analysed the transition of between single and two phase flow at certain values of Re. The results show that the single-two phase transition occurred at high Re and increases as the applied heat flux increases.

Moharana *et al*. (2012) conducted a numerical study on the effect of conjugate heat transfer in simultaneously developing laminar flow, in square ducts. Simulations have been carried out by varied the substrate wall and fluid conductivity ratio,k_s/k_f, substrate thickness, and the flow *Re* number between 100 to 1000. The axial variation

of dimensional heat flux, dimensionless average wall and bulk fluid temperature and local Nusselt number were presented in this study. At a low ratio of solid and fluid thermal conductivity and a uniform or constant heat flux in the axial direction. The temperature difference between wall and bulk temperature attains a constant value in the fully developed region. While, at higher values of the thermal conductivity ratio between solid and fluid, the effect of conjugate heat transfer is dominant, thereby leading to decrease in the average Nu. They indicate that, there exists an optimum value of k_s/k_f which maximizes the average of Nu number.

Hassan *et al*. (2014) noted that the axial heat conduction plays an important role in a parallel flow microchannel heat exchanger. The factors affecting the axial heat conduction are *Re* number, ratio of thermal conductivity, hydraulic diameter and the wall thickness separating the channels. Axial conduction was increasing with increasing Re number, thermal conductivity ratio and thickness of separating wall. While it decreases as the hydraulic diameter increases due to the decreasing effect of wall thickness. Dai *et al*. (2014) investigated the effect of different boundary condition on pressure drop and heat transfer. Two different cross-section geometry; circular and rectangular were tested. They stated that the effect of conjugate heat transfer, entrance effect and temperature dependent viscosity showed a significant influence on heat transfer coefficient in laminar region. Similar conclusions are also seen in a recent report in experimental work conducted by Abdollahi *et al*. (2019). They claimed that deriving a correlation to predict Nu is not reliable by neglecting these effects. In addition, they also stated to ensure the assumptions made in the processing of the experimental data are valid by performing a computational fluid dynamic simulation of the combined channel and wall geometry.

2.7 Single Phase Fluid Flow and Heat Transfer in Multi-Microchannel

Publish friction data for a single microchannel, demonstrated an agreement with the conventional equations in both laminar and turbulent regions. However, a

disagreement of friction values were reported in multiple microchannels as reported by Peng *et al*. (1995a) and Peng and Peterson (1996) and this may be due to the existence of flow maldistribution in multiple microchannels. As reported by Park and Punch (2008) who conducted an experimental and theoretical analysis on single phase laminar flow in a rectangular multi-channel for a Re number range between 69<Re<800. They point out that distortion on the analyses of experimental data was caused by non-uniform distribution of flow in multiple channels. Therefore, the assumption of uniform flow distribution should no longer be accepted in multichannel flow, Wang *et al*. (2011a), and flow maldistribution is important in the analysis of heat exchangers and also in experimental data reduction, Rao *et al*. (2002). The design of a microchannel heat sink requires an accurate description of microchannel flow. Two approaches are commonly used to describe fluid flow and heat transfer in microchannel heat sinks. The first employs simplified analytical methods assuming the solid wall separating microchannels behave as thin fins, and relying on such approximations as uniform fluid temperature, one-dimensional heat transfer, and constant convective heat transfer coefficient along the microchannel walls, evaluated from empirical heat transfer correlations. The other approach involves solving the three-dimensional Navier- Stokes and energy equations. Both of these approaches are based on prior understanding of fluid flow and heat transfer in macrochannels, and are therefore valid only if liquid flow in microchannels follows the same conservations laws as in macrochannels. Several studies have been conducted to explore this important fundamental issue. Most of these studies relied on bulk flow measurements, comparing pressure drop measurement across the channel to macrochannel model/correlation predictions where the results show significant disagreement, Qu *et al*. (2006).

The flow non-uniformity through the heat exchanger is generally associated with improper exchanger entrance configuration, due to poor header design and imperfect passage to passage flow distribution in highly compact heat exchanger caused by various manufacturing tolerances. Several researchers have claimed that the flow maldistribution in microchannnel heat exchangers can significantly reduce the

heat exchanger performance, which leads to the local over-heating and failure of the devices, Ranganatakulu *et al*. (1997); Lalot *et al*. (1999); Lu and Wang (2006) ; Solovitz and Mainka (2011); Li *et al*. (2019). The effect of flow maldistribution from channel to channel that remains in reality during the experiment is incorporated into the value of the heat transfer coefficient. Furthermore, the wide deviation in the micro heat exchanger is less due to accuracy of experiment and more due to the assumption of uniform flow distribution in the data reduction model, Rao *et al*. (2002); Kumaran *et al*. (2013).

Kumaraguruparan *et al*. (2011) performed a numerical and experimental study to investigate the significant factors that might cause flow maldistribution in U- type microchannels configuration. According to their numerical findings, they stated that the flow maldistribution between channels is due to the flow separation and recirculation that occurred in inlet header or manifold. In addition, they claimed that the uniformity of the flow can be achieved by increasing the flow resistance inside channels. For example, by reducing the depth and width of the channel, the number of channels, or increasing the length of channels. Furthermore, Anbumeenakshi and Thansekhar (2016) noted that the uniformity of the flow in microchannel heat sinks if the channel inlet pressure is uniform, however, due to the branching of the fluid which leads to higher static pressure, it is difficult to maintain the uniform channel inlet pressure.

Study was conducted by Pan *et al*. (2008) to optimize the manifold geometries and dimensional variations to obtain comparatively ideal flow distribution between microchannels. They investigated the influence of complex manifold geometries on the flow distribution between microchannels by an analytical model and an equivalent electrical network model. The study consists of an inlet and outlet manifold and the flow patterns of fluid is a Z-shape where the outlet flows in the same direction as the inlet flows. They stated that there are three resistance existed during flowing in the microchannel arrays: a) the local resistances caused by splitting and reverse fluid flow from inlet manifold to microchannel arrays b) the frictional resistances caused by friction effects during the fluid flow inside microchannels arrays c) local resistances caused by combining and turning as the fluid flows from microchannels arrays to outlet

manifold. However, the local resistances are much lower than the frictional resistances, therefore they were neglected in this study to simplify the algorithm of the microchannels array model. The microchannels width was varied from 200 to 500 μm to investigate the effect of microchannels width on both inlet and outlet manifold. The results observed that the division of manifold into number of rectangular channels is a valid method, and the microchannel width dominates the optimization of outlet manifold geometry and dimensional variations.

Jones *et al*. (2008) investigated flow distribution in 76 channels heat sink etched into silicon substrate by using infrared micro-particle image velocimetry. The average channel width and height of the each channel were 110 μm and 371 μm, respectively. Flow maldistribution was observed at high flow rate, where, channels near the lateral edge have a subtantially lower flow rate than those in the middle channels. They stated that this might effect the heat transfer performance. They also noted that a properly design manifold is important in increasing the performance of a microchannel heat sink. As aforementioned, better flow distribution is of a crucial importance to achieve efficient heat transfer and a modification of geometric structures conducted by previous researchers as an effort to enhance heat transfer will discussed in next section.

2.7.1 Effect of Inlet/Outlet Configuration on Flow Distribution

A few studies reported that inlet-outlet flow configurations also had a significant effect on flow distribution in a microchannel heat sink , which affects the microchannel heat sink performance, Liu and Yu (2016). Therefore, it is important to examine the effect of flow arrangement on flow distribution in a microchannel heat sink. They are several ways of flow arrangement reported in the literature since early 1980's. Basically, the flow arrangements are represented using letter which, it shape closed to the flow pattern. For examples, Z-type indicated to the flow pattern similar to Z shape. Datta and Majumdar (1980) carried out a numerical study to predict the flow distribution for reverse flow (U-type) and parallel flow (Z-type) manifolds. They

observed that in the parallel (Z-type) and reverse (U-type) flow manifolds, maximum flow occurs through the last and first port respectively. However, a reverse (U-type) flow manifold provides relatively more uniform flow distribution than parallel (Z-type) flow manifold for identical conditions. Similar results were found by Wang *et al*. (2011) where U-type flow provide more uniform flow compare to Z-type. They stated that the U-Type had better flow uniformity compared to the Z-type due to the uniform pressure difference between inlet and outlet manifold across every tube. They concluded the jet flow phenomenon at the manifold inlet causes the maldistribution flow. However, this is not confirmed in the experimental studied conducted by Siva *et al*. (2014), where they found that the U-type configurations were showing higher amount of flow maldistribution followed by the Z-type.

Furthermore, Lu and Wang (2006) performed a numerical study to investigate the effect of five different inlet configurations on heat transfer performance of microchannel heat sinks consisting of 20 channels. (see Figure 2-2). They observed that flow maldistribution, in multichannel heat sinks, increase with increasing inlet velocity. In addition, they found that the flow recirculation in the multichannel heat sink can lead to flow maldistribution and large temperature difference and as a result, decreased its heat transfer performance.

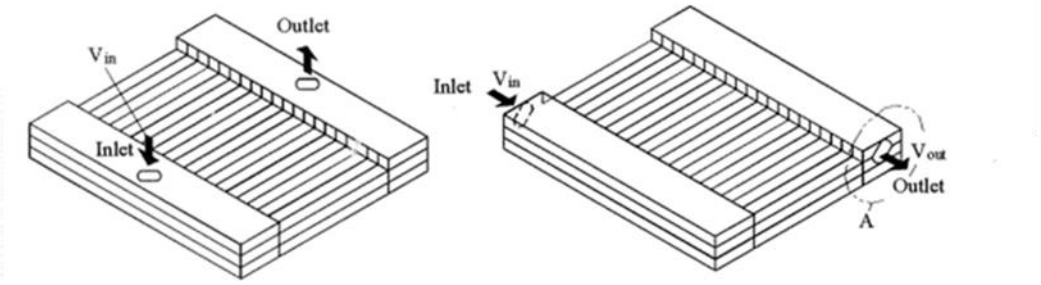

(a) (b)

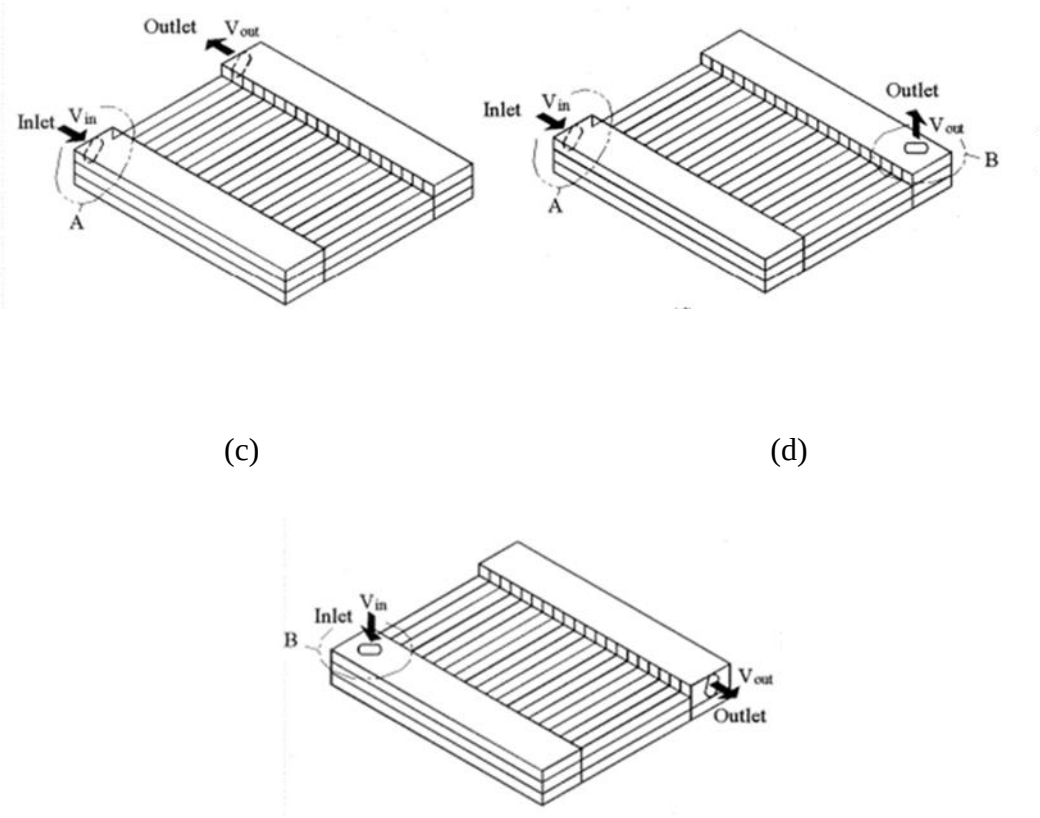

(c) (d)

(e)

Figure 2-2 : Schematic of parallel multichannel with various inlet configuration. (a) I-arrangement (b) Z-arrangement (c)]-arrangement (d) L- arrangement (e) ***Γ***-arrangement, Lu and Wang (2006).

Later Kumaran *et al*. (2013) also highlighted the effect of five different inlet/outlet configurations as shown in Figure 2-3; C- I- Z-, V, and U-type on flow distribution of microchannel heat sinks consisting 25 channels by using three dimensional simulations. Based on their finding, the C-type configurations had less flow maldistribution with the smallest maldistribution factor value; while the V-type configuration showed poor flow distribution. They stated that, poor flow distributions in the V-type configuration is due to two factors; flow impingement and flow recirculation due to entrance and existing flow from opposite site. The same phenomenon has been observed in the Z- and U- type configurations, which also lead

to flow maldistiburion in microchannel heat sinks. However, the inertia force in the C-type flow is less compared to other configurations, therefore, only a small amount of the flow recirculation was observed, which provided better flow distribution. The results reported by Chein and Chen (2009), contradicted the above. They found that the V-type showed the better flow uniformity. Six different inlet/outlet arrangements were studied, i.e I-, N-, S- D-, U-, V- types (see Figure 2-4). In I-,N-, D-, and S- type fluid was supplied and left the heat sinks horizontally, while, for the U- and V- type, fluid was supplied to and leaves the heat sinks vertically. This discrepancy is might due to the difference in the dimension of the manifold. The width of manifold in Kumaran *et al*. (2013) is bigger than Chein and Chen (2009). As discussed in section 2.7.2.1, both groups of researchers concluded that flow uniformity could be achieved by reducing the manifold width.

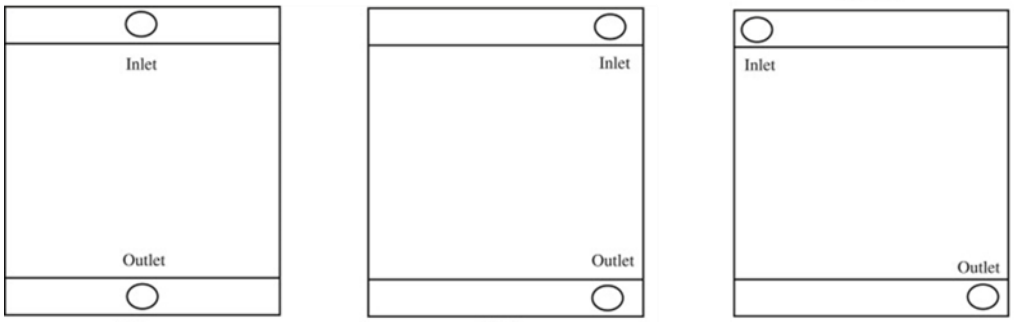

(a) (b) (c)

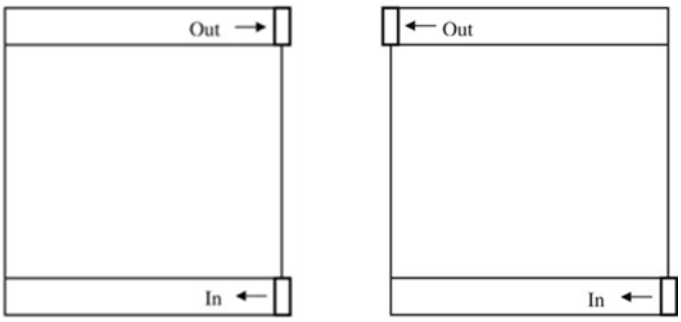

(d) (e)

Figure 2-3 : Geometric configurations of (a) I- type (b) C-type (c) V- type (d) U-type (e) Z-type microchannel heat sinks, Kumaran *et al*.(2013).

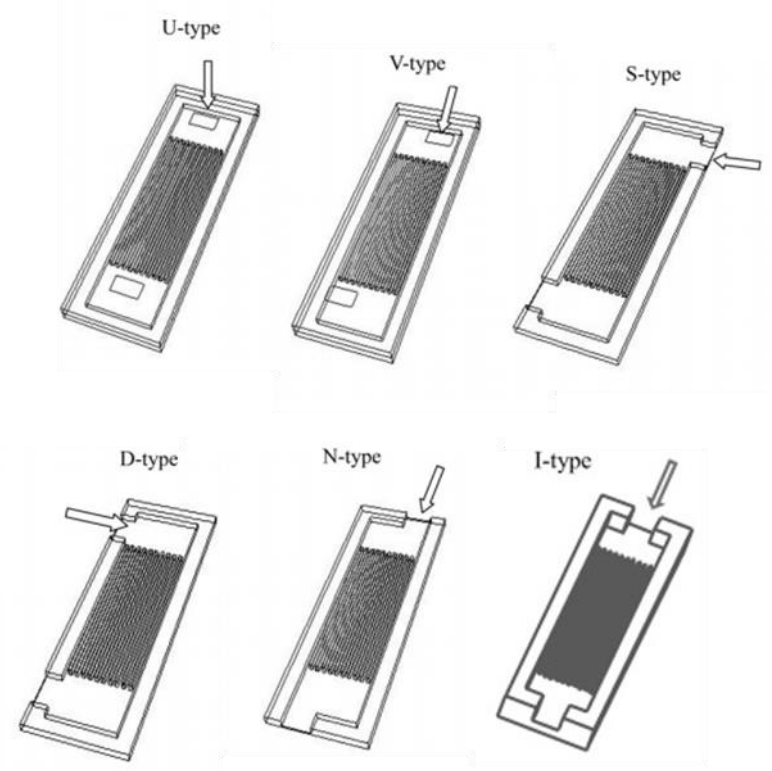

Figure 2-4 : Schematic of D-, N-, I-, U-, V- and S-type of microchannel heat sinks, Chein and Chen (2009).

Xia *et al*. (2015) investigated fluid flow and heat transfer in microchannel heat sinks with different inlet/outlet locations (I-, C- and Z-type), consisting of 30 identical microchannels with hydraulic diameter of 0.15 mm. The fluid is in vertical direction through to the inlet port for all configurations. They found that, the I-type gave a better uniformity followed by the C-type and the Z-type, with maldistribution parameter of 0.159, 0.471, and 0.551, respectively. A similar study was also found in numerical work conducted by Tang *et al*. (2018) using the COMSOL Multiphysics software. They found that the I-type obtained a better flow distribution, lowest pressure drop and better heat transfer performance than C- and Z- type configurations. It is worth noting that, a similar result was observed by Siva *et al*. (2014) and Chein and Chen (2009) in regards I-Type configurations. Additionally, they claimed that, due to the entrance/exit location together with the effect of impingement flow, result in intense flow separation, will lead to high flow maldistribution in the C- and the Z-type configurations.

In addition, some researchers revealed a significant effect of the flow orientation through in/out the manifold on flow distribution in multi-microchannel heat sinks. Anbumeenakshi and Thansekhar (2016) in experimental work found that vertical flow arrangement provided better flow distribution than horizontal direction. In the vertical direction, the fluid entered the inlet manifold in a perpendicular direction to the length of the header, then the fluid impinged the top wall before spreading over the inlet manifold and then enters the channels. This mechanism reduced the momentum of jet flow at the entrance port and hence inhibit the reduction of static pressure at the entrance. For this reason, the flow uniformity could be achieved among the channels when the fluid supplied vertically at the entrance. Similar results were also found in the numerical work conducted by Chein and Chen (2009), where a vertical flow direction at the inlet port and outlet port provided better flow distribution compared to the horizontal direction.

In the numerical work conducted by Pan *et al*. (2013) they found that, the effect of entrance flow direction was insignificant at a small velocity at the entrance. However, for higher velocity, similar conclusions as Anbumeenakshi and Thansekhar (2016) and Chein and Chen (2009) were reached i.e. a better flow distribution could be achieved when the fluid entered and exited in the vertical direction. However, Wang

et al. (2011) reported that the effect of in/out flow direction was insignificant. They investigated the effect three different orientations of fluid; vertical up, vertical down and horizontal direction on flow distribution in Z-type flow arrangement.

Balaji and Lakshminarayanan (2006) noted, that the flow uniformity in the micro heat exchanger has a strong function of the number and the location of the inlet and outlet ports. From the obtained numerical results, they observed that the flow was uniformly distributed when the microdevices inlet and outlet port aligned with microchannels along with two inlets and four outlets. Later similar conclusion was confirmed by Jang *et al*. (2010). They, developed a three-dimensional simulation model to study the effect and geometric parameter and inlet/outlet arrangement on the performance of a micro-methanol steam reformer. Five inlet and outlet manifold arrangements were presented in this works, namely; right inlet/ left outlet, right inlet/ right outlet, right inlet/ central outlet, central inlet/central outlet, and central inlet/ two outlets. Based on the comparison in performance results between all considered designs showed that the configurations of central inlet with two outlets exhibits a better flow distribution.

Recently, Kumar and Singh (2019) proposed modified novel inlet/outlet arrangement with different flow inlet angle such as ($\theta = 90°$, $\theta = 105°$, and $\theta = 120°$) as shown in Figure 2-5. An aluminium heat sinks with twenty-eight of parallel channels are considered and water is used as a working fluid. Based on their results, the significant effect of that flow distribution changes with different flow inlet angle. A better flow distribution is observed for proposed inlet/outlet arrangement with $\theta = 105°$ compared to others flow inlet angle and also to conventional inlet/outlet arrangement. Furthermore, the suggested that the performance of parallel channel heat sink can be improved if coolant enters the distributor header with flow inlet angle $\theta = 105°$ and exit from the middle of the collector header.

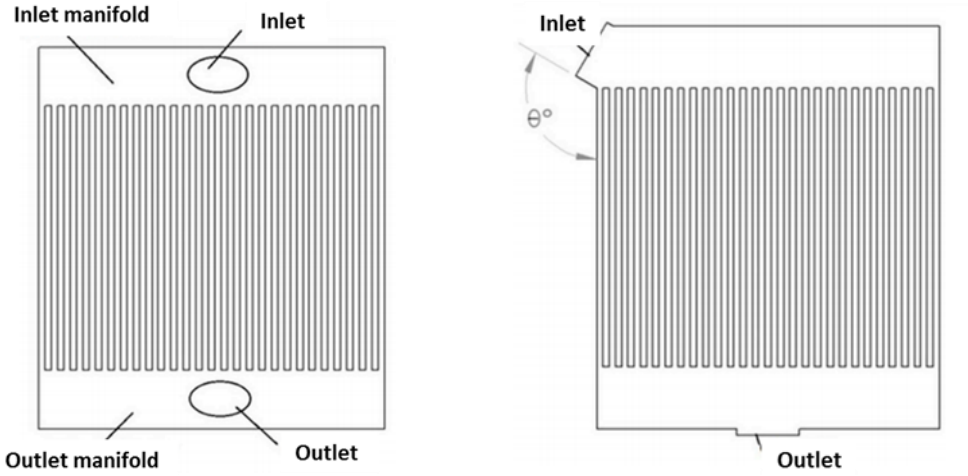

(a) (b)

Figure 2-5 : (a) Conventional inlet/outlet arrangement with rectangular headers (b) Proposed inlet/outlet arrangement with rectangular headers, Kumar and Singh (2019).

2.7.2 Effect of Manifold Design on Flow Distribution

There are several works that were performed to estimate the flow distribution, examine the parameter that affect flow distribution in microchannel heat sinks, which can lead to negative impact on the cooling performance. These studies will help in designing the shape and range of dimensions of the manifold in order to enhance the heat sink performance.

2.7.2.1 Effect of width, length and depth of manifold.

Kumaran *et al*. (2013) employed a three-dimensional numerical simulation to investigate the influence of a rectangular inlet manifold width (48.5, 52.5, 55.5 mm) and depth (5, 7, 11 mm) on flow maldistribution in a 25 channels microchannel heat

sink. It was found that, the manifold with the smallest width tested in this study provided a better uniformity of the flow inside the channels compared to the two other manifolds. They claimed that, the flow recirculation exhibited at the corner of manifold as the width of manifold increased was the reason of undesirable flow distribution. However, numerical results corresponding to the depth of manifold, the lowest depth (5 mm) and the highest depth (11 mm) tested inlet manifold resulting poor flow distributions. Therefore, based on minimum values of pressure drop and reduced flow maldistribution, they suggested that the optimum size of manifold depth is 7 mm. The results are in a good agreement with Kim *et al*. (2011) in their numerical study to invetigate the flow distribution in microchannel devices. The numerical results were validated using micro-PIV technique. The effect of manifold width (5.4, 7.8, 12.6, 15, 19.8 mm) and length (1.5, 2, 3,4,5 mm) were studied at Re number is 33.2. They observed that the flow uniformity could be achieved as the manifold width decreases or the manifold length increases. The improvement of flow distrbution by increasing the length of inlet manifold was also reported in the numerical work conducted by Wang *et al*. (2011a). They also stated that the maldistribution become more severe at shorter inlet manifold length as the flow rate increased. Zhai *et al*. (2017) also claimed that uniform flow distribution could be achieved by appropriate design of entrance region. Where is, they suggested the length of entrance region should be long enough to obtained uniform flow distribution in parallel-channel microchannel heat sinks to eliminate the entrance effect in the inlet.

Pan *et al*. (2013) investigated the effect of seven different inlet and outlet manifold, on flow distribution in Z-type configurations. They separated the manifold structures into three groups, which is centrosymmetric manifold (inlet manifold width = outlet manifold width), large inlet manifold, and large outlet manifold. Based on their numerical results, for centrosymmetric manifold, the velocity distribution in channels was nearly symmetric where, the lowest flow rate was observed at the middle channel and the highest flow rate appeared at both sides of microchannel heat sink. In contrast, for the large outlet manifold the velocity distribution decreased with channel number. However, for the large inlet manifold the velocity distribution is increased with channel number. They concluded that larger area of manifold; either larger inlet

manifold, larger outlet manifold and larger inlet and outlet manifold provided better flow uniformity.

2.7.2.2 Effect of ratio of channel area to the inlet manifold area.

In an open literature, the area ratio, $\overline{AR}$, has a significant effect on flow distribution in multi microchannel heat sink and is one of the most parameter that should be carefully studied in multi microchannel heat sink design, Choi *et al*. (1993); Ghani *et al*. (2017). Generally, the area ratio is defined as the ratio of total channel cross sectional area and the cross-sectional area of header or inlet manifold. In early 1980, Datta and Majumdar (1980) study the effect of the area ratio on flow distribution in both parallel (Z-type) and reserved (U-type) flow manifold. They claimed that the flow maldistibution is increased with increasing area ratio. Similar result was also found in the numerical work conducted by Choi *et al*. (1993). They investigated the influence of area ratio for three different ratios ($\overline{AR}$ =4, 8, 16) in a parallel (Z-type) flow manifold for a Reynolds number of 50. They found that, the smallest $\overline{AR}$ among the three area ratios tested in their study, produced a better flow distribution compared to highest $\overline{AR}$. Webb (2003) investigated the significant influence of area ratio for two different types of manifold shapes, rectangular manifold (I-type) and oblique manifold (U-type). Based on their numerical results, they stated that the flow maldsitribution inside multiple microchannels heat sinks can be minimized if the cross section area of manifold is larger than the total channels cross section area. Furthermore, they also found that oblique manifold provide a better flow distribution compared to rectangular flow manifold.

Tong *et al*. (2009) studied the effect of cross-sectional area of distribution manifold (inlet manifold) on flow distribution by conducting a two-dimensional numerical simulation. In order to study the effect of cross-sectional area of inlet manifold, the ratio of height of the inlet manifold ($H_{manifold}$) and channel width (W_{ch}) was varied the ratio $H_{manifold}/ W_{ch}$ values of 1.4, 2.1, 2.8, and 4.2. They concluded that

the flow distribution can be improved, even at higher flow rate by increasing the cross-sectional area of manifold. Two cases have been considered by Siva *et al*. (2014) with the purpose of examining the effect of manifold area on flow distribution in multiple microchannel consisting of 20 channels with hydraulic diameter of 176 μm at a Re number of 50. In first case, the manifold area is two times larger than the total channel area and secondly, channel area is two times larger than the manifold area. They reported that smaller manifold area produced a poor distribution of the flow inside the channels. This is because of the resistance in the manifold increase, which leads to higher pressure drop in the manifold. In addition, they also observed that the flow maldistribution can give a negative impact to temperature distribution and therefore reduced the performance of the cooling system.

2.7.2.3 Effect of the ratio of inlet manifold area to outlet manifold area.

Choi *et al*. (1993) conducted two-dimensional analysis to investigate the effect the ratio of width inlet manifold ($W_{manifold,\ in}$) to the width of outlet manifold ($W_{manifold,\ out}$) on flow distribution in rectangular parallel (Z-type) flow in liquid cooling systems. The ratio $W_{manifold,\ in} / W_{manifold,\ out}$ was varied between 0.5 to 4.0. The flow distribution improved at the higher of $W_{manifold,\ in} / W_{manifold,\ out}$ value (4.0) where, the ratio of the maximum and minimum channel flow rate is 1.2. This is due to the momentum gained in the outlet manifold decreases as the value of $W_{manifold,\ in} / W_{manifold,\ out}$ is increasing, which also reduces the pressure drop in flow direction and improved a flow distribution. Later, similar conclusion was made by Tonomura *et al*. (2004) in their numerical work by using computational fluid dynamics. They observed the uniformity of flow distribution inside the channel can be achieved with increase the area of outlet manifold. However, they noted that the extension of outlet manifold decreases the efficiency of microdevices.

2.7.2.4 Effect of shape of the manifold.

There were several researcher reports in the open literature examining the significant influence of manifold shape on flow distribution and compared their performance based on the flow distribution to identify and optimum design of manifolds. For example, a numerical study conducted by Kim *et al*. (1995) on the flow distribution with three different manifold shapes (triangular, rectangular, trapezoidal) in parallel flow (Z-type) manifold. They studied the effect of shape of the inlet manifold on the flow distribution at Re numbers 50, 100, 300. They found out that the flow maldsitribution increased with an increasing of *Re* number. This phenomenon is due to the increasing inertia effect as the *Re* number increases. This phenomenon was more pronounced in the rectangular manifold. They concluded that the triangular manifold had a better uniformity compared to the rectangular manifold. Similar results were also found in a numerical analysis conducted by Kumaran *et al*. (2013). However, the effect of both inlet and outlet manifold have been considered by varying the shape of both inlet and outlet manifold. For the first case, to study the influence of the inlet manifold shape, five different shapes of inlet header i.e. rectangular, trapezoidal with three different sizes and triangular were selected. Microchannel heat sinks with a triangular inlet manifold provided a better flow distribution compared to the other cases. They stated that, the friction at the inlet manifold wall tends to reduce the static pressure in the flow direction, which results in a poor flow distribution. In the second case, a rectangular inlet manifold was used and four different outlet manifold shapes (rectangular, trapezoidal with two different sizes and triangular). However, in this case, a better flow distribution was observed with the trapezoidal outlet manifold.

However, study conducted by Xia *et al*. (2015) reached a different conclusion in their three-dimensional numerical simulation on microchannel heat sink consisting 30 identical channels with D_h is 0.015 mm and AR is 0.333. They found that the rectangular manifold provided better flow distribution followed by the trapezoidal manifold and triangular manifolds. They claimed that this phenomenon can be attributed to the interaction of the branching fluid and friction offered by the walls of

the header. Recently,Tang *et al*. (2018) performed a three-diamnesional simulation to study the effect of manifold shape, similar as used in Xia *et al*. (2015) on flow distribution and thermal performance in microchannel hat sink. They also found that a rectangular header with I-type flow arrangement showed a better performance in terms of flow velocity uniformity and heat transfer than others under the same pumping power consumption.

Similar result was also reported by Anbumeenakshi and Thansekhar (2016) in their experimental analysis. However, the performance of these three different shapes (rectangular, trapezoidal, triangular) were depended on *Re* number. They found that, better flow distribution in microchannels was only observed in trapezoidal and triangular inlet manifold at lowest *Re* number, 250. However, for the higher range of Re number, 400-650, a better flow uniformity was found in rectangular inlet manifold followed by trapezoidal and triangular. They carried out an experimental investigation in a microchannel heat sink consisting of 25 rectangular microchannels (D_h =763) by using deionized water. They stated that this phenomenon is due to the fact that increasing flow rate at the entrance produced a vortex, which reduced the static pressure at the upstream of the inlet manifold. Therefore, lesser fluid enters the channels near the inlet leads to increase in flow maldsitribution for trapezoidal and triangular manifold. Amiri (2019) studied effect of four different shape of manifold as shown in Figure 2-6 on flow distribution in parallel microchannel. Similar results was reported by them where manifold with rectangular shape leads to more uniformity than other shapes, while the triangle 90 showing the worst flow distribution.

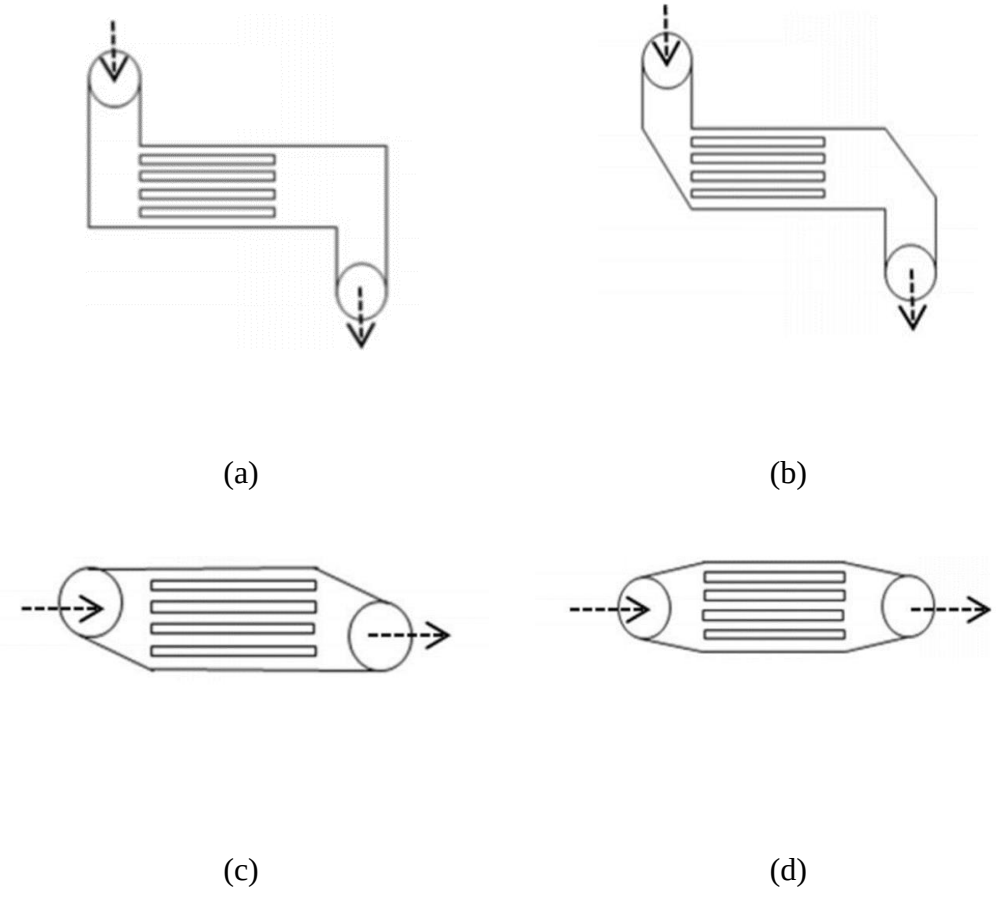

Figure 2-6 : Top views of all shapes of model were used in Amiri (2019), (a) Rectangular (b) Triangle 90 (c) Trapezoidal (d) Triangle .

Webb (2003) studied the influences of two type of manifold designs, a normal rectangular manifold and oblique manifold on flow distribution in parallel microchannels. They claimed that the oblique reverse manifold provided a better flow distribution compared to rectangular manifold. However they stated that the flow distribution in a rectangular manifold could be improved by using a larger inlet port. Later, Jones *et al*. (2008) examined the flow distribution behaviour in a microchannel with a manifold having a rounded corner and a rectangular manifold using CFD analysis. Based on numerical streamlines results, the flow was distributed easily through the manifold, which resulted in a more unifom flow through the channels compared to the manifold with rounded corner. However, recirculation flow was

observed in the inlet manifold having rounded corner, which reduced the space for the fluid to be distributed. Due to this reason, there was an increase in pressure drop and localized velocity within the manifold. In addition , the channel loacted at the center region received a large amount of fluid compared to the channels near the adjacent edge.

Solovitz and Mainka (2011) proposed a new modified manifold design, named optimally-tapered, which was developed based on optimized power law correlation for laminar to provide a uniform flow distribution in multichannel cooling systems. Based on the comparison of flow distribution among channels between the proposed modified manifold design and common manifold considered in this study, the proposed modified showed a better uniformity, with the standard deviation in the mean channel speed relative to the overall mean being less than 3%.

2.7.3 Effect of Channel Dimensions and Number of Channel on Flow Distribution

Commenge *et al*. (2002) analysed the influence of geometrical dimensions of the reactor microstructure on the velocity distribution between channels. Uniform fluid velocities in the microchannels indeed are a necessary condition to have equal mass-transfer coefficients and heat transfer coefficients. It is important, therefore, to design reactor geometries enabling narrow velocity distributions between channels. They give several steps in designing an optimum microstructured : 1) The width and height of the channels are chosen depending on mass-transfer between the bulk fluid and the coated wall: 2) The thickness of the walls between channels can be chosen based on heat transfer rate :3) The channel length and the fluid velocity are chosen, depending on the space time required for the reaction in the channel, as well as the maximum pressure drop through the reactor. 4) The total number of the channels can be calculated depending on the flow rate that must circulate through each plate.

Lu and Wang (2006) investigated the effect of channel number and hydraulic diameter on flow distribution in I-Type configurations of a multiple channel cold plate. However, in their study, the area of multichannel cold-plate was fixed, therefore, the cross-section area of the channels will decrease as number of channels increased. They observed that, the flow distribution in smaller diameter channels is better compared to the larger hydraulic diameter channels tested in their study. They indicated this is due to high pressure drop associated with smaller hydraulic diameter. Therefore, on that point, flow velocities in the channels are less affected by pressure variation in the inlet and outlet manifold, thus resulting in more uniform flow distribution. Later, Mathew *et al*. (2009) concluded that the flow uniformity could be achieved by reducing the microchannel width, which increases the pressure drop in channels. They investigated the effect of three different channel widths, 50 µm, 100 µm and 200 µm on flow distribution in U-Type configurations consisting of 10 square channels. Additionally, they also stated that the flow maldistribution increased as the flow rate increased. Furthermore, similar with Kumaraguruparan *et al*. (2011), they also concluded that the flow distribution could be improved when the flow resistance increases, by reducing the channel depth and width or increase in the channel length. They performed an experimental and numerical simulations in U-type microchannel configuration.

Similar conclusion was reached by Sehgal *et al*. (2012), i.e. the flow distribution within channels is better with decreasing channel width or increasing aspect ratio for all type of flow arrangements tested in their experimental study. They investigated the effect of channel aspect ratio by varying the channel width and keeping constant the channel depth for U-, S- and P-type flow arrangements. Furthermore, they also stated that, a better flow uniformity will reduce heat transfer resistance. The effect of channel aspect ratio on the heat sink thermal resistance have been studied by Biswal *et al*. (2009). They conducted an analytical study for both fully developed and developing single phase in the laminar regime. However, in their study, the channel width remains constant at 100 µm and the depth of channel was varied. They also found that a thermal resistance is lower at the highest aspect ratio. They pointed out that this is because as the channel depth increases, the fins surface area also increases, which reduces the temperature rise inside heat sink. They stated that a higher number of channels obtained by decreasing the width of the channels or the fins

resulted in small thermal resistance and small pressure drop. In contrast, Kou *et al*. (2008) stated that the smaller channel width lead to higher thermal resistance due to interface area between the coolant fluid and the heat sink was small and not enough to dissipate the heat flux. Additionally, they also found the thermal resistance decreased monotically with the decrease of the substrate thickness.

Siva *et al*. (2013) studied the influence of hydraulic diameter and number of channels on flow distribution in a parallel microchannel system. Three different configuration types of parallel microchannel systems were considered. The flow maldistribution was characterized through the ratio of maximum and minimum pressure drop across the channels. Uniform flow could be achieved in microchannel by reducing the size of the channel, due high pressure drop encountered in channels as the as the reducing of channel size. They indicated that the flow maldistribution could result when both inertial and frictional forces are not in balance. The maximum flow was observed in channels nearer to inlet and outlet pipe for all tested configurations in this study. This is due to the higher pressure different, which leads to high velocity flow. They stated that flow maldistribution was increasing as the channel number increased.

As concluded by Lu and Wang (2006) and Mathew *et al*. (2009), uniformity in the flow distribution could be achieved when the pressure drop in the channels is relatively higher than in the manifolds, by reducing the cross-sectional area and width of channel, respectively. Similar conclusion was reached by Tonomura *et al*. (2004), where, the pressure drop in the channel become relatively higher than in manifold, by increasing the length of channels, which also lead to a better flow uniformity. Later, Pan *et al*. (2013) indicated a relative uniform flow distribution can be influenced by microchannel length and microchannel width. The influence of microchannel structural parameters on velocity distributions was studied by varying the length between 10- 50 mm and widths between 0.1-0.7 mm at different flow velocity at the entrance. They indicated that microchannel length has a minor effect on the velocity distribution. However, they suggested that uniform velocity distribution could be achieved with longer microchannels due to the pressure drop becoming higher in longer channel. The velocity distribution was significantly affected by the channel

width, especially at high velocity entrance, where the smallest tested width showed better velocity distribution. They also concluded that this due to better pressure distribution in a small width channel. Similar conclusion was reported by recent experimental and theoretical study conducted by Kim *et al*. (2019).

2.8 Conclusions

Most of the studies conducted in single-phase flow were carried out to check the validity of conventional theory on fluid flow and heat transfer in microchannels and discuss the reasons for discrepancies as reported in the open literature. Although some studies proved the validity of the conventional theory in micro-scale channel, there are some points that should be considered while evaluating friction factor and heat transfer in single-phase flow. As example, the work available in the literature clearly brings out the deviation on heat transfer results can be attributed to axial heat conduction. However, most studies were only focused on the optimal design and neglected the effect of axial conduction. Furthermore, authors studies the effect of geometrical parameters, particularly the effect of the aspect ratio and the hydraulic diameter, reached contradictory conclusions leaving some phenomena unexplained. This is because most people studied the effect of both simultaneously i.e. by varying the channel height for a constant channel width or varying the width for a constant height. This means that the hydraulic diameter and aspect ratio effect used not be separated and it was difficult to identify the relative importance of the aspect ratio and the hydraulic diameter. One of the biggest challenges in multichannel configurations is to achieve uniform flow distribution among the channels, which affects the micro heat exchanger performance as reported by Kandlikar *et al*. (2009). Altough, several studies have been undertaken on multichannel configuration in order to enhance the heat transfer rate and overall thermal performance, further research work is essentially required to identify the most appropriate factor which provides maximum heat transfer performance for the given configuration of the microchannel heat sinks. Therefore,

research carried out in this study, aims to induce all the important factors in order to examine their effect on fluid flow and heat transfer in microchannel.

2.9 Two Phase Fluid Flow and Heat Transfer in Mircochannel

Two phase flow (gas-liquid flow) within microchannles has been studied extensively due to its wide ranging application in micro-electro-mechanical systems (MEMS), electronics cooling, and bioengineering. Numerous studies have been conducted in two-phase microchannels focusing on flow boiling and thus a significant number of reports on flow and heat transfer characteristics and empirical correlations were presented. Additionally, many researchers have conducted visualization of flow patterns in microchannels and presented flow patterns maps in order to understand the relationship between heat transfer and flow characteristics. However, there are still fundamentals questions on flow patterns, heat transfer mechanisms and rates and pressure drop characteristics in microchannel that require further research for clarification and conclusion.

2.9.1 Dimensionless numbers

The introduction of dimensionless numbers is required to define the nature of the slug flow and heat transfer rate in microchannels where, the heat transfer rate is inherently linked to the hydrodynamics. There are three important dimensionless parameters for slug flow and these numbers are revisited here

The Reynolds number, denoted as Re, is the ratio of inertial forces to viscous forces acting on the fluid flowing in a channel:

$$Re = \frac{\rho U D_h}{\mu} \tag{2.22}$$

Where ρ represents the fluid density, U is D_h is the hydraulic diameter, and μ is the dynamic viscosity of the fluid. Reynolds number is commonly used to determine the onset of turbulent conditions in the important and initial steps of numerical simulations. For capillary slug flow, the critical Re that defines the transition from laminar to turbulent flow has been reported in literature to be about 1000 (Talimi *et al*. (2012))

The capillary number, denoted as Ca, is another important quantity in microscale indicating the relative effect of viscous forces to interfacial tension forces:

$$Ca = \frac{\mu U}{\sigma} \tag{2.23}$$

where σ represents the interfacial tension between the primary (liquid) and the secondary(gas) phases. The Weber number, denoted as We, is the ratio between inertial and surface tension forces:

$$We = Re \cdot Ca = \frac{\rho U^2 D_h}{\sigma} \tag{2.24}$$

The importance of surface tension effects in millimeter and micro scale is determine based on Re, Ca, and/or We. It has been suggested that at low Re, Ca plays a more significant role while We is the quantity of interest at higher Re.

The Bond number, Bo, represents the importance of interfacial forces with respect to gravity:

$$Bo = \frac{(\Delta\rho) g {D_h}^2}{\sigma} \tag{2.25}$$

where $\Delta\rho$ is the density difference between the primary and the secondary phases and g is the acceleration due to gravity.

2.9.2 Adiabatic flow patterns

The study flow patterns is important in the study of two-phase flows since it relates to the pressure drop and the heat transfer characteristics. It can be divided into three groups, which are surface tension dominant, inertia dominant and transitional regimes, Shao *et al*. (2009). These three main groups consisting of six common flow regime reported in literature are bubbly flow, slug flow, slug -annular flow, churn flow, annular flow and dispersed flow. Flow patterns of two-phase flow found in literature were shown in Figure 2-7 and Figure 2-8.

Bubbly flow: Bubbly flow is characterized by distinct and sometimes distorted (non-spherical) bubbles generally considerably smaller than the channel diameter. (see Figure 2-8 (a)), Shao *et al*. (2009).

Slug flow: Taylor flow (also known as segmented, slug, plug, elongated bubble or intermittent flow) is characterized by elongated bubbles with an equivalent diameter larger than channel diameter. (see Figure 2-8 (b)) Liquid slug separate the gas bubbles while, depending on channel wettability, a liquid film may form that separates the bubbles and wall, Shao *et al*. (2009).

Slug-annular flow : The merging of slug bubble to form slug -annular pattern due to increase superficial gas velocity, U_{Gs} in slug flow relative to superficial liquid velocity, U_{Ls} which leads to increase gas void fraction.

Churn flow: In this regime, transition Taylor and inertia dominated dispersed flow at high liquid velocities. There are two formation process: 1) unstable close at trailing end of elongated Taylor bubble which leads to disruption and entrainment of gas into the liquid. 2) disruption of liquid film on tube wall due to high inertia of the gas core and frothy slugs and drops appear within the gas.

Annular flow: The long waves of Taylor-annular flow as the U_{Gs} increases. The annular flow corresponds to a gas core surrounded by continuous liquid film adjacent to the tube wall. (see Figure 2-8 (c))

Dispersed flow: With increases U_{LS}, small liquid droplets are entrained in the gas core to form dispersed regime and a liquid film is left in contact with the wall. (see Figure 2-8(d))However, is dispersed flow is rarely observed in microchannels with hydraulic diameter smaller than 1 mm, Shao *et al*. (2009).

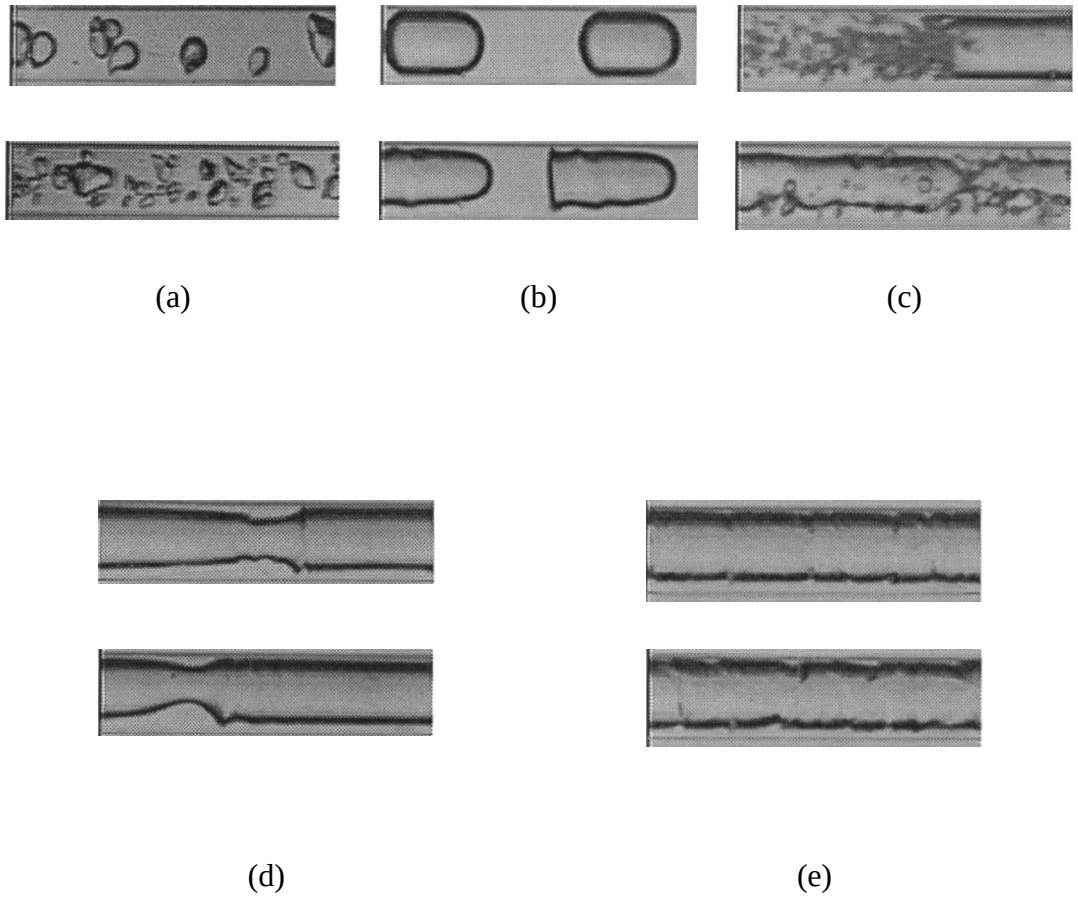

Figure 2-7 : Two phase flow patterns in the 1.097 mm diameter circular (a) bubbly; (b) slug; (c) churn; (d) slug-annular; (e) annular, Triplett *et al*. (1999).

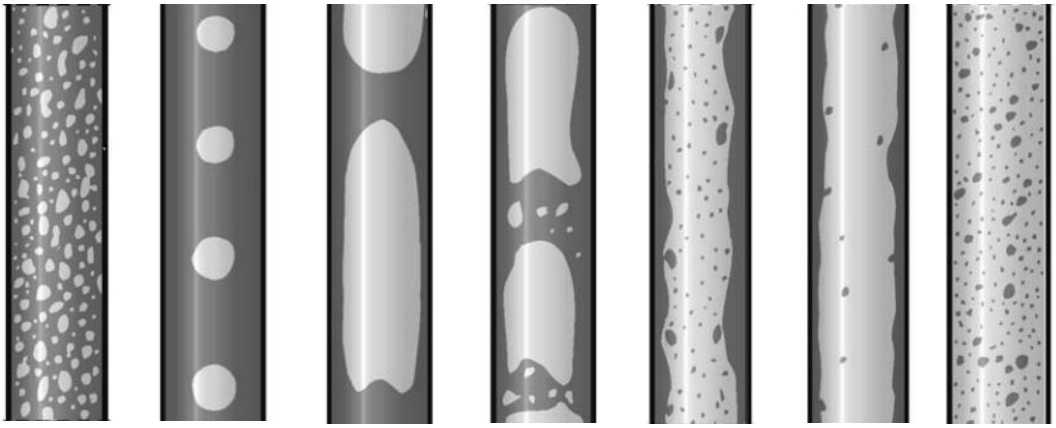

(a) (b) (c) (d)

Figure 2-8 : Schematic flow patterns of two-phase flow in vertical channels (a) bubbly flow (b) slug flow (c) annular flow (d) dispersed flow, Dziubinski *et al*. (2004).

However, there are inconsistency in terminology of two-phase flow patterns. For example, slug flow; Taylor flow and bubble train flow as found in literature refer to the same flow regimes. One of the reason of this discrepancy is the difficulty in classifying and analysing transitional flows. In addition, a high pressure drop in two phase flow systems lead to significantly changing in local velocities with axial length in microchannel. Therefore, there are morphological and flow pattern changes, and disagreements on flow patterns reported under same the flow condition, Shao *et al*. (2009). The most common types of research works done on two-phase gas–liquid flow characteristics in micro-channels have been reviewed by Saisorn and Wongwises (2008) and Rebrov (2010). Based on a visual observations reported by previous researchers the flow patterns or flow regimes that occur depending on the gas and liquid flow rates and can be affected by some factors such as the flow conditions, or geometric conditions.

Geometric conditions such as channel diameter or hydraulic diameter, channel shape, and aspect ratio are considered as the most influencing factor on flow pattern

of gas-liquid flow in microchannel. However, the effect of these factors on flow pattern transitions is not well understood, with conflicting trends reported by different investigators. Coleman and Garimella (1999) observed that the size of tube diameter and channel shapes have significant effect of regime transitions. Bubble, dispersed, elongated bubble, slug, stratified wavy, annular-wavy and annular flow patterns were observed. They conducted an experiments on air-water flow patterns with diameter ranging between 1.3 to 5.5 mm The transition from plug and slug regime to dispersed or bubbly regime shifts to higher superficial liquid velocities , U_{Ls} , as the diameter of tube is decreasing. They stated this due to effect of surface tension and tube diameter, together. Furthermore, they also found a significant effect of channel shape where, the transition to dispersed flow regime for rectangular tube is at higher value of U_{Ls}, compared to the circular tube. Contrary, insignificant effect of channel geometry on flow regimes was concluded by Triplett *et al*. (1999) in their experimental work for semi-triangular (D_h = 1.09 and 1.49 mm) and circular (D = 1.1 and 1.45 mm) test sections. The results obtained for both test sections were showing similar flow regime maps and intermittent flow regimes was covered a wide area of the map. One of the noteworthy observations of this research pertains to the absence of stratified flow, which confirmed the predominance of surface tension.

Cubaud and Ho (2004) investigated a wide range of liquid and gas flow rates air-water two phase flow in square microchannels with hydraulic diameter range of 200 μm and 525 μm. They found that the two-phase flow regime maps were independent of the channel size and the flow regime transition boundaries can be simply determined as a function of the liquid and gas flow rates. Chung and Kawaji (2004) also found the flow pattern and transition lines were similar for channel diameter, D > 250 μm were consistent with those appearing in 1 mm channels. They reported a diameter effect on flow pattern in circular microtubes with diameters of 0.53, 0.25, 0.1 and 0.05 mm. They observed bubbly, slug, churn, slug–annular and annular flow appear for tested channel with D > 250 μm. However, for channel D < 100 μm, only slug flow was identified under the flow conditions investigated. They stated that the absence of bubbly, churn, slug–annular and annular flow in channels D < 100 μm of was attributed to the greater viscous and surface tension effects on the liquid flow. Later, Zhang *et al*. (2011) investigated the channel diameter effect on

nitrogen-water flow patterns in horizontal circular microchannels with inner diameters of 302, 496 and 916 mm. Bubbly flow, slug flow, churn flow and annular flow were observed in this study. They found as the channel diameter decreased, the transition line of slug- bubbly flow, slug- churn flow and slug- annular flow occurred at higher U_{Ls} and U_{Gs}.

Chinnov *et al*. (2016) investigated the effect channel width (9 to 40 mm) and height (100 to 500 μm) of the channel in a short (80 mm) horizontal flat rectangular channel. Experiments were conducted with water and nitrogen/air as working fluid. They found that, significant effect of height and width were more representative, compare to aspect ratio (W/H). They observed that an increase in the channel width leads to an increase of the stratified and churn flows region. With a decrease in the height of horizontal channels, the churn flow zone increases and the zones of the annular, stratified and jet flows decrease. Contrary, Choi *et al*. (2011) found that the substantial effect of aspect ratio on flow pattern of rectangular microchannel working fluid of liquid water and nitrogen gas. They performed an experimental study in horizontal rectangular microchannels with 490, 490, 322 and 143 μm hydraulic diameters and 0.92, 0.67, 0.47 and 0.16 aspect ratios (H/W), respectively. They observed that, the region of the bubble regime becomes wider as the aspect ratio of the rectangular microchannel decreased. The flow patterns including bubbly, slug bubble, elongated bubble, liquid ring flows (as shown in Figure 2-9) are sequentially observed in a rectangular microchannel as gas superficial velocity increased.

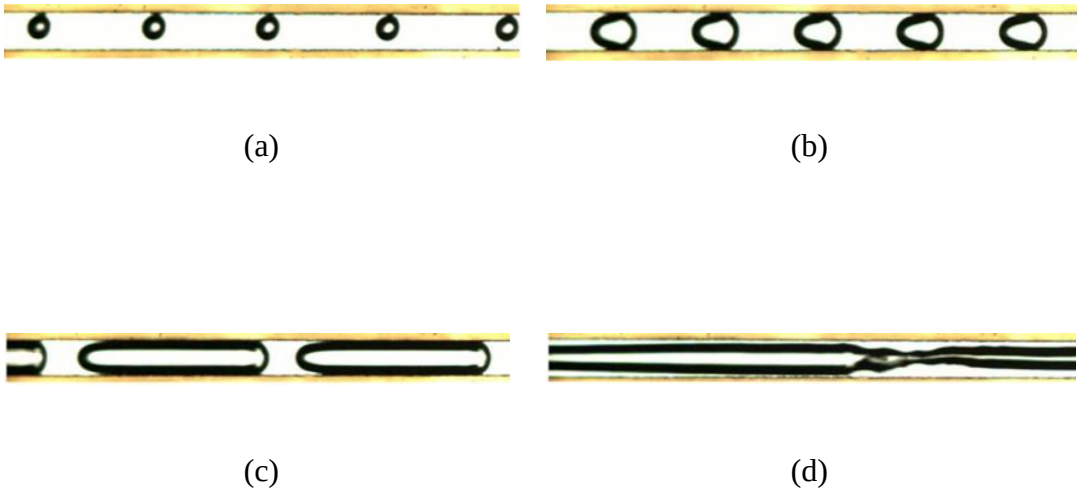

Figure 2-9 : Flow pattern in microchannel for AR=0.92 (a) bubble (b) slug bubble (c) elongated bubble (d) liquid ring flow, Choi *et al*. (2011).

Li *et al*. (2014), present an experimental flow pattern map of nitrogen–water two-phase flow in small vertical upward rectangular channel and an equilateral triangle channel under the same hydraulic diameter, D_h = 1.15 mm. They found a typical flow patterns such as dispersed bubble flow, slug flow, churn flow, and annular flow were obtained by gradually increasing the superficial gas velocity in both a rectangular channel and triangular channel flow. However, significant effect of cross-sectional shape on flow pattern was observed at low superficial velocity, where the capillary bubbly flow does not appear within a rectangular channel. In addition, they found a significant influence of cross-section shape channels on flow transition boundaries where, the slug–churn flow and churn–annular flow transition criteria in the rectangular channel shift to the left relative to the slug–churn flow and churn–annular flow in the equilateral triangle channel.

Channel orientation was also shown to have a significant impact on flow patterns in gas-liquid two phase flow in microchannel. However only a small number of publications, gave information corresponding to gravitational effect for adiabatic two-phase gas–liquid flow condition. Hassan *et al*. (2005) suggested that the flow regime transition lines are affected by the orientation of the channel. Two universal flow regime maps were proposed for both horizontal and vertical channels with a hydraulic diameter ranging between 0.1 mm and 1.0 mm. The resulting universal maps presented by the authors were based on flow regimes observed in all the studies on two-phase flow in microchannels. In more recent study conducted by comparing vertical upward and horizontal flow patterns of air –water were also presented in experimental work conducted by Saisorn and Wongwises (2015) in a 0.53 mm diameter channel and a length 320 mm. Five different flow patterns was observed in this study: slug flow, throat–annular flow, churn flow, annular flow, and annular–rivulet flow. The throat– annular flow, considered a unique flow pattern in micro-scale flow observed in this study. They found that the flow pattern map for vertical upward is not completely compatible with obtained transition lines of horizontal flow obtained in their previous work, Saisorn and Wongwises (2008). Furthermore, at the same flow conditions, the annular flow was only observed in the vertical upward flow channel. The annular flow pattern is not observed in the horizontal channel even at high gas velocities. They stated the formation of the annular flow in vertical upward flow may be attributed to the fact that, the buoyancy and inertia forces play a role in strengthening the gas phase in the mixing chamber, which limited liquid phase to enter the main channel as a smooth liquid film surrounding the gas phase with high kinetic energy.

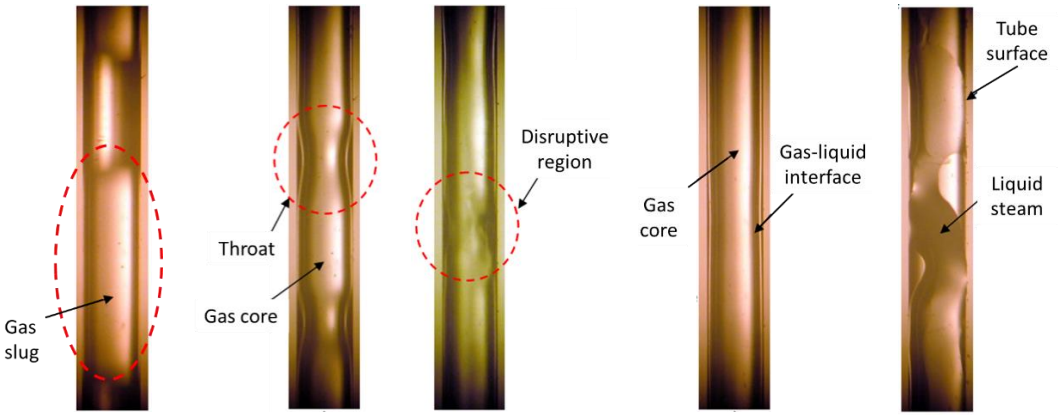

Figure 2-10 : Flow pattern in vertical circular micro-channel with 0.53 mm diameter, Saisorn and Wongwises (2015).

.

2.9.3 Slug Flow in Microchannel without Phase Change

The earliest studies of two-phase flow with slugs of a discontinuous phase in a continuous liquid were reported by Fairbrother and Stubbs (1935), Taylor (1961) and Bretherton (1961). Later an extensive research work has been carried out on two-phase slug flow in microchannels particularly concerning hydrodynamic characteristics such as velocity of bubbles, void fraction, liquid film thickness, pressure loss and heat transfer enhancement. Previous studies on both experimental and numerical studies have been reviewed by Angeli and Gavriilidis (2008), Gupta *et al*. (2010), Talimi *et al*. (2012) and Bandara *et al*. (2015), Bordbar *et al*. (2018).

Slug flow is characterised by the occurrence of regular gas bubbles almost filling the channel, separated by liquid slugs. The liquid slugs are connected by a thin liquid film surrounding the gas bubbles, Gupta *et al*. (2010a). This flow occupied a wide range of flow conditions. In addition, its shape is very regular and of periodic nature flow, Kumari *et al*. (2019). Furthermore, the physical flow pattern provides high interfacial area enhances the rate of heat and mass transfer from the channel wall to

liquid slug. Additionally, gas bubble and liquid slugs have unique hydrodynamic characteristics, such as internal recirculating flow which promote mixing and increases transfer rate, Gupta *et al*. (2010a); Zhang and Li (2018). Therefore, due to these reasons, slug flow provides a promising flow regime for gas-liquid in most of the gas-liquid application in microchannels. Examples include membrane fouling prevention, catalyst coating, microcirculation, pulmonary physiology and microreactors to perform mass transfer limited gas-liquid reactions.

The heat transfer rate for boiling flow in microchannels is much higher than single phase flow due to large heat of vaporization. However, it has the disadvantage of being difficult to control due to back flow and instabilities in the flow. These instability constraints may be overcome while maintain high heat transfer by using a separate fluid phase such as gas or an immiscible liquid into a main continuous liquid-the so-called two phase flow without phase change, Bandara *et al*. (2015). Prior to the heat transfer investigation for the two phase non-boiling flow, two phase flows under adiabatic conditions have been investigated by many researchers. In spite of extensive research, large deviation of the reported results still exists, especially for the observed flow patterns and heat transfer coefficients. However, very few researches have studied heat transfer without phase change in gas –liquid slug flow in microchannels. Lim and Yu (2014) proved the capability of non-boiling system enhanced the heat transfer in micro-tube. They stated that the existence of bubbles could improve the mixing of bulk fluid by lowering down the temperature of liquid layer from the wall to the center of channel.

2.9.3.1 Slug formation

The formation of slug flow development have been reported by several researchers using different types of mixing zone. Guo and Chen (2009) used the VOF method to study the development of the Taylor bubbles and mechanism of Taylor bubbles' breakoff inside a micro-channel T-junction. They observed that the flow is dominated by surface tension for low Ca number, where the effect of shearing force

can be neglected. Therefore, the gas– liquid interface expands and blocks entire liquid flow, which leads to an increased pressure of the liquid phase. The pressure difference between adjacent liquid and the gas phase will pinch off the gas stream and gas slugs. So, with lower surface tension, lower pressure difference is needed for forming a gas slug, and shorter gas slugs are generated. For high Ca number, the mechanism of bubble's break-off is due to the shearing force, the shear stress deforms the gas– liquid interface and the liquid phase shears off the bubble before it blocks the tube. Therefore, the effect of surface tension decreases and the effect of viscous become more dominant, which leads to an increase in the frequency of slug's break-off. This will result in decreasing the slug length. Furthermore at the mixing zone, the main flow direction of the liquid phase is perpendicular toward the gas– liquid interface, and a toroidal vortex is generated in the horizontal tube observed at low Ca number, while at higher Ca number, the main flow direction of liquid phase is toward the horizontal direction and no circulation flow generated (see Figure 2-11).

Similar results were also observed in recent numerical work conducted by Kishor *et al*. (2017) where squeezing regimes are observed at low capillary numbers (10^{-4}~1.5×10^{-3}) and shearing regimes appeared at high capillary numbers (1.5×10^{-3} ~10^{-2}) in slug flow region. Dai *et al*. (2009) conducted a 3D simulation of bubble formation of air-water in a T-junction microchannel of 100 µm diameter under the squeezing regime. They stated that the bubble formation in the T-junction microchannel includes three stages: expansion, collapse and pinching off. Furthermore, the collapse stage is a crucial process in bubble formation and the collapse rate and time are mainly affected by the liquid superficial velocity, viscosity The surface tension of the liquid also influences the collapse stage, where the collapse rate and the collapse time can be presented as a function of the liquid superficial velocity and the capillary number or the Reynolds number.

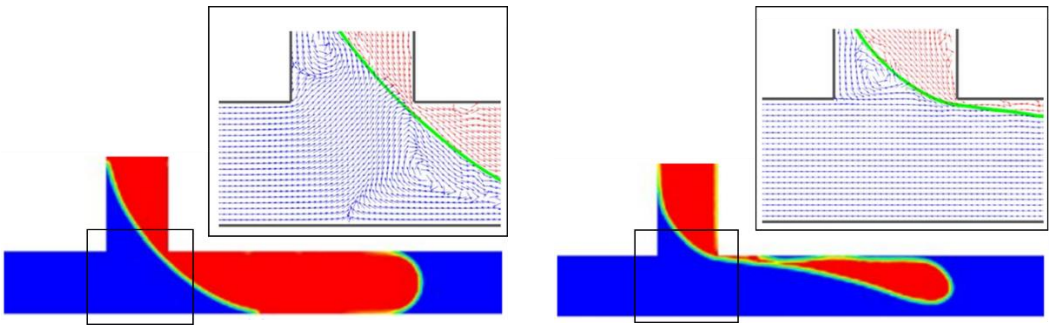

(a) (b)

Figure 2-11 : Mechanism of bubble break-off in T-junction (a) Ca =8.75 × 10^{-4} (b) Ca= 1.4 × $^{10-2}$, Guo and Chen, (2009).

A development of slug formation using concentric nozzles was studied by Shao *et al*. (2008). As seen in Figure 2-12, slug formation using concentric nozzles consists of three stages, which are expanding, contracting, and necking. At the expanding stage, the gas was injected and the gas-liquid interface moves towards the microtube wall. Then at a certain level the bubble grows, where the contracting stage starts, the interface movement reverses and it moves away from the wall towards the axis. The gas bubble grows further in the radial direction by injecting more gas, and leaves only a thin film of liquid to pass. In the necking stage, liquid pressure increases at upstream and the squeezed the lower end of the bubble. As a results, the neck connects the body of the bubble the tip of the gas nozzle is formed. Finally, the neck pinched off and the bubble moves downstream and the shape of the bubble started to change.

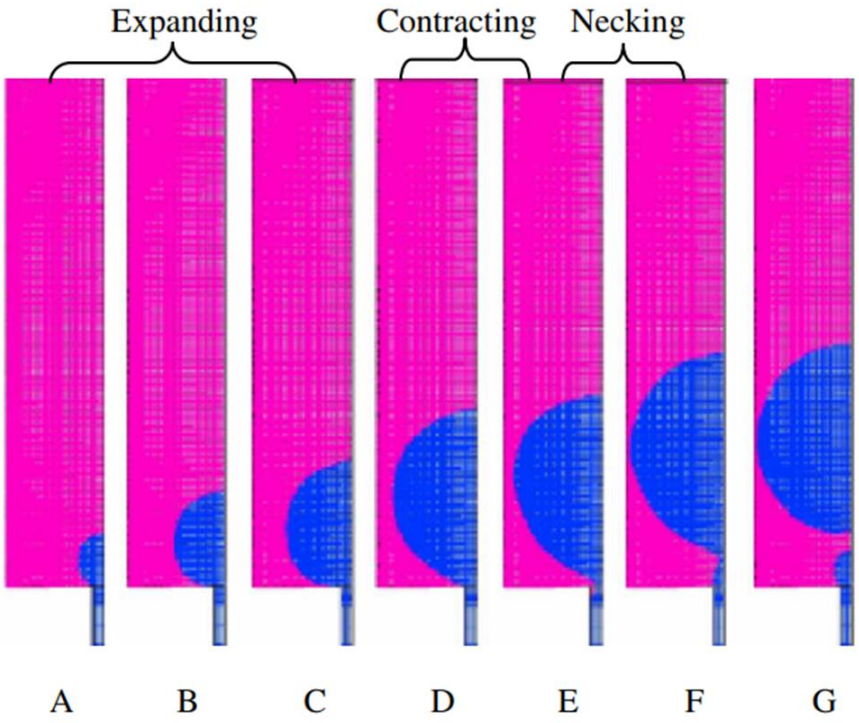

Figure 2-12 : The slug formation in annular/ concentric nozzels, Shao *et al*. (2008).

Chen *et al*. (2009a) carried out numerical work to study the bubble departure size of slug bubbles formation in a 1 mm capillary tube. Air-octane were used as the working fluid. They stated that the bubble size has a significant effect to the ratio of liquid and gas superficial velocities. They observed the departure size and the length of the gas slug increases, as the gas superficial velocity increases or the liquid superficial velocity decreases. Narayanan and Lakehal (2008) focused on the effect of gravity on the breakup of slugs and according to their results, the slug breakup happens slightly earlier for up-flow compared to down-flow orientation, which leads to a higher breakup frequency. Gupta *et al*. (2009) developed numerical simulation on Taylor flow in horizontal microchannels using the VOF method. Later, the performance of VOF and Level Set methods implemented in ANSYS Fluent and TransAT, respectively, were compared, Gupta *et al*. (2010a). According to their bubble formation results from the two techniques, they concluded that both solvers are capable of predicting the interface shape in the slug flow regime.

Recently, Haase (2017) conducted an experiment to study the effect of physical properties of gas and liquid phases and injector diameter on the mechanism of slug formation in a 1 mm square channel. For liquid phase, water, water-glycerol, or water-ethanol mixtures were used, while hydrogen or nitrogen were used as gas phase. They stated that the squeezing mechanism dominates the formation of bubbles at low velocities, while at higher velocities, it is controlled by the dripping mechanism. In squeezing mechanism of bubble formation, the dispersed phase develops a bubble which grows within the flow channel. If this bubble reaches the walls of the channel, the continuous phase can bypass the bubble only in the thin film region between the bubble and the channel wall. In dripping mechanism, the developing gas bubble is split up into two parts within the channel and not at the injector and gas bubble will not block the entire channel cross section in the injector region, Haase (2016). The significant impact of fluid properties and injector diameter were reported on slug formation. At the same operating condition, longer gas bubbles and liquid slug lengths are observed for fluids with a higher surface tension, and smaller viscosity, or by using injectors with a larger diameter.

2.9.3.2 Bubble shape

Heat and mass transfer in the liquid and gas phases and channel wall are strongly affected by the shape of the slug bubble and hydrodynamic slug flow, in particular flow fields around the nose and tail of a bubble behaviour in microchannel. Therefore, the information of shape of bubble and hydrodynamic flow behaviour is important in order to design and develop of the microdevices , Kurimoto *et al*. (2018). Taha and Cui (2004) conducted a numerical 2D axisymmetric model of slug flow inside capillaries using the volume of fluid (VOF) method. The significant effect of capillary number on the bubble shape and liquid film thickness was discussed in this study. They showed that, the shape of the front of the bubble becomes more slender and the liquid film become thicker as the Ca increase. The bubble tail also showed an interesting dependence on the Ca number; for low values of capillary number a wave

disturbance appears near the end of the bubble. Furthermore, the spheroid shape of becomes hemisphere as Ca increases (0.006< Ca <0.77), and at higher tested Ca (2.4) the tail started to penetrate the bubble along its axis creating a re-entrant cavity of liquid at the rear of the bubble. Later, Taha and Cui (2006) found that bubble shape was also affected by liquid viscosity and surface tension. As viscosity of the liquid decreases, the bluntness of the bubble nose increases, which leads in an increase of the liquid thickness. Haase (2017) reported that two-hemispherical caps at the front and the tail of gas bubble for Ca < 0.02 were observed, and as the Ca increases, the gas bubbles shape are more like a bullet shape.

However, Chen *et al*. (2009a), observed a hemispherical cap shape at both the front and rear of slug bubbles, at low Re. The curvature radius of the bubble tip become smaller and the rear cap becomes flattened as the Re number increases. A similar phenomenon was reported by Kreutzer *et al*. (2005). Chen *et al*. (2009) also showed that when the liquid superficial velocity is small enough as compared to the gas superficial velocity, the length of the slug bubbles can be increased by merging a growing bubble with the departed slug bubble in front of it. This approach is called Taylor-pairing or doubling. Zhang and Li (2016) also reported similar results as Chen *et al*.(2009a) and Kreutzer *et al*. (2005); as the *Re* number increases, the inertia force increases, and the tail of slug bubble become flatter and the nose sharper. Additionally, they observed that liquid film thickness and the bubble length increase with increasing *Re*. The significant effect of void fraction on bubble shape was also reported in this study. The void fraction affects the length of the slug bubble and recirculation region inside bubble. As the void fraction increases the length of the slug bubble and inner recirculation region increases. Three recirculation zones in the slug bubble and two recirculation zones in the liquid slug are observed in Taylor flow.

Kurimoto *et al*. (2018) investigated the effect of dimensionless parameters, Ca and Re on the bubble shape and the flow structure inside and outside a bubble. Based on their numerical work, similar results as reported by Zhang and Li (2016), were also observed by them. Three circulations occurred inside the bubble, with small circulation observed in the nose and tail regions and large circulation was occurred in the middle of the bubble, as shown in Figure 2-13. Furthermore, they found that the radius of

curvature at the bubble nose can be well correlated in terms of the capillary number, while for the bubble tail it is depended on both dimensionless parameters, Ca and We. A similar study on the effect of corresponding parameters on bubble shape was also conducted by Taha and Cui (2004). They reported that a significant effect of Ca number on the radius of curvature at the bubble nose. As the Ca number increases, bubble shape becomes slender and the liquid film thickness increases. For the tail of the slug bubble, appearance of a wave disturbance near the tail of a slug was observed at high Re numbers.

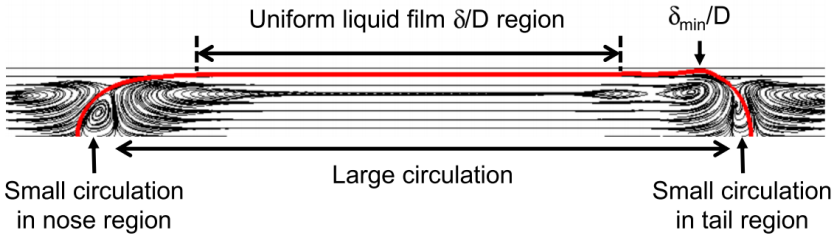

Figure 2-13 : Bubble shape and flow field of slug flow by Kurimoto *et al*. (2018).

1. Bubble and liquid slug length

The length of the bubbles and liquid slugs are playing an important role in determining the pressure drop and heat transfer rates in slug flow. As reported by Lim and Yu (2014) to reach an optimum performance of heat transfer in a microchannel, the ratio of distance between two bubbles to channel diameter should be kept less than 6. They found that the small bubbles give a better heat transfer performance compared to big bubbles, where the distance between two bubbles is reducing as the size of the bubbles increases. Pattamatta *et al*. (2015) concluded that the heat transfer rate increases with increasing bubble length, which can be attributed to a decrease in thermal resistance across the liquid film surrounding the slug bubble as well as due to an increase in film surface area that leads to higher heat transfer rates.

Therefore, the study of length of bubble and liquid slug is important and several correlations have been suggested in the literature to predict the size of bubble slug. Laborie *et al*. (1999) first, proposed an empirical correlation to predict bubble and slug length. Later, Qian and Lawal (2006) conducted a numerical study of slug flow in T-junction microchannels. They used commercial CFD package FLUENT and the volume of fluid (VOF) model was employed in this study. The bubble and slug lengths correlations were proposed by using 148 numerical results obtained in this study. The proposed correlations are showing a significant influence of dimensionless slug length on the phase holdup and slightly on Reynolds and Capillary numbers. Garstecki *et al*. (2006) proposed a simple model which linearly scales with the gas–liquid flow rate ratio for the estimation of bubble lengths in T-junctions. Haase (2017) conducted an experiment on adiabatic gas-liquid downflow in a square minichannel of 1.0 mm at different liquid surface tensions and liquid viscosity by using co-flowing geometry. They used their experimental data to develop new correlations to predict gas bubble and liquid slug lengths, which are based on dimensionless numbers.

There are several factors that affect the length of bubble gas and liquid slug for example the injector diameter, operating condition, liquid and gas properties. Shao *et al*. (2011) found a significant effect on bubble length of the ratio of gas to liquid superficial velocities and gas inlet or nozzle diameter at different liquid properties. Water and octane were used as the liquid phase in this experiment, while nitrogen was used as the gas phase. They observed that the bubble length increased with increasing gas flow rate, gas inlet size, and liquid surface tension and with decreasing liquid flow rate. The length of bubble formation using three different inlet configurations, T-, Y-, and M- junction, were compared. The M-junction, which had the largest mixing volume, produced longer bubbles compared to the Y-junction, which has the smallest mixing volume. New correlations to determine bubble lengths for the T-junction and the Y-junction were proposed. Similar results of a dependency on bubble length on inlet conditions (nozzle size) and surface tension were also reported by Shao *et al*. (2008) and Haase (2017) for a co-flow inlet configuration. Bayareh *et al*. (2020) conducted a numerical study on slug slow in rectangular microchannel by using three different type of inlet configuration (T-, Y-, types). Al2O3-water nanofluid with the volume fraction of 1% and air are used as liquid and gas phases, respectively. They

found that different inlet configurations showing a significant impact on slug and bubble lengths.

In addition, the number of bubbles or bubble frequencies has an important role in predicting the pressure drop accurately in capillaries. However, most of the experimental data in the open literature, do not take these effects into account. Kreutzer *et al*. (2005) reported that the slug length can easily be transformed into a dependence on the number of bubble. They found that more bubbles per unit channel length will result in a higher pressure drop. Choi *et al*. (2010) noted the number of the bubble is highly related with the length of the bubbles and the liquid slug, where the number of the bubbles increased with increasing liquid superficial velocity due to shorter length of the liquid slug. However, for similar liquid superficial velocities, the number of the bubble increased to the maximum number and then decreased as the gas superficial velocity increased. The reason is that the length of bubbles increased with gas superficial velocity. However, the length of liquid slug decreased. And this maximum number of the bubbles is shifted to higher gas superficial velocity with decreasing aspect ratio due to reduced increasing rate of the bubble length. Furthermore, Abadie *et al*. (2012) investigated an effect of fluid properties and operating conditions on gas–liquid Taylor flow in rectangular cross-section microchannels both, experimentally and numerically.

2. Film thickness

Slug bubbles may be separated from the channel wall by the thin liquid film of the primary liquid phase. It is well known that knowledge of the film thickness is important for practical applications that involve heat transfer from the channel wall to the liquid. Pattamatta *et al*. (2015) showed that a smaller film thickness leads to an enhancement in convective heat transfer. This can be attributed to a relatively thinner thermal boundary layer at smaller film thickness and vice-versa. The increase in average bubble temperature with bubble length can be attributed primarily to an

increase in the surface area of the surrounding thin liquid film, which promotes higher heat transfer into the bubble.

Several studies have been conducted in the past both experimentally and theoretically and some of them proposed correlations to predict the liquid film thickness. In experiment study, there are direct and indirectly ways to measure film thickness. In direct measurements using high quality images are used, either free from the optical distortion caused by curved channel walls, or corrected for the optical distortion. For example, in the experimental study conducted by Han and Shikazono (2009), they used a high resolution laser focus displacement meter, to measure the film thickness in a micro-tube. On the other hand, in indirect methods, the film thickness can be measured based on experimental velocity results. However, the knowledge of the velocity profile in the liquid film is needed. Suo and Griffith (1964), introduced a relationship between film thickness and flow velocities and they considered that the film is stagnant. A comprehensive review on the literature concerning the methods used to measure two-phase liquid film thicknesses in macro- and micro-scale systems was presented by Tibiriçá *et al*. (2010) and film thickness correlations found in literature are shown in Table 2-3.

Table 2-3 : Film thickness correlations in literature.

Bretherton (1961)	$\frac{\delta}{D} = 0.643(3Ca)^{2/3}$ for $10^{-3} < Ca < 10^{-2}$	(2.25)
Suo and Griffith (1964)	$\frac{\delta}{D} = \frac{1}{2}\left(1 - \sqrt{\frac{U_{TP}}{U_B}}\right)$	(2.26)
Irandoust and Anderson (1989)	$\frac{\delta}{D} = 0.18[1 - \exp(-3.08Ca^{0.54})]$ for	(2.27)

	$9.5^{-4} < Ca < 1.90$ $0.42 < Re < 860$ $1 < \frac{Re}{Ca} < 140000$	
Aussillous and Quéré (2000)	$\frac{\delta}{D} = \left(\frac{1.34Ca^{2/3}}{1 + 2.5 * 1.34Ca^{2/3}}\right)$	(2.28)
Han and Shikazono (2009)	$\frac{\delta}{D_h} = \left(\frac{0.67Ca^{2/3}}{1 + 3.13Ca^{2/3} + 0.504Ca^{0.672}Re^{0.589} - 0.352We}\right.$ for $Ca < 0.3$ $Re < 2000$	(2.29)
Klaseboer *et al*. (2014)	$\frac{\delta}{D} = \left(\frac{1.34Ca^{2/3}}{1 + 2.79 * 3.35Ca^{2/3}}\right)$	(2.30)
Patel *et al*. (2017)	$\frac{\delta}{D_h} = 0.085Ca^{-0.137}$	(2.31)

Taylor (1961) experimentally obtained the mean liquid film thickness remaining on the wall by measuring the difference of the bubble velocity and the mean velocity. Highly viscous fluids, i.e. glycerine, syrup–water mixture and lubricating oil, were used and thus a wide capillary number range was covered. It is reported that the liquid film thickness increases with capillary number and reaches a certain fraction of the tube diameter. Bretherton (1961) suggested an analytical theory on the liquid film thickness and axial pressure drop across the bubble with the lubrication equations. For low Ca, where inertial forces are negligible, the film thickness can be merely correlated with Ca. He derived that the liquid film thickness was proportional to the capillary number, which is a function of bubble velocity. It is shown that the dimensionless

liquid film thickness can be scaled with $Ca^{2/3}$. Bretherton's analysis is valid for very small liquid film thickness and in the absence of significant inertial and gravitational forces. Aussillous and Quéré (2000) measured the liquid film thickness using fluids with relatively low surface tension. New data obtained with liquids of low viscosity are reported here and compared with Taylor's law. It was found that the liquid film thickness deviates from the Taylor's data at relatively high capillary numbers (Ca>0.3). They improved Bretherton's model and extended its application to higher Ca (Ca < 2) and proposed an empirical relation for film thickness expression based on Taylor's experimental data. Recently, Klaseboer *et al*. (2014) and Cherukumudi *et al*. (2015) derived an analytical solution of liquid film thickness by extending the original results of Bretherton and confirmed the empirical law of Aussillous and Quéré (2000). Klaseboer *et al*. (2014) rederived and analysed Bretherton model for long Taylor bubbles for relatively large Ca numbers. They derived an analytical expression identical in form to the one of Aussillous and Quéré (2000) but with slightly different numerical constant in the denominator (2.79 instead of 2.5), which greatly extended the validity of the Bretherton theory to values of Ca $\sim$ 2.

However, at higher velocities, the effect of inertial could be important. Heil (2001) investigated the effect of inertial force on the liquid film thickness numerically. The results reported show that fluid inertia can play an important role in the Bretherton problem. It is shown that the liquid film thickness and the pressure gradient are dependent on the Reynolds number. Later, the predicted liquid film thickness proposed by Kreutzer *et al*. (2005) showed almost the same trend with Heil (2001). Chaoqun *et al*. (2013) also reported a significant effect of inertia on the bubble generation process where the liquid film thickness was greatly thickened by the inertial effect .

Han and Shikazono (2009) studied the liquid film thickness in circular tubes with diameters ranging from 0.3 to 1.3 mm. They derived an empirical correlation based on Ca, Re and We. Furthermore, they argued stated that liquid film thickness seems to be weakly dependent on the bubble length if the bubble length becomes two times larger than the inner diameter at Ca < 0. 1. Choi *et al*. (2011) observed a significant effect of aspect ratio, (H/W) define on the liquid film thickness which decreased as the aspect ratio decreased. They stated that this is due the confinement

effect. Furthermore, they also stated that the thickness of liquid film inside rectangular microchannel was non-uniform due to corner effect. Similar results was also observed by Wong *et al*. (1995) in their numerical work. They reported that the mean curvature of rectangular cross section decrease as the aspect ratio decreased which lead to reduction in liquid film thickness.

Zhang and Li (2018) observed that as the velocity of the Taylor bubble increases, the relative velocity magnitude in the liquid film increases. Therefore, more fluid tends to flow through the liquid film region which leads to an increase of the film thickness. As a consequence, the dimensionless liquid film thickness increases with increasing capillary number. In contrast, in an experimental work conducted by Patel *et al*. (2017), the film thickness decreases with increasing capillary number. A correlation to predict the film thickness rate was developed based on their experimental data.

2.9.3.3 Pressure drop

The pressure drop plays an important role in two-phase flow in microchannels in terms of design of two phase systems, parasitic energy loss, sizing of pump flow rates and flow stability, Therefore, it is important to quantitatively analyse using experimental, empirical and semi analytical methods, Bandara *et al*. (2015); Walsh *et al*. (2009). In an early study, Bretherton (1961) derived a pressure drop in the long slug bubble in a capillary tube as a function of capillary number with exponent of 2/3, which was based on the bubble velocity. Later, Kreutzer *et al*. (2005) performed both numerical simulation including inertial effects as well as experiments on gas–liquid Taylor flow and compared their results to Bretherton, (1961) work. In their work, the pressure drop due to frictional losses in the gas bubbles and gravity effects in their numerical calculations are assumed to be negligible and used a no-shear boundary condition at the gas–liquid interface. Due to the absence of gravity effects and shear of the gas bubble, the liquid film surrounding the gas bubbles is stagnant and does not contribute to the pressure drop. They suggested the total pressure drop, in a unit cell

of slug flow consist of two components: pressure drop in the liquid slug as a single phase and the pressure drop over the bubble as a function of Re and Ca. Based on the obtained axial wall pressure distribution of a unit cell in gas–liquid Taylor flow, pressure in the liquid slug decreases along the axis, and an oscillation was observed near the slug tail. They stated this is due to oscillation happens because of an inundation on the interface. The pressure variation along the axis and the wall reported by Gupta *et al*. (2009) also in agreement as Kreutzer *et al*. (2005). However, the pressure profile in the slug region behind the bubble is more complex, with significantly different pressure at the wall and the axis close to the bubble. They stated that a complex pressure distribution in this region is due of numerical effects.

The importance of the ratio between Ca and Re in pressure drop modelling of gas-liquid two-phase slug flow was also reported by Walsh *et al*. (2009). In their work, they examined the pressure drop both experimentally and theoretically with varying slug lengths and five different liquids (water, FC40, dodecane, AR 20 silicone oil and n-hexane) and air was used as the gas. The additional pressure drop caused by the interface regions was found to be 40% less than Kreutzer *et al*. (2005). Choi *et al*. (2010) conducted an experiment to study characteristics and pressure drop for a single bubble in a rectangular microchannel of liquid water and nitrogen gas flow in microchannels with AR of 0.92, 0.67, 0.47 and 0.16. They stated that the liquid film thickness that surrounds the bubble has a significant relation with frictional pressure drop for the single bubble in the rectangular microchannel. It indicates that the pressure drop in the single elongated bubble decreased with the aspect ratio of the rectangular microchannel owing to the thinner liquid film. However, they suggested, that the diameter changed with the aspect ratio and further study of independent hydraulic diameter and the aspect ratio is needed for better understanding of frictional pressure drop in the single elongated bubble in a rectangular microchannel.

In addition to the geometrical condition, there are other parameters that have a significant impact on pressure drop was studied by past researchers. For example, as reported by Chen *et al*. (2009a), even at the same liquid and gas superficial velocities, slug and bubble length were significant changed by using different nozzle geometry, which can also effect the pressure drop behaviour inside the channel. They observed

that the pressure drop increases with decreasing slug length or increasing bubble length. Similar observation was also reported by Zhang and Li (2016) in 2D- axis symmetrical model of slug flow in a vertical cylindrical capillaries having diameter of 0.5, 1, 2 mm, where the frictional pressure drop increases as bubble length increasing. Furthermore, frictional pressure drop was also reported to increase with increasing diameters of the tubes. Narayanan and Lakehal (2008) studied the effect of gravity on the pressure drop, where the pressure drop is higher in the case of up flow as compared to zero-gravity and down-flow cases, in that order.

Cherukumudi *et al*. (2015) developed a model to predict a pressure drop of long bubbles flowing in circular tubes based on a combination of lubrication theory and capillary effects (ignoring inertial effects and gravity). A theoretical condition for the minimal length of such a bubble is given in this study. Comparisons with experimental and numerical data for the shape of the bubble, pressure drop and curvature at the front and rear of the bubble for small to intermediate Capillary numbers gave excellent agreement. Kumari *et al*. (2019) performed CFD simulation on air-water slug flow in a channel of hydraulic diameter 1 mm. The pressure in the gas phase of slug flow was almost uniform and the pressure jump at the gas-liquid interface caused was due to surface tension. Furthermore, pressure at the back of the bubble was observed to be slightly lower than that at the front. A significant effect of bubble volume on wall pressure distribution was discussed in this study. The bubble volume was represented by a non-dimensional equivalent sphere radius, ratio of the radius of a sphere having same volume as that of the bubble and channel radius, R_{eqv}. Generally, for all cases, in the gas phase region, the wall pressure decreases and reaches a minimum at the location where the film thickness is thinner. For the smallest volume, the bubble shape is close to spherical, the wall pressure at the middle of bubble is low. As the volume increases, the length of the bubble increases, the wall pressure is almost constant in the middle cylindrical region of bubble.

2.9.3.4 Heat transfer

A significant enhancement of heat transfer in two phase flow slug flow in a mcrochannel was shown by Fukagata *et al*. (2007) and Lakehal *et al*. (2008). Fukagata *et al*. (2007) performed numerical simulation of air– water two-phase flows in a micro tube with 20 μm diameter under constant heat flux. They found the Nusselt number to be up to about twice that for single phase flow for the flow conditions studied. Similar result was reported by He *et al*. (2010) where, the Nusselt number was found to be 2.4 times higher than that of the single-phase laminar flow. The occurrence of a gas bubble causes recirculating flow inside a liquid slug, which increases the heat transfer in slug flow. In a recent study, Zhang and Li (2018) also concluded that recirculation regions in the liquid and gas slugs can enhance the heat transfer coefficient and accelerate the development of the thermal boundary layer. They found that the Nusselt number of slug flow is about 1.16–3.5 times of the fully developed single-phase flow with a constant wall heat flux.

In the numerical work conducted by Lakehal *et al*. (2008), a constant wall temperature boundary condition was employed. They reported that the presence of gas bubbles increases the heat transfer three to four times above that of the liquid-only flow. Furthermore, they observed two separate heat transfer regions in co-flowing configuration, which at the initial breakup and one far downstream in the fully developed region. In break-up region, the local temperature gradient and heat transfer increases due to compressing the thermal boundary layer by the rear area of the slug as indicated by an arrow in Figure 2-14. In the developed region, the fluid flow coming from the liquid film around the bubble into the liquid slug behind the bubble, which was named as a jet-like flow by the authors, was introduced as the responsible mechanism of convective heat transfer. Gupta *et al*. (2010a) compared the local Nusselt number in the unit cell of slug bubble for the constant wall temperature and constant wall heat flux boundary conditions. The local Nusselt number in the slug bubble region is higher for the constant wall heat flux boundary condition, while, in the liquid slug region, the local Nusselt number is slightly higher with the constant wall temperature boundary condition. The average Nusselt number for the two

boundary conditions was showing slight different; for constant wall heat flux the average Nusselt number is 10.9, and for the constant wall temperature is 9.1.

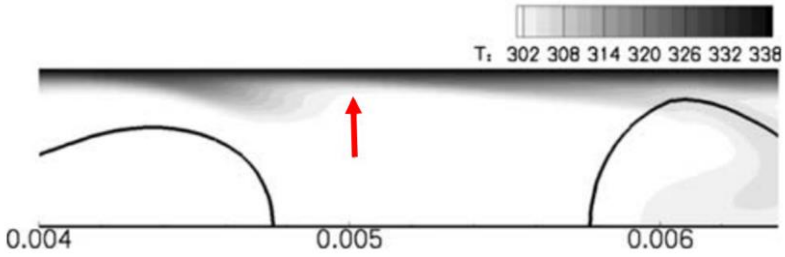

Figure 2-14 : Temperature iso-contours in the break-up zone of the slug flow, Lakehal *et al*. (2008).

Walsh *et al*. (2010) investigated the effect of slug length heat transfer characteristics of air-water slug flow using a 1.5 mm stainless steel under constant heat flux boundary conditions. They varied the slug length-to-diameter ratio from 1.6 to 14.3 for fixed mixture velocity and homogeneous void fraction. They observed that short slugs showed a greater enhancement over single phase flow compared to longer slugs due to internal circulation. Leung *et al*. (2010) conducted an experiment to investigate the dependence of heat transfer rate on slug length and flow parameters, including mixture velocity and homogeneous void fraction. The maximum heat transfer enhancement achieved in this study is 3.2 times that for liquid-only flow. They found the heat transfer enhancement is larger with shorter slugs and higher mixture velocities. The correlation to predict the heat transfer rate of the gas–liquid slug flow was developed based on their experimental data, which indicated that Nusselt number of slug flow was determined by the dimensionless liquid slug length as in Eq (2.32)

$$Nu_{L*} = 4.364 + \frac{0.29}{L_S^* + 0.15 L_S^*} \qquad (2.32)$$

where,

$$L_S^* = \frac{L_S}{Re_{TP}Prd}$$

Contrarily, Lim *et al*. (2013) noted that the bubble size and the length of the liquid slug do not have significant effects on heat transfer. They stated that liquid circulation is no longer important in small channels because the heat from the channel inner surface will easily reach the liquid core. Furthermore, they suggested the optimal heat transfer performance by keeping the pressure drop to a lower level, can be reached by maintaining the bubble size close to the channel diameter.

Lakehal *et al*. (2008) reported a significant impact of bubble length on heat transfer in slug flow. They found that the Nusselt number increased with increases in the gas bubble length. Recently, Kumari *et al*. (2019) performed CFD simulations for air-water slug flow in a channel of diameter 1 mm to investigate the effect bubble volume on the flow and heat transfer. The bubble volume can be represented by a non-dimensional equivalent sphere radius, R_{eqv}ratio of the radius of a sphere having same volume as that of the bubble and channel radius. In this simulation slug length, bubble length and bubble were change with bubble volume. They reported that heat transfer is a strong function of bubble volume and the Nusselt number was found to be highest for the non-dimensional equivalent sphere radius close to one. Liu *et al*. (2019) was carried out an experimental and a 3D numerical simulations on water as liquid phase and R11 as gas phase in rectangular microchannel under a constant wall heat flux. They found that the average Nusselt number is higher for small bubbles (low homogenous void fraction), due to occurrence of the recirculation in the bubbles and slugs. However, as the homogenous void fraction increase, the average Nusselt number decrease. This is because most of the volume in channel is occupied by gas, therefore the heat transfer performance is also getting close to gas only heat transfer. In addition, they noted that under the same void fraction, the average Nusselt is increasing with the increase of gas superficial velocity. They argued that higher gas superficial velocity will lead to a higher mixture velocity which resulting to faster recirculation inside the flow unit and enhance the heat transfer performance.

Choo and Kim (2011) investigated the effect channel diameter (140, 222, 334, 506 μm) on the heat transfer rate. For the large channels of 506 and 334 μm, they found that the Nusselt number increased with increasing gas flow rate, while the Nusselt number decreased with increasing gas flow for the small channels of 222 and 140 μm. They stated this is due to the significant effect of surface tension on the liquid film structure as the channel dimension changes. However, there is no explanation on the relationship of heat transfer and liquid film structure was reported by them. Furthermore, the significant effect of gravity in slug flow on heat transfer was studied by Leung *et al*. (2012) and Narayanan and Lakehal (2008), where in both studies reported that the gravity has a small effect on heat transfer.

2.10 Conclusions

Flow pattern studies during gas–liquid flow in microchannels without heat transfer are reviewed in the present study. Based on the information of visual observations reported in literature, the flow patterns observed during two phase flows in small channels are morphologically similar with large scale system and terminology used in large scale systems is often adopted. However, the different names given by previous researchers to similar flow patterns is the biggest problem these studies. Furthermore, with the development of numerical methods and computational capability, some interface capturing methods are employed to simulate two-phase flow. However, very few works dealt with the numerical simulation of gas−liquid flow regimes in microchannels.

To date, most of the numerical work reported only two dimensional axisymmetric studies of gas–liquid flow due large computational resource requirements needed for three dimensional simulations. But there needs to be further numerical work in three dimensional numerical simulations to determine more information on the flow and heat transfer for model validation. As computational

power grows, and solution algorithms are improved, it will be possible to solve for three dimensional flow in microchannels with gravitational forces included.

2.11 Summary

This chapter has reviewed all the relevant literature used in the study of single and two phase flow in microchannel in both experimental and numerical study. A few of the research gaps in single phase and two phase flow discussed Section 2.8 and Section 2.10, respectively, have been considered in the present research for numerical simulations. A comprehensive summary of numerical studies in single phase and two-phase microchannel is presented in table below. This reviews led to the development of conceptual numerical model. Starting with the effect of axial conduction and geometrical parameter on fluid flow and heat transfer for single channel and rectangular microchannels (see Chapter 3) have been studied. After that, the effect of geometrical parameter of inlet/outlet and number of channel on flow distribution in parallel rectangular microchannels configurations have been considered (see Chapter 4). In two phase flow study, (see Chapter 5) some simulations using fixed frame of reference for circular microchannels have been carried out in order to developed numerical flow regime maps in order to identify the slug flow boundaries in dependence on annular nozzles configurations. In this work, the flow field has been calculated using a two dimensional, axisymmetric geometry due to save computational time and effort. Next is to examine the topology of hydrodynamic flow and heat transfer distribution of slug flow. In the final part, the effect of gas superficial velocity on hydrodynamic and thermal behaviour of the bubble gas for unit cell and a three dimensional work was conducted.

Table 2-4 Review of numerical work in single phase microchannel

Author(s)	Working fluid Channel Material/ Shape/ size/ Re	NA	CE	SE	Remarks
Fedorov and Viskanta (2000)	Water; Silicon; Rectangular; Dh=86 μm; Re=50-400;	3D	√	-	The analysis provides complex heat flow pattern in the channel due to combined convection-conduction effects in the three-dimensional setting
Gao *et al*. (2002)	Water; Silicon; Rectangular; Dh = 0.008-0.077 mm Re=100-8000	2D	-	√	The classical laws of friction in two-dimensional ducts are well verified both in the laminar and the turbulent regimes
Qu and Mudawar (2002)	Water; Rectangular; copper; Dh=	3D	√	√	Excellent agreement between both the pressure drop and heat sink temperature data and corresponding numerical predictions proves the conventional Navier–Stokes and energy equations can accurately predict the heat transfer characteristics of micro-channel heat sinks for the channel size employed in the present study and recommended for practical cooling applications.
Lelea *et al*. (2004)	Water Stainless steel; Circular Di=0.1,0.3, 0.5 mm 50-800	2D	-	√	The local value of Nu is in good agreement with conventional theories including the entrance region.
Tiselj *et al*. (2004)	Water; Triangular; Silicon; N=17 Dh=160μm	3D	√	-	The importance of the second alternative pathway for the heat transfer can be truly appreciated only in three-

	Re =3.2–64				dimensional conjugate heat transfer problem.
Lee *et al*. (2005)	Water; Copper; Rectangular; N= 10 Dh=318-903μm α (H/W)=4.56-5.45 L=25.4mm Re=300 to 3500	3D	√	√	The entrance and boundary conditions imposed in the experiment need to be carefully matched in the numerical approaches
Gamrat *et al*. (2005)	Water Bronze Rectangular Re=200 to 3000	2D, 3D	√	√	No significant size effect on friction factor and heat transfer
Lee and Garimella (2006)	Water Rectangular Stainless steel Dh=200-364um AR=1-10 Re= 200-8000 Recr= 3500-4000	3D	-	√	The increase in local Nusselt number in the microchannel at a larger aspect ratio, since the relative importance of the narrow walls and corners diminishes with increasing aspect ratio
Baviere *et al*. (2006)	Water; Silicon; Rectangular; Dh = 0.008-0.077 mm Re=200-8000 Re_{cr}=3500-4500	2D	√	√	Bias effect on the solid/fluid interface temperature measurement may account for the apparent scale effects The coupling between conduction and convection was weak in the conditions of this study.
Liu *et al*. (2007)	Water Rectangular D=100μm Re=10-200	2D	√	-	The axial conduction introduced by thermal-conductivity-variation was insignificant unless for the cases with very low Reynolds numbers

Gunnasegaran *et al*. (2010)	Water Aluminium Rectangular; trapezoidal; triangular Dh =148-385um N= Re=100-1000	3D	-	√	The smallest hydraulic diameter has the greatest value of heat transfer coefficient
Moharana *et al*. (2012)	Water; Rectangular; D_h=0.4 mm Re= 100-1000	3D	√	-	thermal conductivity ratio k_{sf} is the key factor in determining the effects of axial wall conduction on the heat transport behaviour.
Moharana and Khandekar (2012)	Water; Rectangular; AR=0.45- 4 Re= 100	3D	√	√	for a given flow rate and any value of thermal conductivity ratio ksf, a minimum of average Nusselt number occurs with respect to the channel aspect ratio
Dharaiya and Kandlikar (2012)	Water Rectangular Cooper Dh =27.3-272.7um *AR*=0.1-10 Re=100	3D	-	√	Generalized correlations are proposed for all the possible heated wall configurations to estimate fully developed H2 laminar flow Nusselt number value as a function of channel aspect ratio in rectangular microchannels to represent the numerical results within 0.8% maximum deviation
Hassan *et al*. (2014)	Water Triangular Dh=58-234 um Re=100-400	3D	√	√	The parameters that affect the axial heat conduction are: thermal conductivity ratio Reynolds number Re, hydraulic diameter Dh, channel volume and wall thickness
Wang *et al*. (2016)	Water cooper Rectangular; trapezoidal; triangular Dh=0.172-0.406 mm AR= 1.030 to 20.333	3D	-	√	the shape and geometric parameters of microchannel have a remarkable impact on the flow and heat transfer characteristics of microchannel heat sink

	N=12 Re=100-700				

Table 2-5 Review of numerical work in single phase flow and heat transfer in multichannel

Author(s)		NA	Remark(s)
Choi et al. (1993)	Working fluid: Water Manifold shape: Rectangular Flow arrangement: Z Number of channel:8	2D	numerical study of the effect of area ratio on the flow distribution in parallel flow manifolds
Kim et al. (1995)	Working fluid: Water Manifold shape: Rectangular, trapezoid, triangular Flow arrangement: Z Number of channel:8	2D	the flow rate concentration in the last channel is the main reason for the nonuniform flow distribution.
Webb (2003)	Working fluid: Water Manifold shape: Rectangular, oblique Flow arrangement: I Number of channel:8	2D	The flow uniformity is significantly enhanced with increasing area ratio
Tonomura et al. (2004)	Working fluid: Water Manifold shape: Rectangular Flow arrangement: Z Number of channel:5	3D	Flow acceleration can be reduced by expanding the outlet manifold area to enhancement the flow uniformity
Lu and Wang (2006)	Working fluid: Water Manifold shape: Rectangular Flow arrangement: I-, Z-,]-, L-, Γ- Number of channel:20, 40, 60	3D	the lowest heat transfer performance is due to occurance of flow recirculation and maldistribution
Chein and Chen (2009)	Working fluid: Water Manifold shape: Rectangular Flow arrangement: I-, N-, S- D-, U-, V- Number of channel:11	3D	The flow maldistribution more pronounced in horizontal inlet-outlet flow arrangements
Tong et al. (2009)	Working fluid: Water Manifold shape: Rectangular Flow arrangement: Z Number of channel:10	2D	The strategies that are most effective for the attainment of the goal of outflow uniformity :(a) enlargement of the cross-sectional area

			of the distribution manifold (b) variation of the cross-sectional areas of the outflow channels (c) linear tapering of the cross-sectional area of the distribution manifold, and (d) non-linear tapering of the cross-sectional area of the manifold by means of quarter-elliptical contouring of the manifold wall
Jang et al. (2010)	Working fluid: Methanol Manifold shape: Rectangular Flow arrangement: right inlet/ left outlet, right inlet/ right outlet, right inlet/ central outlet, central inlet/central outlet, and central inlet/ two outlets Number of channel:20	3D	A correlation expression for the methanol conversion ratio is presented in terms of wall temperature, channel geometry, inlet and outlet manifold configuration, and flow rate
Kim et al. (2011)	Working fluid: Water Manifold shape: Rectangular Flow arrangement: Number of channel:10	3D	the effect of the radius of curvature at the corners of the manifold is negligible
Kumaragurupar an et al. (2011)	Working fluid: Water Manifold shape: Rectangular Flow arrangement: U Number of channel:5-20	3D	It is evident that the flow separation and recirculation occurring in the inlet header are primary responsible for the flow mal-distribution between the channels
Kumaran et al. (2013)	Working fluid: Water Manifold shape: Rectangular ; Trapezoidal Triangular Flow arrangement: C- I- Z-, V, and U-type Number of channel:25	3D	Flow recirculation exhibited at the corner of manifold as the width of manifold increased was the reason of undesirable flow distribution
Pan et al. (2013)	Working fluid: Water Manifold shape: Rectangular Flow arrangement: Z Number of channel:	3D	A relatively uniform flow distribution can be obtained by the following conditions: longer microchannel, smaller microchannel width,

			symmetric manifold structure, larger manifold area, and perpendicular direction of inlet/outlet to the microchannel plane.
Siva et al. (2014)	Working fluid: Water Manifold shape: Rectangular Flow arrangement:U, I, Z Number of channel:5-20	3D	The local variation of pressure drop helps to identify the probable location of hot spot as the trend of flow distribution is parabolic, which is unlike the high Reynolds number flow observed in macrochannels
Xia et al. (2015)	Working fluid: Water Manifold shape: Rectangular ; trapezoidal (symmetry) ; Triangular Flow arrangement: U, I, Z Number of channel:30	3D	The fluid flow mechanism can be attributed to the interaction of the branching of fluid and the friction offered by the walls of the header.
Tang et al. (2018)	Working fluid: Water Manifold shape: Rectangular ; trapezoidal (symmetry) ; Triangular Flow arrangement: U, I, Z Number of channel:25	3D	The major reason for the difference between the Z- and C-type configurations is the difference in pressure distribution at the inlet and outlet locations along the radial direction
Amiri (2019)	Working fluid: Blood Newtonian fluid; power-law non-Newtonian fluid Manifold shape: Rectangular, trapezoidal, Triangular Flow arrangement: U, I, Z Number of channel:5	3D	The trend of variation of uniformity with power-law non-Newtonian fluid is similar as blood Newtonian fluid; however, there is a difference in the values of uniformity for each distributor.
Kumar and Singh (2019)	Working fluid: Water Manifold shape: Rectangular Number of channel: 28	3D	The proposed inlet/outlet arrangement with flow inlet angle $\theta = 105°$ has the lowest value of maldistribution factor

Table 2-6 Review of numerical work in two phase flow in microchannel.

Author(s)	Working Fluid/ Channel	Numerical dimension	Remark(s)

Heil (2001)	Water-Air 0.05<Ca<5 0<Re<280	2D T-junction	The largest of these vortices is located near the bubble tip where it significantly affects the pressure distribution and leads to a noticeable increase in the overall pressure rise across the bubble tip
Taha and Cui (2004)	Water-Air 0.01<Ca<10	2D axisymmetric	Velocity and bubble profile were obtained as functions of capillary number
Kreutzer *et al*. (2005)	Water-Air 0.002<Ca<0.04 Re<900	2D axisymmetric	The Laplace pressures are significant with respect to the viscous losses in the slug
Taha and Cui (2006)	Water-Air 0.01<Ca<10	2D axisymmetric	The bubble shape was found to be dependent upon liquid viscosity and surface tension but not on the bubble length
Qian and Lawal (2006)	Water-Air	2D T-junction	The results show that the slug length is not uniform throughout the channel especially for channel cross-sectional dimensions exceeding 1 mm We have confirmed that gravity does not have much of an effect in slug flow in microchannels, so the Froude number can be ignored
Fukagata *et al*. (2007)	Water-Air 16<Re<490 0.0087<Ca<0.27	2D axisymmetric	It is also found that the length of the computational domain, i.e., the period of bubbles, considerably affects the flow pattern.
Lakehal et al. (2008)	Water-Air	2D axisymmetric	Detailed computational microfluidics flow simulations have been performed to study the effect of varying flow regime on the heat transfer in small tubes
Shao *et al*. (2008)	Water; Octane; Semi-octane - Air	2D, axisymmetric	Bubble formation mechanism and bubble size at different operating conditions and fluid

Narayanan and Lakehal (2008)	Air-water Ca= 0.0154 Re=1110	2D, axisymmetric Level set method	Gravity has an impact on the breakup time/length, where the effect of gravity counters inertia when the flow is against gravity, thus making surface tension more dominant. However. the heat transfer results are only marginally affected by gravity,
Guo and Chen (2009)	Water- Air 100<Re<500 $6.4x10^{-4}$<Ca< $1.7x10^{-2}$	2D domain T-junction VOF method	The slug length is not a uniform value, and the non uniformity increases with increasing gas and liquid interfacial velocity
Chen *et al*. (2009a)	Air-Octane	2D axisymmetric Level set method	The Taylor bubble formation in a liquid co-flow is found to be weakly dependent on the contact line dynamics which is not the case for bubble formation in a quiescent liquid
Dai *et al*. (2009)	Water; Semi-water -Air	3D T-junction VOF method	Three stages of bubble formation in squeezing regime were proposed via: expansion, collapse and pinching off. Collapse stage was found as most important stage in bubble formation process.
Gupta *et al*. (2009)	Water-Air Ca= 0.006 Re=280	2D axisymmetric VOF method	The liquid film at the wall has not been captured successfully in many numerical studies performed to model Taylor flow, largely due to the poor near-wall resolution
Gupta et al. (2010a)	Water-Air Ca= 0.006 Re=280	2D axisymmetric VOF method Level set method	The results obtained from the two techniques are very similar giving confidence in the veracity of the numerical results
Abadie et al. (2012)	Ethanol/ Water/ Sugarcane syrup-Air	2D axisymmetric VOF method	Numerical simulations confirm the hypothesis of a stagnant liquid film and provide information on the thickness of the liquid film.

Lim and Yu (2014)	Air-Water	2D axisymmetric VOF method	Analysis of the velocity and temperature profiles near a bubble shows that the bubble obstructs the path of the liquid flow, forcing the redistribution of the axial and radial velocities around the bubble, which redistribution enhances the thermal mixing and the heat transfer performance
Pattamatta et al. (2015)	FC-72	2D axisymmetric VOF method	The increase in Nu* with bubble size can be attributed to a decrease in thermal resistance across the liquid film surrounding the vapor bubble as well as due to an increase in film surface area that leads to higher heat transfer rates
Zhang and Li (2016)	Water–Nitrogen 100<Re<500 0.00055<Ca <0.013.	2D axisymmetric VOF method	The results indicate that the dimensionless liquid film thickness and bubble rising velocity increase with increasing capillary number
Kishor *et al*. (2017)	Air-water 100<Re<500 6.4x10-4<Ca< 1.7x10-2	3D domain VOF method T-junction	The study indicates that VOF method is an efficient tool for realizing and analysing slug flow in microfluidic devices.
Zhang and Li (2018)	Water–Nitrogen 0.5 mm - 2 mm 100<Re<500 0.00055<Ca< 0.013	2D axisymmetric VOF method	The results indicate that the dimensionless liquid film thickness and bubble rising velocity increase with increasing capillary number
Kurimoto *et al*. (2018)	Water-air	2D axisymmetric Level-set method	Numerical simulations of slug flows in circular microchannels were carried out using an interface tracking method based on the volume of fluid method in this study to investigate the relationship between the

			bubble shape and the flow field
Kumari *et al*. (2019)	Water-air 115<Re<560	2D axisymmetric VOF method	The bubble volume can be represented by a non-dimensional equivalent sphere radius, ratio of the radius of a sphere having same volume as that of the bubble and channel radius.
Bayareh et al. (2020)	Al2O3-water nanofluid -air	2D VOF method T- , Y- junction	The characteristics of the slug flow of Al2O3-water nanofluid with the volume fraction of 1% were studied for three different inlet configura- tions of microchannels
Liu *et al*. (2020)	Water-R11	3D VOF and Level Set method T- junction	Wall temperature and fluid temperature are distributed in a periodical manner along the flow direction which is due to the periodical distribution of the bubble and slug

3 CFD MODELLING OF SINGLE PHASE FLUID FLOW IN RECTANGULAR SINGLE MICROCHANNEL

3.1 Introduction

Numerical simulations were performed on single phase fluid flow in a rectangular microchannel embedded in a test module. The computational setup was selected to match the detailed description of the experimental facility given by Mirmanto *et al*. (2012). The test section was made of an oxygen-free copper block with a width of 12 mm, a height of 25 mm and a length of 72 mm. A single rectangular microchannel with a height of 0.39 mm, a width of 1 mm and a length of 62 mm was cut in the top surface of the block. The test section was heated using a cartridge heater embedded below and parallel to the channel. De-ionized water was used as a test fluid and the material of microchannel device was made from copper.

This section describes the geometric model setup and the validation of the results for single phase fluid flow in a single rectangular microchannel. The aim is to study the effect of channel aspect ratio,$AR = {}^{H}/_{W}$ and hydraulic diameter, $D_h = {}^{2HW}/_{(H+W)}$. Also, conjugated heat transfer results, simulating the channel embedded in the copper block with heater will be compared to the non-conjugate approach (simulating only the heated channel) that is usually adapted, Lee and Garimella (2006); Dharaiya and Kandlikar (2012).

3.2 Effect of axial conduction on heat transfer

3.2.1 Model descriptions

Numerical simulations were performed to solve the conjugate heat transfer problem in a microchannel, accounting for both convections in the channel and conduction in the copper substrate. As listed below, four different approaches were used in the single channel configuration to examine the accuracy of different numerical schemes tested in this study, through comparing the predicted friction factor and Nusselt number with experimental data and conventional theory.

1. **Model 1**: the geometry used in this model is depicted in Figure 3-1 where a 2D simulation was conducted with a constant heat flux boundary condition applied at the bottom surface of the channel only while the top surface was adiabatic.

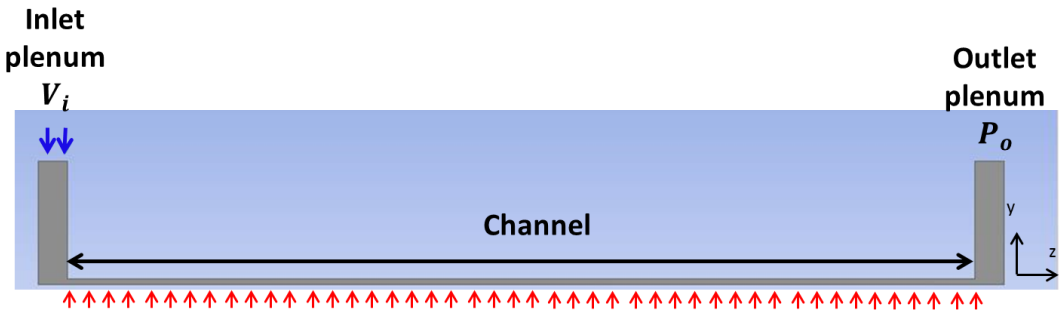

Figure 3-1 **:** 2D computational domain of a single microchannel system (**Model 1**).

2. **Model 2**: the geometry used in this model is depicted in Figure 3-2. In this model, a 3D thin-wall approach was adopted with zero wall thickness (no axial conduction). A constant heat flux boundary condition was applied at the bottom surface only while the other three walls were considered adiabatic. Hereafter, this model is referred to as the "3D thin-wall one side heated model" as seen at

the top left corner of Figure 3-2. In the thin-wall model, the thermal boundary conditions are applied at the outer surface of the wall (at the solid-fluid interface), ANSYS Fluent.

3. **Model 3**: this model is similar to Model 2 except that the constant heat flux boundary condition was applied at the bottom and the two side walls while only the top wall was kept adiabatic. This model referred to as the "3D thin-wall three sides heated model" as seen at the top left corner of Figure 3-2.

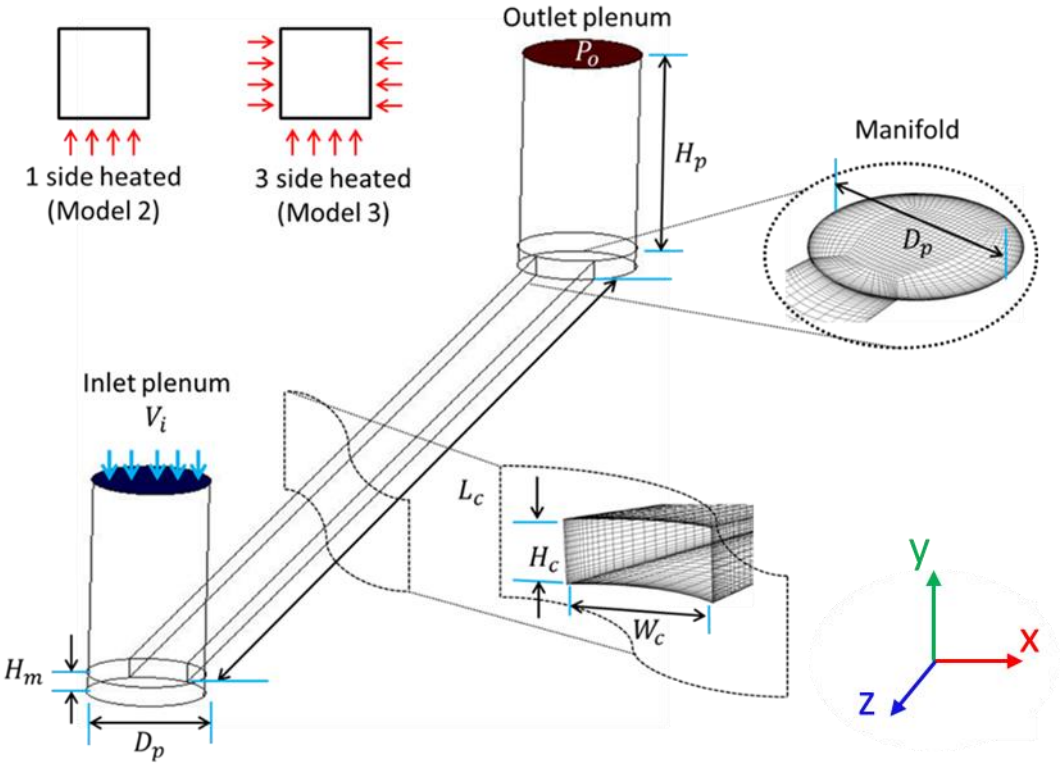

Figure 3-2 : Computational domain of single microchannel system (Thin-wall **Models 2** and **3**).

4. **Model 4**: the geometry used in this model is depicted in Figure 3-3. Here, a 3D fully conjugated model was simulated. In this model, the complete copper block, similar to the one used in the experiment conducted by Mirmanto *et al*. (2012) was simulated. A constant heat flux boundary condition was applied at the location of the cartridge heater.

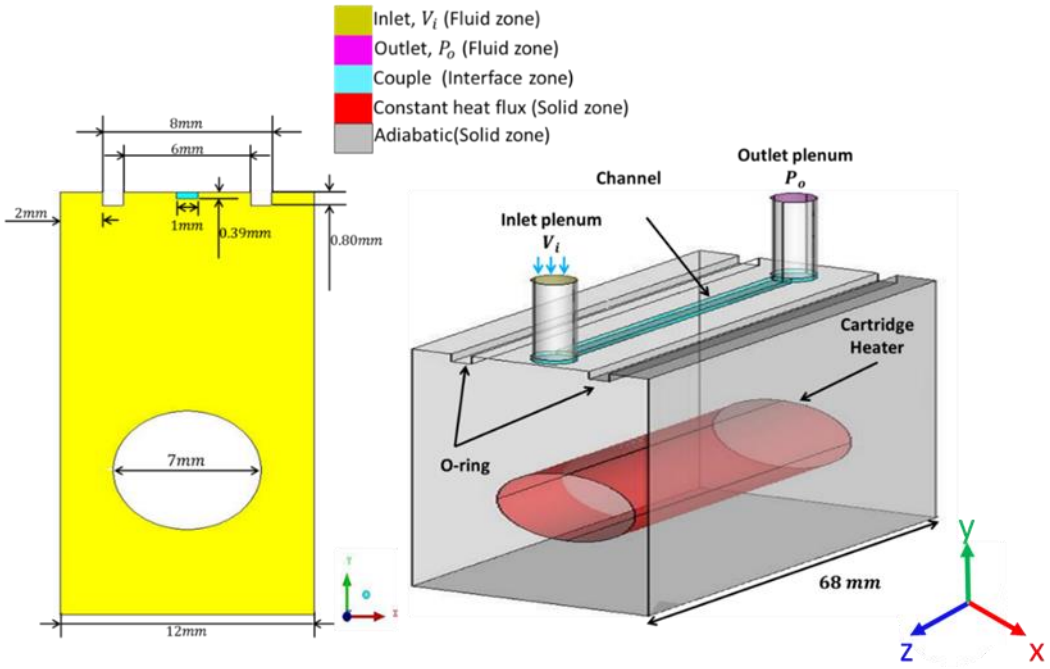

Figure 3-3 : 3D fully conjugated computational model of single microchannel system (**Model 4**).

3.2.2 Numerical Method

A CFD analysis was carried out to investigate the characteristics of fluid flow and conjugate heat transfer in microchannels. The following assumptions were adopted:

1. Steady state fluid flow and heat transfer.

2. Incompressible fluid

3. Negligible radiative heat transfer

4. Constant solid and fluid properties

Based on the above assumptions, the governing differential equations used to describe the fluid flow and heat transfer in the microchannel are given by:

Conservation of mass (continuity)

$$\nabla\left(\rho\vec{V}\right) = 0 \tag{3.1}$$

Conservation of momentum

$$\vec{V} \cdot \nabla\left(\rho\vec{V}\right) = -\nabla p + \nabla \cdot (\mu\nabla\vec{V}) \tag{3.2}$$

Conservation of energy for fluid

$$\vec{V} \cdot \nabla\left(\rho c_p T_f\right) = \nabla \cdot (k_f \nabla T_f) \tag{3.3}$$

Conservation of energy for solid

$$\nabla \cdot (k_s \nabla T_w) = 0 \tag{3.4}$$

The boundary conditions for the governing equations are given as,

Inlet plenum:

$$V = V_{in} \qquad T = T_{in} \tag{3.5}$$

Outlet plenum:

$$P = P_{out} \tag{3.6}$$

A number of uniform inlet velocities were selected in order to match the Reynolds number values obtained in the experiment conducted by Mirmanto *et al*. (2012). The water temperature employed at the inlet is 308.15 K. The properties of liquid water at 308.15 K are ρ_f = 994 kg/m^3, $c_{p,f}$= 4182 J/(kgK), k_f= 0.6 W/(mK), for density, heat capacity and thermal conductivity, respectively. As stated previously, the temperature dependency of fluid and solid properties can be neglected due to the small changes of fluid and wall temperature which will presented and discussed later. At the outlet a pressure outflow boundary condition was employed. The no slip (zero roughness) boundary condition was assigned to all wall boundaries. The heat loss through the top cover was considered to be negligible.

$$-k_s \frac{\partial T_s}{\partial n} = 0 \tag{3.7}$$

Hence, in the thin wall approach (**Model 2** and **Model 3**) adiabatic conditions were employed at the top wall while along the bottom (and also the side walls for the 3D simulation) a constant heat flux q'' (6235.812 W/m^2) was applied.

$$-k_s \frac{\partial T_s}{\partial n} = q'' \tag{3.8}$$

For the 3D full conjugate analysis (**Model 4**), the continuity of the temperature and heat flux is used as the conjugate boundary condition to couple the energy equations at the fluid and solid interface, which are expressed as:

Fluid–solid interface

$$\vec{V} = 0, T = T_s \qquad -k_s \frac{\partial T_s}{\partial n} = -k_f \frac{\partial T_f}{\partial n} \tag{3.9}$$

A constant heat flux, q'' was applied at the location at the cartridge heater.

$$-k_s \frac{\partial T_s}{\partial n} = q'' \tag{3.10}$$

where the q'' is calculated from $P_w/A_{catridge}$. P_w is the total electric power input measured using the wattmeter and $A_{catridge}$ is the area of the cartridge heater. Adiabatic boundary conditions are applied to all other boundaries of the solid region. The properties of the solid used in the numerical simulation are, ρ_s = 8978 kg/m^3, c_p= 381 J/ (kgK), k_s= 387.6 W/(mK), for density, heat capacity and thermal conductivity, respectively.

The computations were performed using the commercial software package FLUENT 14.5. ICEM 14.5 was utilized for the geometry construction and mesh generation. The viscous laminar model or the standard k-Omega model was used for laminar ($Re < 2000$) and turbulent ($Re > 2200$) flow, respectively. The SIMPLE scheme, Patankar (1980) is used to resolve the pressure-velocity coupling. The flow momentum and energy equations are solved with a first-order upwind scheme. The simulations are performed using a convergence criterion for the residuals of 10^{-6}. The hexa meshing grid scheme was used to mesh the system. A highly compressed non-uniform grid near the channel walls, as shown in Figure 3-4, was adopted in order to properly resolve viscous shear layers. As in Fedorov and Viskanta (2000) and Qu and Mudawar (2002) grid nodes were also concentrated along the axial direction in the entrance of the channel in order to properly resolve the flow and thermal development regions.

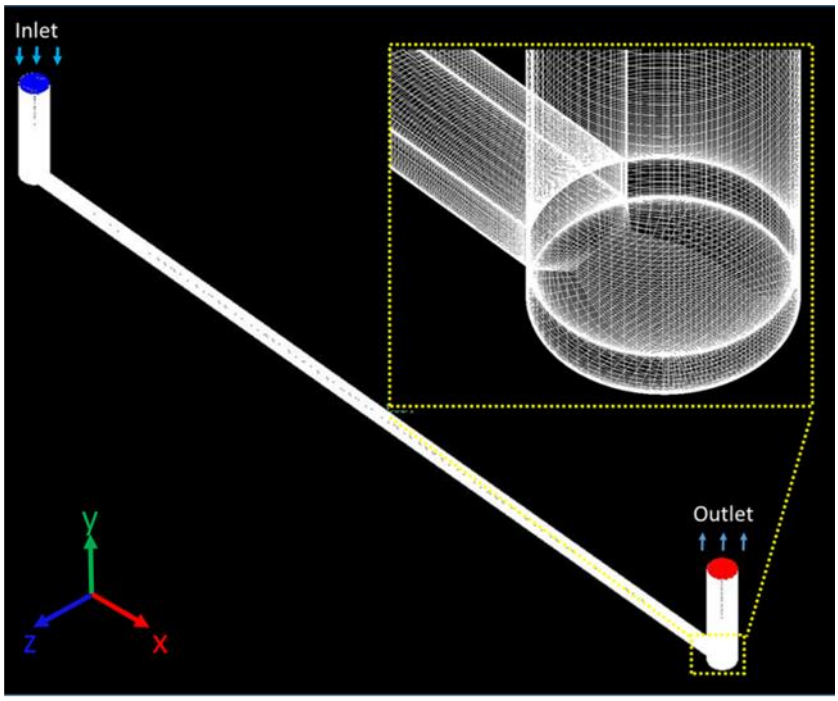

Figure 3-4: Schematic and computational meshes of geometrical model.

A grid dependency study was conducted in a single channel system at the highest and lowest Re number, using the friction factor as a criterion to ensure the results are independent of the mesh. It was carried out for the 3D model (thin wall **Model 3**) by varying the number of grid points in the microchannel. Three different grid sizes of $20 \times 15 \times 300$ (Grid 1), $20 \times 15 \times 600$ (Grid 2) and $20 \times 50 \times 600$ (Grid 3) were used in the x-y-z direction representing width, height and length, respectively. A grid sensitivity study was conducted in both the laminar and turbulent region. In the laminar region, the predicted friction factor changed by less than 1% when replacing the $20 \times 15 \times 300$ grid by the $20 \times 50 \times 600$ grid. While in the turbulent region, the predicted friction factor changed by 3.5% when replacing the first by the second grid, and only by a further 1 % when using the finest gird. Hence the intermediate grid size of $20 \times 15 \times 300$ was chosen in order to save computational time.

Table 3-1 Percentage difference predicted friction factors for each of the different grids considered.

Grid	Deviation from (Grid 1) [%] based on Re<2000	Deviation from (Grid 1) [%] based on Re>2000
$20 \times 15 \times 300$ (Grid 1)	-	-
$20 \times 15 \times 600$ (Grid 2)	± 0.05	± 3.5
$20 \times 50 \times 600$ (Grid 3)	± 0.08	± 1

3.2.3 Data analysis

The local heat transfer coefficient is defined as:

$$h(x) = \frac{q''(x)}{T_{w,av} - T_{f,av}} \tag{3.11}$$

where the temperatures $T_{w,av}$ is wall temperature average and $T_{f,av}$ is fluid temperature , which both parameters are determined by taking the average of five locations along the channel width at each axial distance *x*. The local Nusselt number is defined by:

$$Nu(x) = \frac{h(x)D_h}{k_f} \tag{3.12}$$

The average heat transfer coefficient is defined by:

$$h_{av,num} = \frac{1}{L_{ch}} \int_0^{L_{ch}} h(x)dx \,, \tag{3.13}$$

where L_{ch} is the length of the channel.

$$Nu_{av,num} = \frac{h_{av,num} D_h}{k_f} \tag{3.14}$$

3.2.4 Discussion of the results

The predicted numerical friction factor results were verified using results obtained in the experiments carried out by Mirmanto *et al*. (2012), the Shah and London (1978) correlations for developed and developing laminar flow and the Blasius (1913) equation for turbulent flow as seen in Figure 3-5. The figure depicts the validation of the friction factor predicted by the 2D and 3D models. It indicates that the 2D model underpredicts the values by about 30% while the 3D model agrees very well with the experimental data. This could be attributted to the reduction in wall shear stress arising from ignoring the channel side walls in the 2D simulation. Additionally, it is obvious that both the 3D model and the experimental data exhibit a transition change at $Re \approx 1600$, which agrees with the findings of Harms *et al*. (1999) and Zhang *et al*. (2014). Harms *et al*. (1999) investigated water flow in a rectangular microchannel, with D_h is 401μm and found that the transition occurrs at $Re \approx 1500$. Recently, Zhang *et al*. (2014) studied flow and heat transfer characteristics of six rectangular microchannels with D_h ranging from 0.48 mm to 0.84 mm. The experimental results indicated that the laminar to turbulent transition occurs in the range $\mathrm{Re} = 1200 - 1600$. The early transition that takes place at Re less than 1000, as reported by Mala and Li (1999), was

not observed in the present study. Researchers who reported early transition thought that it occurs due to channel size reduction as reported by Peng *et al*. (1995) and Pfund *et al*. (2000).

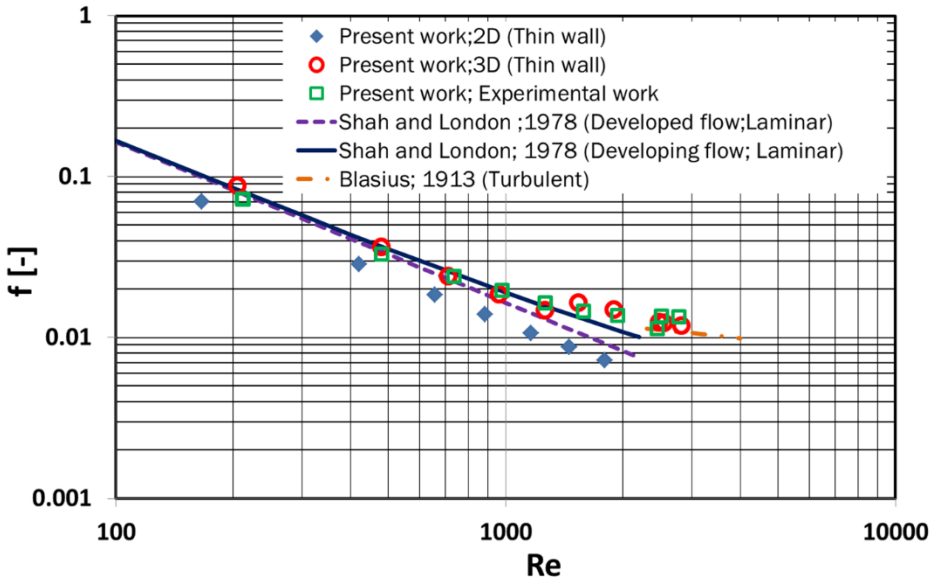

Figure 3-5 **:** Comparison of predicted friction factor with existing experimental results and existing correlations.

Figure 3-6 presents a comparison of the computationally predicted average Nusselt number (Eq. (4.8)) in the laminar and turbulent regions with existing experimental data and correlations. The figure shows that the 2D thin wall model (**Model 1**) agrees very well with Shah and London (1978) for developing laminar flow but highly under-predicts the experimental values. This could be due to the fact that Shah and London solved the 2D problem because the predicted average Nusselt number only showing a good agreement with Shah and London (1978) but it does not agree with the predicted average Nusselt number using 3D thin-wall models, . It is worth mentioning that the experimental data presented in this figure were calculated based on the assumption of a uniform and constant heat flux boundary condition. In order to validate the numerical method, 3D thin-wall models were simulated using the same assumption as used in the experimental data reduction (uniform and constant heat flux) and the results are shown

in Figure 3-6. The figure shows that the 3D thin-wall models (**Models 2 and 3**) exhibit excellent agreement with the experimental values and the insignificant difference between the two models could be due to the short height of the channel, which is 0.39 mm . The excellent agreement of the thin-wall models with the experimental data arises from the similarity in the assumption of uniform constant heat flux, which may be true or may not as will be discussed later.

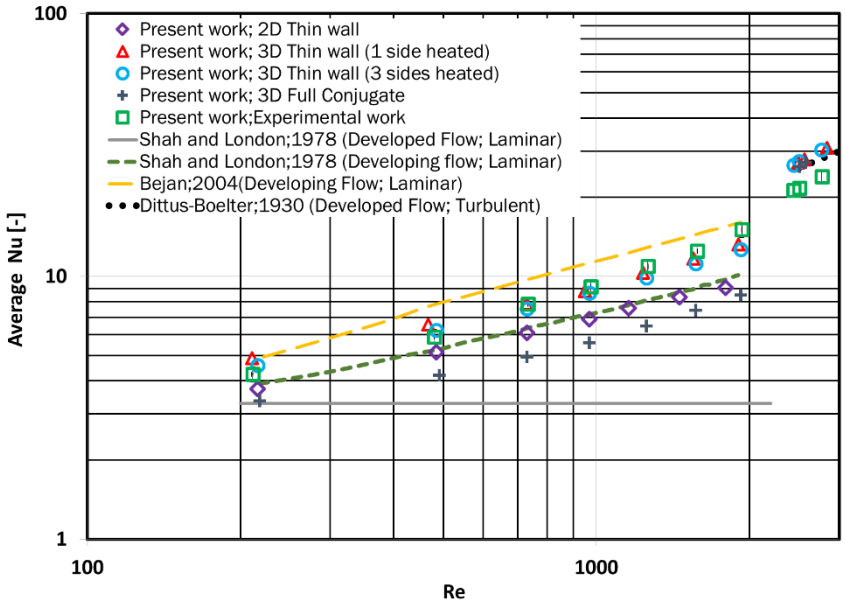

Figure 3-6 : Comparison of predicted average Nusselt number with experimental data and correlations.

On the contratry, the 3D full conjugated model Model 4 (simulating the experiment) demonstrated significant deviation, as shown in Figure 3-6. This deviation may be attributted to the conjugate effect, i.e. heat flux is not uniformly distributed along the channel. Iaccarinno *et al*. (2002) reported that the conjugate effects should be taken into consideration. To clarify this point, the local heat flux along the channel predicted using the 3D full conjugate model was plotted in Figure 3-7 for the bottom and side walls.

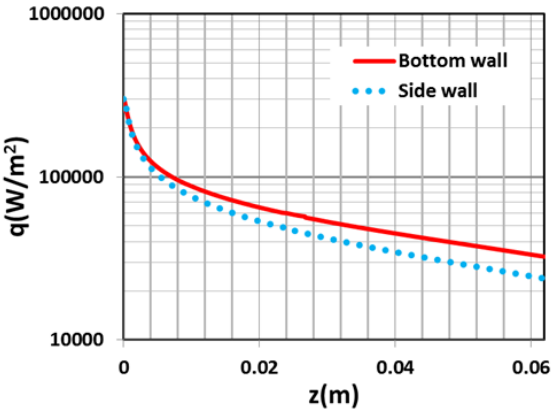

Figure 3-7 : Prediction local heat flux distribution for bottom and side wall along the channel length (**Model 4**).

The local heat flux is defined by $q'' = k_f \Delta T / \Delta y$. The figure demonstrates that the heat flux is very high near the entry region due to the thin thermal boundary layer, after which it decreases continously along the channel. Thus, the average Nusselt number is expected to be lower than in the thin-wall models in which the heat flux is assumed constant. The high heat flux in the entry region was also found by Qu and Mudawar (2002) and Tiselj *et al*. (2004). As illustrated in Figure 3-7, the heat flux varies in the cross-stream direction where the heat flux at the bottom wall was found to be higher compared to that at the side walls. This is due to the fact that the near-wall flow velocity in the middle of the bottom wall is larger than in the middle of the (smaller) side walls. A higher near-wall velocity results in an increased (wall-averaged) heat transfer rate.

Figure 3-8 depicts the fluid and channel bottom wall temperature along the channel length for the 3D thin-wall **Model 3** with three side walls heated (see Figure 3-8) and the 3D conjugate heat transfer calculations from Model 4 (see Figure 3-9) at Re=216. It is worth mentioning that in the thin wall approach a uniform heat flux (at the bottom

and side walls) boundary condition was assumed. In the fully conjugated heat transfer approach, the complete copper block including the embedded cartridge heater was simulated, which is exactly the same as in the experiment. As seen in Figure 3-8, and as expected from the theory for constant heat flux boundary condition, the fluid and wall temperature increase linearly in the fully developed region. This trend is expected to occur because the wall thickness was assumed to be zero, i.e. there is no conjugate effect. In contrast, Figure 3-9 demonstrates a very clear conjugate effect where the change in the wall and fluid temperatures is not linear, even though a constant heat flux boundary condition was assumed at the location of the cartridge heater. The high thermal conductivity of copper makes the heat transfer problem multi-dimensional and consequently the wall temperature approaches an isothermal condition. The wall temperature measured in experimental work, Mirmanto *et al*. (2012) at six axial locations is also included in Figure 3-9. The measured values were corrected using 1D heat conduction to consider the 1.5 mm distance between the thermocouple and channel base. As seen in the figure, the simulation predicts a similar trend as the experiment but with slightly higher values.

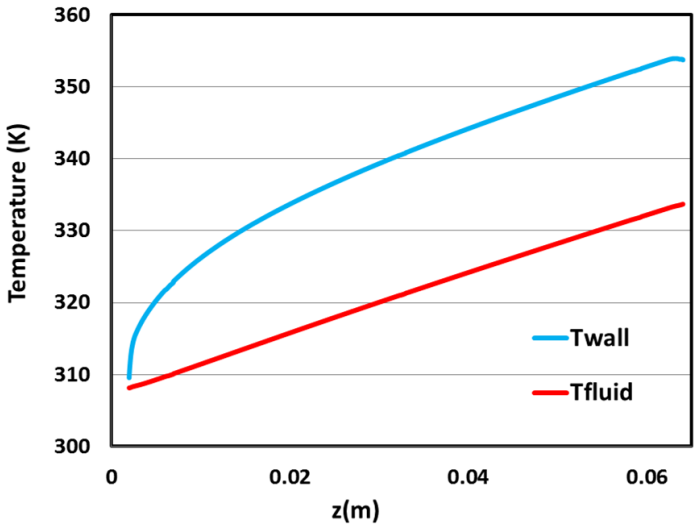

Figure 3-8 : Axial temperature variation of fluid and bottom wall along the channel at Re=216 (Thin wall analysis).

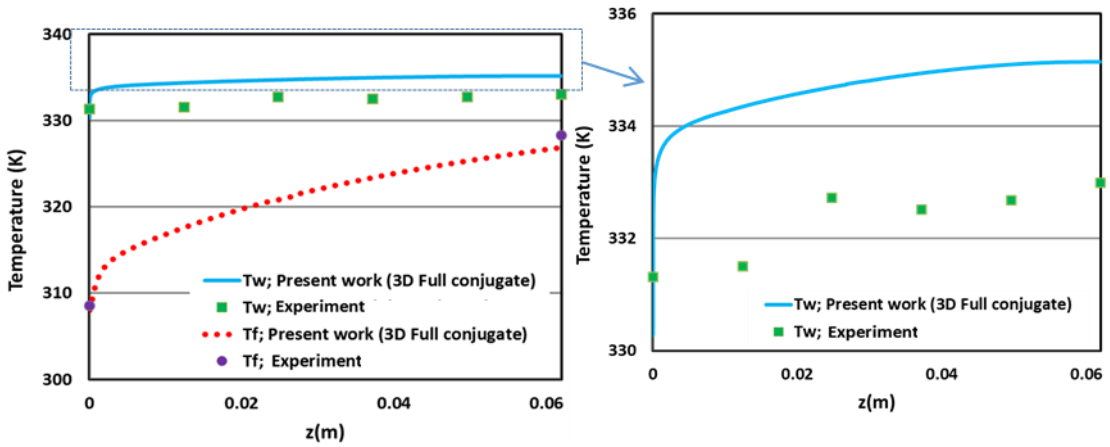

Figure 3-9 **:** Comparison of an axial temperature variation of fluid and bottom wall along the channel single channel system at Re=216 with existing experimental data by Mirmanto *et al*. (2012).

Figure 3-10 presents the local Nusselt number versus axial distance for the four models at Re = 216. It is clearly shown that *Nu* predicted by Model 1 (2D model) and **Model 2** and **Model 3** (3D thin-wall models) approaches fully developed constant values of 2.37 and 3.34, respectively. On the contrary, the *Nu* predicted by the 3D fully conjugated model (**Model 4**) decreases continously with axial distance. This confirms that the boundary condition at the channel walls is not a constant heat flux as previously discussed in Figure 3-7. Comparing the 2D and 3D thin wall simulation results in Figure 3-5 and Figure 3-6, it can be seen that the predicted friction factor and local Nusselt number in the 2D simulation are lower than in the 3D simulation. This is due to the presence of side-walls in the 3D simulation that give rise to cross-stream fluid motions resulting in higher values for both *f* and *Nu*.

The numerical results found in this study agree with the findings of Moharana *et al*. (2012) They conducted a numerical study on simultaneously developing flow under conjugate conditions in a square microchannel. By studying the effect of substrate thickness and thermal conductivity on heat transfer characteristics they found that the local heat flux becomes uniformly distributed along the channel after the entry region

when the substrate thickness becomes very small (thin wall approach in the present study) or when the substrate thermal conductivity becomes very low. In this case, they found that the wall and fluid temperatures increase linearly as also found in the current study, see Figure 3-8. When the substrate thickness and the thermal conductivity was high (fully conjugated model in the present study), the heat flux was found to decrease with axial distance, similar to what is depicted in Figure 3-10.

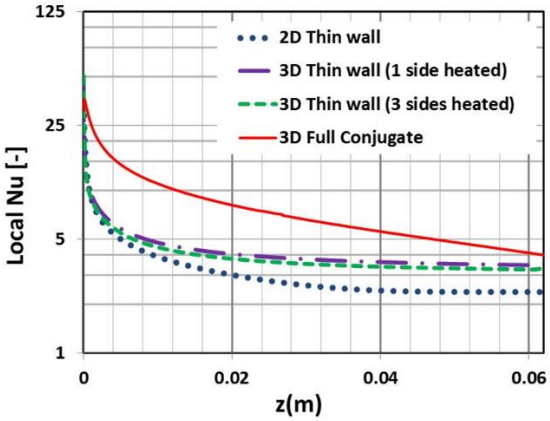

Figure 3-10 : Variation of local Nusselt number along the channel.

It is worth mentioning that Lee *et al*. (2005) did not find a significant difference between the thin-wall and full conjugate models in their numerical study. Thus they recommended using the thin-wall approach for simulating heat transfer in microchannels. This result seems to contradict the results of the present study and requires further scrutiny. The insignificant difference between the two models reported by Lee *et al*. (2005) could be due to the fact that the substrate thickness in their study was too small (1.5 mm). This could be valid for simulating thin test sections that incorporate integrated heaters. On the contrary, the design investigated in the present study uses a large copper block with embedded cartridge heaters which may result in significant conjugate effects. This explains the significant difference between the two models found in the current study. The design adopted in the present study is very common in literature, see for example Blasius (1913), but researchers ignored the conjugate effects. In conclusion, the thin-wall model could be used with certain

precautions, i.e for thin substrates. Additionally, the excellent agreement between the experimental data and the thin-wall model in the present study could be misleading for researchers because the uniform heat flux assumption does not hold true when there are significant conjugate effects.

3.3 Effect of aspect ratio and hydraulic diameter on fluid flow and heat transfer

This section presents and discusses effects of aspect ratio and hydraulic diameter on single phase flow and heat transfer in a single rectangular microchannel.

3.3.1 Model descriptions

In order to understand the effect of hydraulic diameter and aspect ratio, the influence of other parameters such as conjugate effects should be eliminated. Accordingly, the 3D thin-wall model that ignores the conjugate effects was used in this study. A constant heat flux boundary condition was applied at the bottom wall and both vertical side walls of the channel, while the upper channel wall was considered adiabatic (**Model 3**). This simulates the boundary conditions encountered in several flow boiling studies when there is a glass window on the upper side for flow visualization. The same heat flux was applied at the three heated walls for all tested channels in the present study. At the inlet plenum, a uniform velocity was prescribed, and a zero static pressure was employed at the outlet plenum. Since laminar flow is the dominant flow regime in microchannels, the simulation was conducted for a range of Reynolds numbers between 100 and 2000 and water was used as the working fluid. The same properties of water as in previous section (Section 3.2) were also used in the present study. In the first set of simulations, the hydraulic diameter was varied from 0.1 to 1 mm while the aspect ratio was kept constant at 1. In the second set of runs, the

aspect ratio was varied from 0.39 to 10 while the hydraulic diameter was kept constant at 0.56 mm, see Table 3-2.

Table 3-2 : Channel dimensions used for the numerical simulations in the present study, $\boldsymbol{L_{ch} = 62}$ mm.

Run	W_{ch} (mm)	H_{ch} (mm)	D_h (mm)	AR (H_{ch}/W_{ch})
1	1	0.39	0.56	0.39
2	0.56	0.56	0.56	1
3	0.46	0.7	0.56	1.52
4	0.42	0.84	0.56	2
5	0.35	1.4	0.56	4
6	0.32	2.4	0.56	7.50
7	0.31	3.1	0.56	10
8	0.1	0.1	0.10	1
9	0.3	0.3	0.3	1
10	0.5	0.5	0.50	1
11	0.7	0.7	0.7	1
12	0.9	0.9	0.9	1
13	1	1	1	1

3.3.2 Effect of Aspect Ratio

3.3.2.1 Hydrodynamic entry length

The effect of aspect ratio on the dimensionless hydrodynamic entry length (L_e/D_h) is investigated for an aspect ratio range of 0.39 – 10 and D_h = 0.56 mm. The entry length (L_e) can be defined as the length from the channel inlet to the location at which the velocity attains 99% of its fully developed value Shah and London (1978). Figure 3-11 (a) depicts an example on how the entry length was obtained in the present study for *Re* = 235, 591, 873 and D_h = 0.1 mm while Figure 3-11(b) shows how the velocity profile develops along the channel until it reaches the fully developed shape for *AR* = 0.39 and *Re* = 181.

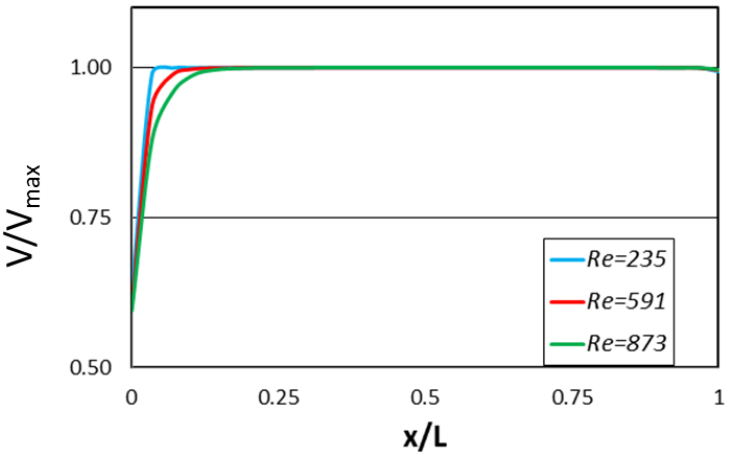

(a)

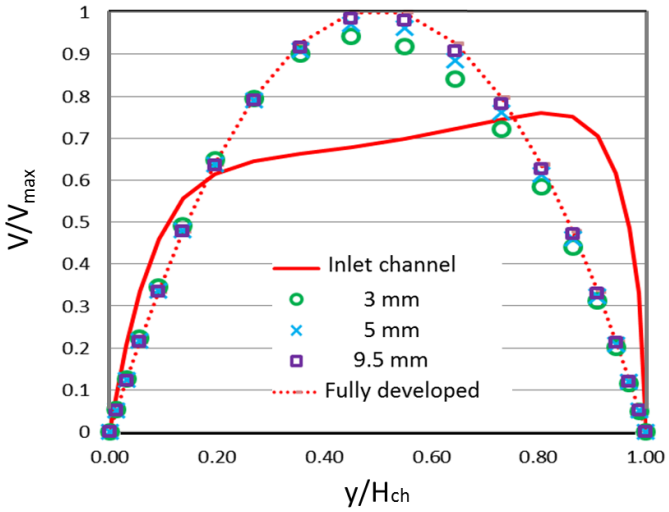

(b)

Figure 3-11: Hydrodynamic entry length identification, (a) maximum velocity attains 99 % of the fully developed value for D_h = 0.1 mm, (b) development of the velocity profile for Re = 181, D_h = 0.56 mm and AR = 0.39.

The thermal entry length is not included in this study because the channel is not long enough and the flow is hydrodynamically developed, but thermally developing for all examined conditions. Figure 3-12 illustrates the flow development along the channel for the highest (AR =10) and the lowest (AR=0.39) aspect ratios used in this study. It can be seen that the flow becomes hydrodynamically fully developed between x = 10 mm and x = 30 mm, but thermally the flow did not reach a fully developed state at any x location.

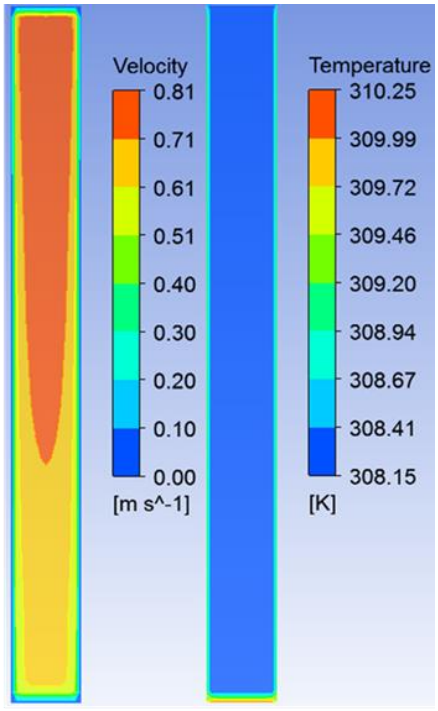

x= 0 mm (inlet)

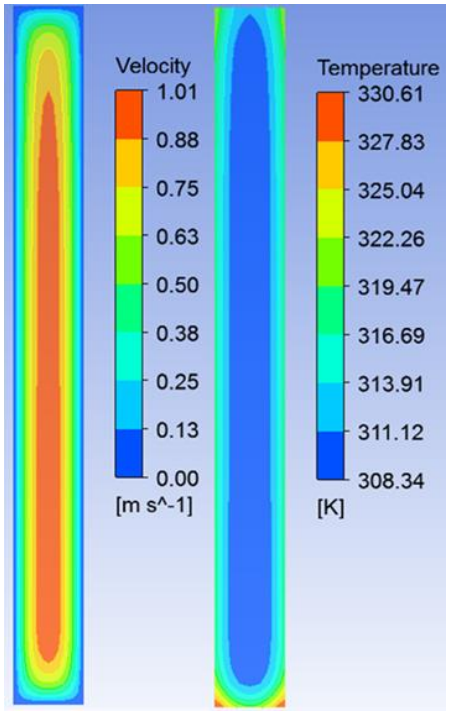

x= 10 mm

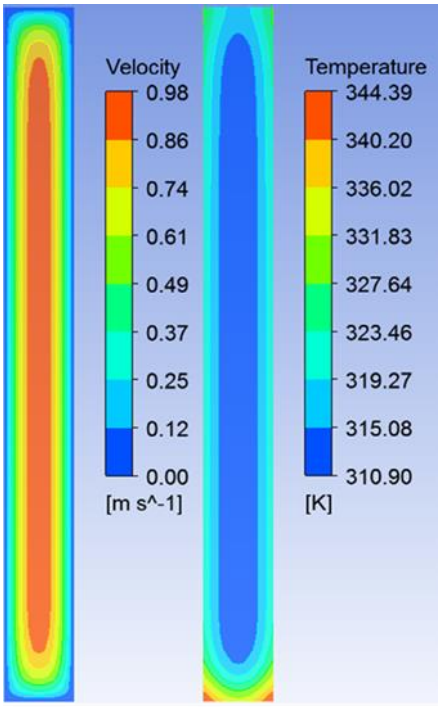

x= 30 mm

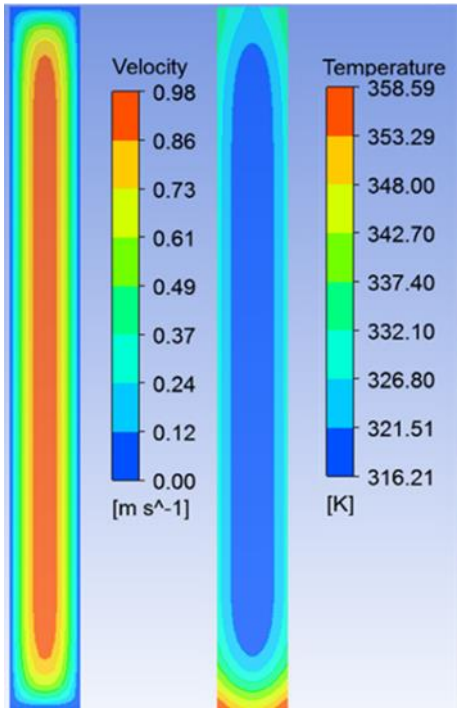

x= 62 mm (outlet)

(a)

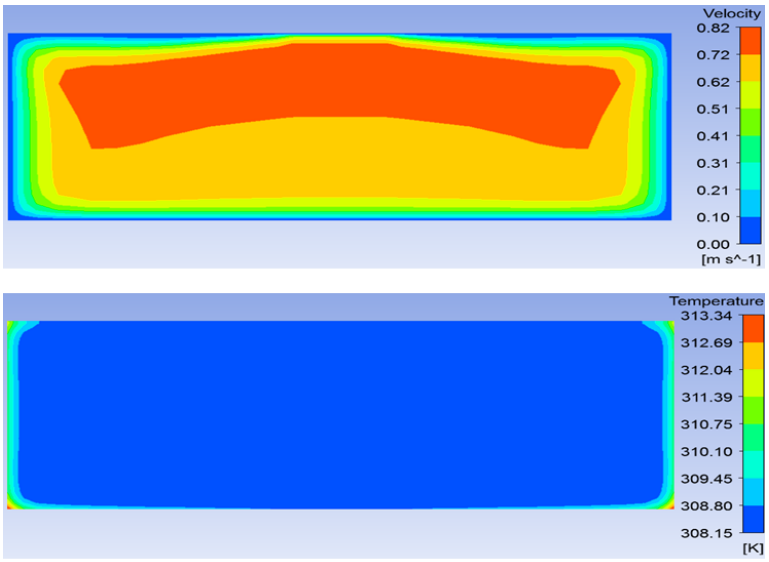

x= 0 mm (inlet)

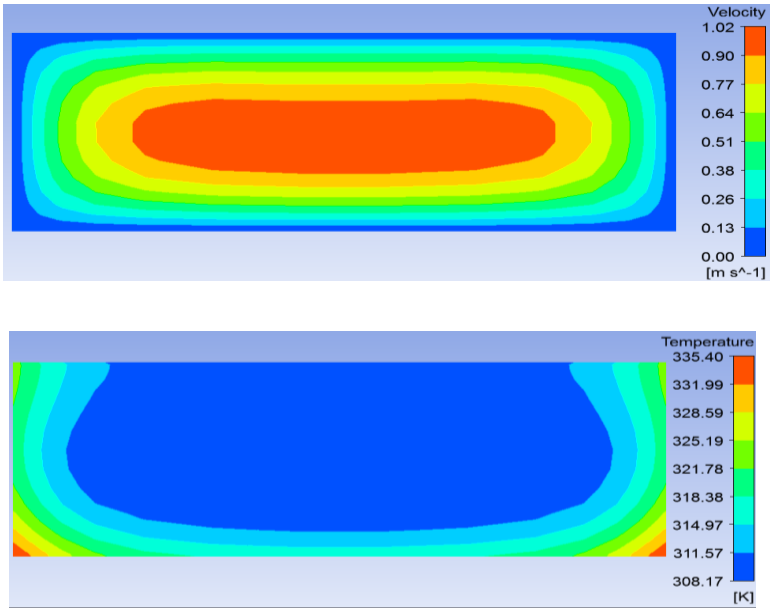

x=10 mm

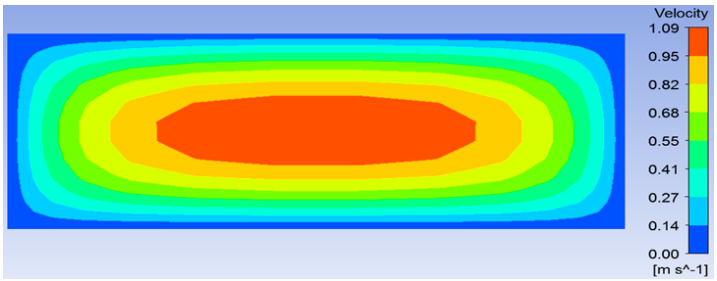

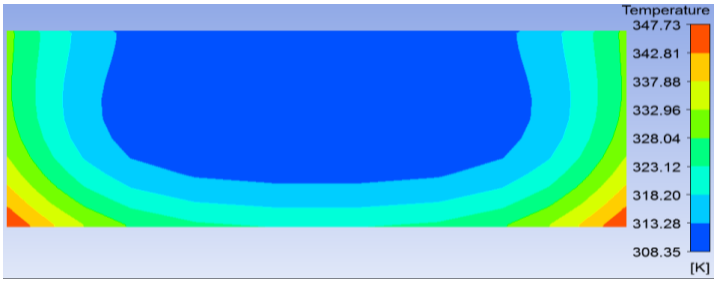

x=30mm

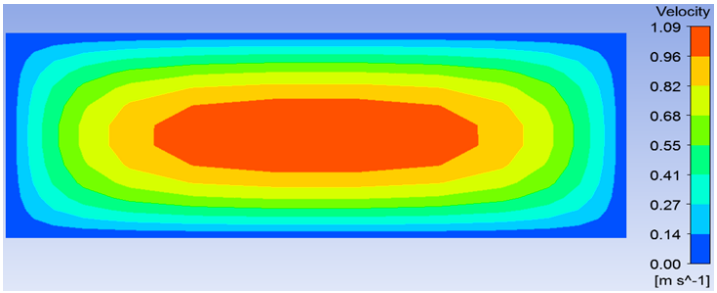

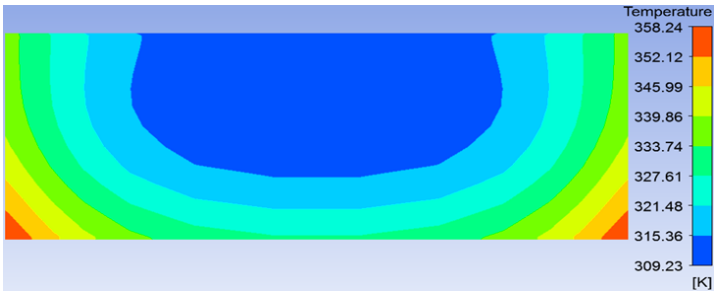

X=62 mm (outlet)

(b)

Figure 3-12 : Velocity and temperature contour at (a) AR=10 and (b) AR=0.39 along the channel.

The numerical approximation of the dimensionless hydrodynamic entry length was compared with correlations proposed by Ahmad and Hassan (2010) and Galvis *et al*. (2012). It is worth mentioning that Galvis *et al*. (2012) proposed four different correlations and each correlation is valid for a certain aspect ratio and Re < 50. They reported that for Re > 50 the effect of aspect ratio on the dimensionless entry length is insignificant and any of the four proposed correlations can be used. Figure 3-13 shows the effect of aspect ratio on the dimensionless hydrodynamic entry length (L_e/D_h) compared to the predictions given by Ahmad and Hassan (2010) and Galvis *et al*. (2012). As seen in the Figure 3-13, the aspect ratio does not have a significant effect on the dimensionless hydrodynamic entry length and the numerical results are in reasonable agreement with Ahmad and Hassan (2010) (the mean absolute error ranged from 1.527 to 24.059 %) and Galvis *et al*. (2012) (the mean absolute error ranged from 1.008 to 23.659 %). Although the two correlations give a similar range for the mean absolute error, the average value of the mean absolute error from the correlation of Galvis *et al*. (2012) is smaller than that from the correlation of Ahmad and Hassan (2010) (7.63 % versus 13.6 %). These small deviations could be due to differences in entry conditions. It is worth mentioning that in the numerical study of Galvis *et al*. (2012) the velocity was assumed to be uniform at the channel inlet while in the present study the velocity was assumed uniform at the inlet of the plenum. In the experimental study of Ahmad and Hassan (2010) the test section consisted of a planar large reservoir (plenum) which was 100 times greater and deeper than the microchannel hydraulic diameter only at the upstream side.

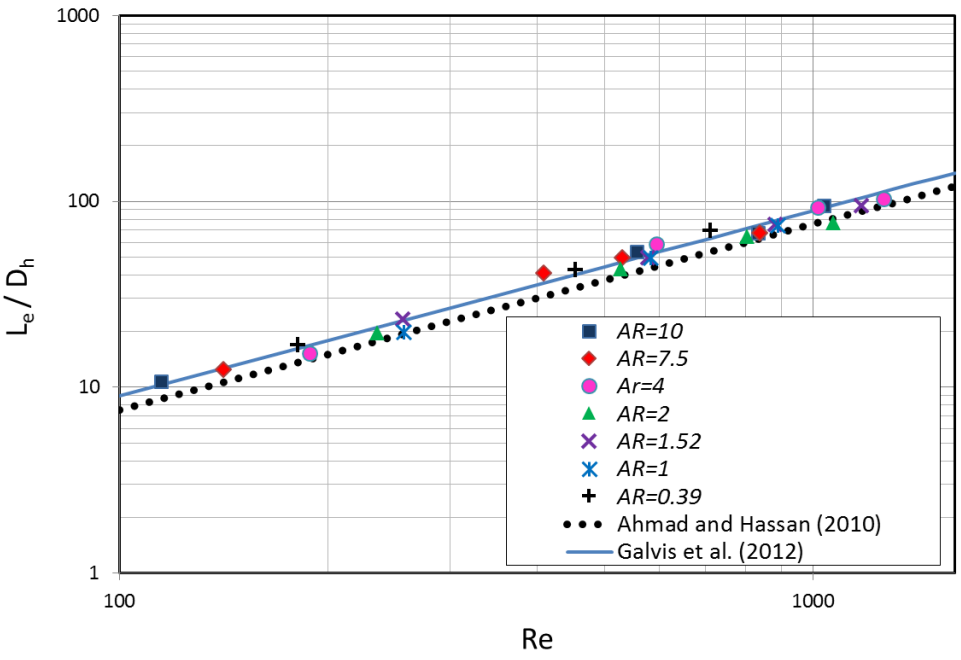

Figure 3-13 : Comparison of numerical dimensionless entrance length and existing correlations Ahmad and Hassan (2010) and Galvis *et al*. (2012) at different channel aspect ratios ($0.39 < AR < 10$) with D_h = 0.56 mm.

On the contrary, in the present study, symmetrical cylindrical inlet and outlet plenums were allocated at the upstream and downstream of the microchannels for all tested channels as shown in Figure 3-2 (see Section 3.2.1). Also, the channels in the present study were simulated with a sharp edge corner at the inlet of the microchannel. This produced a flow separation or vena contracta effect in the inlet region of the microchannel, as shown in Figure 3-14. The vena contracta effect was observed only at the corner formed by the top wall and the plenum wall. On the contrary, a non-symmetric vena contracta was observed at the top and bottom wall of the channel in the study of Ahmad and Hassan (2010) due to the presence of a deeper inlet plenum.

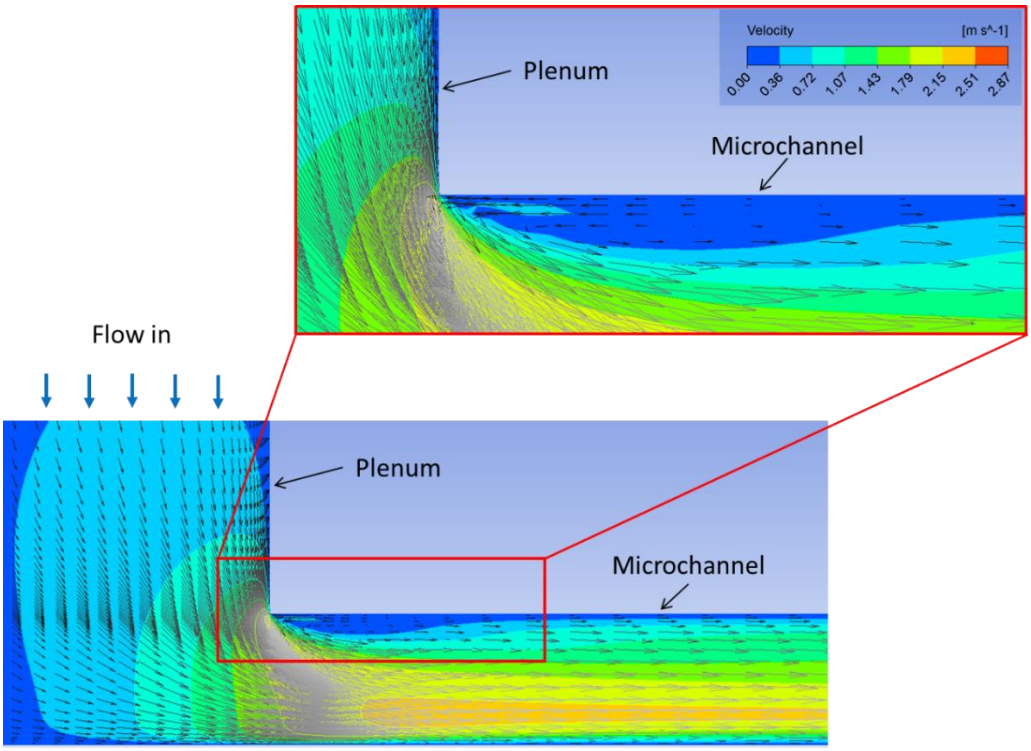

Figure 3-14 : Vena contracta effects produced by sharp edge corner at the microchannel inlet.

Figure 3-15 shows velocity streamlines at the channel inlet and it can be seen that vortices exists near the side walls. This phenomenon was due to the flow separation at the channel inlet when the flow enters the microchannel from the plenum as stated in Qu *et al*. (2006). Therefore, the inlet velocity profile needs to be carefully considered in order to estimate the entrance length. As reported by Baviere *et al*. (2006), the inlet velocity profile is dependent on the geometry of the transition section between the plenum and the channel.

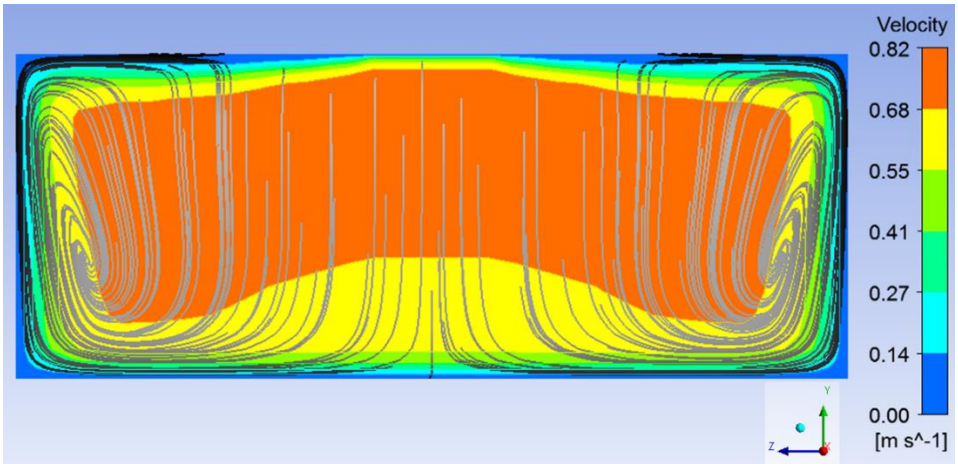

Figure 3-15 : Velocity contour and streamline at inlet channel.

3.3.2.2 Friction factor

Figure 3-16 illustrates the effect of aspect ratio on the friction factor for a fixed hydraulic diameter value of 0.56 mm. The numerical results are compared with the correlations proposed by Shah and London (1978) for fully developed and developing flow. Figure 3-16 (a) demonstrates that for aspect ratio values from 0.39 to 2, there is no significant effect on the friction factor and the trend and magnitudes are very close to the prediction from the correlation of Shah and London (1978) for developing flow. For aspect ratios greater than 2, the magnitude of the friction factor and the slope of the line are larger than those predicted using the Shah and London (1978) correlation, particularly in the low Re number region (Re < 400). Figure 3-16 (b) shows the friction factor plotted versus aspect ratio for *Re* = 500 and 1500. It can be seen in the figure that the magnitude of the friction factor remains almost constant with increasing aspect ratio up to *AR = 2*, after which the values start to increase slightly with aspect ratio for *Re = 500* and, finally, increase significantly with aspect ratio for $Re = 1500$. The friction factor increased by 10.7 % for $Re = 500$ and increased by 36.24 % for $Re = 1500$ when the aspect ratio was increased from 2 to 10. In other words, for design purposes, the aspect ratio should be less than 2 in order to achieve a low pressure drop and, consequently, pumping power.

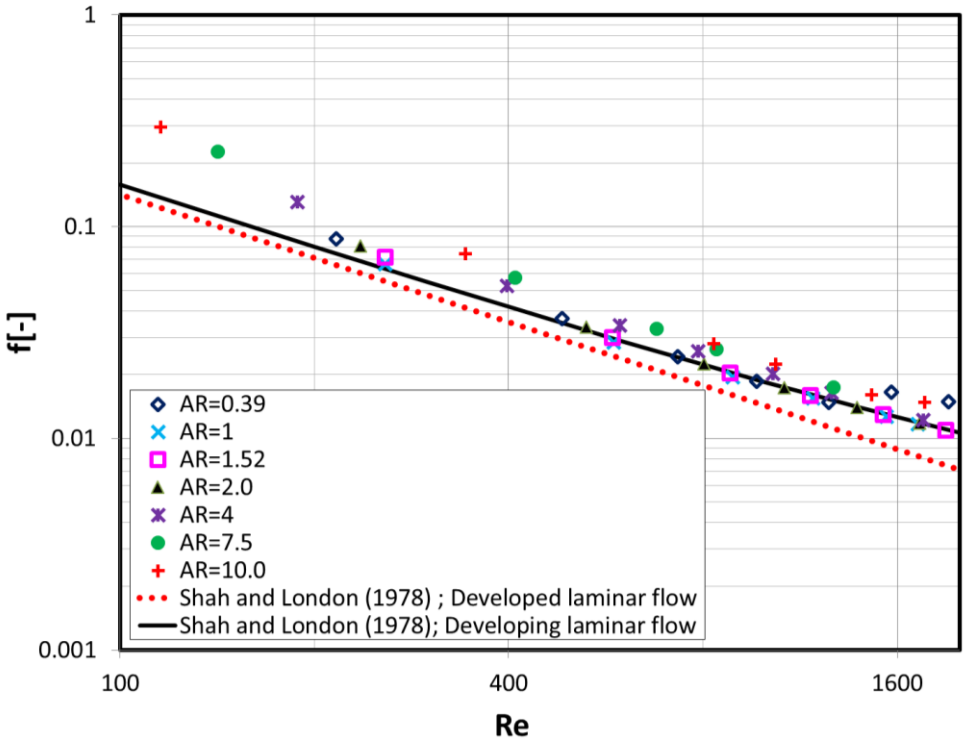

(a)

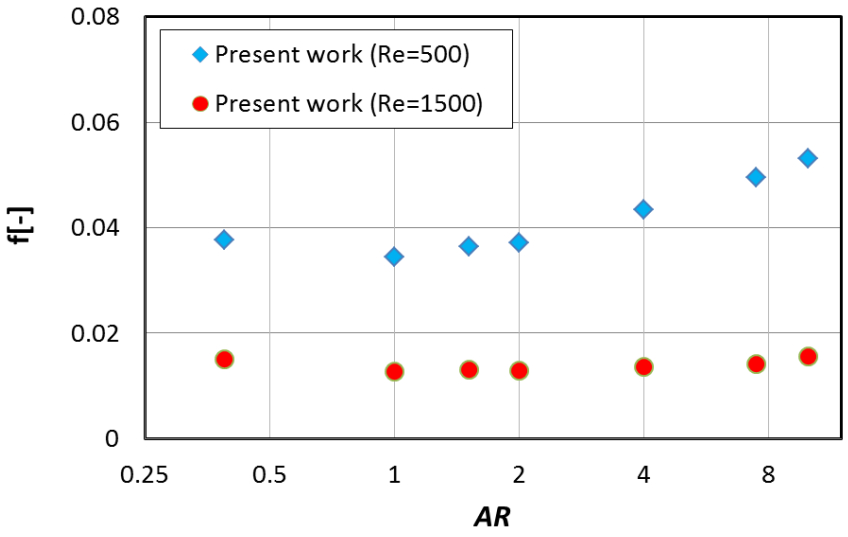

(b)

Figure 3-16: (a) Comparison between predicted friction factor and existing correlations (b) Variation of friction factor with varying channel aspect ratio.

The effect of aspect ratio on the friction factor can be explained by plotting the fully developed velocity profile along the channel height and width as seen in Figure 3-17 for the lowest aspect ratio (*AR* = 0.39), for aspect ratio = 2 and for the highest aspect ratio (*AR* = 10). Figure 3-17 indicates that there is a small change in the slope of the velocity profile at the channel wall along the channel width when comparing AR = 0.39 to the other two aspect ratios. For AR = 2 and AR = 10 the slopes, and hence the wall shear stresses are nearly identical. On the contrary, the velocity profile along the channel height only indicates a similarity between the slopes of the velocity profiles for *AR* = 0.39 and 2, indicating a similar wall shear stress and thus a similar friction factor for these two aspect ratios. Increasing the aspect ratio beyond 2 resulted in significant changes in the velocity profile as seen for *AR* = 10. The velocity profile became flatter with steep velocity gradient (large slope) near the channel wall, i.e. higher wall shear stress and thus higher friction factor. This may explain why the friction factor increases with aspect ratio for *AR* > 2 in the present study.

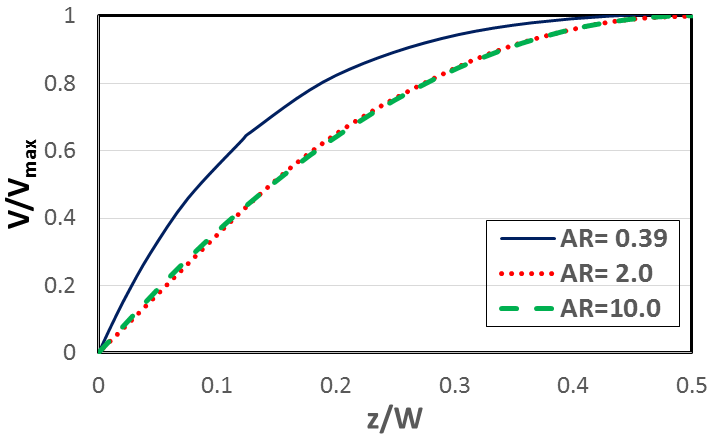

(a)

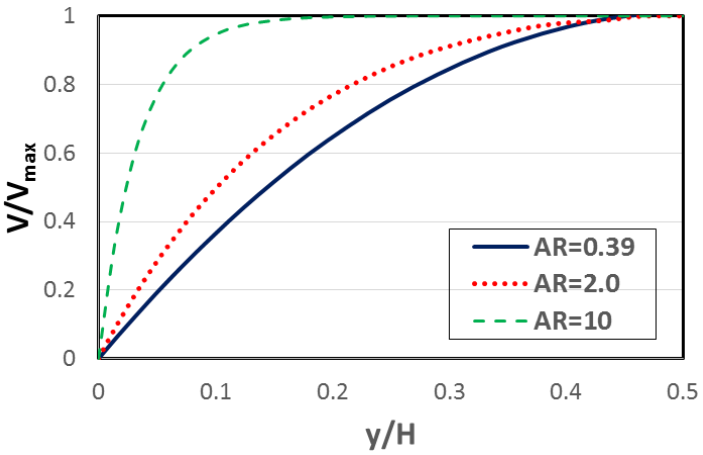

(b)

Figure 3-17 : Fully developed velocity profile against (a) channel width and (b) channel height for AR=0.39, 2 and 10 at Re ≈ 500.

Gunnasegaran *et al.* (2010) investigated numerically the effect of geometrical parameters on water flow in multi-microchannel configurations. It was reported that the Poiseuille number, fRe, increases when the ratio W_{ch}/H_{ch} increases (when the aspect ratio decreases). This contradicts the results of the present study, where there is no clear effect of aspect ratio up to AR = 2. They attributed the increase of the Poiseuille number with decreasing aspect ratio to the decrease in flow area and the vortex effects, which become more significant with decreasing aspect ratio. However, inspecting the values of channel depth and width in their study, one can see that increasing the ratio W_{ch}/H_{ch} results in an increase in the flow area, which contradicts their explanation.

Figure 3-18 depicts the effect of Reynolds number and aspect ratio on the Poiseuille number. The figure demonstrates that the Poiseuille number decreases moderately with *Re* in the very low Reynolds number region then it remains almost unchanged before it increases slightly with *Re* in the high *Re* number region. At low *Re* number, the developing length is very small and the flow is found to be fully developed over a significant part of the channel length while at high *Re* number the friction factor increases due to the fact that the flow is developing over a significant part of the

channel length. Additionally, it is obvious that the Poiseuille number increases with increasing aspect ratio for $AR > 2$. Where, as mentioned before, this may because, for cases $AR > 2$, as the aspect ratio increase, velocity profile was observed became flatter near the channel wall. This induced a with high velocity gradient which lead to higher wall shear stress and thus giving a higher friction factor.

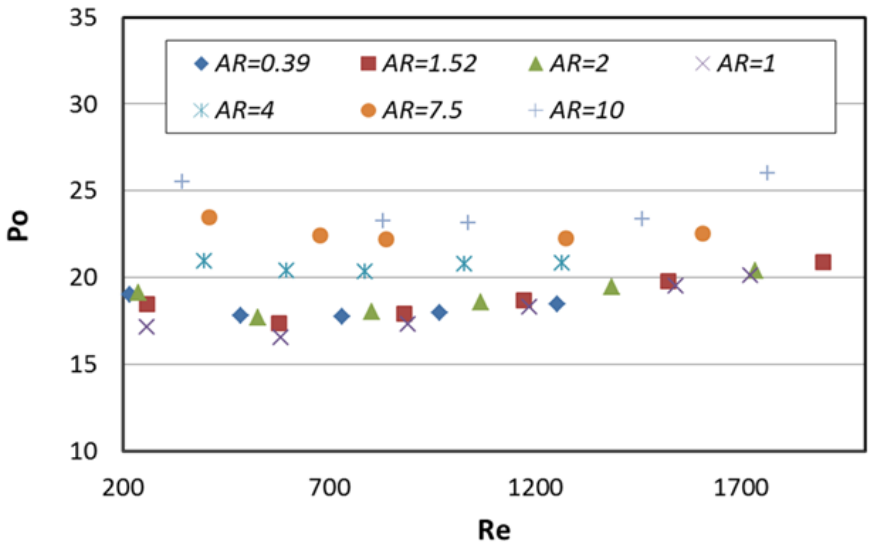

Figure 3-18 : Effect of Reynolds number and aspect ratio on Poiseuille number.

Xing *et al.* (2013) conducted a theoretical study to investigate the effect of aspect ratio on a fully developed laminar flow in rectangular ducts. Their results showed that the Poiseuille number increases as the aspect ratio decreases, which seems to contradict the results of the present study. It is worth mentioning that the definition of the aspect ratio in their study was such that it was always less than 1 (the ratio of the shortest to the widest side). They gave a simplified equation for the prediction of the friction factor, which is valid for aspect ratios less than 0.2, as defined in Eq. (4.9) below. For the sake of comparison with this equation, the aspect ratio was defined similarly as in Xing *et al.* (2013) and the results of the comparison are shown in Figure 3-19. It is clearly shown that there is a good agreement between the results of the

present study and the results of Xing *et al*. (2013), i.e. the friction factor increases as the aspect ratio (shortest side/widest side) decreases.

$$Po = \frac{24}{(1+AR)^2(1-0.6274AR)} \tag{4.9}$$

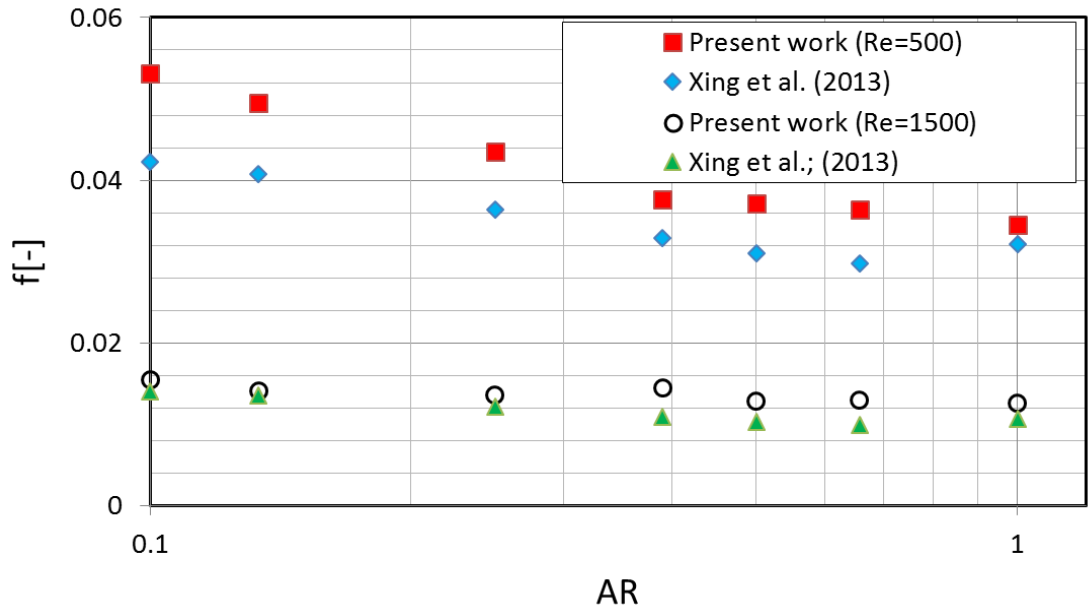

Figure 3-19 : The friction factor versus aspect ratio compared to the results of Xing *et al*. (2013).

This initial decrease of Poiseuille number with aspect ratio observed in Figure 3-18 was also reported by Kashaninejad *et al*. (2012). They investigated both analytically and numerically the effects of aspect ratio on friction factor and velocity profile in rectangular microchannels. They reported that the *Po* number decreases sharply from 24 at an aspect ratio near zero to 14.25 at an aspect ratio of 1 as the aspect ratio increases for $AR < 1$. In their study, the aspect ratio was defined as the width to height ratio. For aspect ratios greater than 1, the Po increased with increasing aspect ratio until it reached again 24 (the value for parallel plates). Finally, they concluded that

$AR \approx 1$, which is a square cross-section channel, generates the lowest friction factor and as the channel cross section deviates from the square shape, the frictional pressure losses increase.

3.3.2.3 Heat transfer

Figure 3-20 shows the average *Nu* plotted versus *Re* for different aspect ratios and constant hydraulic diameter. Also included in the figure are the comparisons with Bejan (2004) (Eq. 4.10) and Shah and London (1978) correlations for hydrodynamically developed (Eq. 4.11-a) and thermally developing flow. (Eq. 4.11-b)

$$Nu = 1.375\ (\frac{L}{RePrDh})^{-0.5} \tag{4.10}$$

$$Nu = 1.953\ (RePrDh/L)^{1/3}\ ;\left(\frac{RePrDh}{L}\right) \geq 33.3 \tag{4.11-a}$$

$$Nu = 4.364 + 0.0722\ (RePrDh/L)\ ;\left(\frac{RePrDh}{L}\right) < 33.3 \tag{4.11-b}$$

It is obvious that the average Nusselt number increases with *Re*, which indicates that the flow is thermally developing, bearing in mind that the flow is laminar. Also, the aspect ratio effect on *Nu* is insignificant. Additionally, the results agree reasonably well with the correlation of Shah and London with values that are slightly higher. The correlation of Bejan (2004) however, over predicts the data significantly.

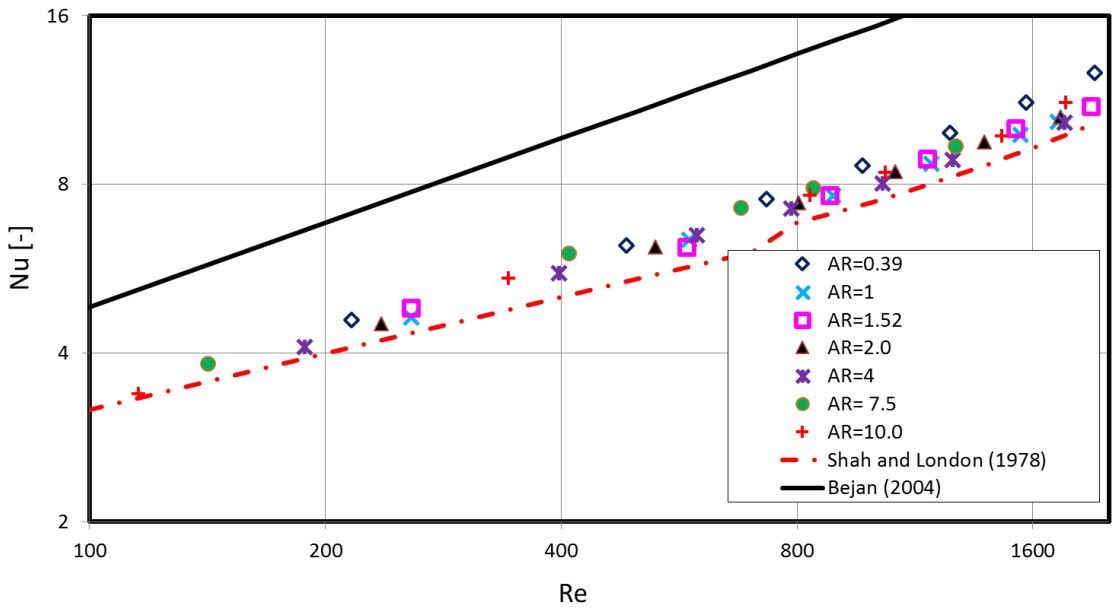

Figure 3-20 : Comparison between predicted Nusselt number and existing correlations, Shah and London (1978) and Bejan (2004).

In order to clarify the effects of aspect ratio, the data of Figure 3-20 were plotted in Figure 3-21 as average *Nu* versus aspect ratio for *Re* = 500 and 1500. The channels were classified into shallow channels ($AR < 1$), square channels ($AR = 1$) and deep channels ($AR > 1$). The figure shows that the effect of aspect ratio on the average Nusselt number is insignificant. It is worth mentioning that a constant heat flux was applied at the bottom and side walls of all tested channels and the hydraulic diameter was kept constant. Thus, the insignificant effect of aspect ratio on heat transfer rates in this study could be attributed to the behaviour of the wall and fluid temperature.

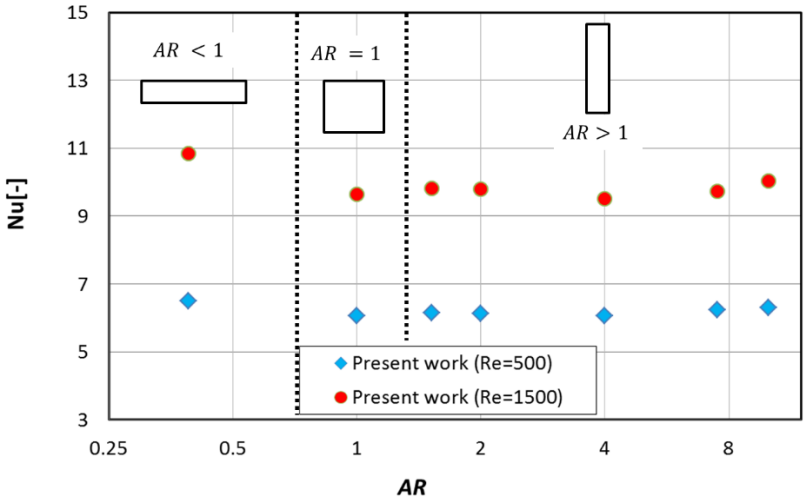

Figure 3-21 : Variation of Nusselt with varying channel aspect ratio.

Figure 3-22(a) and Figure 3-22(b) depict the fluid and wall temperature distribution along the channel for *Re* = 500 and *Re* =1500, respectively and for the lowest and highest aspect ratio. It is clearly shown that the temperature difference between the wall and fluid is almost the same for the two channels. Therefore, the *Nu* values at a given *Re* number showed insignificant deviation for all cases. The results obtained in this study agree with Harms *et al*. (1999) who reported that the effect of aspect ratio on heat transfer rates is insignificant.

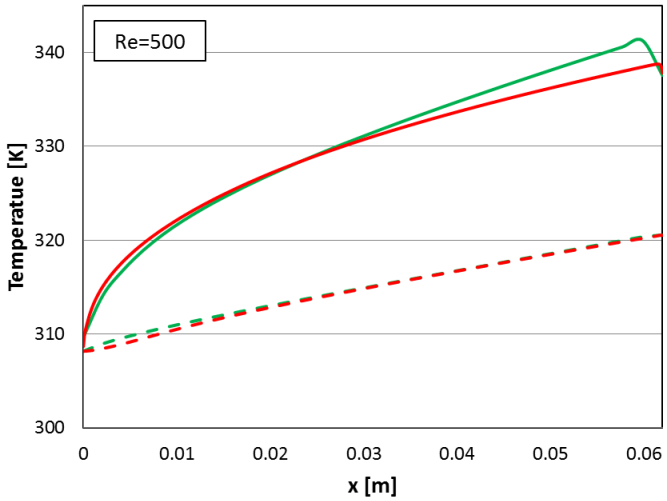

(a)

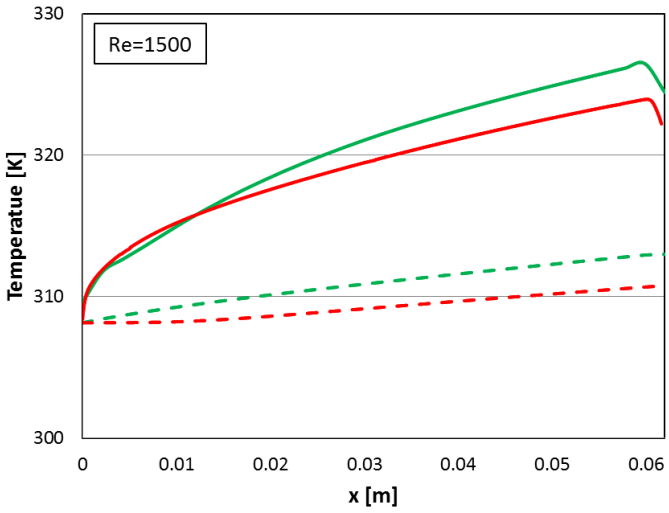

(b)

Figure 3-22 : Comparison of wall temperature (solid line) and fluid temperature (dotted line) for tested aspect ratio at (a) Re≈500 (b) Re≈1500 ; [red] *AR*=0.39;[green] *AR*=10.

3.3.3 Effect of Hydraulic Diameter

In this section, the effect of hydraulic diameter was studied by varying D_h between 0.1 and 1 mm while the aspect ratio was kept constant at $AR = 1$. The dimensionless entrance length for all tested microchannels was compared with existing correlations by Ahmad and Hassan (2010) and Galvis *et al*. (2012) and was depicted in Figure 3-23. Similar conclusions can be drawn as in section 3.3.2.1, as the dimensionless entrance length was observed to become independent of hydraulic diameter and the results were found to agree well with Ahmad and Hassan (2010).

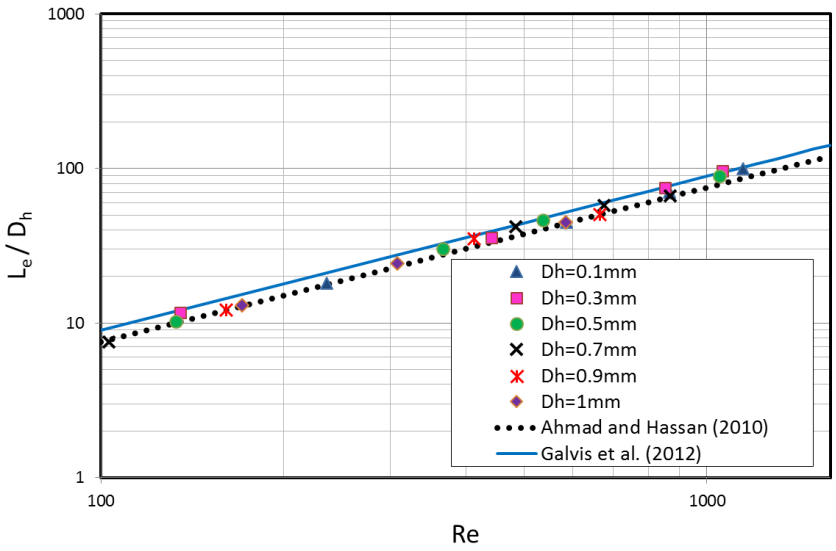

Figure 3-23 : Comparison of obtained dimensionless entrance length at different channel hydraulic diameter (0.1< D_h (mm) <1) with existing correlations.

In Figure 3-24, the friction factor data are plotted against *Re* and compared with existing correlations Shah and London (1978). The figure shows that the friction factor is in a reasonable agreement with Shah and London (1978) and no clear effect of the hydraulic diameter on the friction factor could be identified. The friction factor at *Re* = 500 and *Re* = 1500 is plotted against the hydraulic diameter in Figure 3-25 in order to clarify the effect of hydraulic diameter.

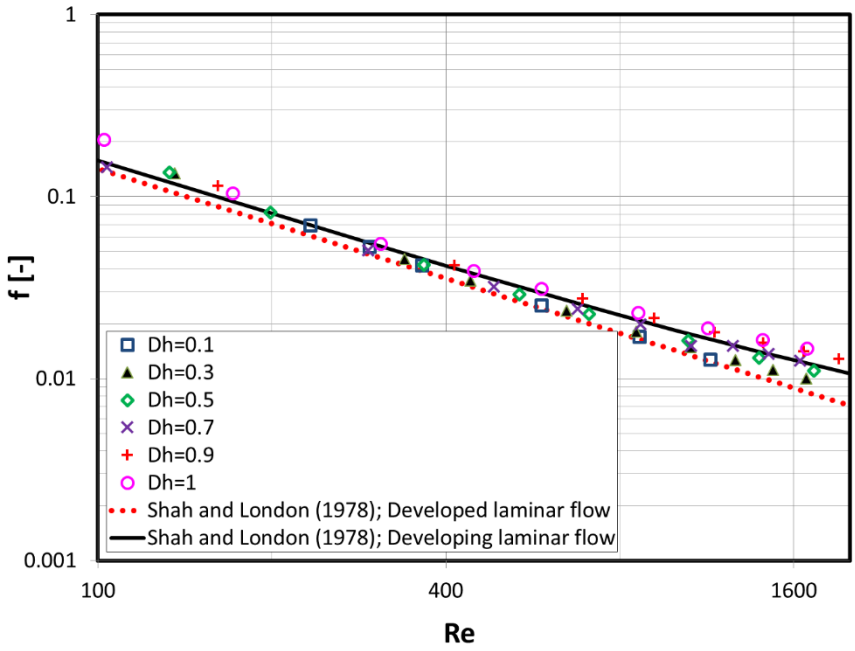

Figure 3-24 : Comparison between predicted friction factor and existing correlations

Figure 3-25 shows that the friction factor increases with increasing hydraulic diameter, which agrees with the results of Peng *et al*. (1995) and Xu *et al*. (2000), but contradicts the findings of some researchers, Guo and Li (2003); Rosa *et al*.(2009); Beavers *et al*. (1970) who reported an insignificant effect of hydraulic diameter on the friction factor. The friction factor in the present study increased by 22.94 % for Re = 500 and increased by 32.53 % for Re = 1500 when the hydraulic diameter increased from 0.1 mm to 1 mm. Silverio and Moreira (2008) studied the pressure drop and heat transfer in fully developed flow in channels with square and circular cross section with hydraulic diameters ranging from 0.05 mm to 0.5 mm. Three different working fluids were used: distilled water, methoxy- nonafluorobutane and methanol. They stated that the microscale effect is negligible in channels with a hydraulic diameter larger than 0.2 mm and for smaller channels the results were found to deviate from the classical theory at Re < 100.

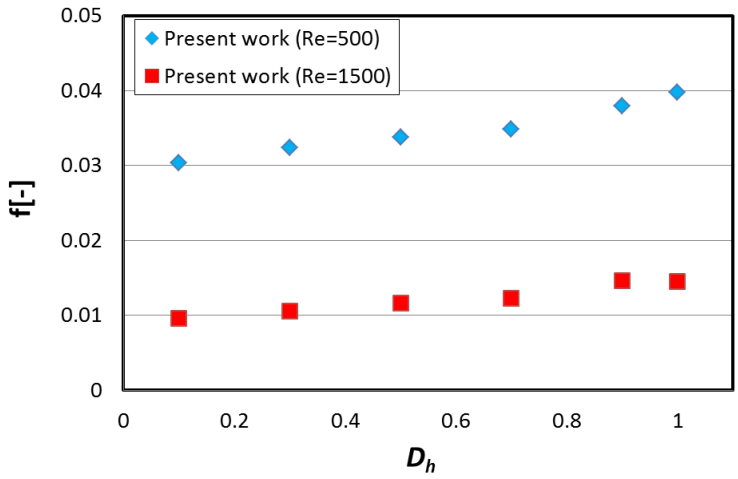

Figure 3-25 : Variation of friction factor with varying channel hydraulic diameter, D_h.

In order to explain the effect of hydraulic diameter in the present study, the fully developed velocity profile along the channel width and height were plotted for D_h = 0.1, 0.5 and 1 mm for both *Re* = 500 (Figure 3-27), and *Re*=1500 (Figure 3-27). The figures demonstrate that the velocity profiles plotted along the channel width and height are very similar with insignificant changes as the hydraulic diameter increases. The similarity of the velocity profile along the channel width and height arises from the fact that all examined channels have a square cross sectional area (*AR = 1*). This similarity in the velocity profiles leads to the conclusion that the local wall shear stress and thus the local friction factor values are similar in the fully developed region irrespective of the value of the hydraulic diameter. Accordingly, the increase of friction factor with hydraulic diameter found in the present study cannot be explained using the velocity profile and shear stress. Hence, the most likely reason is the increase of the hydrodynamic entry length (the dimensional value) with increasing the hydraulic diameter and Reynolds number. As the length of the entry region increases, the average pressure drop, and thus the average friction factor, increases.

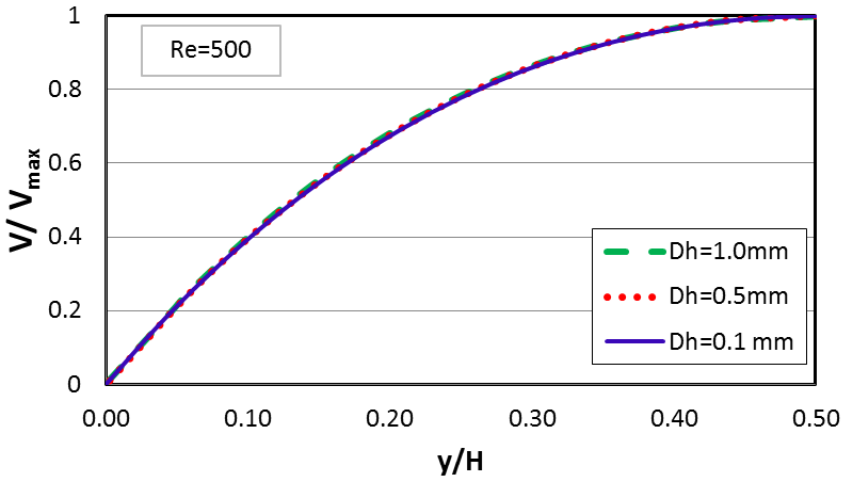

(a)

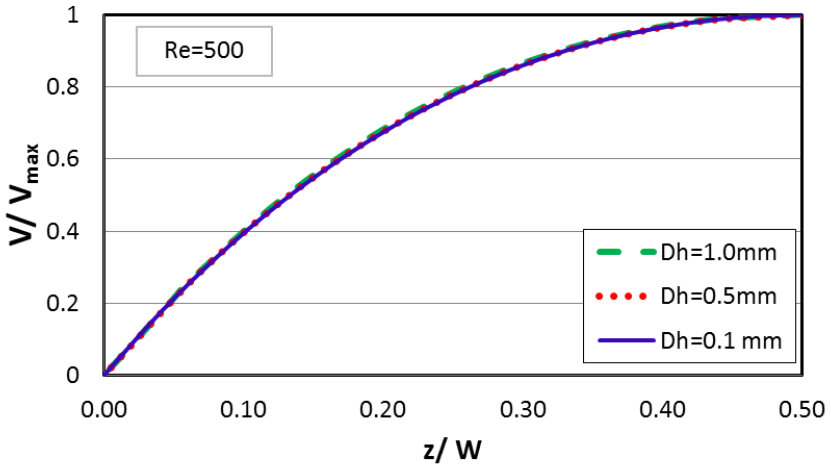

(b)

Figure 3-26 : Fully developed velocity profile against channel (a) height and (b) width for Dh =0.1 mm, 0.5 mm and 1 mm at Re ≈ 500.

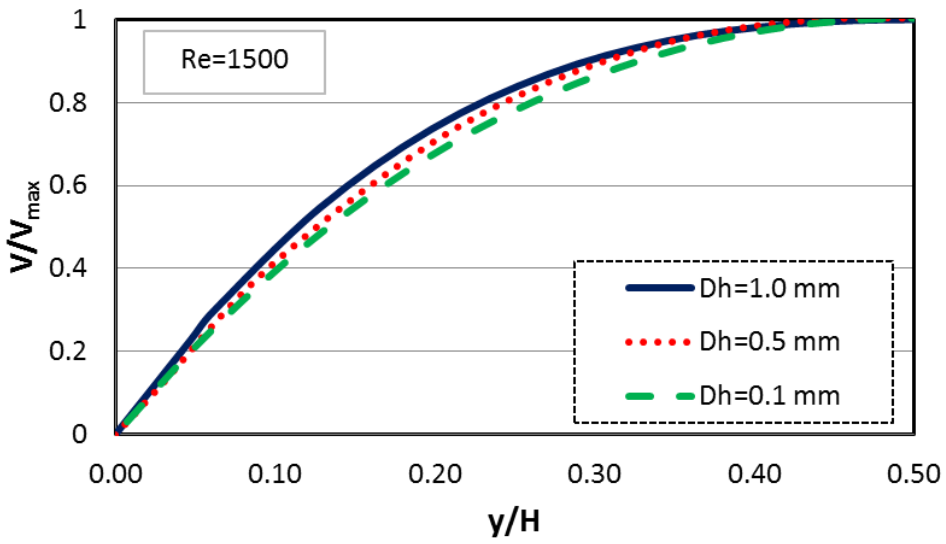

(a)

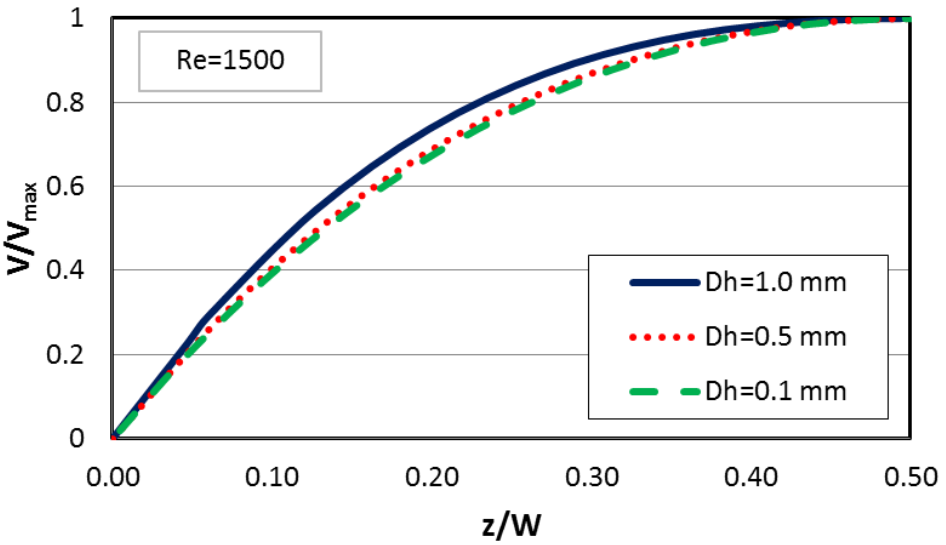

(b)

Figure 3-27： Fully developed velocity profile against channel (a) height and (b) width for D_h =0.1 mm , 0.5 mm and 1 mm at Re ≈ 1500.

The effect of hydraulic diameter on Nusselt number was illustrated in Figure 3-28. As seen in the figure, the Nusselt number increases with *Re* as expected and the numerical values agree reasonably well with the predicted values using the correlation of Bejan (2004) for the whole diameter range except D_h = 0.1 mm, where a significant deviation was observed.

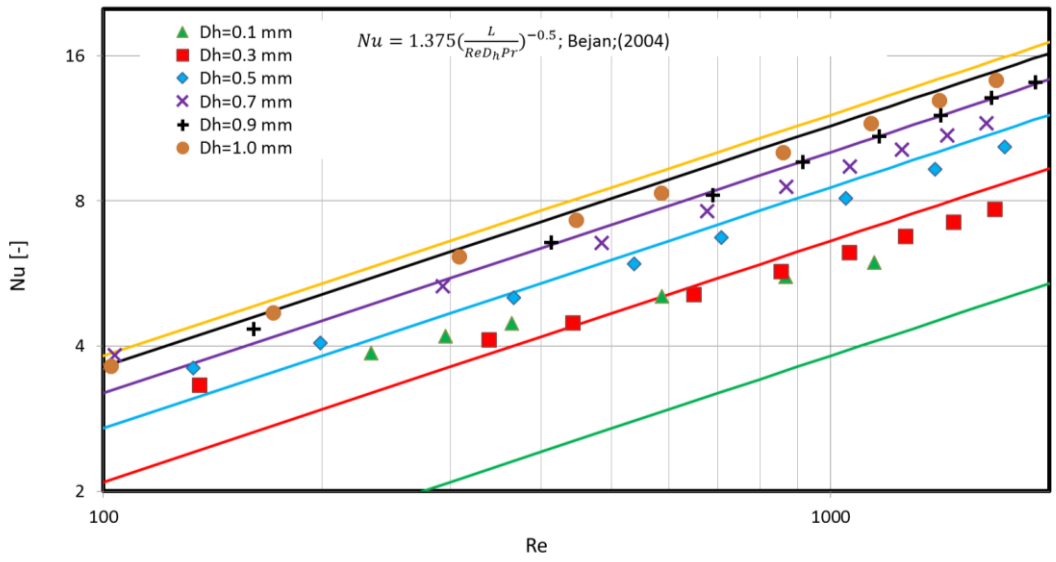

Figure 3-28 : Comparison between numerical Nusselt number predictions and the correlation of Bejan (2004). (solid lines: [**orange**] 1 mm ;[**black**] 0.9 mm ; [**purple**] 0.7 mm ; [**blue**] 0.5 mm; [**red**] 0.3 mm; [**green**] 0.1 mm) with varying channel hydraulic diameter.

The effect of the hydraulic diameter on *Nu* is shown in Figure 3-29 for *Re* = 500 and 1500 and the results are compared to the predictions from Shah and London (1978). As seen in this figure, the hydraulic diameter affects significantly the average Nusselt number as *Nu* is found to increase with increasing hydraulic diameter. This phenomenon is further explained below. Also, the figure demonstrates that the numerical data are in excellent agreement with the predictions using the Shah and London (1978) correlation.

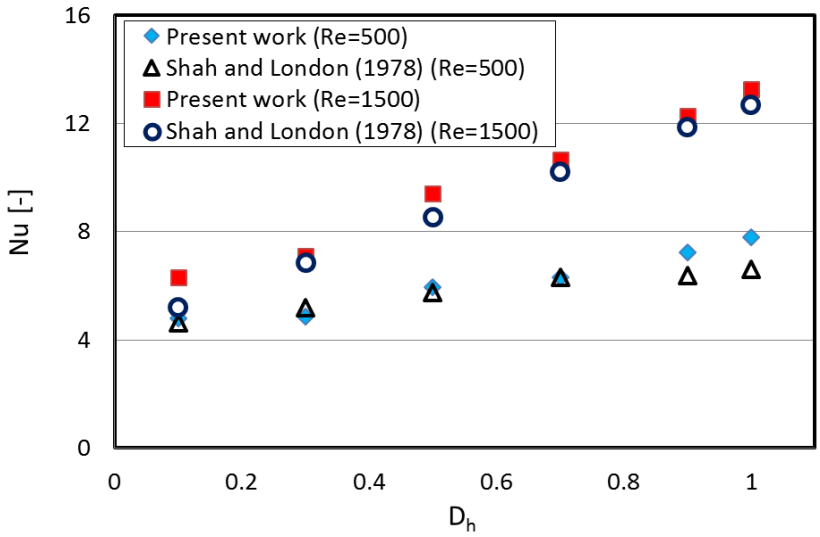

Figure 3-29 : Variation of Nusselt number with varying hydraulic diameter.

Figure 3-30 shows the wall and fluid temperature at *Re* = 500 and *Re* =1500 for the lowest and highest D_h tested in this study in order to explain the effect of the hydraulic diameter. The figure indicates that the temperature difference between wall and fluid for D_h = 1 mm is higher than for D_h = 0.1 mm. Therefore, the magnitude of the dimensional heat transfer coefficient at D_h = 0.1 mm is higher than at D_h = 1 mm. In other words, the dimensional heat transfer coefficient increases when the hydraulic diameter decreases. On the contrary, Figure 3-29 depicts the opposite effect for the relation between hydraulic diameter on Nusselt number. This is arising from the fact that the Nusselt number depends on two variables namely the hydraulic diameter and the heat transfer coefficient ($Nu = hD_h / k$). Since the heat transfer coefficient (h) decreases as D_h increases, the value of *Nu* will depend on which variable has a more dominant effect.

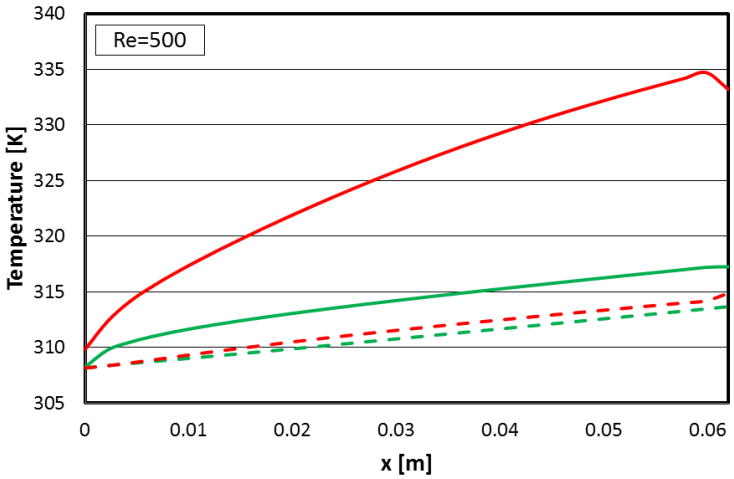

(a)

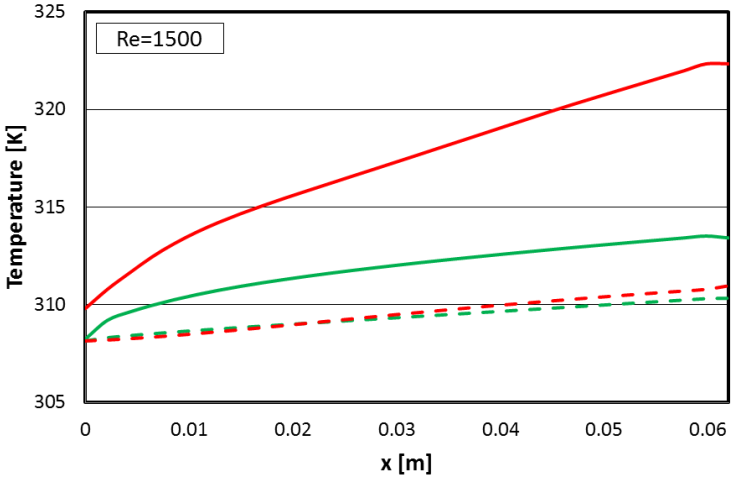

(b)

Figure 3-30 : Comparison of wall temperature (solid line) and fluid temperature (dotted line) for the tested aspect ratio at (a) Re≈500 (b) Re≈1500 ; [**red**] D_h =1 mm ;[**green**] D_h =0.1 mm.

Figure 3-31 clarifies this point by plotting the local heat transfer coefficient and *Nu* against the axial distance for D_h = 0.1 – 1 mm and *Re* = 500 & 1500. The figure shows clearly that the local heat transfer coefficient increases with decreasing hydraulic diameter while the opposite occurs for *Nu*. Also, the figure shows that for Re = 500 the flow is thermally developing for all diameters except for D_h = 0.1 where the values reached almost a constant value. The same result was found in the numerical work of Lee and Garimella (2006) for laminar, thermally developing flow in microchannels having a hydraulic diameter and an aspect ratio range between 200 to 364 μm and 1 to 10, respectively. The local and average Nusselt numbers showed a decrease with decreasing hydraulic diameter and increasing aspect ratio. Dharaiya and Kandlikar (2012) also studied the effect of aspect ratio, ranging from 0.1 to 10, in a rectangular microchannel. The hydraulic diameter varied as the aspect ratio changed. So from this study it is difficult to determine which geometric parameter has the most significant effect on heat transfer. It is interesting to note that the predicted *Nu* for fully developed flow obtained in five different cases showed an inconsistent trend for each tested case. In this present study, the average *Nu* number increased with increasing hydraulic diameter and followed the same trend as found for the one heated-wall boundary-condition presented by Dharaiya and Kandlikar (2012). As shown in the sections above, the present results indicate that the hydraulic diameter has the most significant effect on heat transfer while the effect of the aspect ratio on heat transfer at a given hydraulic diameter is negligible. Furthermore, as shown in Figure 3-29, the present results were found to be in a good agreement with the correlation of Shah and London (1978) for the entire range studied.

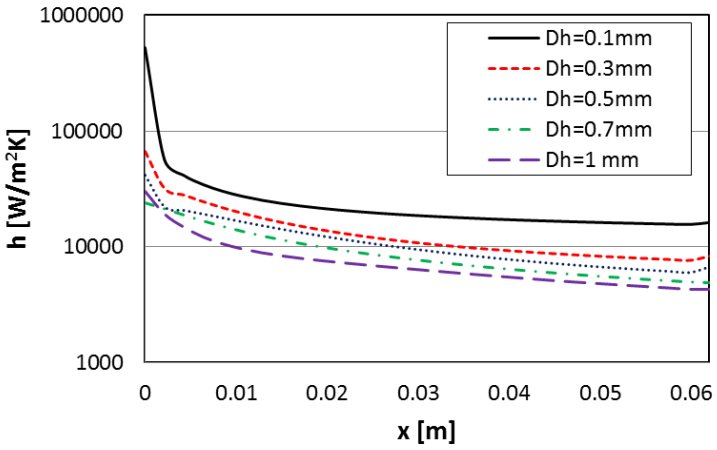
1000000
100000
10000
1000
h [W/m²K]
0
0.01
0.02
0.03
0.04
0.05
0.06
x [m]
Dh=0.1mm
Dh=0.3mm
Dh=0.5mm
Dh=0.7mm
Dh=1 mm

(a)

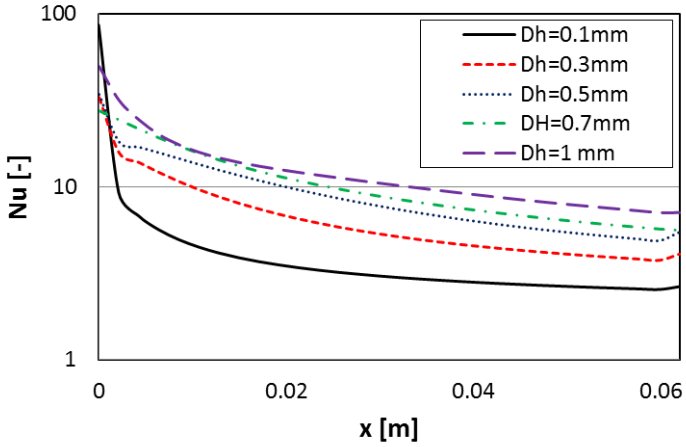
100
10
1
Nu [-]
0
0.02
0.04
0.06
x [m]
Dh=0.1mm
Dh=0.3mm
Dh=0.5mm
DH=0.7mm
Dh=1 mm

(b)

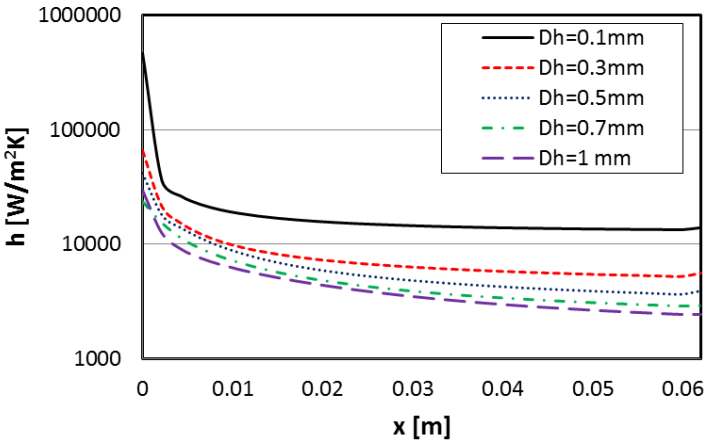
1000000
100000
10000
1000
h [W/m²K]
0
0.01
0.02
0.03
0.04
0.05
0.06
x [m]
Dh=0.1mm
Dh=0.3mm
Dh=0.5mm
Dh=0.7mm
Dh=1 mm

(c)

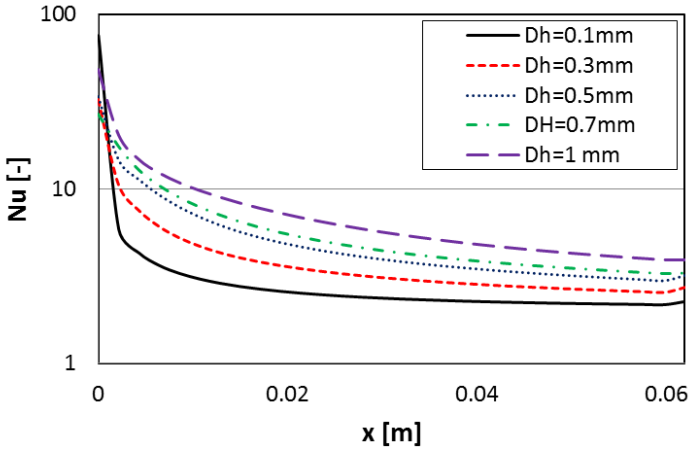

(d)

Figure 3-31 : Axial heat transfer coefficient and Nusselt number at Re=1500 (a,b) and Re 500 (c,d).

3.3.4 Effect of channel geometry on entry/exit losses

In most experimental studies, the channel pressure drop was estimated by subtracting all minor losses (sudden contraction and enlargement) from the total measured pressure drop. The minor losses were calculated using equations proposed for large geometries, implicitly assuming that the flow structure would be the same in micro geometries. In the present study, the minor losses were examined in order to assess whether they can be ignored or not. Figure 3-32 shows the pressure variation along the test section from the mid plane of the inlet plenum to the mid plane of the outlet plenum. It is obvious that there is a sudden decrease in pressure from the inlet plenum to the channel inlet due to the 90^0 change in flow direction, further downstream the pressure decreases linearly up to the channel exit where a sudden increase occurs due to pressure recovery in the outlet plenum. Also, the small pressure recovery due to vena contracta at the channel inlet is not observed, i.e. there were negligible losses due to the sudden contraction. The entry and exit losses (combined losses due to change in flow direction and change in flow area) are estimated in the present study and the values are summarized in Table 3-3.

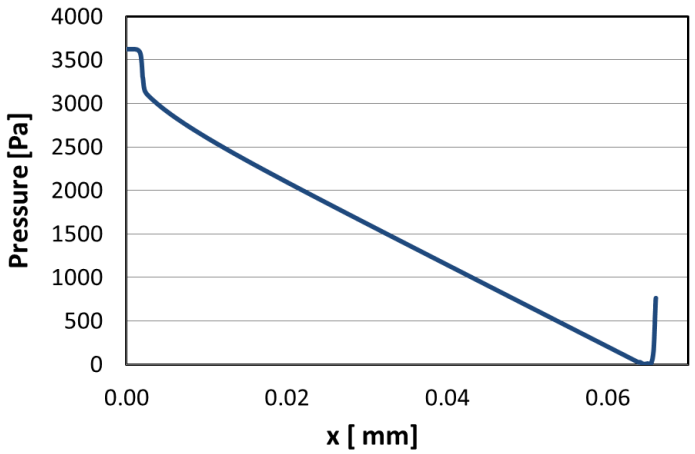

Figure 3-32 : The total pressure along the test section for *Re* = 578, $\boldsymbol{D_h}$ = 0.56 mm , *AR* = 1.52.

Table 3-3: Entry and exit pressure losses

Run	*AR*	D_h *(mm)*	*Re*	ΔP_{total} (Pa)	$\Delta P_{entry,num}$ (%)	$\Delta P_{exit,num}$ (%)	$\frac{\Delta P_{entry,num}}{\Delta P_{entry,con}}$	$\frac{\Delta P_{exit,num}}{\Delta P_{exit,con}}$
1	0.39	0.56	657	5191.99	10.51	10.68	0.933	0.610
2	1	0.56	585	3635.64	9.65	22.35	0.844	0.597
3	1.52	0.56	600	3491.38	10.07	13.25	0.892	0.598
4	2	0.56	520	3327.79	7.74	16.46	0.787	0.604
5	4	0.56	574	4310.94	7.38	5.29	0.777	0.628
6	7.5	0.56	637	5325.94	7.77	1.96	0.822	0.678
7	10	0.56	637	5540.39	7.33	1.97	0.813	0.714

8	1	0.1	586	528469.00	2.37	1.36	0.902	0.547
9	1	0.3	648	23783.50	6.24	10.07	0.787	0.560
10	1	0.5	537	4523.58	8.09	16.31	0.788	0.586
11	1	0.7	677	2537.00	12.88	29.67	0.827	0.628
12	1	0.9	666	1168.85	14.19	28.65	0.850	0.685
13	1	1	585	766.77	13.99	27.83	0.876	0.721

As mentioned in section 3.2.1, a uniform velocity was employed at the inlet plenum. Differences in channel area, however, resulted in different velocities in the channel. Therefore, a Reynolds number between Re = 520 and 677 was chosen in order to compare the entry and exit losses for all tested channels. The table demonstrates that the entry losses ranged from 7.33 to 10.51 % for AR = 0.39 – 10 and D_h = 0.56 mm and ranged from 2.37 to 14.19 % for D_h = 0.1 – 1 mm and AR= 1. The exit losses ranged from 1.96 to 22.35 % for AR = 0.39 – 1 and ranged from 1.36 to 29.67 for D_h = 0.1 – 1 mm. This means that regardless of the geometrical parameter (aspect ratio or hydraulic diameter) the entry and exit losses could be significant and should be taken into consideration. In the last two columns of Table 3-3, the numerical values were compared with the values predicted using conventional macroscale equations given below for sudden expansion, sudden contraction and 90^0 changes in flow direction. These equations (4.12) to (4.14) are taken from ref. Munson *et al*. (2009). For the entry losses, the numerical values were lower by 6.7 % to 22 % compared to the prediction using the conventional equations. For the exit losses the difference was significant where the numerical values were 28 – 45 % lower. In conclusion, using the conventional equations for predicting the minor losses in microchannels could result in significant error in the calculations of the experimental friction factor and thus caution should be exercised when comparing with the laminar flow theory.

The sudden expansion losses are calculated by:

$$\Delta p_{ex} = \left(1 - \frac{A_{ch}}{A_p}\right)^2 \times \frac{1}{2}\rho V_{ch}^2 \tag{4.12}$$

For sudden contraction, the contraction losses are defined using a loss coefficient K_c as given in Eq. (4.13). The value of this coefficient ranges from 0 to 0.5 depending on the small to large area ratio (A_{ch}/A_p), which is given in Beavers *et al*. (1970) in the form of a chart.

$$\Delta p_c = K_c \times \frac{1}{2}\rho V_{ch}^2 \tag{4.13}$$

For a sharp change in flow direction by 90^0, the following equation was used:

$$\Delta p_{90} = K_{90} \times \frac{1}{2}\rho V_p^2, \qquad K_{90} = 1.1 \tag{4.14}$$

3.3.5 Thermal Performance Index (TPI)

The thermal performance index defined in Hasan *et al*. (2012) as the ratio between the heat exchanger effectiveness (ratio of the actual heat transfer rate to the maximum possible heat transfer rate) and pressure drop is a useful means for comparison between heat exchangers. In this study, only the single channel case was investigated rather than a complete microchannel heat exchanger. However, the same principle can be applied to evaluate the effect of hydraulic diameter and aspect ratio on the thermal-hydraulic performance. The thermal performance index is defined in this study by:

$$\xi = \frac{\dot{m} c_p (T_{out} - T_{in})}{q'' A_{ht} \Delta p} \quad (4\text{-}15)$$

where, $\dot{m}$ is mass flow rate and A_{ht} is the total heat transfer area, $(W + 2H)L$.

Figure 3-33(a) depicts the effect of aspect ratio on the performance index while Figure 3-33(b) shows the effect of hydraulic diameter. Both figures indicate that the performance index decreases with increasing Reynold number. The aspect ratio did not affect the performance index significantly for AR > 1 while compared to the other aspect ratios the performance index was found to be highest for AR = 0.39. Figure 3-33(b) clearly indicated the effect of the hydraulic diameter where for constant Reynolds number the performance index increased with increasing diameter. The conclusion based on the performance index is different from the conclusion based on the separate analysis of the friction factor. For example, in this study, it was concluded previously that channels with aspect ratio between 1 and 2 are recommended to achieve low pressure drop. On the contrary, based on the thermal-hydraulic performance index, a channel with aspect ratio 0.39 gave the highest performance. This means that the performance index should be included for the analysis of thermal-hydraulic performance of microchannels heat exchangers.

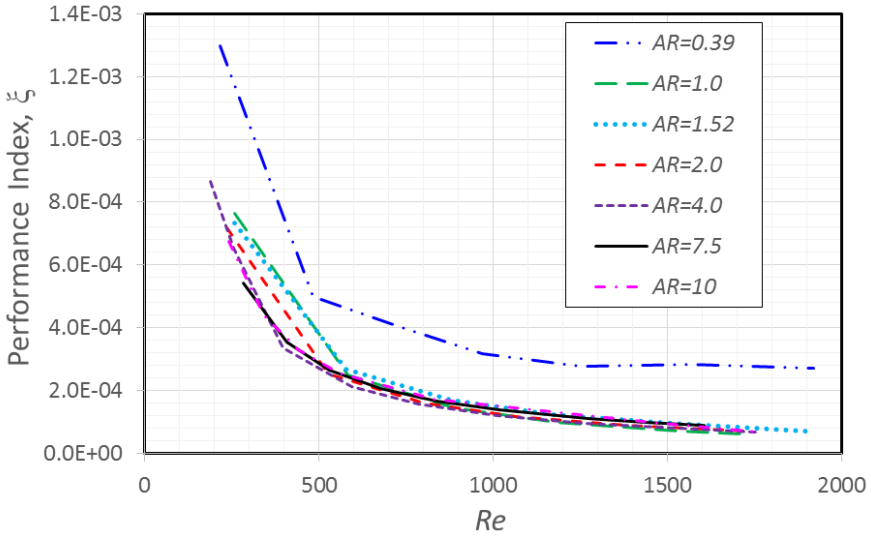

(a)

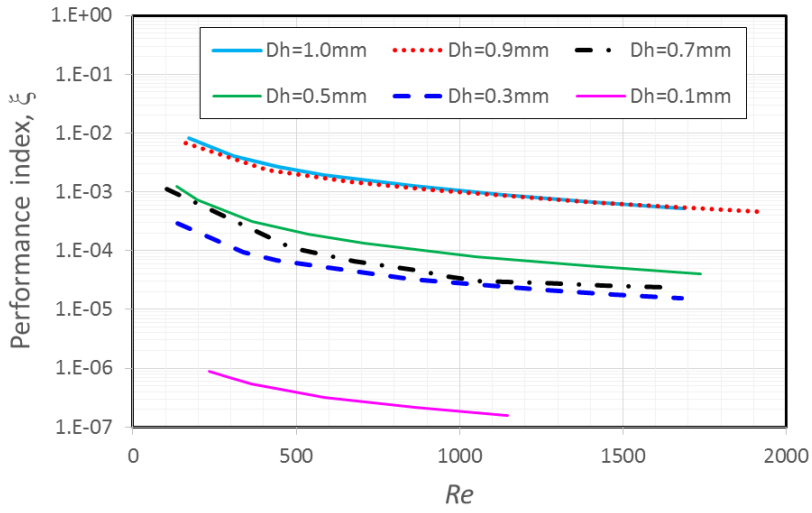

(b)

Figure 3-33 : Variation of thermal performance index against Re at different (a) *AR* and (b) $\boldsymbol{D_h}$

3.4 Summary

In this chapter, a numerical study of single fluid flow and heat transfer in single microchannels was conducted using the computational software package ANSYS Fluent. In the first part of this chapter a significant effect of conjugate on heat transfer was investigated. In this study, four numerical models, using 2D thin-wall, 3D thin-wall (heated from the bottom), 3D thin-wall (three-side heated) and 3D fully conjugated geometries were developed. The present friction factor and heat transfer results obtained by numerical work were compared with existing correlations and experimental data. The simulations were conducted for Reynolds numbers ranging from Re = 100 to Re=3000 and water was used as the working fluid The setup of the 3D thin-wall model simulation used thermal boundary conditions that were very similar to those assumed in the accompanying experiments (uniform heat flux), resulting in the numerical friction factor and heat transfer results showing an excellent agreement with the existing experimental data. On the contrary, the results of the 3D fully conjugated model demonstrated that there is a significant deviation (more than 50%) when compared to the 3D thin-wall and the experimental data. The results of the 3D fully conjugated model indicated that there is a significant conjugate effect and the heat flux is not uniformly distributed along the channel.

In the second part of this chapter, the effect of aspect ratio and hydraulic diameter on fluid flow and heat transfer was investigated. In this study, the 3D thin-wall approach was employed to avoid conjugate heat transfer effects. Two sets of simulations were conducted, where in the first set of simulation, the effect of hydraulic diameter was studied by varying the channel width and depth while keeping the aspect ratio constant. The range of hydraulic diameters was 0.1–1 mm and the aspect ratio was fixed at 1. In the second set of simulations, the aspect ratio ranged from 0.39 to 10, while the hydraulic diameter was kept constant at 0.56 mm. The simulations were conducted for a range of Reynolds numbers, Re = 100–2000, and water was used as the working fluid. Based on the presented results, the friction factor was found to decrease slightly with aspect ratio up to AR $\approx$ 2, after which it increased with increasing aspect ratio. The results demonstrated that the slope of the velocity profile

at the channel wall changes significantly with aspect ratio for AR > 2. The effect of the aspect ratio and hydraulic diameter on the dimensionless hydrodynamic entry length is not significant. Also, the aspect ratio does not affect the heat transfer coefficient, while the dimensionless Nusselt number as well as the friction factor were found to increases with increasing hydraulic diameter.

4 CFD MODELLING OF SINGLE PHASE FLUID FLOW IN A RECTANGULAR MICRO MULTICHANNEL

4.1 Introduction

In this section, results of numerical simulations are presented of a single phase fluid flow in twenty-five parallel rectangular microchannels cut out from the top surface of an oxygen free copper block. The dimensions of the copper block were 15 mm width, 20 mm length and 74 mm height. The nominal dimensions of the microchannel were 0.297 mm width, 0.679 mm depth, 0.209 mm fin thickness (thickness of the wall between channels) and 20 mm length. A detailed description of the experimental facility that was modelled was given in Fayyadh *et al*. (2015). Refrigerant R-134a was used as a test fluid. This numerical study focuses both on the flow distribution over the channels in the multi-microchannel configuration and on possible conjugate effects on heat transfer between channels and copper block.

Furthermore, the effect of various parameters (inlet/outlet area manifold, inlet/outlet flow arrangement and the number of channels) on fluid flow and heat transfer were discussed. Finally, a microchannel with a newly designed inlet manifold is proposed in this chapter of which the flow distribution is compared with the existing design. The computations were performed using the commercial software package FLUENT 14.5, while ICEM 14.5 was utilised for the geometry construction and mesh generation. The hexa meshing grid scheme was used to mesh the system.

4.2 Model Descriptions

The chosen approach for the simulation of flow in a multichannel system in this study is based on simulation results obtained for the single channel configuration (Chapter 4). As discussed in previous section, due to conjugate effects the heat flux is not uniformly distributed along the channel. Hence, the assumption that the heat flux

is uniformly distributed no longer holds true, as concluded in Chapter 4. Therefore, in the multichannel case, it is important to also take conjugate effects into account. Hence, the multichannel system was simulated using the 3D full conjugated model similar to the single channel system studied in the previous chapter (see Figure 4-1). This model closely follows the set-up of the experiment by Fayyadh *et al*. (2015) excluding the inlet and outlet plenums. The dimensions of the channel cross section are shown in Figure 4-2.

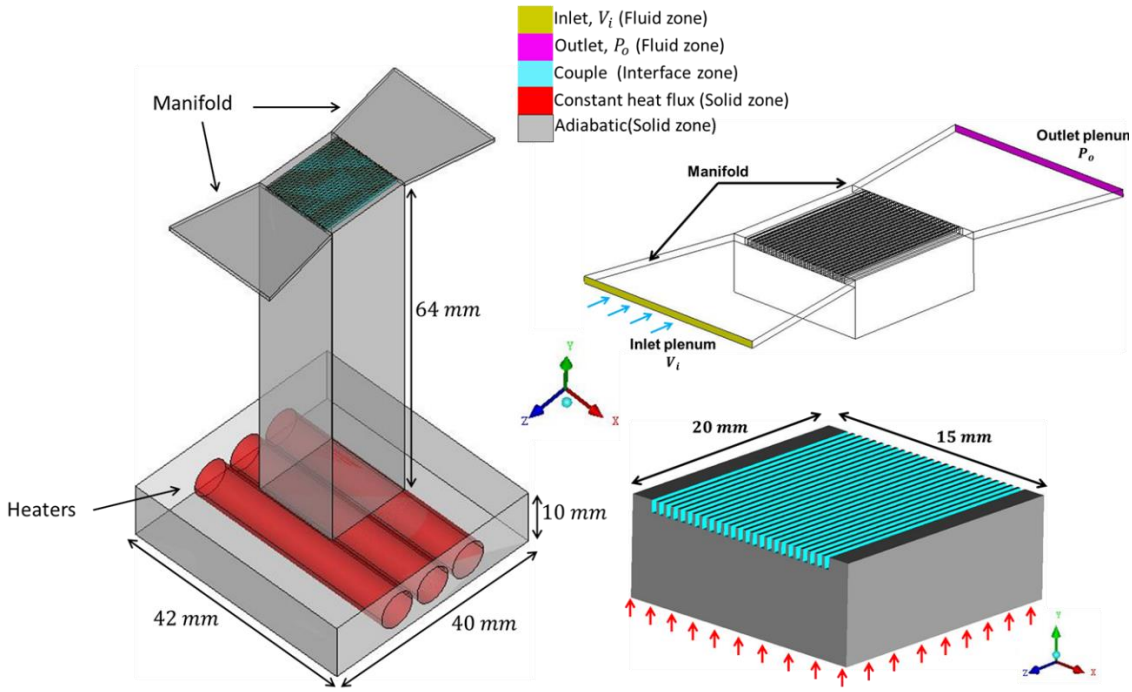

Figure 4-1 : 3D fully conjugated computational model of multi-microchannel system.

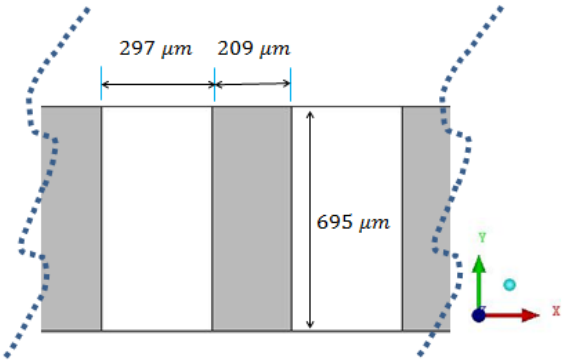

Figure 4-2 : Channel cross-section domain.

4.2.1 Numerical Method

A CFD analysis was carried out to investigate the flow distribution inside the parallel channels when considering the conjugate effect on heat transfer. Similar assumptions as used in the single channel configuration were also adopted in the multi-channel configuration, namely:

1. Steady state fluid flow and heat transfer.
2. Incompressible fluid
3. Negligible radiative heat transfer
4. Constant solid and fluid properties

Based on the above assumptions, the governing differential equations used to describe the steady fluid flow and heat transfer in the microchannel are given as:

Conservation of mass (continuity)

$$\nabla\left(\rho\vec{V}\right) = 0 \tag{5-1}$$

Conservation of momentum

$$\vec{V} \cdot \nabla\left(\rho\vec{V}\right) = -\nabla p + \nabla \cdot (\mu\nabla\vec{V}) \tag{5-2}$$

Conservation of energy for fluid

$$\vec{V} \cdot \nabla\left(\rho c_p T_f\right) = \nabla \cdot (k_f \nabla T_f) \tag{5-3}$$

Conservation of energy for solid

$$\nabla \cdot (k_w \nabla T_w) = 0 \tag{5-4}$$

The boundary conditions for the governing equations are given as,

Inlet plenum:

$$V = V_{in} \qquad T = T_{in} \tag{5-5}$$

Outlet plenum:

$$P = P_{out} \tag{5-6}$$

In this study, a number of uniform inlet velocities were selected in order to match the Reynolds number values obtained in Fayyadh *et al*. (2015). At the outlet a pressure outflow boundary condition was employed. A no slip boundary condition was assigned for all wall boundaries. The heat loss through the top cover was considered to be negligible, which was modeled by a zero-heat flux boundary condition. The continuity of temperature and heat flux was used as the conjugate boundary condition to couple

the energy equations at the fluid and solid interface, which are expressed as

Fluid–solid interface

$$\vec{V} = 0, T = T_s \qquad -k_s \frac{\partial T_s}{\partial n} = -k_f \frac{\partial T_f}{\partial n} \tag{5-7}$$

A constant heat flux, q'' was applied at the location at the cartridge heater.

$$-k_s \frac{\partial T_s}{\partial n} = q'' \tag{5-8}$$

where the q'' is calculated from $P_w/A_{catridge}$. P_w is the total electric power input measured using the wattmeter and $A_{catridge}$ is the area of the cartridge heater. Adiabatic boundary conditions are applied to all other boundaries of the solid region. The properties of the solid used in the numerical simulation are, ρ_s = 8978 kg/m^3, c_p= 381 J/ (kgK), k_s= 387.6 W/(mK), for density, heat capacity and thermal conductivity, respectively.

4.2.2 Results validation

The average velocities in the microchannels are compared in Figure 4-3 for six different grid sizes to investigate the effect of grid sensitivity. The average velocity distributions were found to slightly change from grid 1 to 6. Based on the results shown in Figure 4-3 computational Grid 5 was employed for multichannel configurations in this study as the results obtained are very close to those obtained on the finer mesh from Grid 6.

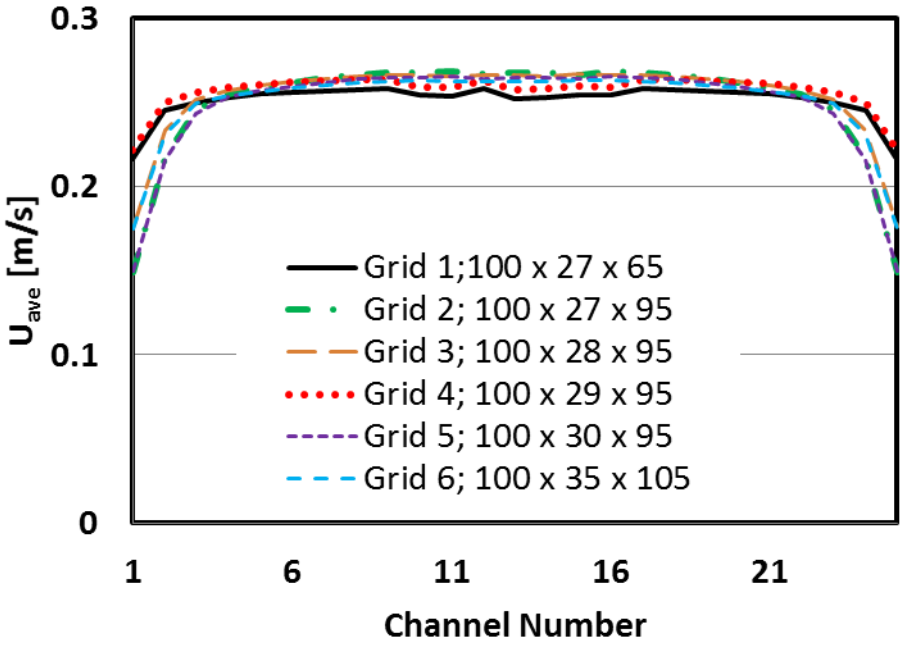

Figure 4-3 : Effect of grid size on average velocity in microchannels in multichannel system.

The simulation results of friction factor and heat transfer are compared with experimental results and existing correlations, see Figure 4-4 and Figure 4-5. Figure 4-4 depicts that the predicted Fanning friction factor shows a similar trend but with values 38% lower than those calculated by Shah and London (1978) in the laminar region and Phillips (1987) in the turbulent region. While the values of the predicted friction factor show an excellent agreement with the experimental results for the Reynolds number range 500–1200 and a reasonable agreement up to *Re=2000*. The predicted values also show that the laminar to turbulent transition jump occurs between *Re =2000–3000*. The existing experimental results presented by Fayyadh *et al*. (2015) did not show any transition jump similar to this prediction. The comparison with the prediction after *Re=2000* is not conclusive due to lack of experimental data in the transition and turbulent region. Figure 4-5 compares the predicted average Nusselt number (Eq (4.8) as found in Chapter 4) values against existing experimental results , Fayyadh *et al*. (2015) and existing correlations. The figure depicts that the

experimental *Nu* is higher than the ones predicted by the current simulation and the Shah and London (1978) correlation for developing laminar flow. Also, it increases almost linearly with Reynolds number at a higher rate than in the predictions. The predicted *Nu* from the current simulation is slightly lower than that the one predicted by Shah and London (1978) with only a small dependency on Reynolds number. The deviation between the simulation and Shah and London (1978) tends to be larger at low Reynolds numbers. This could be attributed to the effect of axial heat conduction which becomes important as the Reynolds number decreases. The axial wall and fluid temperature for the multichannel system were depicted in Figure 4-6. This figure shows a similar trend as in the single channel system, which might be due to conjugate heat effects. Unfortunately, there are no experimental data for local wall temperature and fluid flow. For the lowest *Re*, the heat loss due to axial conduction was 1% while at the highest *Re* the value was 0.3%. This is confirmed in the transition (early turbulent) region, where there is an excellent agreement between the experiment and all predictions. The under-prediction of the experimental values in the laminar region could be attributed to the conjugate effects and flow mal-distribution which are not considered in the experimental data reduction as discussed earlier for the single channel configuration.

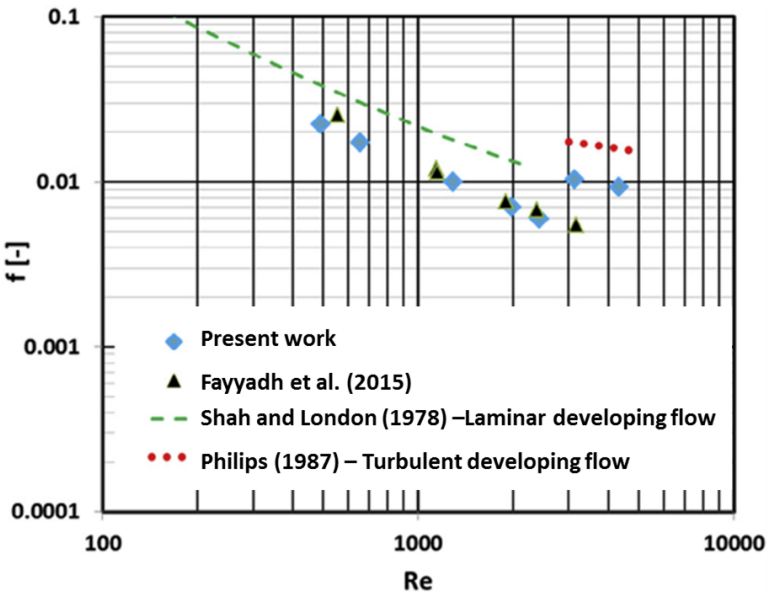

Figure 4-4 : Comparison of predicted friction factor with experimental results and correlations.

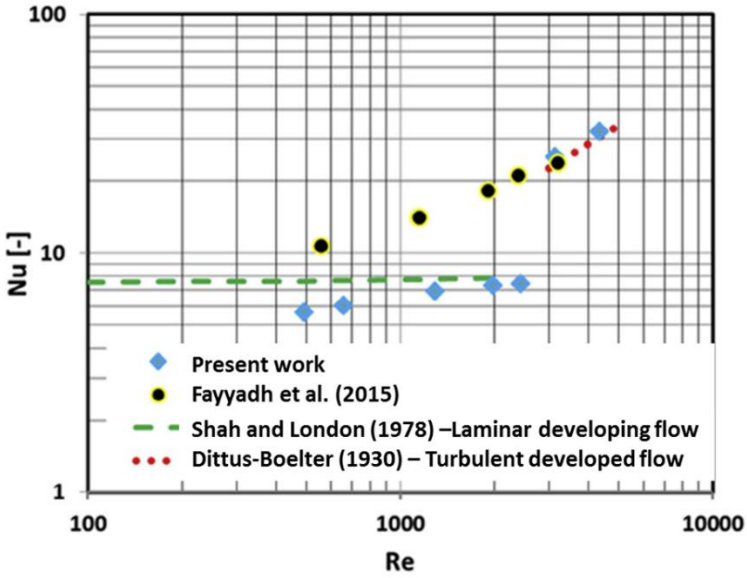

Figure 4-5 : Comparison of predicted Nusselt with experimental results and correlations.

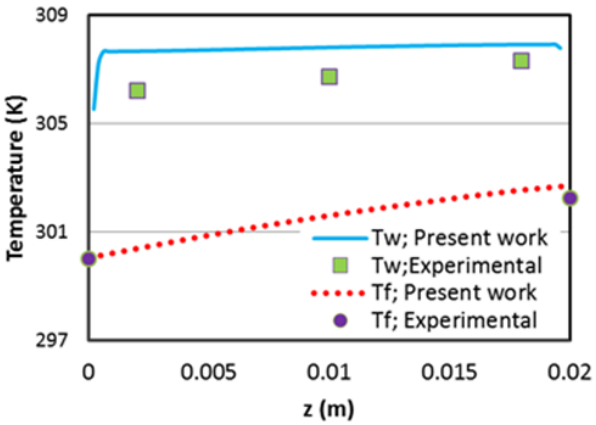

Figure 4-6 : Axial temperature variation of fluid and bottom wall along the channel for multichannel system at Re=585 (3D fully conjugated analysis).

4.2.3 Results discussions

The average velocity and fluid temperature inside the twenty five channels are plotted in Figure 4-7 and Figure 4-8, respectively. The velocity and fluid temperature are averaged along the centreline of each channel. The two figures indicate that the flow distribution depends on the Reynolds number. The flow tends to be uniformly distributed as the Reynolds number decreases. For Re=492, the flow is uniformly distributed along the channels except for the two channels at each side. As the Reynolds number increased above 656, the flow was found to be uniformly distributed only along the center channels (N=3–23). This could be due to the large losses at sharp corners of the inlet manifold which increased with Reynolds number. It can be concluded from these figures that the investigated manifold geometry achieved a very reasonable flow distribution.

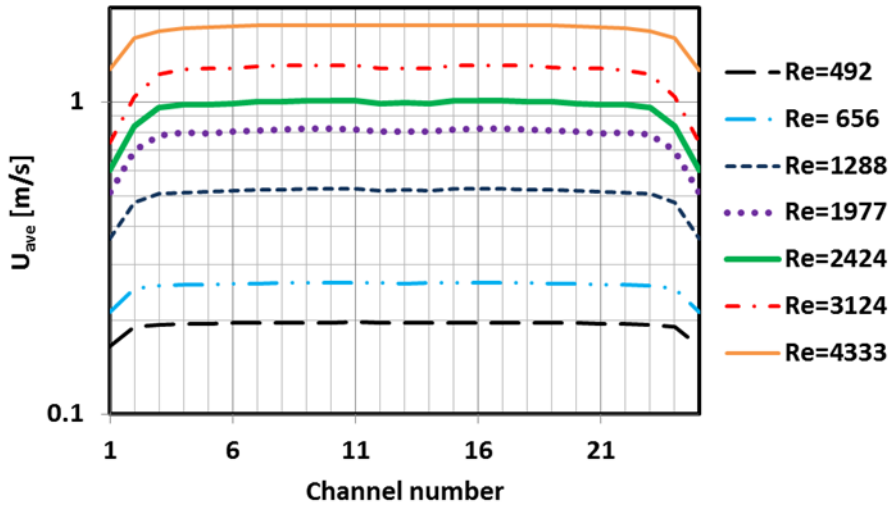

Figure 4-7 : Average velocity in each channel at various Reynolds numbers.

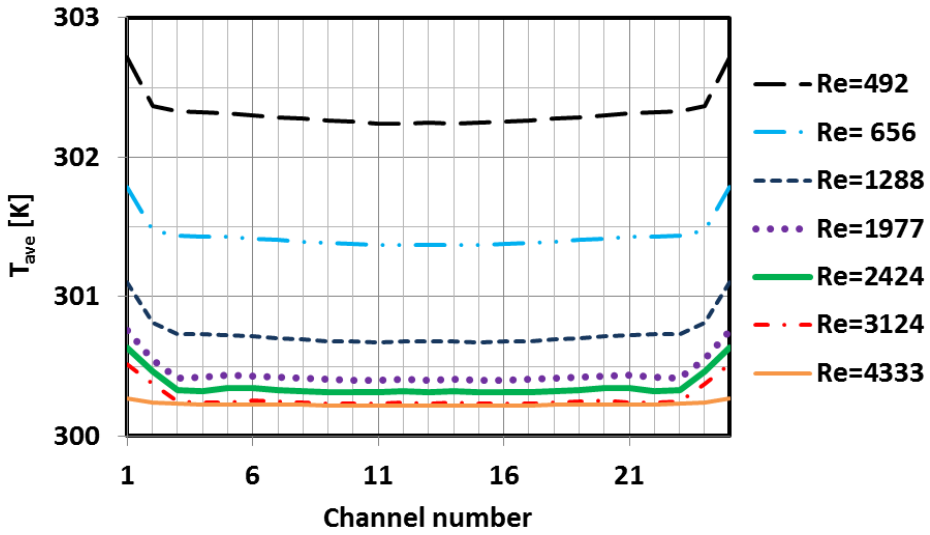

Figure 4-8 : Average temperature in each channel at various Reynolds numbers.

4.2.4 Effect of Various Parameters on Flow Distribution

4.2.4.1 Effect of inlet and outlet manifold area on flow distribution

Controlling the area of the manifold is equivalent to varying the intensity of different forces in the manifold that governs flow distributions, Siva *et al*. (2014). In this section the numerical study focused on the effect of the inlet and outlet manifolds on the flow distributions. Rectangular inlet and outlet manifolds of various sizes were selected, which were connected by 25 parallel micro channels as shown in the schematic of Figure 4-9. Details of the geometrical parameters for the inlet/outlet manifold modifications are given in Table 4-1. The sizes of the 25 micro channels were identical and each channel had a rectangular cross section of 695 µm × 297 µm and a length of 20 mm. Numerical simulations were conducted with various inlet and outlet manifold areas to study their effect on the flow distribution inside the array of micro channels.

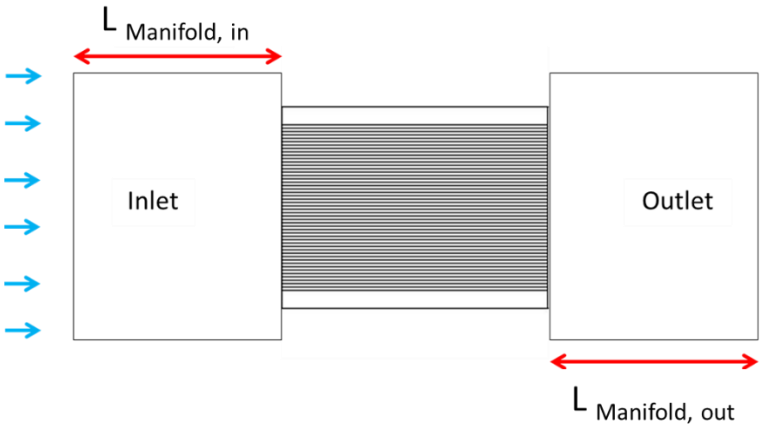

Figure 4-9 : Schematic diagram of rectangular manifold.

Table 4-1 : Various inlet and outlet manifold parameters for numerical study.

Parameters	Type	$L_{Man,\ in}$ (mm)	$L_{Man,\ out}$ (mm)	$nA_{ch}/A_{man,in}$	$A_{man,in}/A_{man,out}$
Rectangular manifold dimensions	Type D-1	16	16	0.019	1
	Type D-2	8	8	0.038	1
	Type D-3	4	4	0.076	1
	Type D-4	16	8	0.019	2
	Type D-5	16	4	0.019	4
	Type D-6	8	16	0.038	0.5
	Type D-7	4	16	0.076	0.25

Three different velocity inlet values, 0.03m/s (*Re*=223), 0.0645 m/s (*Re*=475) and 0.1133 m/s (*Re*=828) were employed at the inlet manifold in this study. Therefore, in order to quantify the flow distribution over the parallel channels, the dimensionless channel flow ratio

$$\beta_k = {Q_k}/{Q_{total}} \tag{5-9}$$

is introduced, where Q_k (m^3/s) denotes the volume flow rate of channel *k* and Q_{total} (m^3/s) is total volume flow rate. In order to quantify the overall flow maldistribution of the whole fluidic system, the maldistribution factor

$$MF = \sqrt{\frac{1}{N-1}\sum_{k=1}^{N}\left(\frac{\sigma_k - \bar{\sigma}}{\bar{\sigma}}\right)^2} \tag{5-10}$$

is introduced, where $\bar{\sigma}$ is the mean flow rate in the parallel micro channels, defined by

$$\bar{\sigma} = \frac{\sum_{k=1}^{N} \sigma_k}{N} \tag{5-11}$$

Note that a uniform flow distribution is achieved when the *MF* value approaches 0.

The flow ratio in the N = 25 parallel channels of the rectangular manifold are given in Figure 4-10(a)-(c). Each figure shows the comparison of the flow ratio for all tested types of multi parallel microchannel heat sinks, under different inlet velocity conditions. It was found that the flow distribution was symmetrical for all tested types of microchannel heat sink. This might be because the location of the inlet flow and outlet flow is the same. In the meantime, it was also clearly shown that the channels located at the lateral edges (k = 1 and k = 25) had a smaller flow ratio compared to the channels located at the centre. As discussed in the above, this is due the losses that occur at the sharp corners of the inlet manifold as seen in Figure 4-11. Kumaraguruparan *et al*. (2011) also concluded the flow maldistribution between channels is due to flow separation or recirculation that occurred in the inlet header or manifold. Small flow separation areas were observed at the sharp corners of the inlet manifold due to the vortex flow, which lead to reduction of flow rate in the channels, as also concluded by Wang *et al*. (2011a).

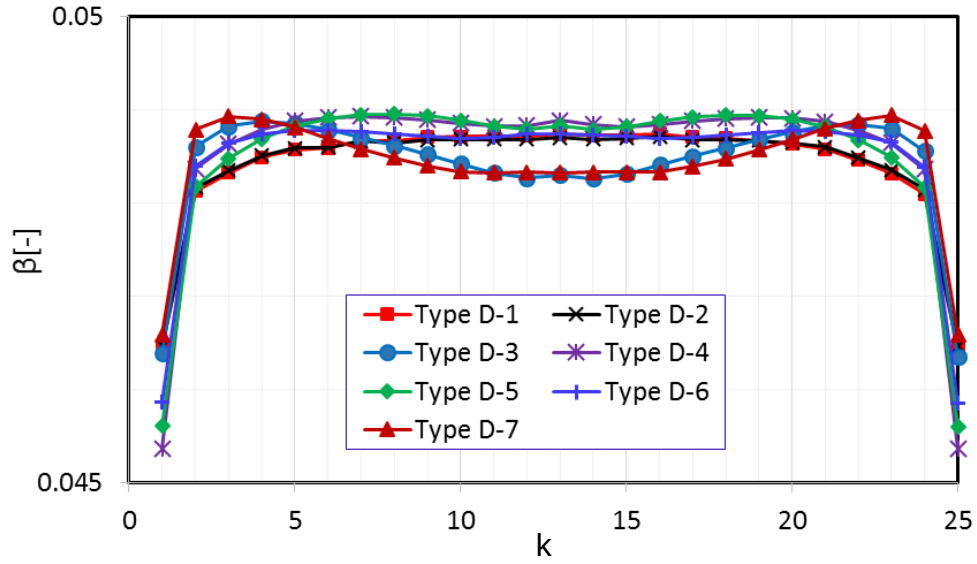
0.05
0.045
β[-]
0
5
10
15
20
25
k
Type D-1
Type D-2
Type D-3
Type D-4
Type D-5
Type D-6
Type D-7

(a)

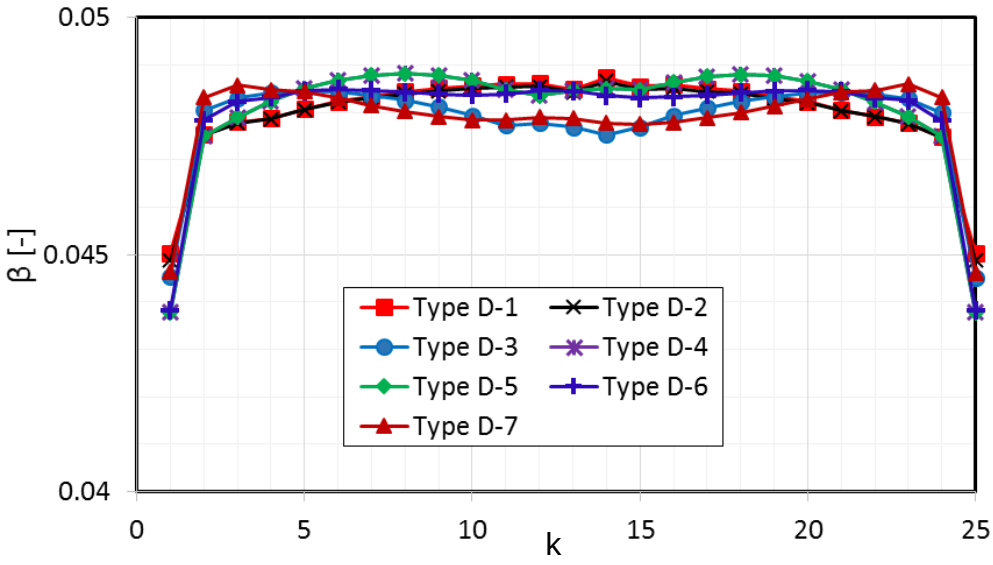
0.05
0.045
0.04
β [-]
0
5
10
15
20
25
k
Type D-1
Type D-2
Type D-3
Type D-4
Type D-5
Type D-6
Type D-7

(b)

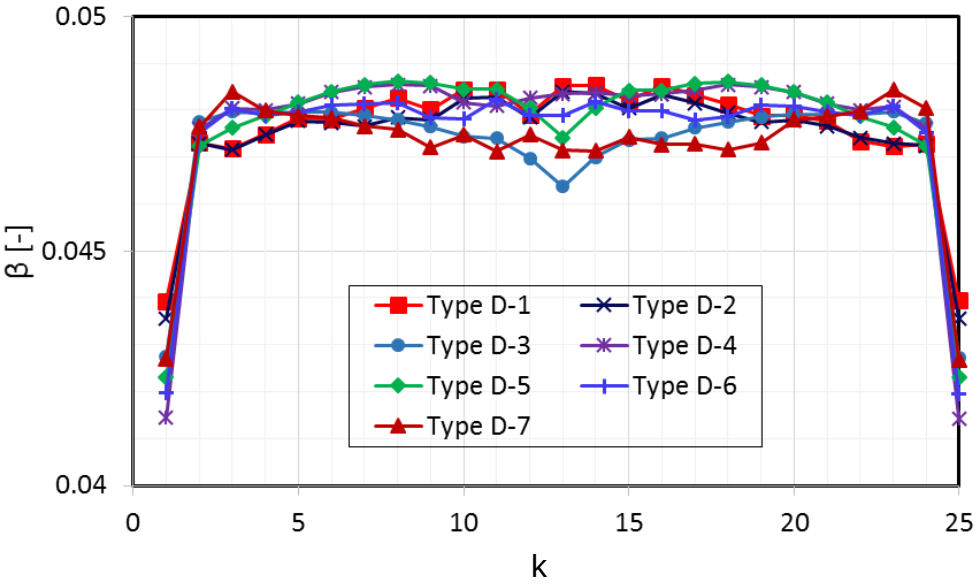

(c)

Figure 4-10 : Flow ratio in each channel of microchannel heat sinks with various inlet/outlet manifold area; (a) V_{in}=0.030 m/s (b) V_{in}=0.0645 m/s (c) Vin=0.1133 m/s.

Additionally, for velocity inlet conditions, V_{in}=0.030 m/s and V_{in}=0.0645 m/s, the flow ratio among the channels was uniformly distributed at the centre region of the microchannel heat sinks for all types excepted for types D-3 and D-7. A possible explanation of this phenomena is clearly shown in Figure 4-12 showing the velocity contour near to channel entrance region. For the smallest area of the inlet manifold, the velocity profile showed a higher velocity in channels 1 to 5 and 20 to 25. This might explain that for type D-3 and D-7, channel 2 to 5 and 21 to 24 showed a higher flow ratio compared to the channels located at the centre region (6 to 20). It is important to mention that the inlet manifold area has a significant influence on the flow behaviour inside channel. For the highest velocity inlet condition (V_{in}=0.1133 m/s), it is hard to explain the flow distribution profile shown in Figure 4-10(c), which appears to be complex and shows a significant flow maldistribution.

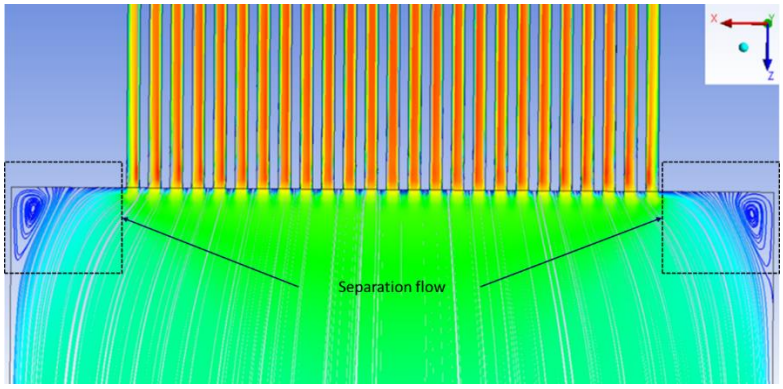

Figure 4-11 : Velocity streamlines of microchannel heat sink.

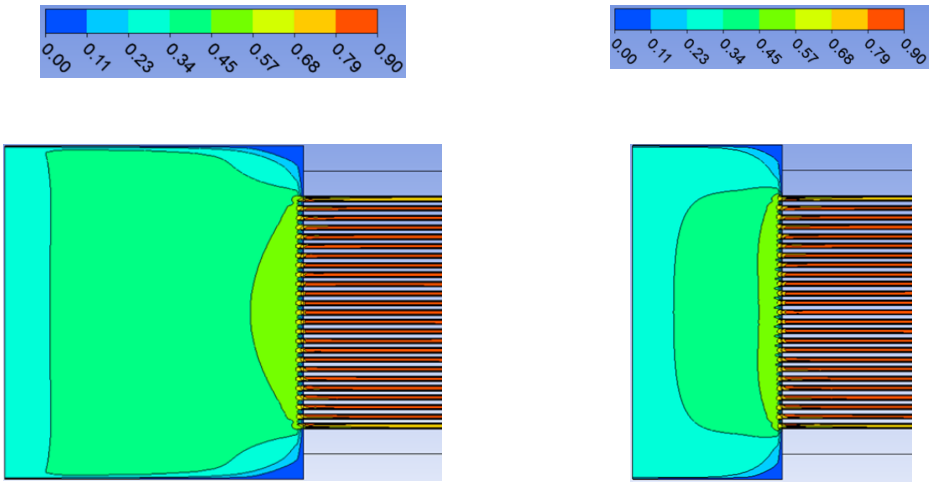

(a) (b)

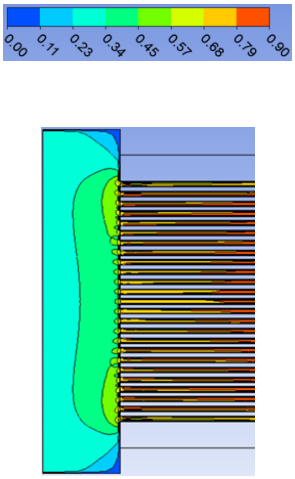

(c)

Figure 4-12 : Velocity contours of inlet manifold for various area (a) Type D-1, D-4, D-5 (b) Type D-2, D-6 (c) Type D-3, D-7.

Therefore, to quantify the flow distribution for all velocity inlet conditions and to verify the effect of inlet/outlet area on the flow maldististribution, the value of MF has been evaluated. Table 4-2 gives a comparison of the flow distribution uniformity (measured by MF) for different velocity inlet conditions. According to Table 4-2, a very similar performance may be observed, for a certain type at a certain velocity inlet. For example, at a velocity of 0.03m/s, show similar values of MF (0.013). On the other hand, based on the graph showing MF value against velocity inlet condition, type D-4 generally shows a higher flow maldistribution, while type D-1 shows a lesser flow maldistribution for all velocity inlet conditions. According to Zhai *et al*. (2017), a uniform flow distribution in parallel-channel microchannel heat sinks could be achieved by eliminate the entrance effect in the inlet manifold, therefore the length of inlet manifold should be long enough. In this study, Type D-1 and Type D-4 are having the longest length of inlet manifold, however, the length of outlet manifold of Type D-4 is smaller than Type D-1. According to MF value, Type D-1 are showing a better flow distribution compared to Type D-4 for all velocity inlet conditions. Here, we can conclude that, both inlet and outlet manifold should long enough to obtained uniform

flow distribution in parallel-channel microchannel heat sinks, Additionally, Figure 4-13 shows that the flow maldistribution increases with increasing inlet velocity. Similar results were shows in numerical work conducted by Kumar and Singh (2019). The main explanation for this phenomenon is associated with the higher inertial force at the higher velocity, therefore the fluid enters the channels preferentially as also pointed out by Pistoresi *et al*. (2015) in their numerical work in parallel micro channels.

Table 4-2 : Comparison of non maldsitribution factor (MF).

Type	Velocity inlet (m/s)	Re (-)	MF (-)
D-1	0.03	223	0.013
	0.0645	475	0.020
	0.1133	828	0.025
D-2	0.03	223	0.013
	0.0645	475	0.020
	0.1133	828	0.026
D-3	0.03	223	0.013
	0.0645	475	0.022
	0.1133	828	0.030
D-4	0.03	223	0.020
	0.0645	475	0.028
	0.1133	828	0.040

D-5	0.03	223	0.019
	0.0645	475	0.028
	0.1133	828	0.035
D-6	0.03	223	0.016
	0.0645	475	0.026
	0.1133	828	0.035
D-7	0.03	223	0.012
	0.0645	475	0.021
	0.1133	828	0.030

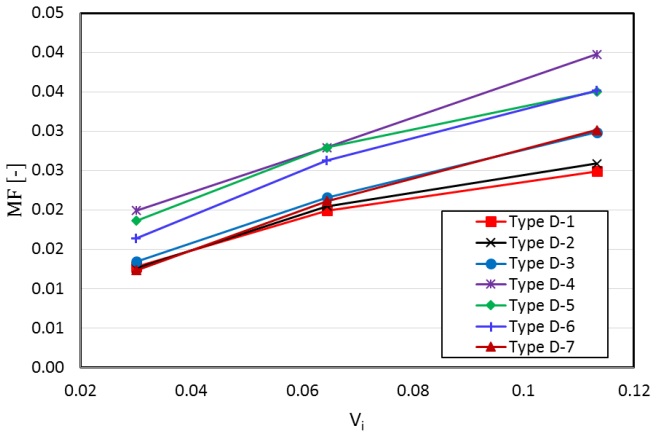

Figure 4-13 : Influence of inlet/outlet condition area on flow distribution/ maldistribution under different inlet velocity conditions.

4.2.4.2 Effect of inlet/outlet arrangement on flow distribution.

In this section, the effect of flow arrangement on flow distribution has been examined. In the following, two different inlet and outlet manifolds, Type D-1 and Type D-2, as described in the previous section (Section 4.2.4), have been chosen. The actual inlet and the outlet areas were changed from those used in the previous section. Three different inlet and outlet arrangements, i.e. U-type (reverse flow), Z-type (parallel flow) and I-Type (normal flow), have been selected to study their effect on the flow distribution. The schematic of the inlet and outlet of the multichannel heat sink is illustrated in Figure 4-14 and information on the inlet flow (velocity inlet) and outlet flow (pressure outlet) can be seen in

Table 4-3 . Four different velocity inlet values, 0.1951m/s, 0.4042 m/s, 0.6403 m/s and 0.7971 m/s were employed for the inlet manifold in this study.

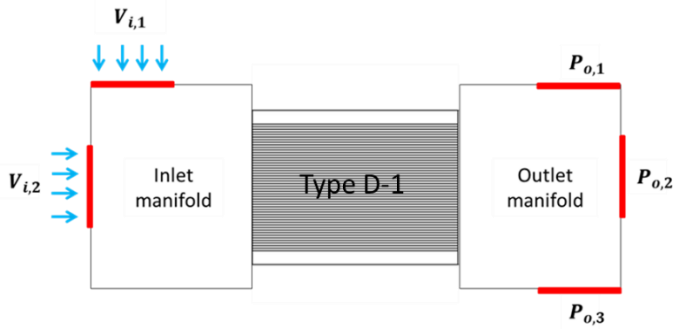

Figure 4-14 : Schematic of 25 channels multichannel heat sinks.

Table 4-3 : Inlet and outlet information for U-, Z-, I- Type.

	U-type	I-type	Z-type
Inlet	$V_{i,1}$	$V_{i,2}$	$V_{i,1}$

Outlet	$P_{o,1}$	$P_{o,2}$	$P_{o,3}$

Figure 4-15 shows a comparison of the flow behaviour in microchannel heat sinks with different inlet / outlet locations, i.e. Figure 4-15 (a) I-type, (b) U-type, (c) Z-type for both Type D-1 and Type D-2, at an inlet velocity of 0.1951m/s. Flow recirculation (secondary flow) was observed at the edges of the inlet and outlet manifolds due to the flow restriction by the manifold walls. As seen in Figure 4-15, different flow arrangement provided a different behaviour of the flow recirculation (secondary flow) at the edges of both inlet and outlet manifold. However, when compared to a different area of the inlet/outlet manifold for the same flow arrangement, only Type-U and Type-Z flows show a significant different flow distribution inside the microchannels. Additionally, U-type and Z-type flows showed a similar flow behaviour inside their inlet manifolds but due to the different location of the outlet port, the flow behaviour in the outlet manifold was found to differ. The reason for the above behaviour can be clearly observed from the velocity streamlines presented in Figure 4-15.

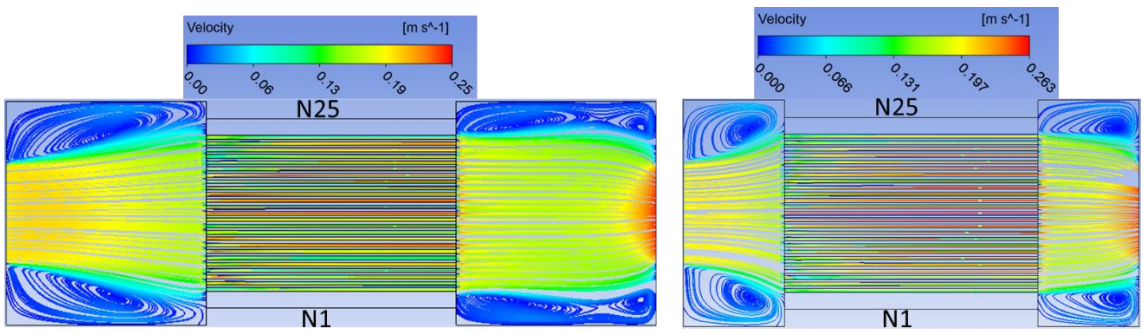

(i) (ii)

(a)

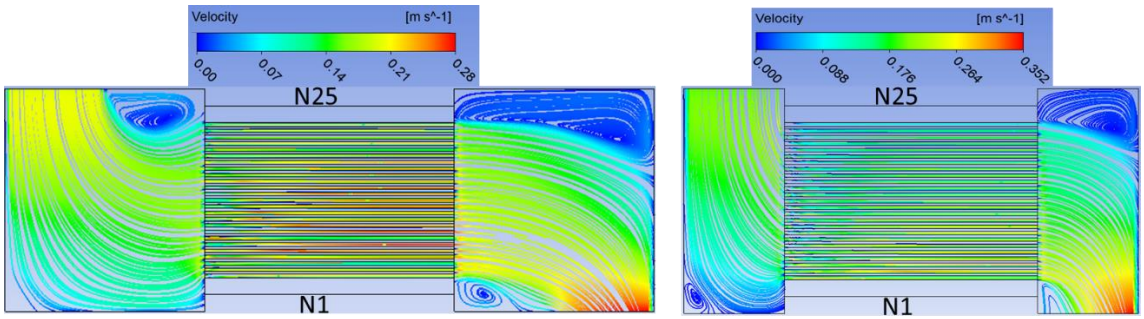

(i) (ii)

(b)

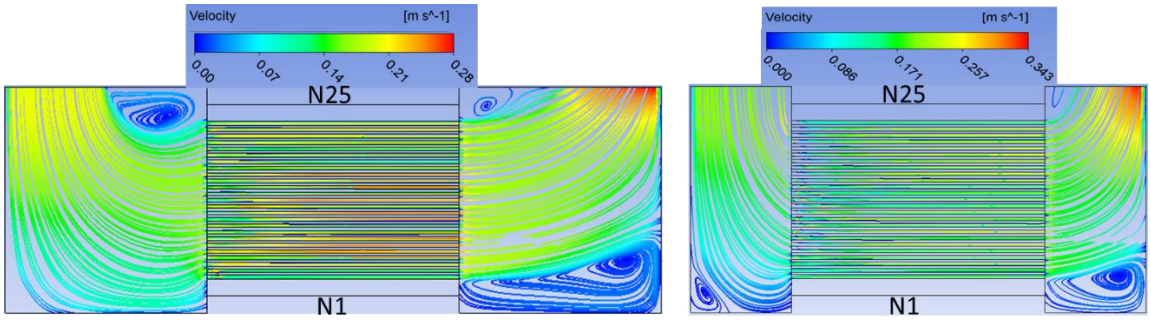

(i) (ii)

(c)

Figure 4-15 : Comparison of velocity streamlines of (a(i)) I-type , (b(i)) U-type , (c(i)) Z-type for microchannel heat sink Type D-1 and (a(ii)) I-type , (b(ii)) U-type , (c(ii)) Z-type for microchannel heat sink Type D-2.

Furthermore, in order to investigate the effect of the flow arrangement of inlet/outlet manifold on the flow distribution inside the microchannels, details of the flow distribution within each channel for different types of inlet/outlet flow configuration have been evaluated using the dimensionless parameter β_k defined in Eq

(5.5). The comparison of the flow ratios of I-type flows for both Type D-1 and Type D-2, at different inlet velocities, are shown in Figure 4-17. As seen in this figure, at all inlet velocities, the flow ratio for the first channels and last channels is significantly lower when compared to channels located at the centre region. For example, at the lowest inlet velocity, V_i=0.1951m/s, the flow ratios in the first two channels (k=1-2) and the last two channels (k=24-25) are lower than those located in the middle region (k=3-23) of the microchannels heat sink. As reported by Wang *et al*. (2011a), the reason for the reduction of flow ratio among the channels, is because of recirculating flow in the inlet manifold. Velocity streamlines obtained in the inlet manifold, shown in Figure 4-17, clearly show the presence of recirculating flow at the edges of both sides in the inlet manifold. This phenomenon could explain the reduced flow ratio in several channels near to edges of the microchannel heat sink. A similar phenomenon was observed by Lu and Wang (2006). They stated that this is associated with flow impinging on the edge wall as well as flow turned around from the base wall flowing towards the edge of microchannel wall causing a flow maldistribution.

With increasing inlet velocity, the number of channels with smaller flow rates increased. For example, at the higher inlet velocity condition, V_i=0.7971m/s, the flow ratio is much smaller in the first and last four channels (k=1-4, 21-25) compared to others. This trend will lead to an increase in flow maldistribution inside the microchannels. This indicates that the secondary flow, due to recirculating flow in the inlet manifold, gets more pronounced when the flow rate increases, as seen in Figure 4-17. This will lead to increased flow maldistribution inside the microchannel heat sink. Furthermore, a symmetrical flow distributions was observed in I-type arrangement, for both Type D-1 and Type D-2. This is because both inlets an outlet are located at the centre region of the microchannels, which induced a symmetrical recirculating flow at both sides of the inlet manifold. Similar observations for the symmetrical behaviour of flow inside the microchannels for the I-type configuration was reported earlier by Lu and Wang (2006), Kumaran *et al*. (2013) and recently reported by Liu and Yu (2016).

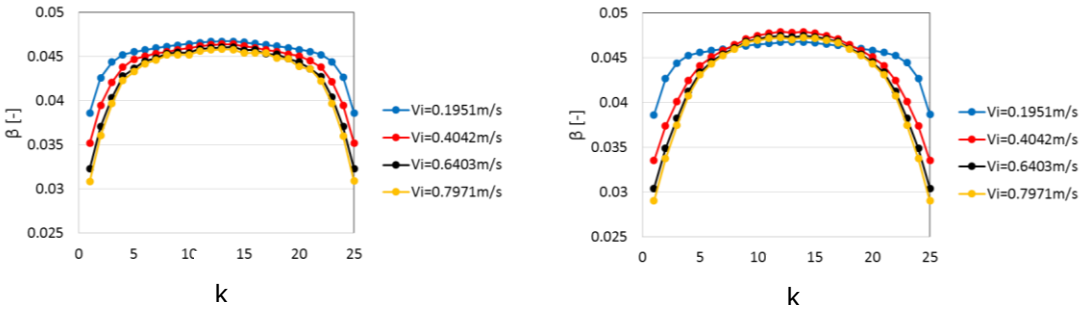

(a) (b)

Figure 4-16 : Flow ratio of the rectangular header, (a) Type D-1 and (b) Type D-2 for I-Type flow

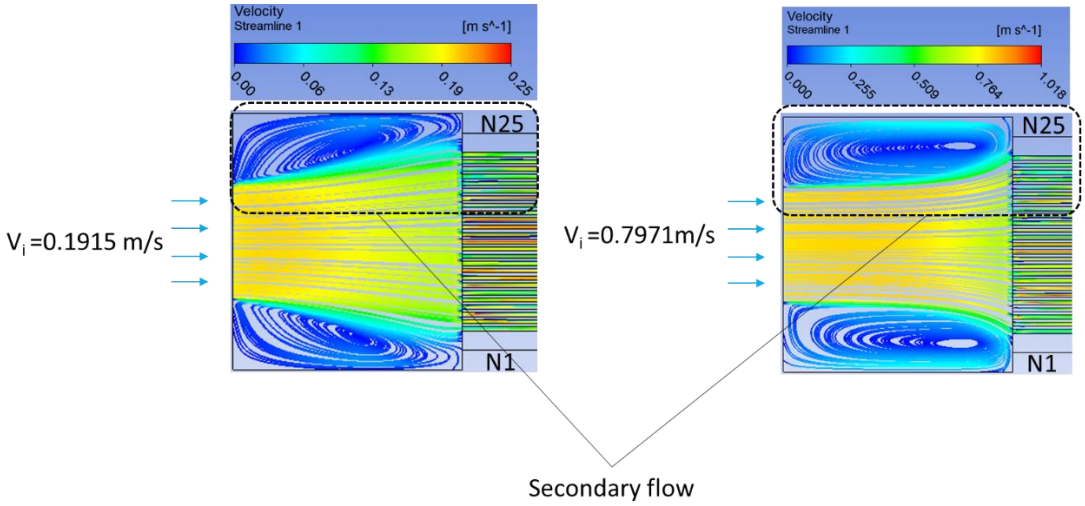

Figure 4-17 : Comparison of secondary flow behaviour at the inlet manifold at V_i = 0.1915 m/s (left-hand side) and V_i = 0.7971 m/s (right-hand side) for I-type flow

As expected, a symmetric flow distribution inside microchannels was not observed for U-type configurations. As seen in Figure 4-18, for the lowest tested inlet velocity (V_i=0.1951m/s) channels 2-20 showed the maximum flow ratios. It should be noted that the channels located furthest from the entrance flow showed the smallest flow ratios compared to channels in the centre region. A possible explanation of this

phenomenon is that as the fluid travels from the inlet to the other side (the dead end) of the inlet manifold, the flow rates decrease and less fluid entered the channels. However, channels located near the entrance (k=19-25) also showed lower flow ratios, which is explained by the appearance of secondary flow at the edge of the sharp corner, leading to a reduction in flow rates. Furthermore, the number of channels having maximum flow ratios was reduced when the flow rates increased. For example, for the highest inlet velocity, V_i=0.7971m/s, only channels 3 to 19 were observed to have the maximum flow ratio. As seen in Figure 4-19, as the inlet velocity increased, the secondary flow near to entrance became more pronounced. This can be explained by the reduction in the number of channels having maximum flow ratio, which caused the flow maldistribution.

In contrast to I-Type flow, for different inlet/outlet manifold area, Type D-1 and Type D-2 show different distributions of flow ratios among the channels. For Type-D1, as mentioned before, the maximum flow ratios were observed in several channels located in the centre region of the microchannels (k=2-20). However, for Type D-2, as can be seen in Figure 4-18 (b), flow velocity peaks are found at the entrance region (k = 18-24) and the lowest velocity was found at the edge of the microchannel. As shown in the previous figure (Figure 4-15(c)), due to the absent wall restriction at the edge of the inlet manifold, secondary flow is not observed near the entrance region in Type D-2. Furthermore, it is worth mentioning that the flow ratio in each channel for Type D-2 (U-type) is increasing until the 22th channel after which it decreases towards channel 25. As seen in Figure 4-15 (c(ii)) , the velocity flow rate inside the inlet manifold is reduced as it is far from the entrance port, therefore, it can be concluded that channels located furthest from the entrance port have the lowest flow ratios.

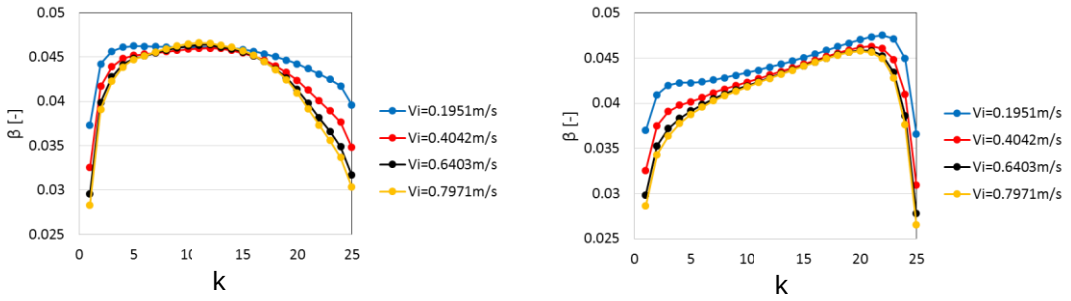

(a) (b)

Figure 4-18 : Flow ratio of the rectangular header, (a) Type D-1 and (b) Type D-2 for U-Type flow.

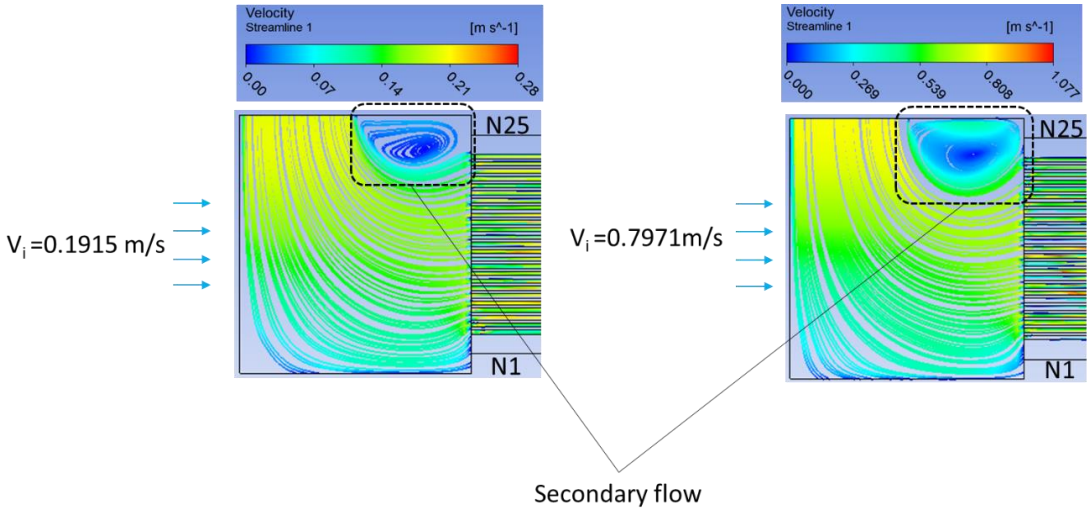

Figure 4-19 : Comparison of secondary flow behaviour in the inlet manifold at V_i = 0.1915 m/s (left-hand side) and V_i = 0.7971 m/s (right-hand side) for U-type flow.

The comparison of flow ratios for the Z-type configuration for both Type-D1 and Type-D2, at different flow rates are show in Figure 4-20. As seen in Figure 4-20 (a), the flow ratio of the first channel for Type D-1 is lower, which as discussed before, may be related to the small quantity of fluid (smaller flow rate) that was observed at the dead end of the inlet manifold. The maximum flow ratios were observed in

channels 2 to 14. However, for Type D-2, the flow distribution inside the channels significantly differs from the distribution observed for Type D-1. As showed in Figure 4-20 (b), only channels 2 to 9 showed the maximum flow ratio. However, for both types (Type D-1 and Type D-2) the flow ratios reduced after the second channel. It is also interesting to see that for both Type D-1 and Type D-2 all inlet velocities produced similar flow ratios in the 14th channel and 9th channel, respectively.

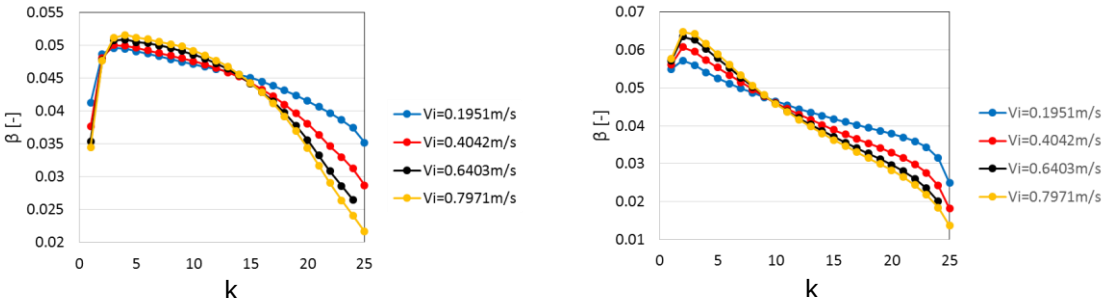

(a) (b)

Figure 4-20 : Flow ratio of the rectangular header, (a) Type D-1 and (b) Type D-2 for Z-Type flow

As mentioned before, the flow patterns in the inlet manifold for U- and Z-type, either for Type D-1 and Type D-2 were showing similar trends where the fluid was traveling from the entrance port to the dead end of inlet manifolds. Similar observations were also reported in the numerical work by Kumaran *et al*. (2013). They also stated that flow separation occurring in the inlet manifold caused a poor flow distribution between the channels. Furthermore, it should be mentioned that the two configurations (U- and Z-type) were found to lead to a significant variation in flow distribution as seen in Figure 4-18 and Figure 4-20. While similar flow patterns were obtained in the inlet manifold, the flow patterns in the outlet manifold had different directions. This is due to the different location of exit port for the U- and Z-type configurations. Therefore, it can be concluded that, the locations or the arrangement

of the inlet and outlet port has a significant effect on the flow distribution inside channels.

The maldistribution factor (MF) has been evaluated and summarized (see Table 4-4) in order to quantify the flow maldistribution for both microchannel heat sinks (Type D-1 and D-2) for different types of flow arrangements, for various inlet velocities. The lower the value of MF is, the better the uniformity is. The influence of the flow arrangement on the flow distribution can be clearly seen in Figure 4-21. The flow maldistribution is found to increase with velocity inlet condition. Figure 4-21 indicated that Type D-1 exhibits a smaller maldistribution compared to Type D-2, for all three type of flow arrangements (I-, U-, Z- type) tested in this study. Furthermore, a strong maldistribution can be observed for the Z-type configuration combined with an inlet/outlet manifold identical area and at the same inlet velocity. While, I-type with a large inlet and outlet manifold header was showing a better flow distribution. Similar observation was also reported by Tang *et al*. (2018).

Table 4-4 : Comparison of the maldistribution factor (MF) for Type D-1 and Type D-2 for I-,U-,Z- flow arrangement under different inlet velocity.

Type		Velocity inlet (m/s)	MF (-)
D-1	U-type	0.195	0.0510
		0.404	0.0856
		0.640	0.1129
		0.797	0.1258
	Z-type	0.195	0.0911

		0.404	0.1490
		0.640	0.1992
		0.797	0.2253
	I-Type	0.195	0.0498
		0.404	0.0742
		0.640	0.0955
		0.797	0.1054
D-2	U-Type	0.195	0.0647
		0.404	0.0935
		0.640	0.1146
		0.797	0.1242
	Z-Type	0.195	0.1852
		0.404	0.2743
		0.640	0.3360
		0.797	0.3637
	I-Type	0.195	0.0498
		0.404	0.1018

		0.640	0.1252
		0.797	0.1363

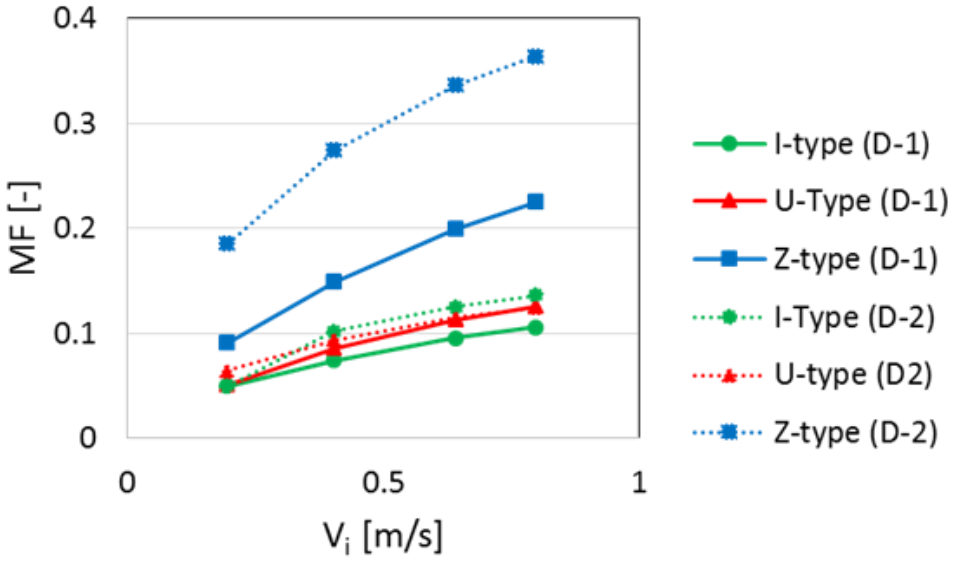

Figure 4-21 : Influences of the inlet/outlet flow arrangement on flow maldistribution under different inlet velocity conditions.

4.2.4.3 Effect of number of channel on flow distribution.

In this section, the effect of number of channels on the flow distribution has been studied. Based on the numerical results presented in section 4.2.4.2, the Type D-1 manifold was used as it produced a better uniformity compared to the others. In the following part, six different number of channels (N= 9, 13, 17, 25, 33) were selected while keeping the hydraulic diameter of each channel and the area of microchannels constant. To maintain the same overall width of the heat sink, the thickness of the fins

is adjusted accordingly. Three different velocity inlet values, 0.03m/s, 0.0645 m/s and 0.1133m/s were employed at the inlet manifold in this study (see Table 4-5).

Table 4-5 : Structure dimension of fin thickness microchannel heat sinks

N	W_{ch} (µm)	Fin thickness (µm)
9	297	1221
13	297	715
17	297	462
25	297	209
33	297	82.5

Surface velocity contours for five different number of channels at different inlet velocities are shown in Figure 4-22. For similar inlet-velocities using a different number of channels can be seen to result in different velocity rates inside the channels. Therefore, different number of channels will produce different Reynolds numbers at a similar inlet velocity. The range of Reynolds numbers have been summarized in Table 4-6. From the tables, it can be concluded that fewer channels lead to higher range of Reynolds numbers due to large mass flow rate that needs to be distributed in every channel. It is also interesting to see from Figure 4-22 that the velocity contours in the inlet and outlet manifold show different profiles for different channel numbers. Fewer channels separated by thicker fins cause a large circulation at the upstream of the outlet manifold area.

Vi=0.03m/s

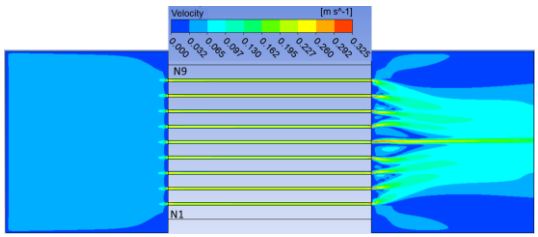

Vi=0.0645m/s

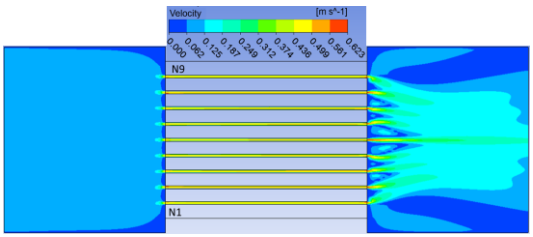

Vi=0.1133m/s

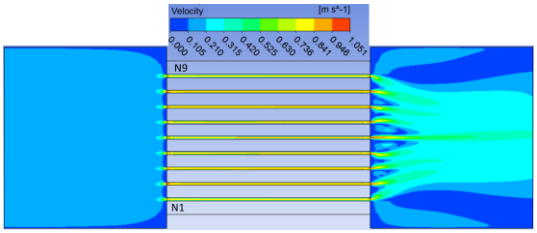

(a)

Vi=0.03m/s

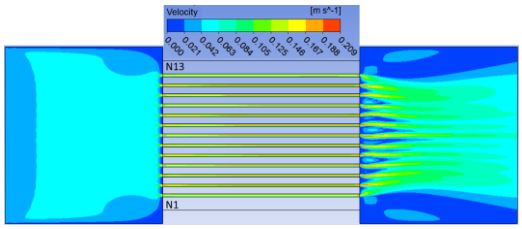

Vi=0.0645m/s

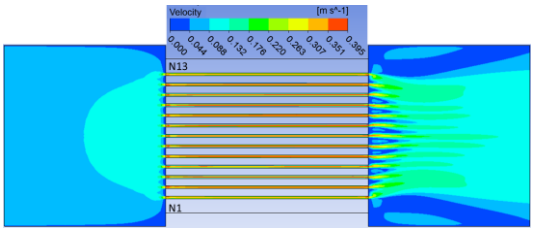

Vi=0.1133m/s

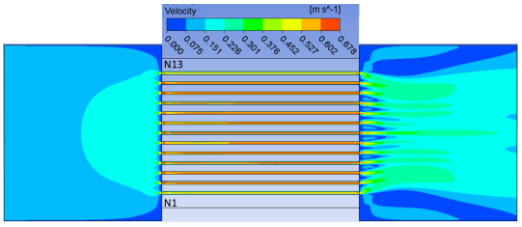

(b)

Vi=0.03m/s

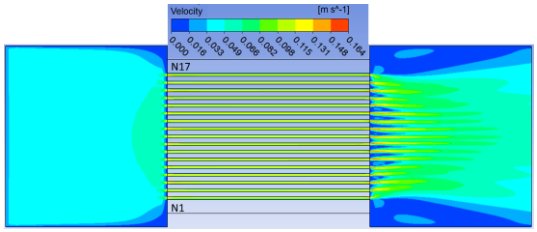

Vi=0.0645m/s

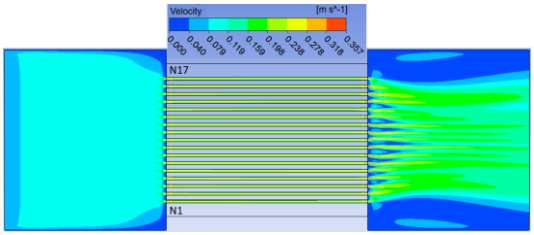

Vi=0.1133m/s

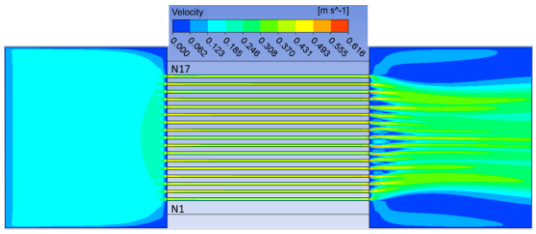

(c)

Vi=0.03m/s

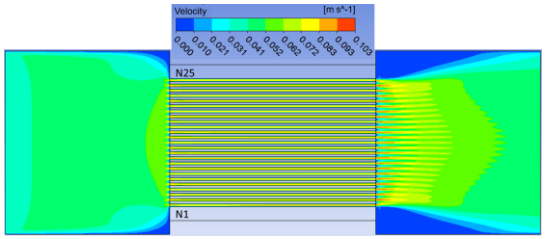

Vi=0.0645m/s

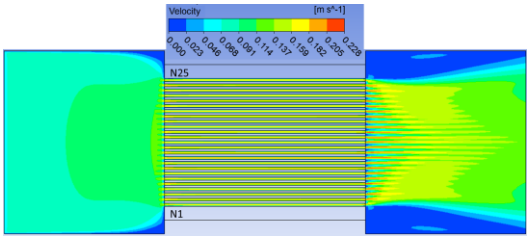

Vi=0.1133m/s

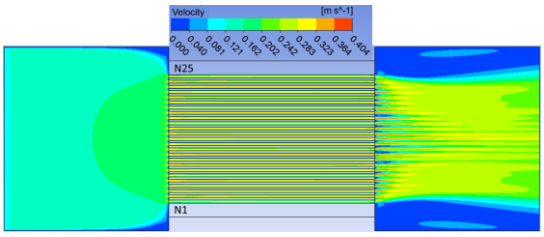

(d)

Vi=0.03m/s

Vi=0.0645m/s

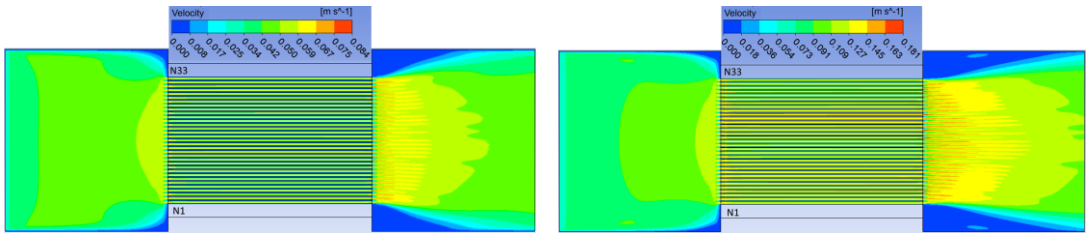

Vi=0.1133m/s

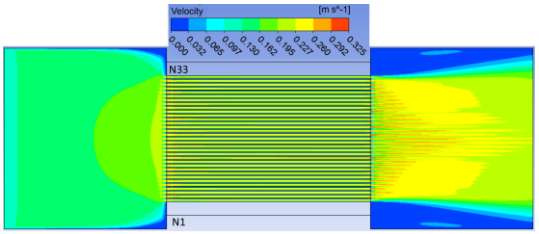

(e)

Figure 4-22 : Surface velocity contour for (a) N=9, (b) N=13, (c) N=17, (d) N=25, (e) N=33.

The comparison of normalized flow distribution against number of channel (N_i/N_{max}) for three different inlet velocities (a)V_i =0.03m/s, (b)V_i =0.0645 m/s and (c) V_i =0.1133m/s. As expected, the channels located at the edge of microchannels area (the first and last channels) showed a lower flow ratio compared to the others, which is due to the large losses occurring at the sharp corners of the inlet manifolds as discussed in previous section.

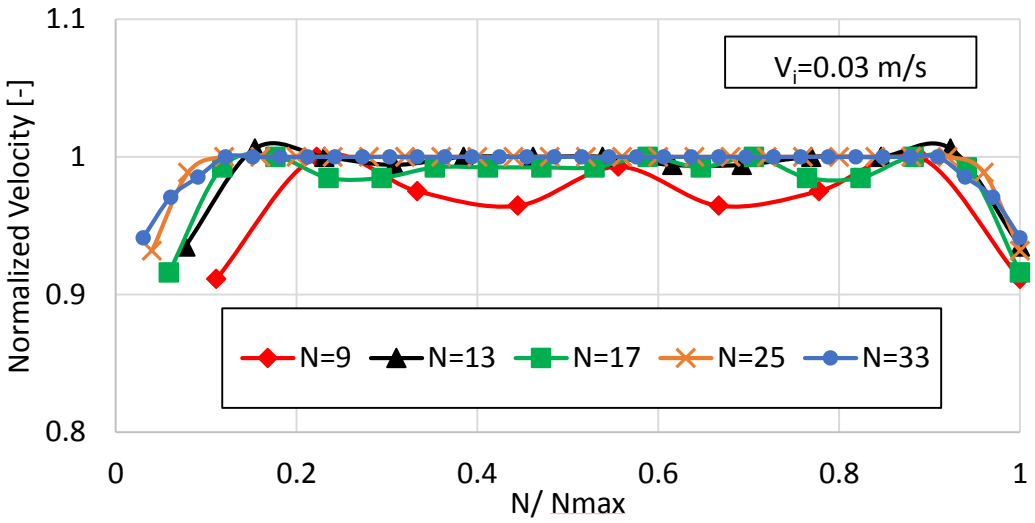
1.1
1
0.9
0.8
Normalized Velocity [-]
V$_i$=0.03 m/s
N=9
N=13
N=17
N=25
N=33
0
0.2
0.4
0.6
0.8
1
N/ Nmax

(a)

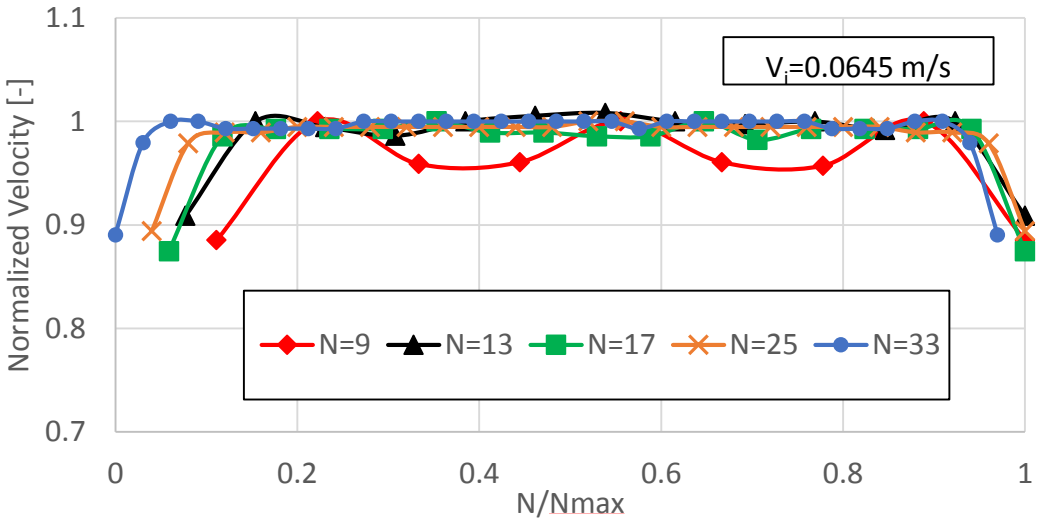
1.1
1
0.9
0.8
0.7
Normalized Velocity [-]
V$_i$=0.0645 m/s
N=9
N=13
N=17
N=25
N=33
0
0.2
0.4
0.6
0.8
1
N/Nmax

(b)

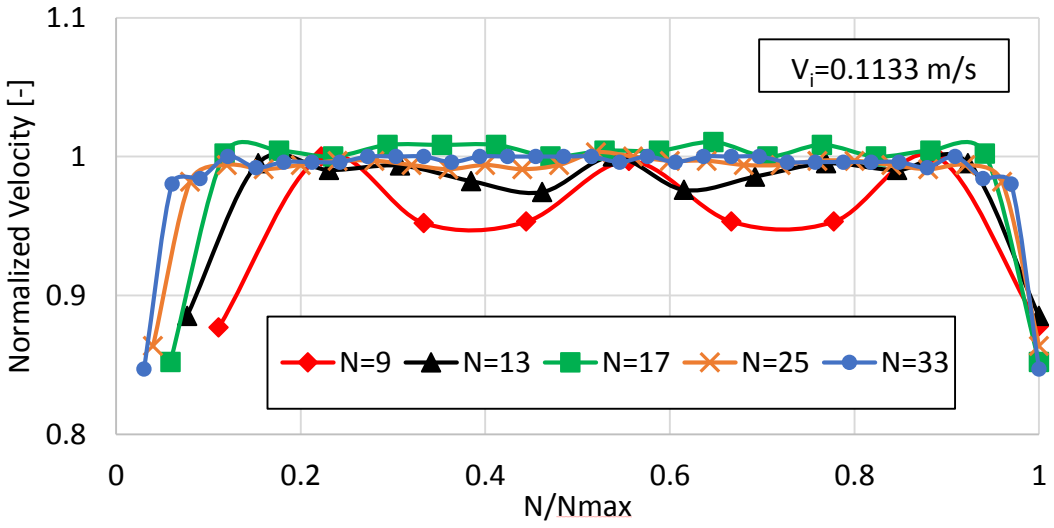

(c)

Figure 4-23 : Comparison of normalized velocity distribution profile within channels for (a)V_i =0.03m/s, (b)V_i =0.0645 m/s and (c) V_i =0.1133m/s

The maldistribution factor (MF) has been quantified and is summarized in Figure 4-6 to show the significant effect of the number of channels on the flow distribution at different inlet velocities. As mentioned earlier, lower values of MF are associated to a better flow uniformity among the channels. The flow maldistribution is found to increase with the inlet velocity, resulting in higher Reynolds numbers. Similar results were found in Siva *et al*. (2014) and Lu and Wang (2006) where for higher Reynolds number the friction factor is smaller, leading to more non-uniformity.

Table 4-6 : Comparison of maldistribution factor (MF) for trapezoid, rectangular and proposed manifold.

Number of Channel (N)	Velocity inlet (m/s)	Re (-)	MF (-)
9	0.03	1218	0.026
	0.0645	2428	0.035
	0.1133	4143	0.037
13	0.03	696	0.025
	0.0645	1427	0.035
	0.1133	2392	0.042
17	0.03	426	0.026
	0.0645	904	0.040
	0.1133	1555	0.052
25	0.03	382	0.019
	0.0645	807	0.028
	0.1133	1379	0.037
33	0.03	223	0.016

	0.0645	475	0.027
	0.1133	828	0.037

Figure 4-24 shows the maldistribution factor as a function of number channels. Two phenomena can be observed. Firstly, when the number of channels increases from N=9 to N=17, the flow maldistribution increases. These results are in accordance with Siva *et al*. (2014), Siva *et al*. (2013), Pistoresi *et al*. (2015) and Kumaraguruparan *et al*. (2011), who reports that flow maldistribution could easily be reduced by limiting the number of channels. However, it is worth mentioning that, the maximum number of channels in the stated studies was limited to twenty. Furthermore, it may be observed that the difference on the flow distribution uniformity between cases N=9 and N=13, is relatively small given inlet velocities of less than 0.0645m/s. However, the value of MF increases rapidly with an increasing number of channels at high inlet velocity conditions. (V_i =0.1133m/s).

On the other hand, for the cases where the number of channels exceeds twenty, it is seen that the value of the maldistribution parameter again reduced and only small changes were observed in MF compared to the situation at N=33. A similar study was conducted by Lu and Wang, (2006), who studied the effect of the number of channels for large N (N=20, 40, 60). They reported that the maldistribution parameter reduces with increasing number of channels.

Therefore, based on the results presented above, there are two different conclusions that may be reached from this study. Firstly, the maldistribution value was found to increase as the number of channels increases when the number of channels is less than twenty. In contrast, if the number of channels exceeds twenty, the maldistribution value reduces with increasing number of channels.

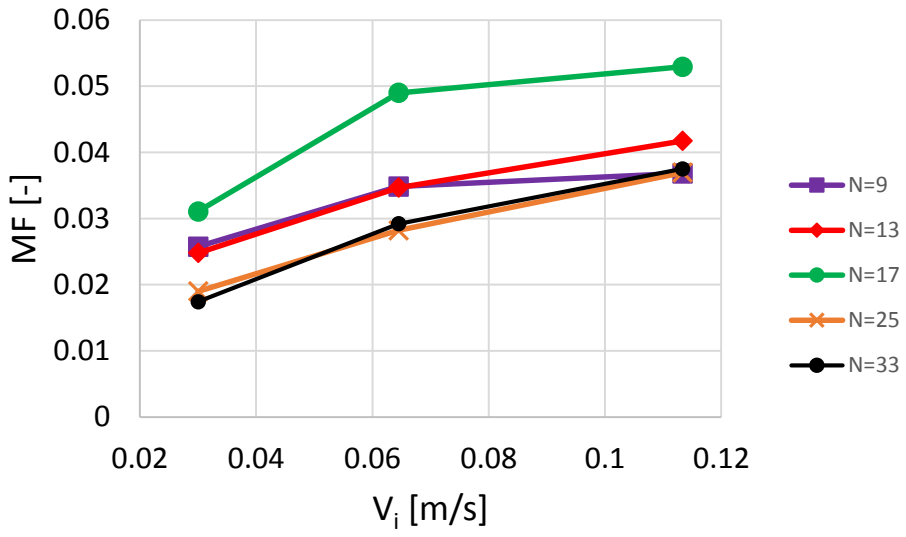

Figure 4-24 : Maldistribution factor of (a) N=9, (b) N=13, (c) N=17, (d) N=25, (e) N=33 at different velocity inlet conditions.

4.2.5 Proposed manifold design

The manifolds design (Figure 4-25 (a) Trapezoid (b) Rectangular) appear to cause a flow restriction at the lateral edges resulting in reduced flow rates in the channels in this region. As discussed in previous section, this phenomenon is due the large losses at sharp corners of the inlet manifold. Therefore, to examine the significant influence of the separated flow occurring at the sharp corner in the inlet manifold on the flow distribution inside the microchannels, a heat sink with a curve edge (shown in Figure 4-25(c)) was investigated numerically. The dimensions of the heat sink and associated boundary conditions are kept the same as in previous section, so the only difference is the shape of the manifold.

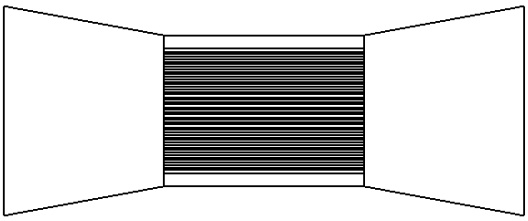

(a)

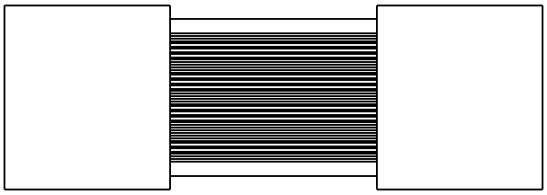

(b)

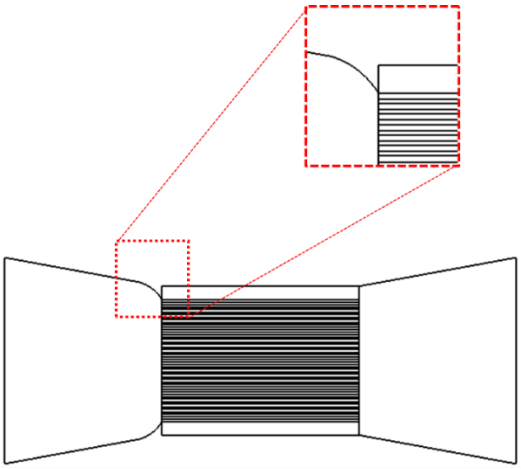

(c)

Figure 4-25 : Schematic diagram of (a) Trapezoid manifold (b) Rectangular manifold (c) Proposed manifold.

Figure 4-26 shows the normalized velocity for three different manifolds design at the velocity inlet (a) Vin=0.030 m/s (b) Vin=0.0645 m/s (c) Vin=0.1133 m/s. A small flow maldistribution was observed at the lower flow rate. However, a significant flow maldistribution was observed at higher flow rate. Once again, for all three cases, the

channels near the centerline having a greater flow ratio compared to the channels near the lateral edges of the heat sink. At a higher velocity inlet, the relative difference between the maximum and minimum flow ratio through the channels is approximately 12%, 13%, 6 % for trapezoid manifold, rectangular manifold and modified manifold, respectively.

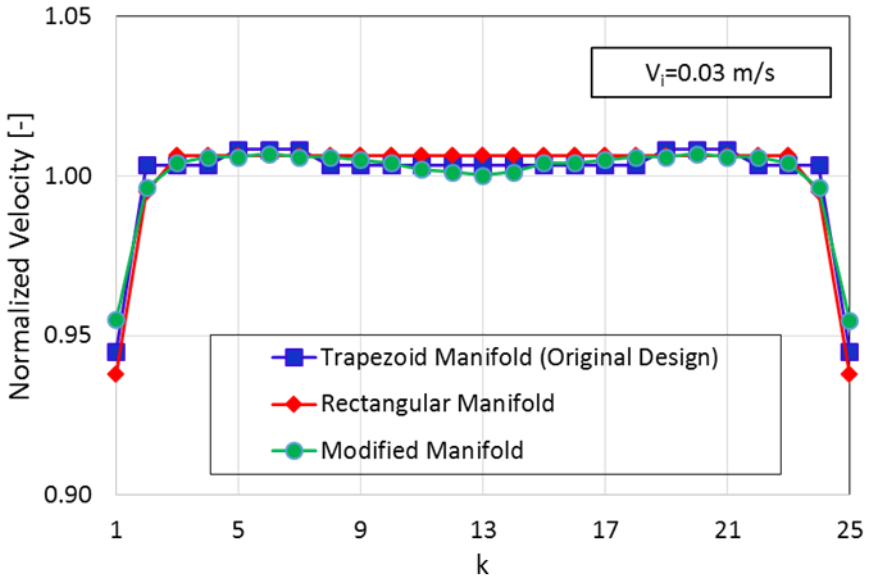

(a)

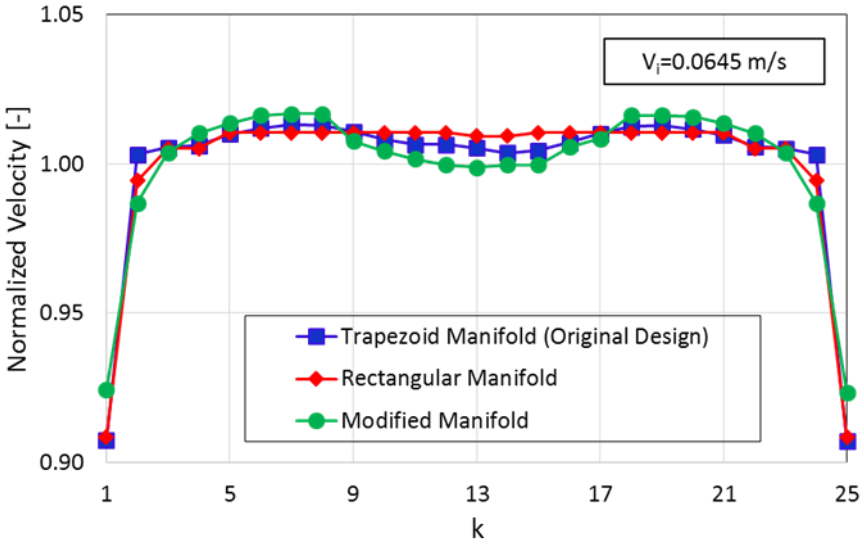

(b)

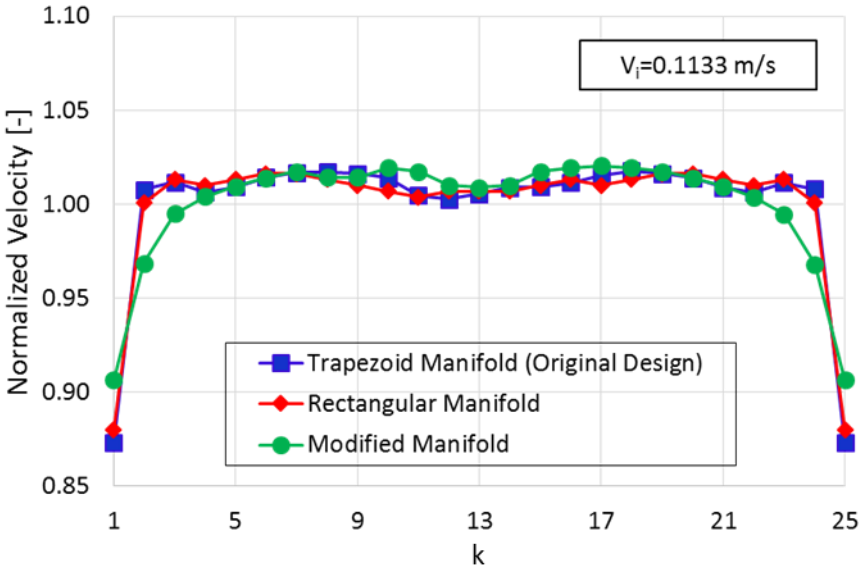

(c)

Figure 4-26 : Normalized velocity in each channel of (a) Trapezoid manifold (b) Rectangular manifold (c) Proposed manifold at different inlet conditions ; (a) V_{in}=0.030 m/s (b) V_{in}=0.0645 m/s (c) Vin=0.1133 m/s.

Therefore, to quantify the flow distribution for all three cases at various velocity inlet conditions, the value of MF has been evaluated and plotted in Figure 4-27. Based on Figure 4-27, MF indeed increases when inlet velocity increases. It is also interesting to note that the modified manifold clearly provides a better uniform flow distribution through the heat sink, with maldistribution factors 0.014, 0.025, and 0.032 at inlet velocities 0.03 m/s, 0.0645 m/s and 0.1133 m/s, respectively, compared to the other two. Note that only small differences are observed between the trapezoid manifold and the rectangular manifold.

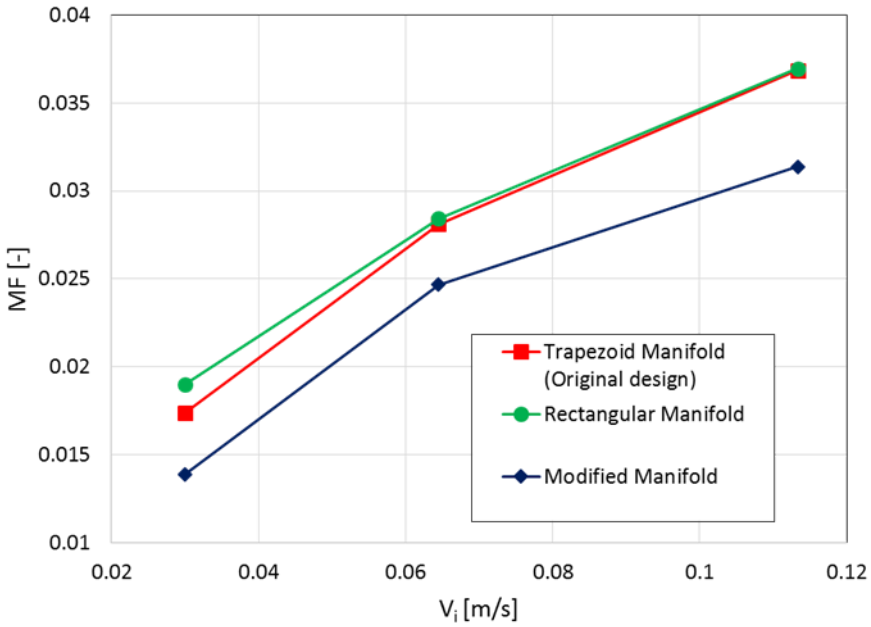

Figure 4-27 : Maldistribution factor for different inlet manifolds at various inlet velocity conditions.

The reasons for the better flow performance of the proposed manifold design are clearly illustrated in Figure 4-28. As mentioned previously, the formation of secondary flow (see Figure 4-28 (a) Trapezoid manifold and (b) Rectangular manifold) at corners in the inlet manifold was identified as the root cause of the reduction of flow ratio in the channels at the lateral edges. As noted earlier by Jones *et al*. (2008) a recirculation region identified in the inlet manifold constricts the available space into which the fluid is distributed, which resulting in higher localized velocities and larger pressure drops within the manifold. The fluid feeding the channels near the centreline has a more direct path through the manifold, so that the central channels receive a larger portion of the flow than channels near the lateral edge.

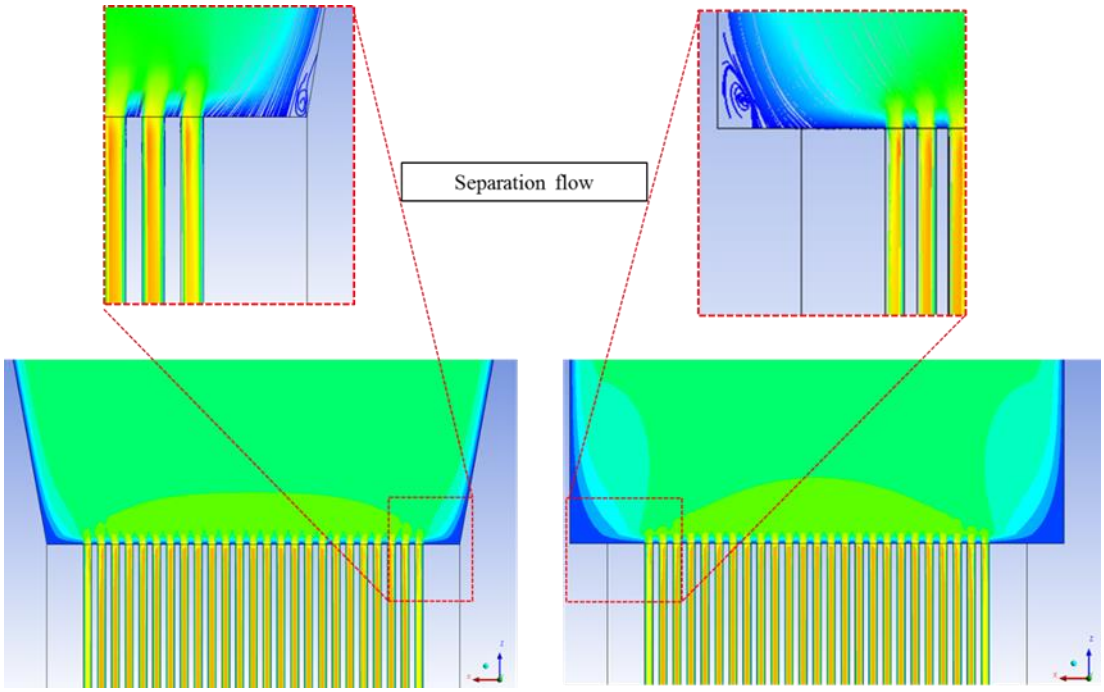

(a) (b)

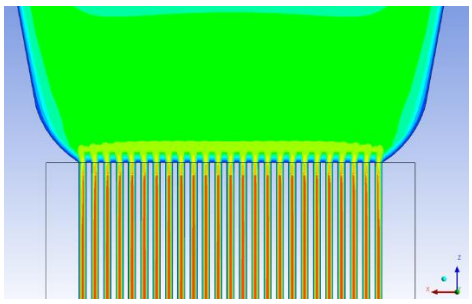

(c)

Figure 4-28 : Velocity contour in the inlet manifold (a) Trapezoid manifold (b) Rectangular manifold (c) Proposed manifold.

However, the numerical results for the proposed manifold indicate that there is no secondary flow occurring in the inlet manifold so that the mass flow rate remains almost the same in all channels. In fact, the relative difference in mass flow rates reduces to 6%. Similar results were found by Siddique *et al*. (2017), hence, it can be concluded that the proposed manifold distributes flow more uniformly in channels than the other collector shapes considered.

4.3 Summary

In this chapter, the numerical study was conducted to study the flow distribution inside a multichannel configuration with twenty-five parallel channels. The numerical study was carried out using R134a as a working fluid. As a validation of present numerical work, a detailed description of the experimental facility that was modelled was given in Fayyadh et al. (2015) and friction factor and Nusselt number were compared. Subsequently, the effect of various parameters such as, inlet/outlet area manifold, inlet/outlet flow arrangement and number of channels on the flow distribution inside channels was examined. The dimensionless channel flow ratio and flow maldistribution factor were introduced to quantify the flow distribution inside individual channels and the uniformity of this flow distribution. In the final part of this chapter, a newly design for the inlet manifold was proposed in this study, where edges with a curved shape were suggested in order to reduce the occurrence of flow recirculation at the sharp edges. This resulted in a better flow distribution over the parallel channels.

5 CFD MODELLING OF TWO PHASE FLUID FLOW AND HEAT TRANSFER IN MICROCHANNEL

5.1 Introduction

Numerical simulation can serve as a complementary method to predict the characteristics of bubble slug fluid flow and heat transfer with less expense. The design of numerical works pursued two aims. The first aim was to developed numerical flow regime maps in order to identify the slug flow boundaries in dependence on annular nozzles configurations and on liquid properties. In this work, the flow field has been calculated using a two dimensional, axisymmetric geometry due to save computational time and effort. Secondly, to examined the topology of hydrodynamic flow and heat transfer distribution of slug flow. Lastly, in the final part of this chapter the effect of gas superficial velocity on hydrodynamic and thermal behaviour of the bubble gas for unit cell. For this part, a three dimensional work was carried out.

5.2 Two phase flow pattern in 1 mm circular microchannel

5.2.1 Model description

A numerical flow patterns map for two phase flow in a vertical circular microchannel with a diameter of 1 mm under adiabatic conditions is produced by performing simulations for 82 different sets of flow conditions. The microchannel is modelled as a two dimensional axisymmetric domain of diameter D to save computational time and effort. The effect of gravity has been accounted for a schematic of the channel and the boundary condition applied is shown in Figure 5-1. The gas was introduced at the centre of the inlet, while simultaneously the liquid was entered in an

annulus around the gas core. A pressure outlet boundary condition was applied at the outlet. A non-slip boundary condition was employed at the wall. The superficial gas velocity ranges from 0.01 to 2 m/s, and the envelope of superficial liquid velocity ranges from 0.01 to 6 m/s. The two-phase flow of R134a in the channel is assumed to be incompressible, adiabatic and to possess constant physical properties.

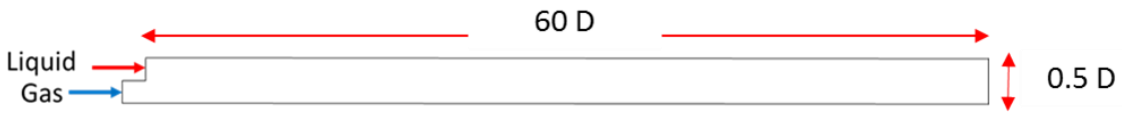

Figure 5-1 : Schematic representation of the geometry and boundary condition used in simulations.

Table 5-1 : Properties of gas and liquid used in simulation**s.**

	Density, $\frac{kg}{m^3}$	Viscosity, $\frac{kg}{ms}$	Surface tension, $\frac{N}{m}$
R134a (Liquid)	1149	0.0001625	0.006207
R134a (Gas)	49.23	0.00001265	-

A structured mesh as shown in Figure 5-2 was used for the simulations. As recommended by Gupta *et al*. (2010a) and Talimi *et al*. (2012), to capture the liquid film, the mesh is refined closed to channel wall. Talimi *et al*. (2012) to get accurate shear stress distribution on the wall and heat transfer from the wall to the flow. In addition, Gupta *et al*. (2010a) suggested that the mesh elements with aspect ratio of one is the best element used at the center of the channel, where the gas bubble break-off, which giving rise to significant variation in surface tension force and it direction.

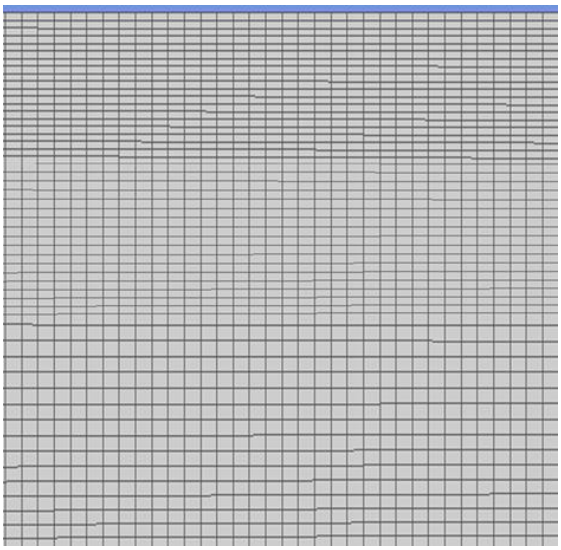

Figure 5-2 : The computational mesh used in the simulations. The mesh is refined near the wall (top of figure) to capture liquid film.

Three different meshes consisting of different number of nodes, 300,000 (Grid 1), 675, 000 (Grid 2), and 1,200,000 (Grid 3) number of nodes was used. As can be seen from Figure 5-3, the velocity profile of liquid slug obtained by three meshes are almost the same, therefore mesh containing 675,000 nodes was choose for further simulations.

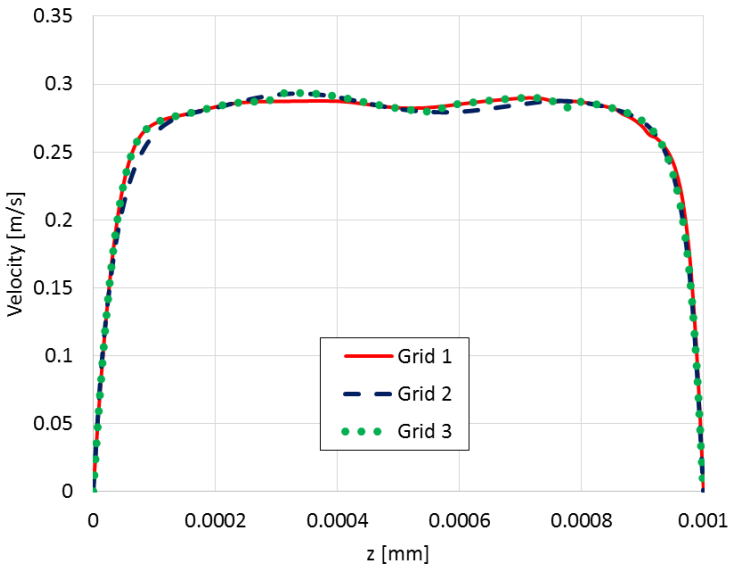

Figure 5-3 : Velocity profile for different mesh.

5.2.2 Governing equations

In the present work, the Volume of Fraction (VOF) method has been employed to model the two-dimensional, axisymmetric flow in a circular microchannel of 1 mm cross section. The continuity equation and momentum equation are given by:

Conservation of mass (continuity)

$$\frac{\partial \rho}{\partial t} + \nabla\left(\rho \vec{V}\right) = 0 \tag{5-1}$$

Conservation of momentum

$$\frac{\partial \rho}{\partial t} + \vec{V} \cdot \nabla\left(\rho \vec{V}\right) = -\nabla p + \nabla \cdot \left(\mu \nabla \vec{V}\right) + \rho g \; + \boldsymbol{F}_{\sigma} \tag{5-2}$$

The continuum surface force (CSF) model of Brackbill *et al*. (1992) was used to model the surface tension. According to the CSF model, a source term was added to the momentum equation:

$$\boldsymbol{F}_{\sigma} = \sigma \frac{\alpha_l \rho_l \kappa_g \nabla \alpha_g + \alpha_g \rho_g \kappa_l \nabla \alpha_l}{\left(\rho_l + \rho_g\right)/2} \tag{5-3}$$

Where σ is the surface tension, $\alpha_l$is the liquid farction, α_g is the void fraction, ρ_l is the liquid density, ρ_g is the gas density and κ is the curvature which was computed from the divergence of the unit surface normal vector **n**:

$$\kappa = \nabla \cdot \mathbf{n} = \nabla \cdot \frac{\mathrm{n}}{|\mathrm{n}|} \tag{5-4}$$

The surface normal vector n is defined as the gradient of α_q, where α_q is the volume fraction of the q^{th}phase.

$$n = \nabla \alpha_q \tag{5-5}$$

The VOF method is utilized to capture the movement of the gas–liquid interface on a Eulerian computational grid, where a volume fraction, α, is defined to identify each phase. It represents the ratio of the cell volume occupied by the primary phase and hence ranges from 0 to 1.where α_G = 1 α_L = 0) in the gas phase and α_G = 0 (α_L = 1) in the liquid phase. Therefore, the gas–liquid interface exists in the cells where α_G lies between 0 and 1.

The volume fraction α_G could be obtained by solving a continuity equation for the volume fraction:

$$\frac{\partial \alpha_G}{\partial t} + \vec{V} \cdot \nabla(\rho \alpha_G) = 0 \tag{5-6}$$

5.2.3 Flow solver

The simulations are performed in commercial CFD solver ANSYS Fluent (release 17.1) and the simulation are run in a transient mode. The pressure-based solver option was used. The volume fraction equation is solved implicitly, and the standard finite difference interpolation method is applied to calculate the volume integral value in the current time step. In addition, under the convergent condition, the second-order upwind scheme is used for the momentum equation, turbulent kinetic energy equation and turbulent diffusivity equation in order to improve calculation accuracy. The PRESTO method is used for the discrete pressure, and the flow field is solved by means of the SIMPLE method which is a pressure-velocity coupled scheme. An implicit second order scheme was used to integrate the momentum and energy conservation equations in time and third order schemes were used for their spatial discretization. The time step is set between $1x10^{-5}$ to $1x10^{-7}$ s, which ensured the convergence of calculation to be relatively stable and sufficiently assure the accuracy

of the simulation results. A variable time-step is computed by the solver based on a maximum Courant number of 0.25.

5.2.4 Results and discussion

5.2.4.1 Model validation.

A two-dimensional axisymmetric simulation of flow patterns inspired by the work of Chen *et al*. (2006) was carried out. Chen and co-workers conducted an experimental study of flow patterns in R134a vapour–liquid two-phase flow in vertical small-diameter tubes. In order to validate the accuracy of the numerical method, the present results are verified through comparison with the visualization results obtained in the experiments of Chen *et al*. (2006) (see Figure 5-5). The selected flow parameters for the verification studies are listed in Table 5-2 and are plotted in Figure 5-4. Most of the chosen points were located near to the predicted transition boundaries of the flow patterns as suggested by Chen *et al*. (2006).

Table 5-2 : Flow operating conditions of numerical simulation study for model verification

Case	U_{GS}	U_{LS}	Flow patterns
1	0.01	0.12	Bubble
2	0.05	0.40	Bubble
3	0.19	0.94	Bubble
4	0.02	0.06	Bubble-Slug

5	0.18	0.06	Slug
6	0.1	0.12	Slug
7	0.23	0.12	Slug
8	0.29	0.4	Slug
9	0.9	2	Slug-annular
10	0.9	0.94	Slug-annular
11	1	0.4	Slug-annular
12	0.5	0.12	Slug-annular
13	1.53	0.06	Annular
14	2.62	0.94	Annular
15	2.16	0.4	Annular
16	1.53	0.12	Annular

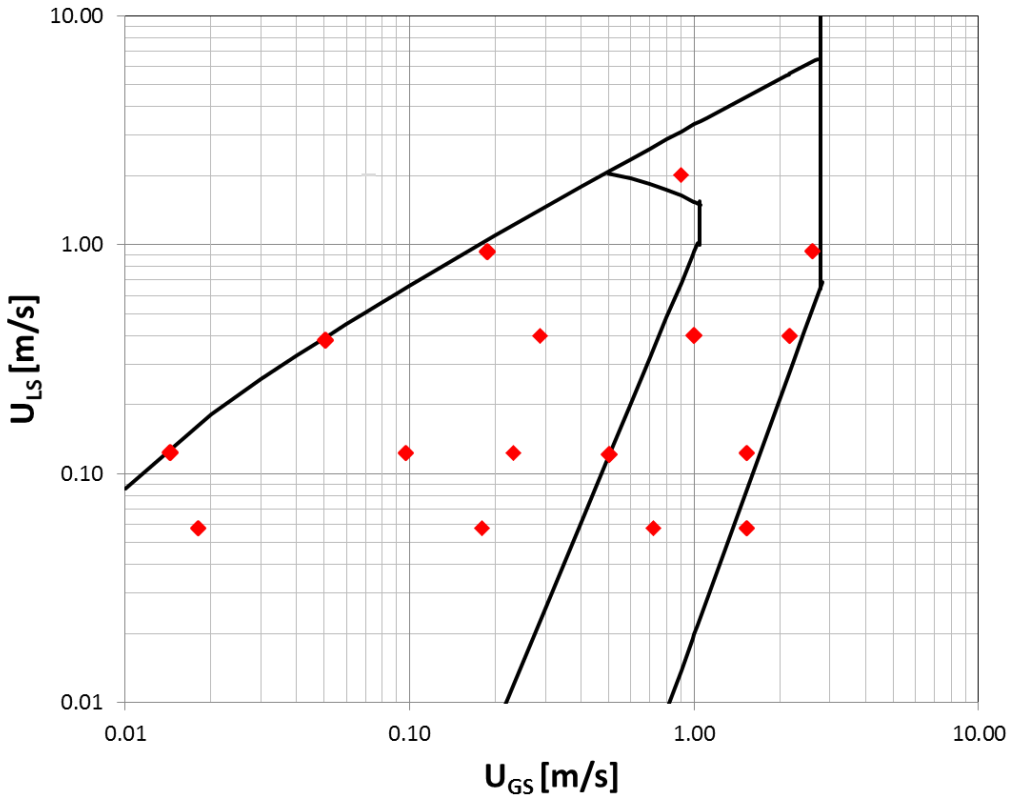

Figure 5-4 : Numerical simulation conditions cases for model validation on the flow pattern map of Chen *et al.* (2006).

The flow patterns obtained in the cases selected for the verification study showed an agreement with the predicted flow pattern map provided by Chen *et al*. (2006). A comparison of the present visualization results with the experimental results provided by Chen *et al*. (2006) is illustrated in Figure 5-5. In both the simulations and the experiments the same flow patterns were obtained under the same work conditions. It can be seen that the numerical visualizations results provided are in a good agreement with experimental results of Chen *et al*. (2006). Therefore, it can be concluded that the numerical method used in this study is capable of accurately capturing the gas–liquid interface. However, the terminology of flow patterns used in study is differs slightly from the ones used by Chen *et al*. (2006). For example, the

confinement flow (see Figure 5-5 (b)) and churn flow (see Figure 5-5(d)) regimes are not always applicable for the flow patterns found in this study. The flow pattern characteristics observed in this study will be discussed in more detail in the next section.

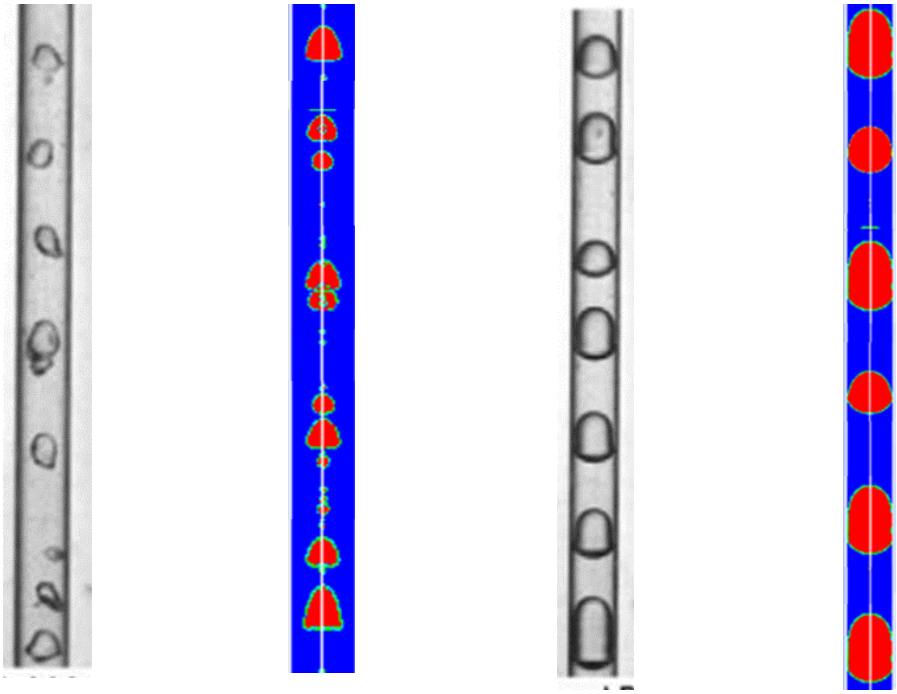

(a) (b)

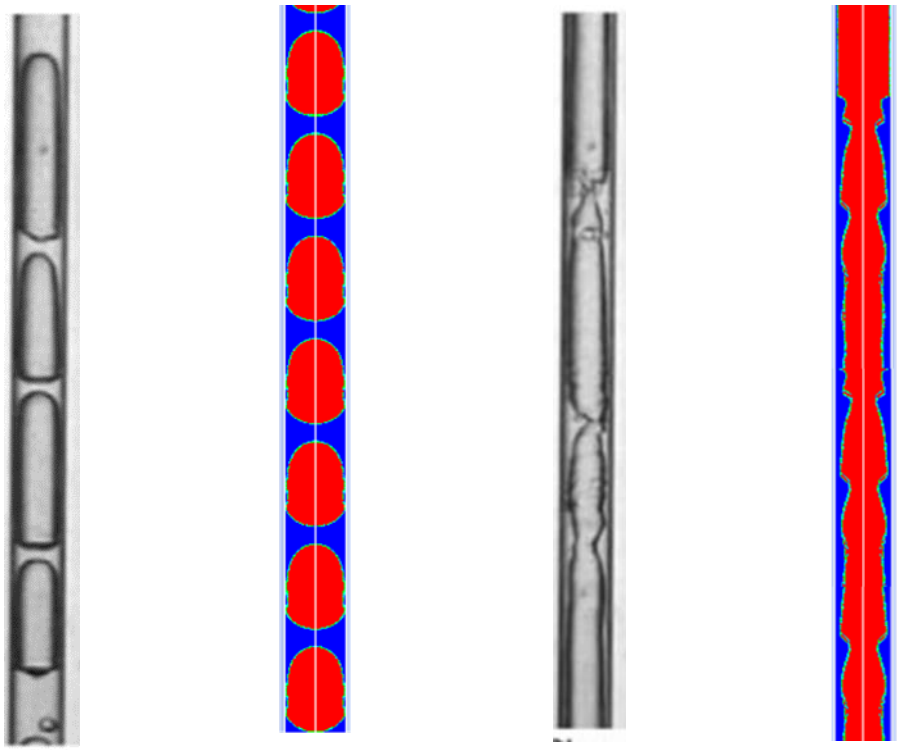

(c) (d)

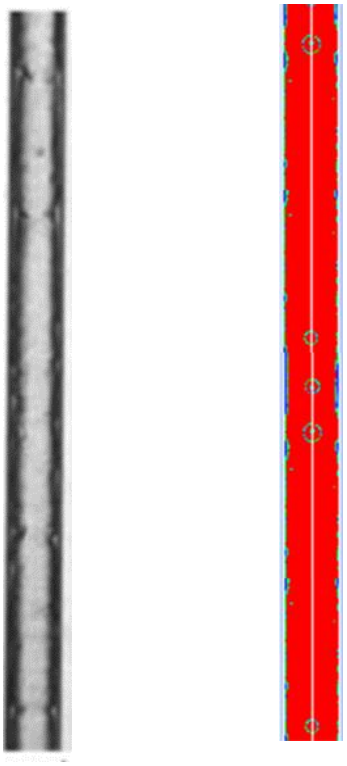

(e)

Figure 5-5 : The flow patterns of obtained in the numerical simulation validation runs: (a) bubbly flow; (b)-(c) slug flow; (d) slug-annular; and (d) annular flow.

5.2.4.2 Characteristics of two-phase flow

The R134a two-phase flow in the circular microchannel of 1 mm diameter are simulated. Different flow patterns were obtained by varying the inlet flow rates of liquid and gas. The setup of the numerical simulations was in accordance with the experiments conducted by Chen *et al*. (2006) and a reasonable agreement was obtained between the visualized flow patterns obtained in the numerical simulations and those obtained by Chen *et al*. (2006). Therefore, it can be concluded that the numerical method used in this study is capable of predicting the flow patterns for the two phase flow of R134a in a circular microchannel.

One of the major problems in the visualization study of flow patterns in two phase flow are inconsistencies in the flow pattern terminology which lead to discrepancies of inflow pattern maps reported in the open literature, Mahmoud and Karayiannis (2016). The terminology, used in this study to classify the obtained flow regimes is based on the terminology used by Triplett *et al*. (1999). As shown in Figure 5-9, four typical flow patterns, namely bubbly flow, slug flow, slug-annular flow and annular flow are observed. The description of the flow patterns occurring in this study is given below.

a) **Bubbly flow**: Figure 5-9 shows the numerical results of bubbly flow in this study. As illustrated in the present study, in this regime two different bubble shapes can be observed: spherical bubbles Figure 5-6 (a)-(c)) and bubbles with a cap shape (Figure 5-6 (d)-(e)). The spherical bubbles were flowing in the centre of the tube having a diameter smaller than the channel size, suggesting

the dominance of the surface tension force, which The tends to minimize the surface free energy by reducing the surface area. In this region (U_{GS} < 0.06 m/s), the shape of bubbles and the distance between adjacent bubbles along the channel is regular. However, bubbles flowing at U_{GS} > 0.07 m/s were observed to behave differently and exhibited a cap-shaped head. Furthermore, in this region, the size and the shape of the bubbles is inconsistent.

b)

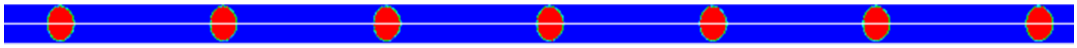

$U_{GS} = 0.01\ m/s$ $U_{LS} = 0.12\ m/s$

(a)

$U_{GS} = 0.03\ m/s$ $U_{LS} = 0.4\ m/s$

(b)

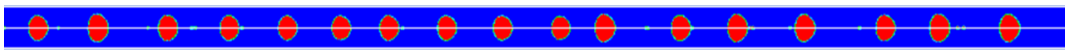

$U_{GS} = 0.07\ m/s$ $U_{LS} = 0.6\ m/s$

(c)

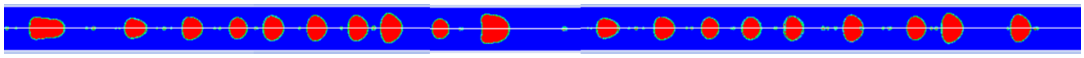

$U_{GS} = 0.09\ m/s$ $U_{LS} = 0.94\ m/s$

(d)

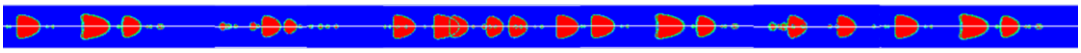

$U_{GS} = 0.18\ m/s$ $U_{LS} = 2.02\ m/s$

(e)

Figure 5-6 : Bubble flow patterns for R134a in 1mm circular microchannel

c) **Slug flow:** The size of the bubbles enlarges up to the diameter of channel with the increase of U_{GS}. As seen in Figure 5-7, the shape of the enlarged bubble looks like a bullet where the head of the bubble slug is hemispherical with a smooth cylindrical body in the middle and a generally flat tail. The vapour phase was separated from the tube wall by a thin liquid film surrounding the bubble slug. Furthermore, two slug bubbles, which are also known as Taylor bubbles, are separated by liquid slugs (or liquid bridges). It is worth mentioning that at U_{LS} <0.12 the distance between the bubbles and their shape are almost identical, (see Figure 5-7(a)-(b)). As the superficial gas velocity,U_{GS}, increases the length of the Taylor bubbles increases. A similar behaviour is also observed in the slug region, where the distance between the bubbles slug become inconsistent at higher superficial liquid speeds (U_{LS} > 0.22). The reason for this is that increases in the liquid flow rate causes some of the slug bubbles to merge.

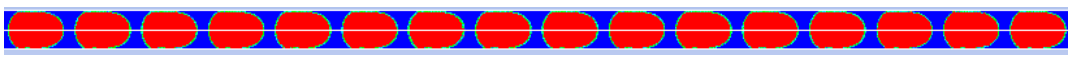

$U_{GS} = 0.1\ m/s$ $U_{LS} = 0.06\ m/s$

(a)

$U_{GS} = 0.23\ m/s$ $U_{LS} = 0.12\ m/s$

(b)

$U_{GS} = 0.29\ m/s$ $U_{LS} = 0.22\ m/s$

(c)

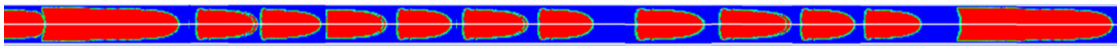

$U_{GS} = 0.29\ m/s$ $U_{LS} = 0.6\ m/s$

(d)

$U_{GS} = 0.29\ m/s$ $U_{LS} = 0.94\ m/s$

(e)

Figure 5-7 : Slug-flow patterns for R134a in 1 mm circular microchannel

d) **Slug-annular flow**: As shown in Figure 5-5(d), given similar inlet conditions, the present slug-annular flow was found to be in good agreement with the flow pattern observed by Chen *et al*. (2006), who, however identified the observed pattern as churn flow. Generally, the churn flow is considered to be chaotic, which was not observed in the present study. Instead, a gas core, surrounded by a large-amplitude waves liquid film (see in Figure 5-8) was observed. This flow pattern is a transitional regime that is obtained from slug flow by increasing the gas velocity and is called slug-annular flow. The flow pattern develops from merging elongated slug flow patterns where, as the gas flow rate increases, the length of bubble slug increases leading to a decrease of the distance between two bubble slugs. As a result, the liquid slug becomes too short to stably separate two consecutive gas slugs. Gas slugs start to penetrate upstream liquid slugs and symmetrical equidistant liquid rings are constructed. Slug-annular flow is also known as Taylor-annular ,Shao *et al*. (2009), liquid ring , Serizawa *et al*. (2002), ring flow , Sur and Liu (2012) or throat-annular flow, Saisorn and Wongwises, (2015).

$U_{GS} = 0.5\ m/s$ $U_{LS} = 0.22\ m/s$

(a)

$U_{GS} = 0.29\ m/s$ $U_{LS} = 0.06\ m/s$

(b)

Figure 5-8 : Slug–annular flow pattern for R134a in 1 mm microchannel.

e) **Annular flow**: As shown in Figure 5-9, the characteristics of annular flow and Taylor-annual flow are almost identical when the channel is nearly filled with gas surrounded by a liquid film. However, the long waves disappear when the superficial gas velocity, U_{GS}, in the slug–annular flow increases. An oscillatory interface also occurred between the liquid film and the gas core. The annular flow pattern was found to be more stable than other flow patterns.

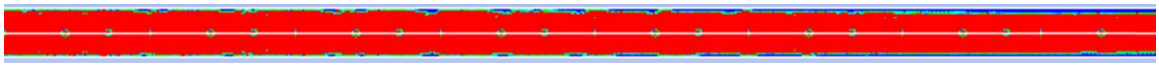

$U_{GS} = 1.53\ m/s$ $U_{LS} = 0.06\ m/s$

(a)

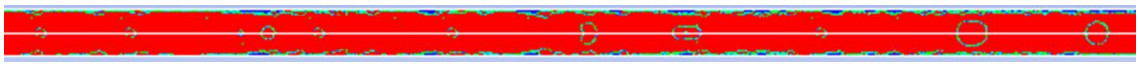

$U_{GS} = 1.53\ m/s$ $U_{LS} = 0.12\ m/s$

(b)

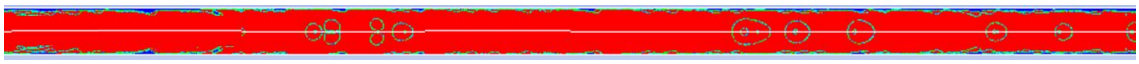

$U_{GS} = 2.16\ m/s$ $U_{LS} = 0.4\ m/s$

(c)

Figure 5-9 : Annular flow pattern for R134a in 1 mm microchannel

5.2.4.3 Flow regime maps

The flow pattern map of two-phase flow of R134a in the vertical circular microchannel with a diameter of 1 mm is depicted in Figure 5-10 . The horizontal and vertical axis represent the superficial gas velocity,U_{GS} and the superficial liquid velocity, U_{LS}, respectively. These data were based on the superficial gas and liquid velocities calculated at the entrance. The flow pattern maps can be roughly divided into several regions which include bubbly flow, slug flow, slug-annular flow and annular flow. According to the graph (see Figure 5-10), bubbly flow appears in high liquid superficial velocity ($U_{LS} > 0.1$) and low gas superficial velocity ($U_{GS} < 1$) and at increased U_{GS} for U_{LS} < 1, the transition to the slug flow starts to occur and the bubbly flow pattern transforms into a slug flow pattern.

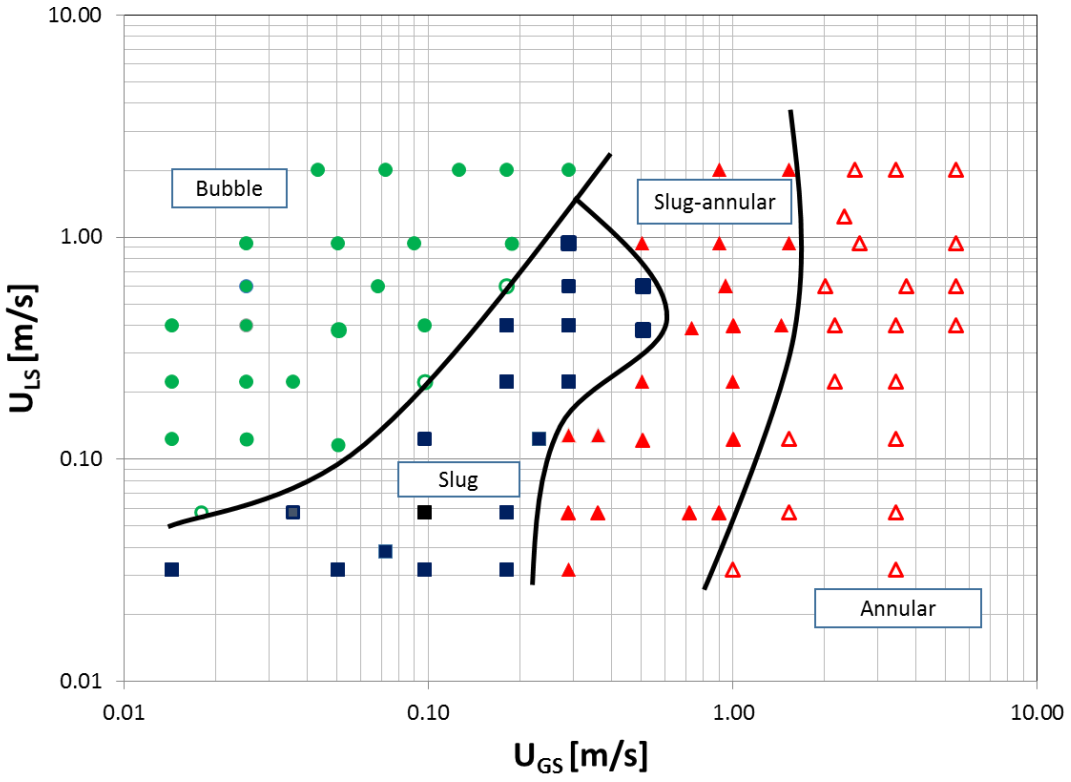

Figure 5-10 : Flow regime map for R134a (●-Bubble, ○-Bubble-Slug, ■- Slug, ▲ - Slug-Annular, △-Annular)

As seen in the above flow patterns maps generated from the numerical results, there are some points (flow patterns) that can be considered to be on the transitional line between bubble flow and slug flow, showing bubble-slug flow patterns. The transitional bubble-slug flow patterns were clearly shown in Figure 5-11, where unstable bubbles and bubbles slug were observed at the same times. The same phenomenon was also shown in the experimental work of Zhang *et al*. (2011). They identified such flow patterns as slug-bubbly or unsteady slug flow patterns. In the unstable slug flow regime, characterized by variable gas and liquid slug lengths, sometimes two or more trailing gas bubbles merge to form a bubble-train slug.

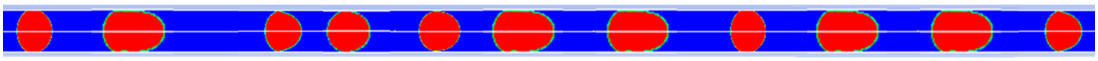

$U_{GS} = 0.02\ m/s$ $U_{LS} = 0.06\ m/s$

(a)

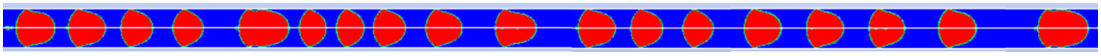

$U_{GS} = 0.1\ m/s$ $U_{LS} = 0.22\ m/s$

(b)

$U_{GS} = 0.18\ m/s$ $U_{LS} = 0.6\ m/s$

(c)

Figure 5-11 : Bubble-slug transition flow pattern for R134a in 1 mm microchannel.

In the flow pattern map, the slug-annular flow is a transitional flow pattern, and was observed before the annular flow. Annular flow is generally observed at a superficial gas velocity greater than 1 m/s. When the superficial liquid velocity is under 1 m/s, bubble flow, slug flow, slug-annular flow, and annular flow occurs sequentially with increasing superficial liquid velocity. When the superficial liquid velocity is greater than 1 m/s, bubble flow, slug-annular and annular flow are sequentially observed with the gradual increase of superficial gas velocity.

1. Comparison with existing flow regime maps.

As mentioned above, numerical simulations were performed to try and reproduce the flow patterns observed in the experiments of Chen *et al*. (2006). In order to verify the accuracy of the numerical method employed in this study, the numerically obtained flow patterns were compared to the flow regime maps provided by Chen *et al*. (2006). It was found that for the selected inflow conditions the observed flow patterns were in good agreement with the flow patterns observed by Chen *et al*. (2006). Below, numerically obtained flow patterns will be compared with existing flow regime maps. Figure 5-12 shows comparisons between the numerical results for all data ranges with the predicted flow patterns transition line suggested by Chen *et al*. (2006). As seen in this figure, a difference in the location of bubble-slug transition was identified compared to the numerical results, where, bubbly flow is predicted to occur at high liquid superficial velocity. Also, it is worth noting that, instead of churn flow, the slug-annular flow pattern was observed in the churn flow region as assigned in Chen *et al*. (2006), though it occurred slight earlier compared to the transition slug-churn or churn. However, the comparison between the visualization of the numerical results and the visualization of the experimental results provided by Chen *et al*. (2006) showed a reasonable agreement. Furthermore, the data set for annular flow also showed a good agreement with the predicted transition line suggested by Chen *et al*. (2006).

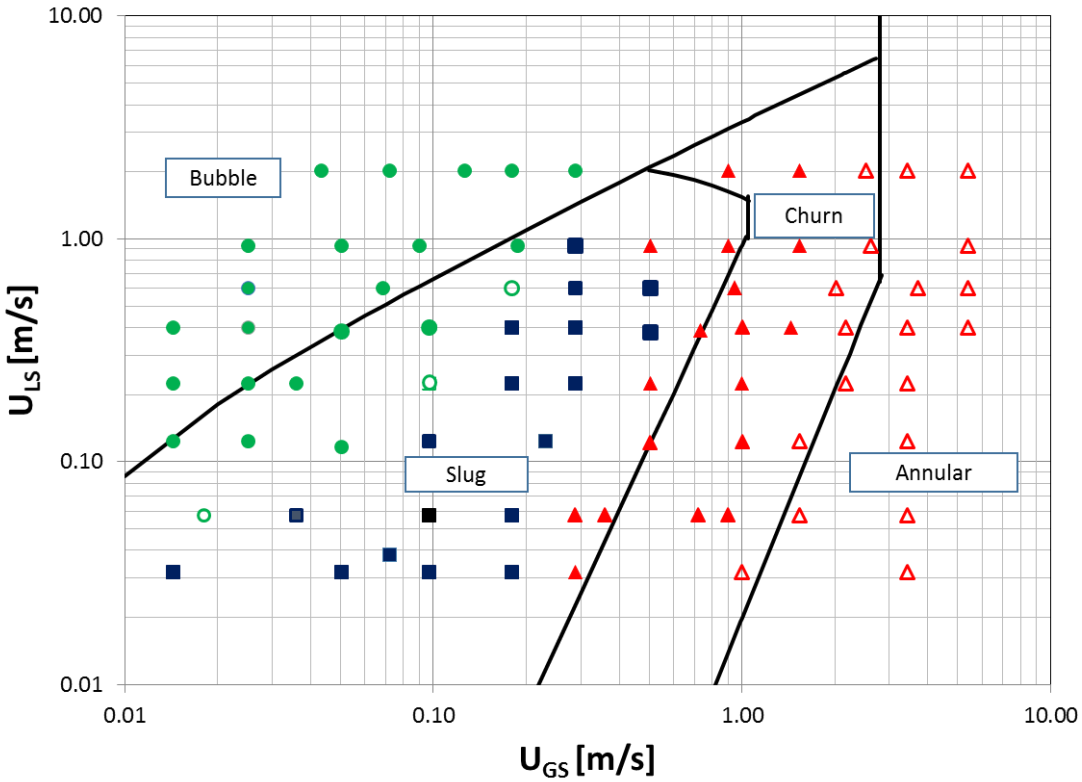

Figure 5-12 : Comparison of the present numerical results with the flow regimes maps of Chen *et al*. (2006) -solid line.

Figure 5-13 shows the comparison of flow maps obtained in this study with other flow regime transition maps found in the open literature. The dotted line expresses the flow pattern transition boundary by Triplett *et al*. (1999) and the solid line expresses the Chung and Kawaji (2004) transition line. Comparing the presented flow map with flow regime maps by Chung and Kawaji (2004) and Triplett *et al*. (1999), it can be seen that the transition line shows a similar trend, however, a major disagreement was found to occur between the locations of the slug and slug-annular regions where, the transition line was shifted to the left at lower U_{GS}. It is worth mentioning that disagreement between presented data could be related to the vertical orientation of the channel, as both researches were conducted in horizontally orientated channels. According to Shao *et al*. (2009) annular flow occurred earlier (low U_{GS})

compared to the horizontal channel due to a buoyancy effect resulting in a larger effect of inertia-assisted buoyancy over surface tension forces in a vertical channel. Additionally, due to the same reason, buoyancy effects in vertical channels favours bubble detachment at the inlet and assists the formation of small bubbles. As a result, the bubble flow regime was observed to be extended to lower U_{Ls} compared to the Chung and Kawaji (2004) and Triplett *et al*. (1999) transition lines. Furthermore, according to the flow regime transition suggested by both researches, churn flow was observed to occur at higher U_{Ls} than slug–annular flow. However, as noted from the previous section, churn flow didn't occur in the present study. Perhaps due to the limited size of the channel diameter in this study, the churn flow become less chaotic (as seen in Figure 5-5(d)) than stated by Karayiannis and Mahmoud (2017).

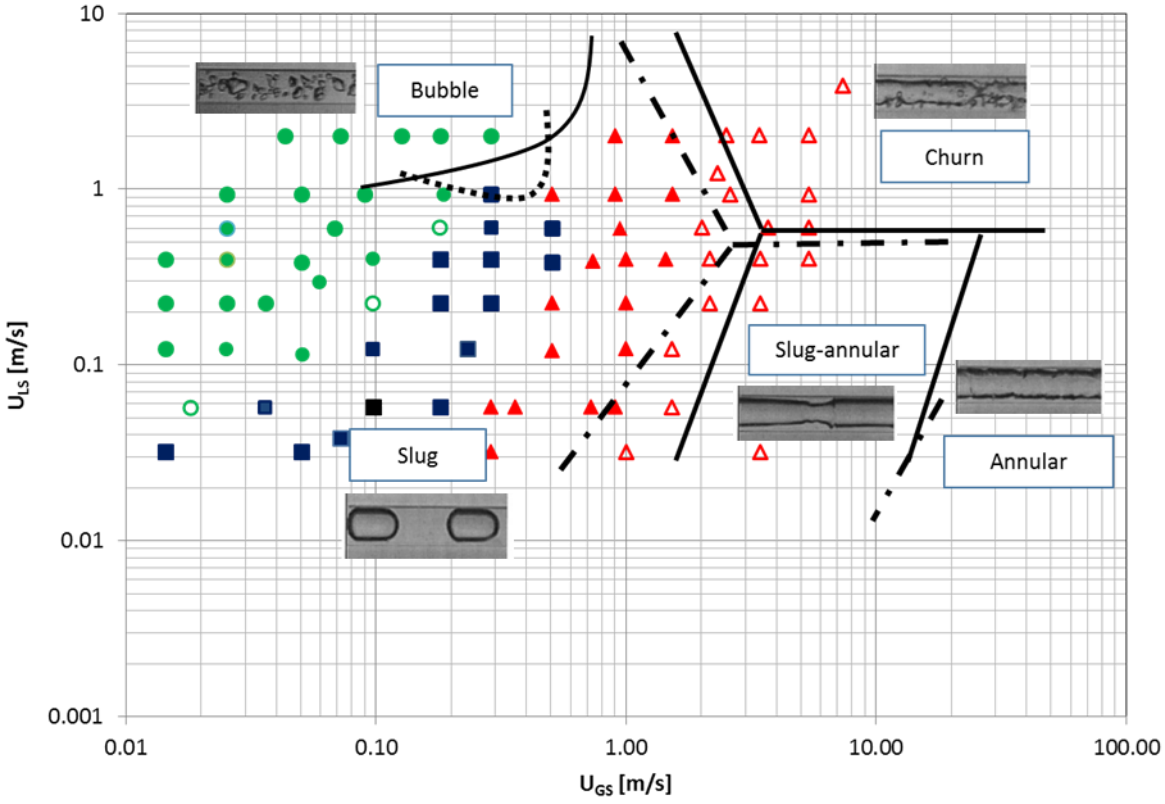

Figure 5-13 : Comparison of present numerical results with flow regimes maps of Chung and Kawaji (2004)-dotted line Triplett *et al*. (1999)-solid line.

Therefore, in order to approve the significant effect of channel orientation on flow regime maps, it is also worth to compare the present flow regime with the available flow regime maps in vertical flow orientation. Hassan *et al*. (2005) suggested that the effect of flow orientation on two phase flow regime map is significant. They also proposed a universal map for horizontal and vertical channel orientation flow. As shown in Figure 5-14, the transition between bubble and slug obtained in the present flow regime data was in agreement with the transition in the universal flow regime map for vertical orientation suggested by Hassan *et al*. (2005). However, opposed to the findings of Hassan *et al*. (2005) in the present study no churn flow was observed.

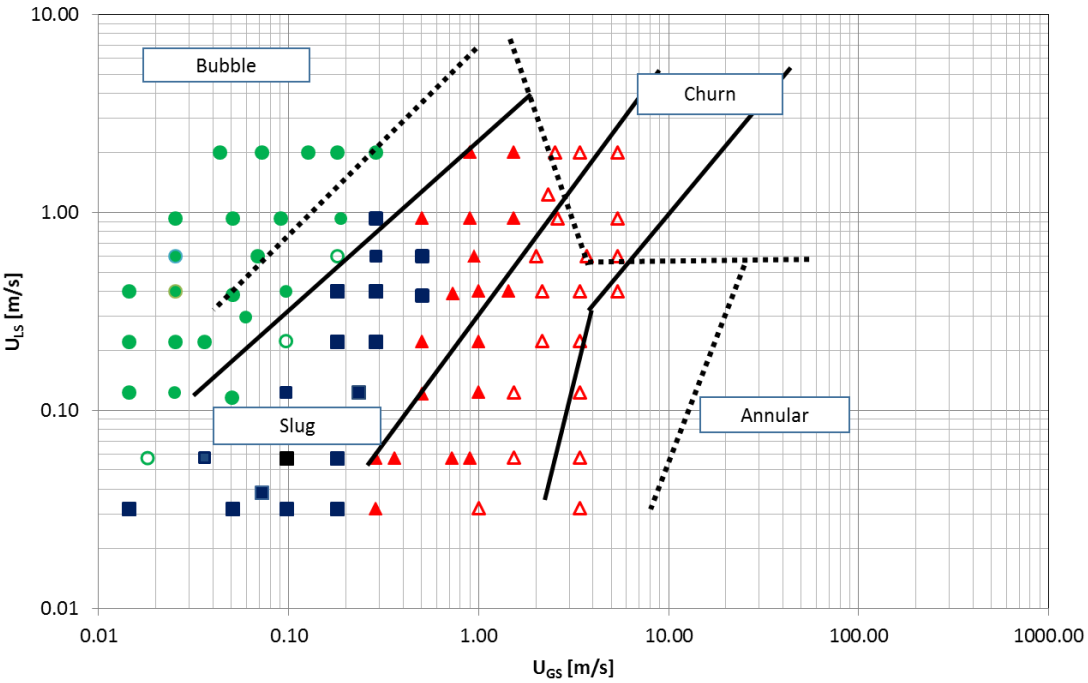

Figure 5-14 : Comparison of present numerical results with flow regimes maps of Hassan *et al*. (2005) for different orientations (Horizontal line-dotted line; Vertical - solid line).

The numerical study of flow regime maps in micochannels with a diameter less than 1 mm is rather time consuming limiting the number of available studies in the literature. Therefore, the present flow regime map is compared with the numerical

study conducted by Wei *et al*. (2017) simulating air-water in a rectangular narrow channel with 2 mm and 5 mm channel gap size. They developed a flow regime map using their own numerical results. Four typical flow patterns were observed, namely, bubbly flow, slug flow, churn-turbulent flow and annular flow. According to Figure 5-15, the result showed satisfactory agreements with the smallest channel gap data obtained by Wei *et al*. (2017), especially when focussing on the bubble–slug transition boundaries. A similar conclusion as above concerning the absence of churn flow can also be drawn here, where the reduced size of the channel may have contributed to the observed disappearance of churn flow. Similar results were also reported in by Choi *et al*. (2011) and Kawahara *et al*. (2002). Kawahara *et al*. (2002) stated that the absence of churn flow patterns may be mainly attributed to the laminar nature of the liquid flow in the microchannel, even at the highest superficial liquid velocity tested.

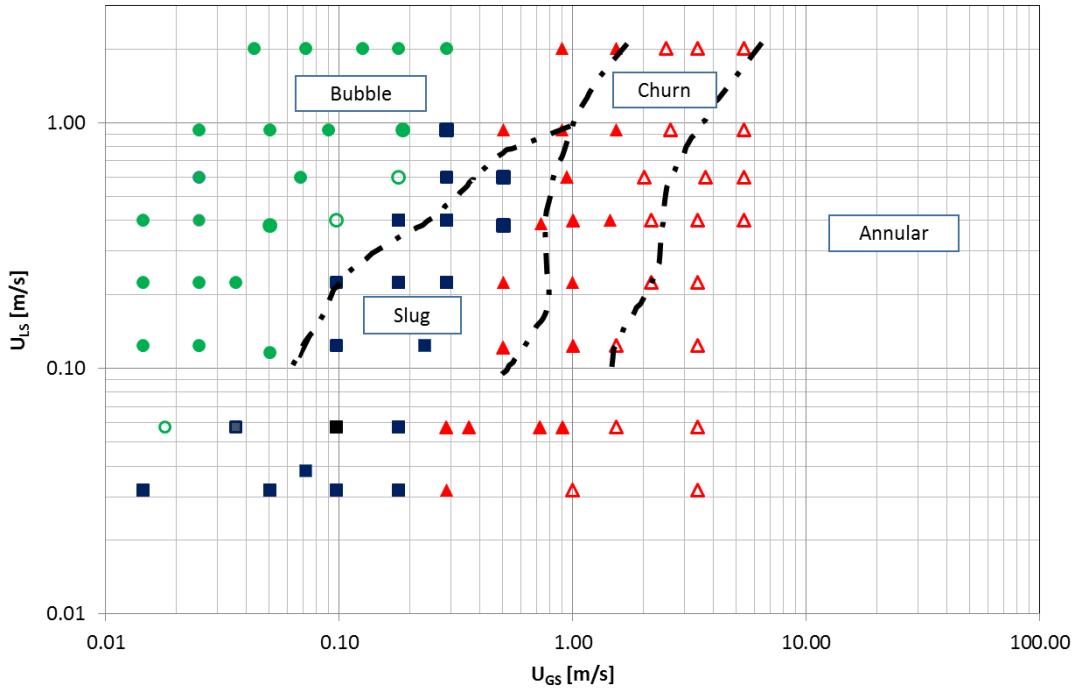

Figure 5-15 : Comparison of present numerical results with flow regimes maps of Wei *et al*. (2017).

5.3 Two phase slug flow without phase change in 1 mm circular microchannel

5.3.1 Model description

A two-phase gas-liquid flow in a cylindrical pipe with a diameter of 1 mm was considered in this study. In the present work, slug formation by an annular (concentric) nozzles configuration, as conducted by Shao *et al*. (2008) was studied. As shown in the schematic in Figure 5-16, the gas enters in the centre of the channel via a nozzle while the liquid flows around the nozzle as an annulus. The flow field has been calculated using a three-dimensional geometry so that the effect of gravity could be taken into account. A constant heat flux is assumed along the wall of the channel. R134a refrigerant was used as the working fluid. It is assumed that each phase is incompressible and phase change does not take place. The properties of the working fluid are listed Table 5-1 shown in section 5.2. The superficial velocities (phase volumetric flow rate per unit channel cross-sectional area) of gas and liquid are 0.23 m/s and 0.13 m/s respectively. These flow conditions correspond to $Ca = 0.09$ and $Re_L = 1.9$

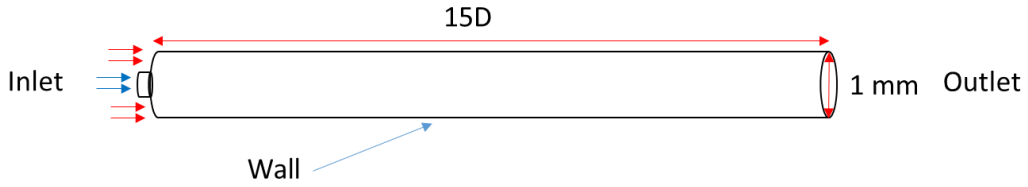

Figure 5-16 : Schematic representation of the geometry and boundary conditions used in the simulation.

5.3.2 Results and discussion

5.3.2.1 Flow topology

The bubble evolution from the initial breakup to the development of single slugs with time is shown in Figure 5-17. The figure shows the colour contours of the volume fraction of the flow, where the red and blue represent the gas and liquid phase, respectively, while the yellow line indicate the interface between gas and liquid phase. This simulation is well within the "slug-flow" regime as can be seen from the distribution and shape of the gas bubbles in the fluid. A similar mechanism of the bubble formation was also observed by Shao *et al*. (2008), where mechanisms that consist of expanding, contracting and necking processes occur at the lower end of the bubble, close to the nozzle. In the expanding process, (t=4.5 ms), the gas bubble emerges and more and more displaces the liquid region. At the same time the gas–liquid interface moves away from the tube central axis. As the gas bubble grows and pushes forward in the channel, it fills up almost the entire channel before the contracting process occurs where the interface retracts back towards the central axis.

Subsequently, the necking process takes place (t=7.5 ms), where the gas bubble starts blocking the channel leaving only a thin liquid film close to the wall. At the rear, the bubble is squeezed and a neck forms at the centre of the channel that connects the bubble body with the tip of the gas nozzle. Finally, the bubble breaks off and subsequently moves further and further downstream through the channel. The bubble is elongated by the action of interfacial shear, and it breaks when surface tension effects exceed the inertia.

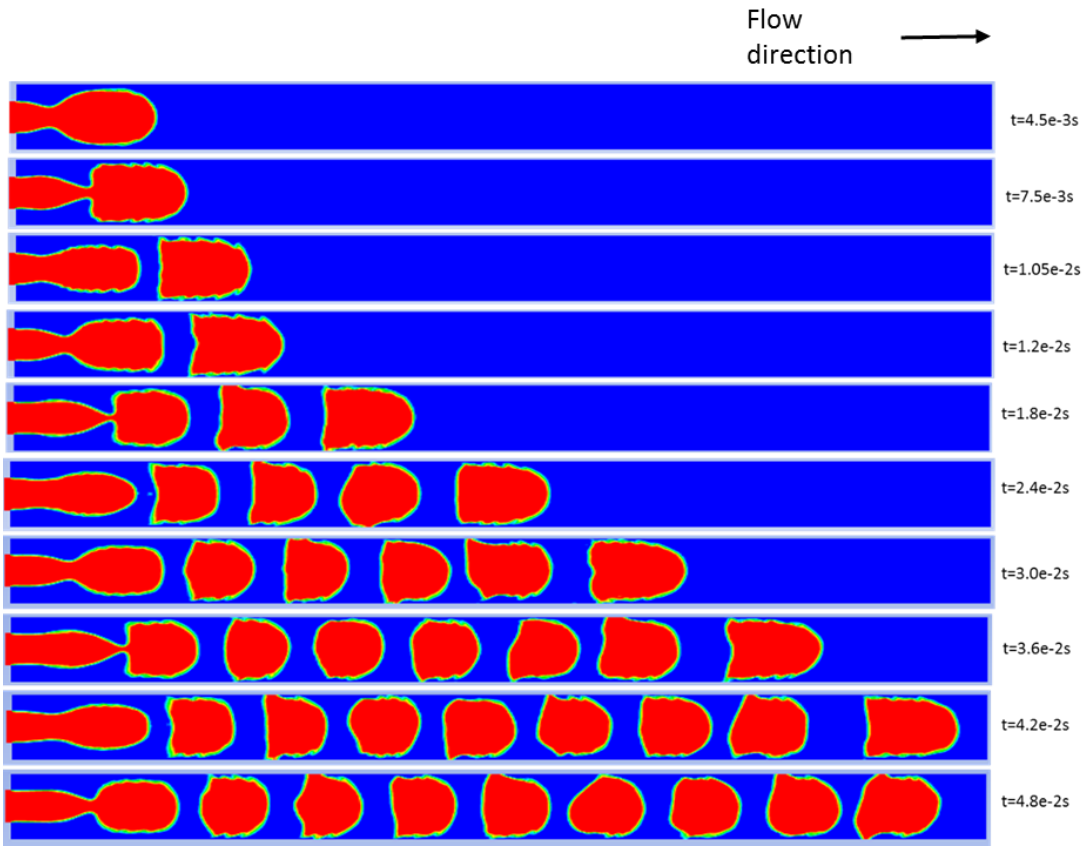

Figure 5-17 : Cross sectional contours showing slug flow formation and evolution for $\boldsymbol{U_{Gs} = 0.23}$ and $\boldsymbol{U_{Ls} = 0.12}$ red: gas phase, blue: liquid phase.

The process of bubble separation is periodic. However, the length and shape of the first and second bubbles are not similar. This is because the initial bubble takes much longer to break-off compared to subsequent bubbles observed in the simulation. The liquid and gas slug length in the microchannel used in this study were obtained by measuring the axial distance between the front and the rear of the bubble in both the gas and liquid phase. The comparison of the gas and liquid slug along the channel is shown in Figure 5-18. As observed in that figure, the liquid slug length is shorter than the gas slug length with a void fraction of almost 0.65. Similar results were found by Li and Hrnjak (2019) in their experimental study. Additionally, the longest gas slug length is 1.14 mm and the longest liquid slug is 0.502 mm. Also, it can be seen that the lengths of the bubble and the liquid slug are almost uniform, where the percentage

difference of the bubble lengths compared to the longest bubble length observed was between 8%-20%, while the same difference for the liquid slug length was 6%-33%.

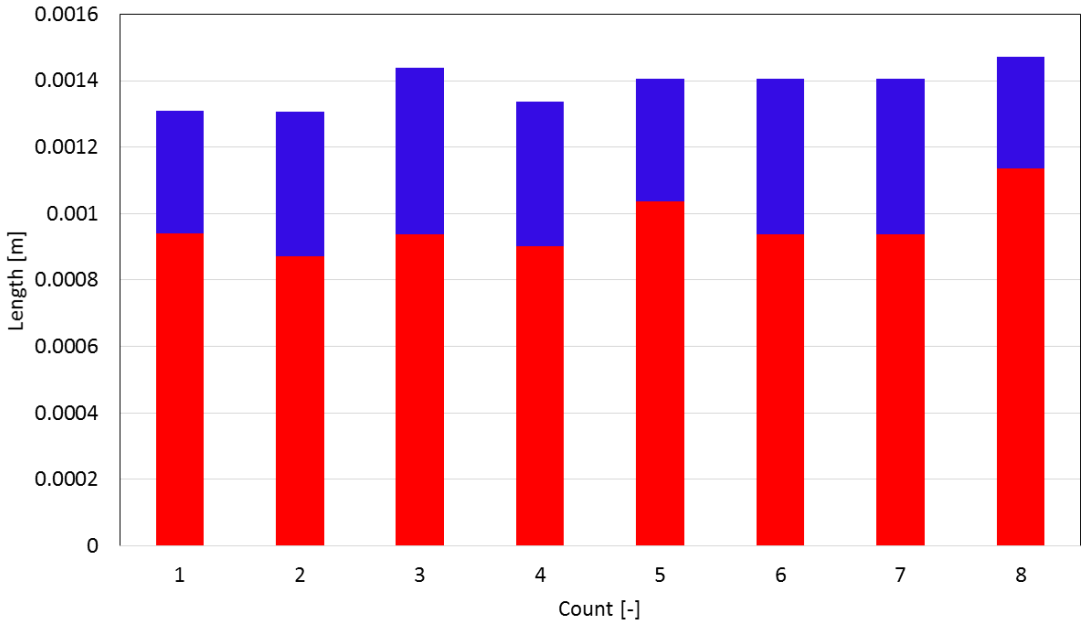

Figure 5-18 : Measurement of each gas (red) and liquid (blue) slug.

In Figure 5-19 the bubble lengths obtained from this study were compared with existing correlations. The equation

$$L_B = L_{UC}\varepsilon_G = \frac{L_S}{\varepsilon_L}\varepsilon_G = \frac{L_S}{(1-\varepsilon_G)}\varepsilon_G \tag{5.7}$$

of Liu *et al* .(2005) was used to transform liquid slug length L_S into bubble length L_B, which was needed as some authors reported only liquid slug length.

As can be seen from Figure 5-19, that the results of the present numerical work are in good agreement with the correlations of Garstecki *et al*. (2006) with an average percentage difference of 8%. A similar good agreement with the aforementioned correlations was obtained in the numerical simulations by Shao *et al*. (2008). However,

both the present results and the results obtained by Shao *et al*. (2008) do not agree well with the other correlations. Shao *et al*. (2008) attributed the observed discrepancy to the wide range and larger values of the channel size and superficial gas and liquid velocities (wide range of Ca) used in the literature. Furthermore, they suggested that detailed knowledge on inlet conditions is needed to accurately predict the length of bubble.

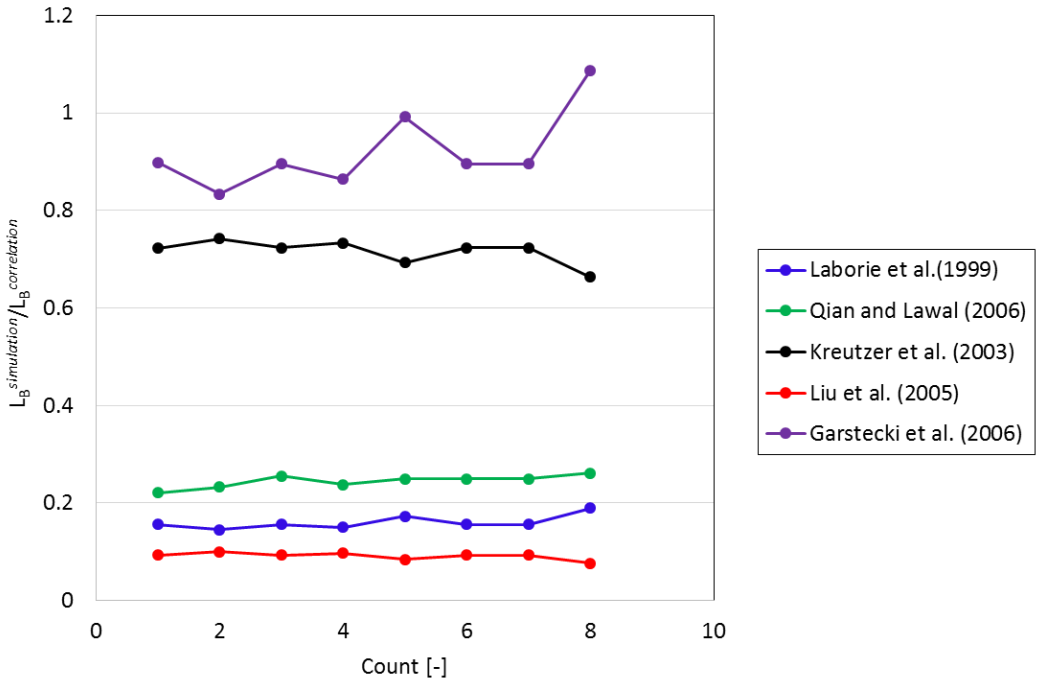

Figure 5-19 : Comparison of bubble length obtained in present simulation with existing correlation.

Previously, most researchers assumed the flow to remain axisymmetric to safe computational time. This assumption lead to identical bubble slugs. However, the process of bubble generation using the axisymmetric assumption is not acceptable and a transient simulation is required, Asadolahi *et al*. (2011). In the present study, for instance, a non-identical shape of the gas bubble slugs was observed, (as shown in

Figure 5-20). Cells with a dry zone and irregular shapes have been obtained in 3-D numerical work. Therefore, several individual cells with different behaviour and shape are carefully selected in order to understand the characteristics of the hydrodynamic and thermal behaviour. Two different zones at advanced time were selected; zone 1 – initial zone; zone 2 – middle zone.

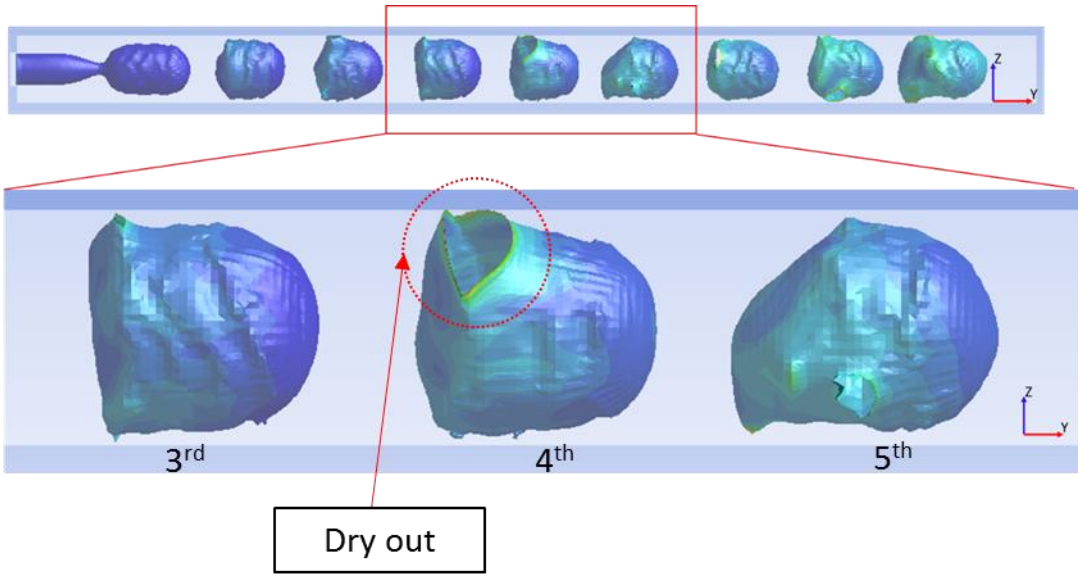

Figure 5-20 : Three dimensional visualisation identifying the gas bubbles.

Figure 5-21 shows the comparison of the obtained visualisation of slug flow pattern with the slug flow pattern discovered by Chen *et al*. (2006). Based on the figure, the comparison of slug flow pattern in both studies showed a reasonable agreement. However, a strong interaction between the slug and the wall, where there are some small amplitude waves that can be observed at the film-bubble interface is clearly shown in this study. This phenomenon does not being observed in experimental work conducted by Chen *et al*. (2006), where the flow pattern was observed and recorded by using high-speed digital camera (Phantom V4 B/ W, 512 × 512 pixels resolution). A continuous white light source was carefully positioned under the measurement area to reflect on the interface, which appeared as a bright line. It is worth to note, the presented slug flow pattern shown in Figure 5-21 by using ISO–surface of

volume fraction 0.5, in post-processing in ANSYS Fluent. This gives rise to some differences in the slug flow pattern for both studies. Yet, this is similar to the simulation results of the rear meniscus of a long bubble by Giavedoni and Saita (1999) and Taha and Cui (2004). Therefore, it can be concluded that the void fraction distribution along the tube axis is well reproduced by ANSYS Fluent.

(a) (b)

Figure 5-21 : Comparison of present simulation work with the study conducted by Chen *et al*. (2006).

1. **Break-up zone (Zone 1)**

Figure 5-22 presents the pressure, the temperature surface contour and the velocity vector in the initial zone (Zone 1) breakup region. As seen in Figure 5-22, a high radial pressure gradient was observed at the breakup location and the pressure at the front of gas slug is much higher than at the core of the gas slug. During this stage, the necking process has occurred further upstream, where the gas is accelerated leading

to a large pressure drop across the neck, as also discussed by Narayanan and Lakehal (2008). Simultaneously, a circulation was found at the core of bubble close to the wall. Additionally, the wall temperature was found to be locally higher at the location where necking and circulation occurred.

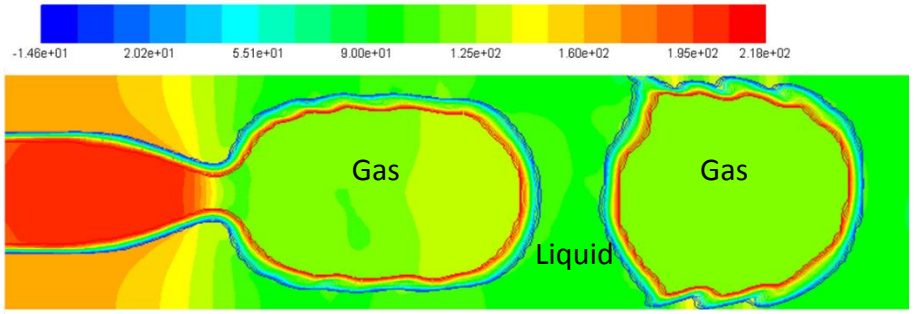

(a)

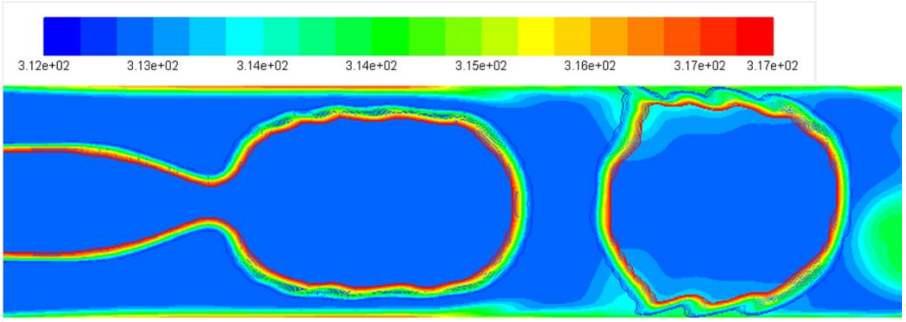

(b)

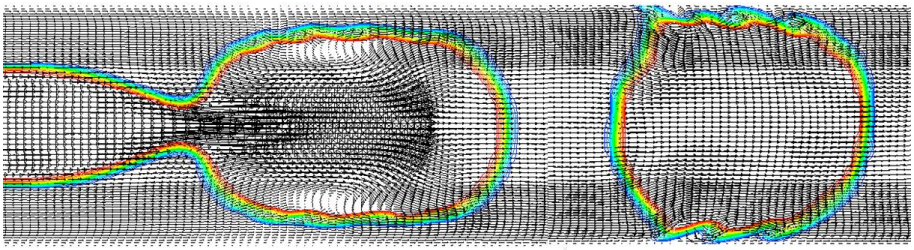

(c)

Figure 5-22 : (a) Pressure surface contour (b) temperature surface contour and (c) velocity vector at breakup region (Zone 1) at t =4.8 ms. The boundaries of the cells are identified by colours lines ; Red (gas phase) , Blue (liquid phase), Yellow-green (gas-liq liquid interface).

2. Middle zone (Zone 2)

Figure 5-23 till Figure 5-25 show the velocity and temperature profiles of the three selected individual cells (#3, #4, #5) of slug gas located in the middle region of the channel identified by the rectangular box in Figure 5-20. The profiles are labelled in the figure by y1, y2, y3, y4, y5, y6, y7. The analysis of the results indicates that the locations y1 and y7 were not affected by the presence of gas slug. y2 and y6 were located at the interface between gas and liquid phase. However, the locations y3, y4, y5 show velocity profiles inside the gas phase where y4 is in the middle of the gas slug.

The 3rd cell shows a perfect bullet shape with a flatter tail. The velocity profiles at y1 and y7 show similar trends, where the velocity of the flow reduces at the center of the channel. These results are similar to the ones obtained by Fukagata *et al*. (2007). On the contrary, He *et al*. (2010) found that the velocity profile of the liquid slug is nearly parabolic, which is similar to single phase laminar flow. Additionally, in the liquid slug the velocity field is nearly symmetrical. Also, a recirculation occurred in

the liquid film region, while only small recirculation was observed inside the liquid slug near the rear of tail of bubble slug. This phenomenon, was also observed by Bayareh *et al*. (2020) (called vortex in their study) in their numerical study of slug flow heat transfer in rectangular microchannels. Contrary, for the flow inside the gas slug, the maximum velocity was observed at the centre of the channels and the velocity profile at the centre of the gas slug was close to the parabolic profile. Also, the velocity was found to be minimum near the wall region, where a small circulation exists at y3, y4, and y5. Furthermore, the velocity of gas bubble is slightly higher than the continuous fluid velocity. This is because of shear stress on the bubbles from the liquid film is much smaller than the shear stress on the wall from the liquid film. (Bandara, *et al*. (2015))

The temperature contour plot of the 3rd cell obtained here, shows distribution of heat from the wall down starting at the front of the bubble slug. According to the temperature contours, the coldest region is located at the front of the gas slug and the temperature is highest near the tail of the bubble area. It can be seen that the mechanism of heat removal was essentially by convective heat transport at the back of the slug. Furthermore, as shown in that figure, the heat is much easier transferred from the wall to the liquid film and bubble slug. Besides, a jet-like flow forms that is responsible for the heat penetration into the core of bubble slug (convective heat transfer mechanism). A similar observation of this phenomenon was made by Lakehal *et al*. (2008).

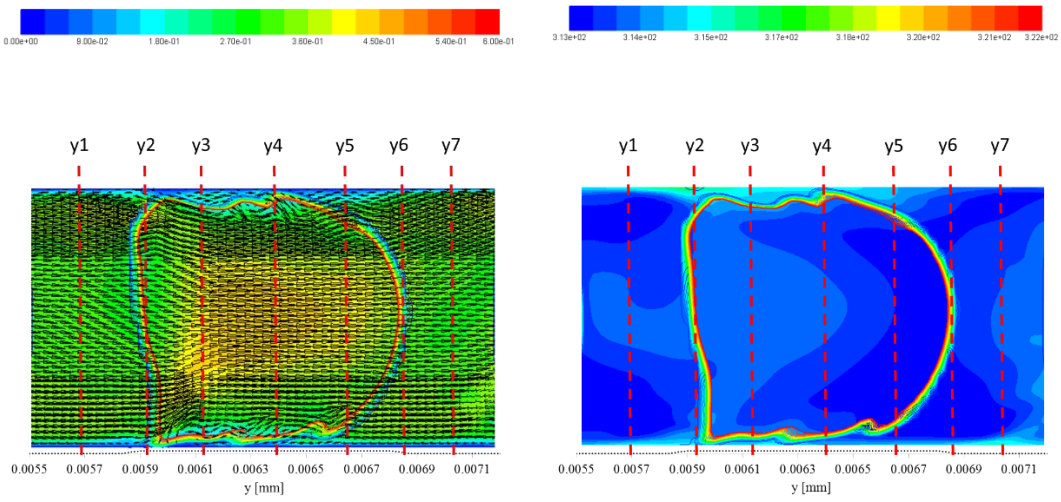

(a) (b)

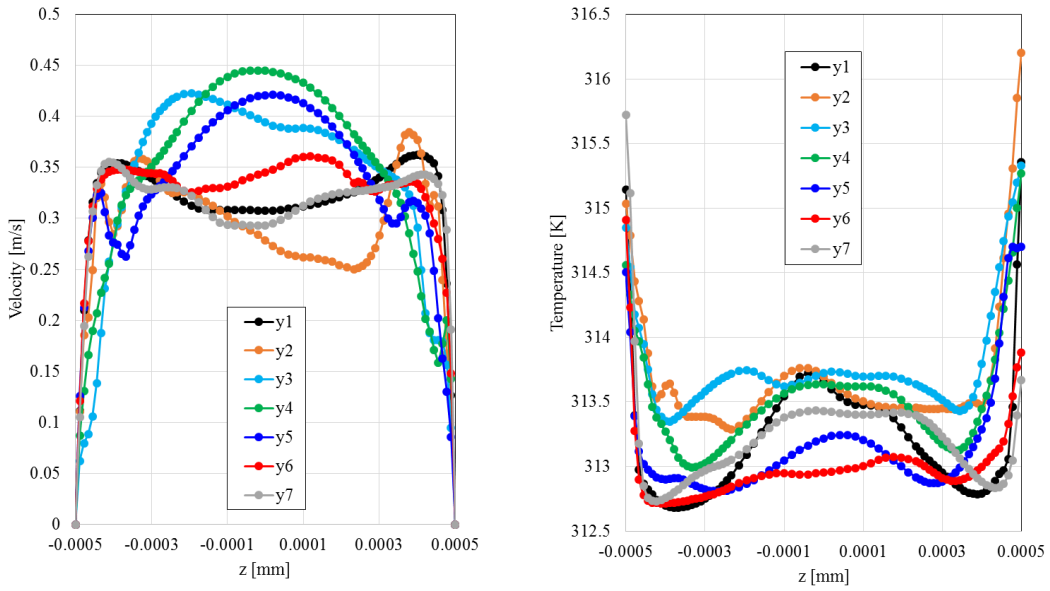

(c) (d)

Figure 5-23 : (a) Velocity vector and (b) temperature contour of 3rd cell ; (c) velocity profiles and (d) temperature profiles at selected locations of 3rd cell.

As mentioned before, a slug cell with a dry zone has been found in this study. Gupta *et al*. (2010) concluded that dry-out is one of the problem in numerical work in and it can be avoided by constructed numerical grids and algorithm, properly. Contrary, Talimi *et al*. (2012) suggested that the appearance of a real dry-out condition, in numerical work is not because of a poor mesh resolution which could leads to nonphysical results, however further study on this phenomenon is needed. In order to study the flow and thermal behaviour of the slug cell with dry zone, the 4th cell located at the middle of channel has been selected. At noticed in this figure, the 4th bubble cell has a similar velocity profile as the 3rd bubble cell. However, a gas phase occurred at the wall (dry-out zone) at 0.074 m < y < 0.0755 m, which led to a maximum value of the temperature at the wall of the microchannel tube as plotted in Figure 5-24. Besides, the liquid film thickness at the top area of the bubble is thicker compared to the bottom of the bubble. The thermal behaviour resembles that found in the 3rd cell. A jet like flow was also observed at the core of the bubble slug.

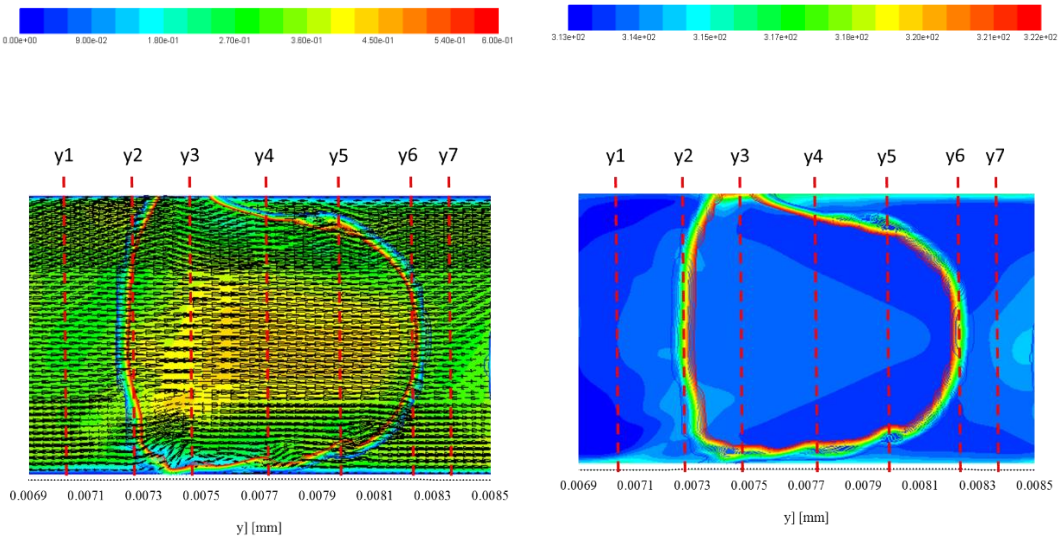

(a) (b)

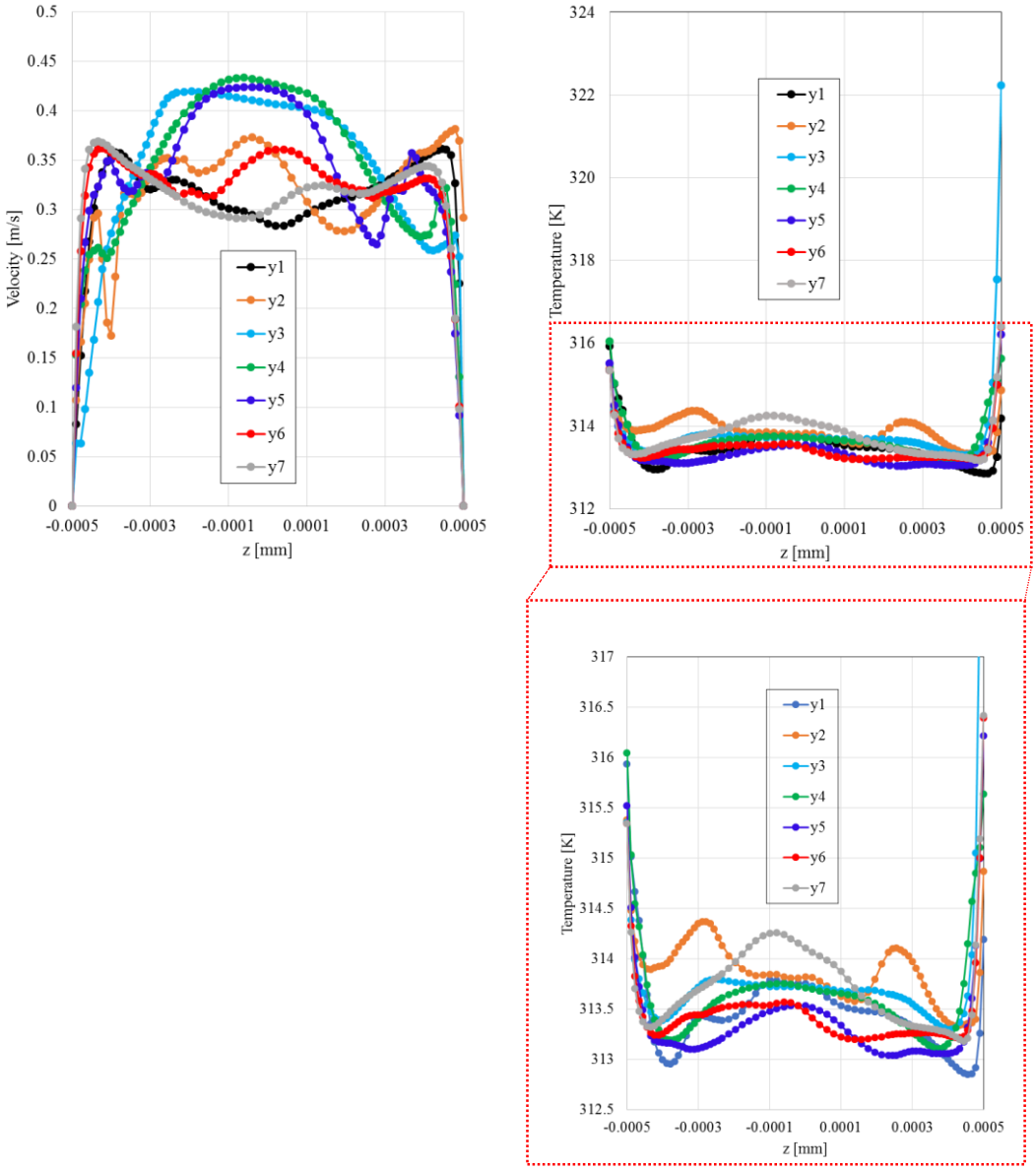

(c) (d)

Figure 5-24 : (a) Velocity vector and (b) temperature contour of the 4th cell ; (c) velocity profile and (d) temperature profile of selected location on the 4th cell.

Contrarily, the 5th cell of bubble gas shows an irregular tail shape, which evidences the non-axisymmetric behaviour of the bubble slug. A 'jet- like' thermal behaviour bubble slug occurs, but the shape is a bit different when compared to the 3rd and 4th bubble slug cell due to the irregular shape at the rear of the bubble slug, especially at the tail. This trend is similar to what was observed in both the numerical and experimental work of Asadolahi *et al*. (2012). In their work, the bubble tail shape fluctuates in time between convex and concave. Such an oscillation of the bubble tail shape has also been captured in the present study as seen in Figure 5-26.

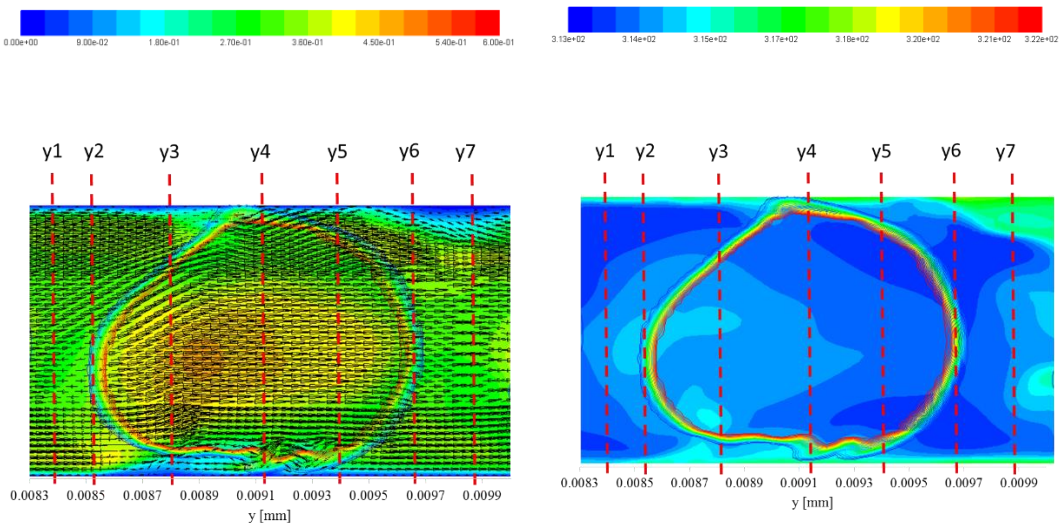

(a) (b)

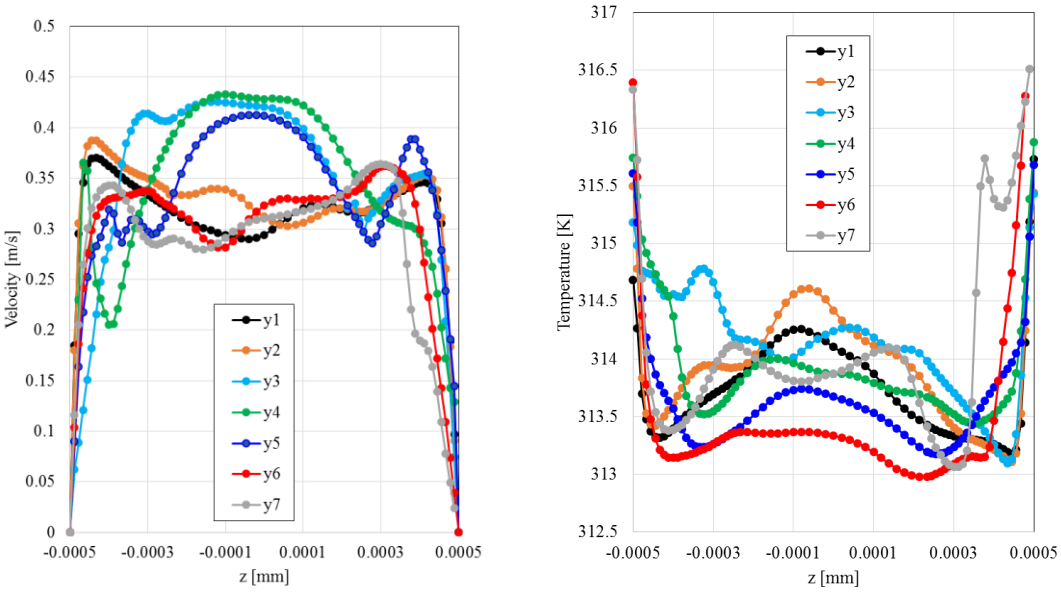

(c) (d)

Figure 5-25 : (a) Velocity vector and (b) temperature contour of 5th unit cell ; (c) velocity profile and (d) temperature profile of selected location on 5th unit cell.

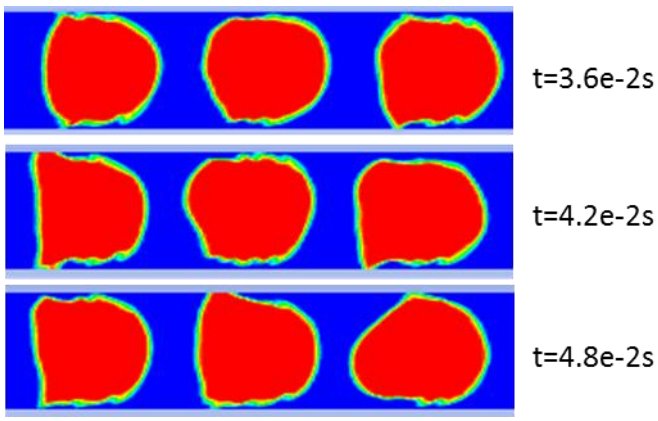

Figure 5-26 : Bubble shape as obtained in CFD simulations at three different time.

5.3.2.2 Pressure distribution.

Figure 5-27 shows the distribution of the wall pressure and pressure in the axial direction at the advanced time of t=4.8 ms. As discussed before, a high pressure was observed in the upstream channel due the necking process, where gas flow accelerates leading to a large pressure drop across the neck. Therefore, the pressure pulse will have to be taken into account at mentioned by Narayanan and Lakehal (2008). Furthermore, the axial pressure is decreasing along the microchannel tube and it is obviously showing a big difference between liquid slug and gas bubble. Similar results were shown by Gupta *et al*. (2009), who attributed it to the interfacial pressure together with a contribution from the dynamic head. Furthermore, the pressure in the gas bubble is constant was reported by Gupta *et al*. (2009), however, there was slightly increases (almost constant) in gas bubble was observed in this study. Similar trend was also observed in very recent study conducted by Kumari *et al*. (2019). While the pressure in the liquid slug region ahead of the bubble shows a decrease with distance. The wall pressure was showing some fluctuation in the bubble slug region, with its value decreasing from the bubble tail to the front of the bubble gas slug. Similar results were also reported by Kreutzer *et al*. (2005) and they claimed that oscillation happens due to an inundation on the interface. In numerical point of view, Gupta *et al*. (2009) reported a complex pressure distribution in this region because of numerical effects.

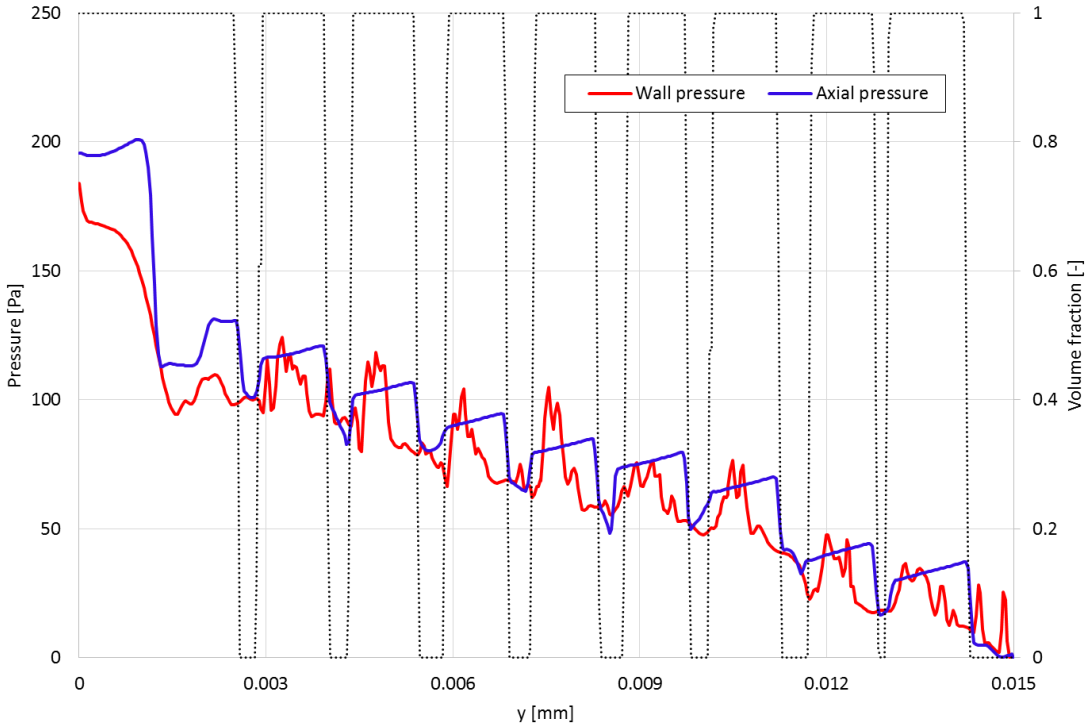

Figure 5-27 : Variation of wall pressure and axial pressure distribution at t=4.8 ms.

5.3.2.3 Heat transfer distribution

Figure 5-28 shows the numerical results of the axial variation of the bulk temperatures and wall temperature at time t=4.8 ms. The bulk temperature increases from the upstream in the liquid slug region and reaches its peak value at the rear of bubbles before subsequently decreasing in the gas region. This is explained by the fact that the heat capacity of the liquid is much larger than that of the gas. Furthermore, the wall temperature in the gas region is much higher compared to the liquid slug region. The peak value for the wall temperature was observed at the bubble tail where recirculation is generated and it subsequently decreased in bubble slug. Similar results were also found in numerical work conducted by Bayareh *et al*. (2020). They stated that the liquid is more contact with the wall due to the occurrence of recirculation. Moreover, the temperature was observed to reach its maximum values in the dry-out zone at the 4^{th}, 6^{th}, 7^{th} and 8^{th} bubble slug.

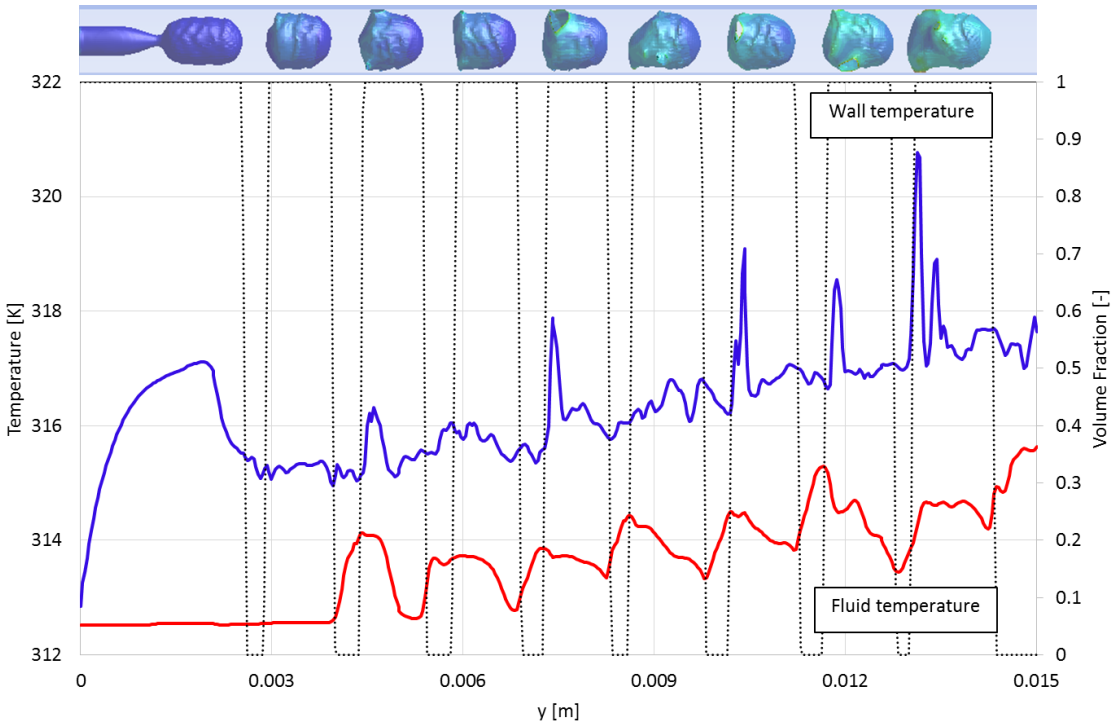

Figure 5-28 : Bulk temperature variation and wall temperature in the axial direction at a time t=4.8ms obtained from Ansys Fluent.

In this study, a constant heat flux was adopted at wall of the channel, and the Nusselt number was determined by the difference of the wall temperature and the bulk temperature as defined in Eq. (6.8), Figure 5-29 shows the variation of the local Nusselt number (Nu_x) with the axial coordinate.

$$Nu_x = \frac{q_w}{T_w - T_{bx}} \frac{d}{k_L} \tag{6.8}$$

The calculated local Nusselt numbers are higher in the gas region than in the liquid slug region. Nu_x gets its high value near the rear of the bubble. Some fluctuations in the local Nusselt numbers are observed in the gas region due to a recirculation phenomenon especially near the tail of the bubble. This profile is similar to the

numerical results of the local Nusselt number presented by Gupta *et al*. (2010) and Zhang and Li (2016).

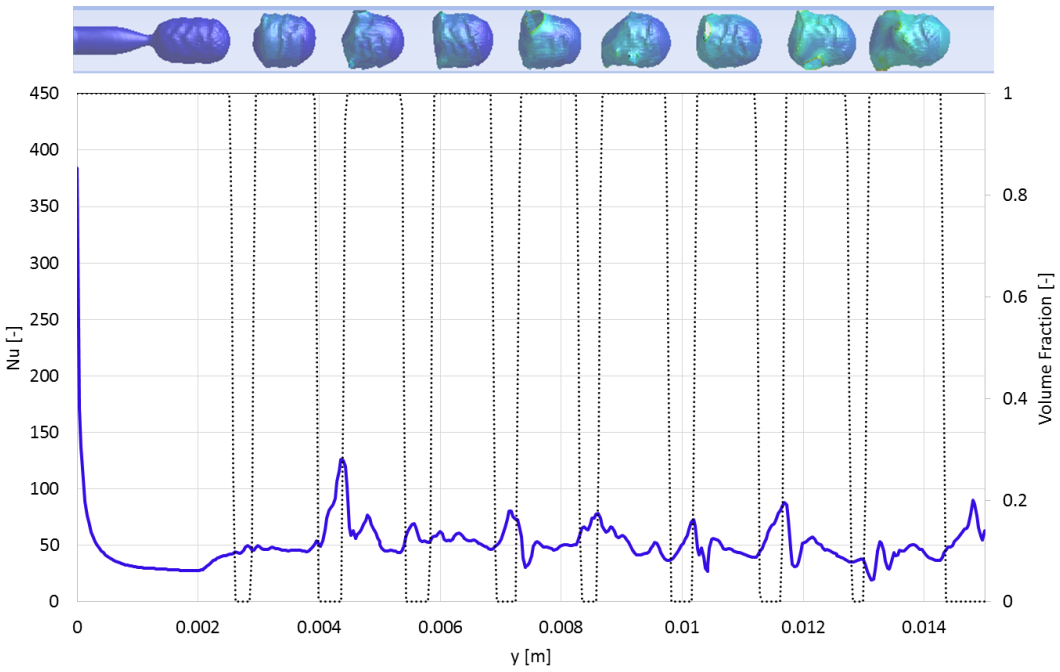

Figure 5-29 : Local Nusselt number at 4.8e-2s in axial direction.

The Nu_x obtained at specific locations on the tail and the nose of the bubble slug are clearly shown in Figure 5-30, where the maximum value of Nu_x is ~102 is reached at the tail of 2nd cell slug. As shown in this figure, the higher value of Nu_x is obtained at the tail of bubble slug and the lower one at the nose of the gas bubble. However, it also interesting to see that the Nu_x of the 8th cell slug shows a different trend compared to the others. For this cell, the value of Nu_x at the rear of bubble is lower than its value at the nose of the bubble. This is due to the dry-out phenomenon that occurred at the tail of the bubble slug, which minimizes the heat transfer rate.

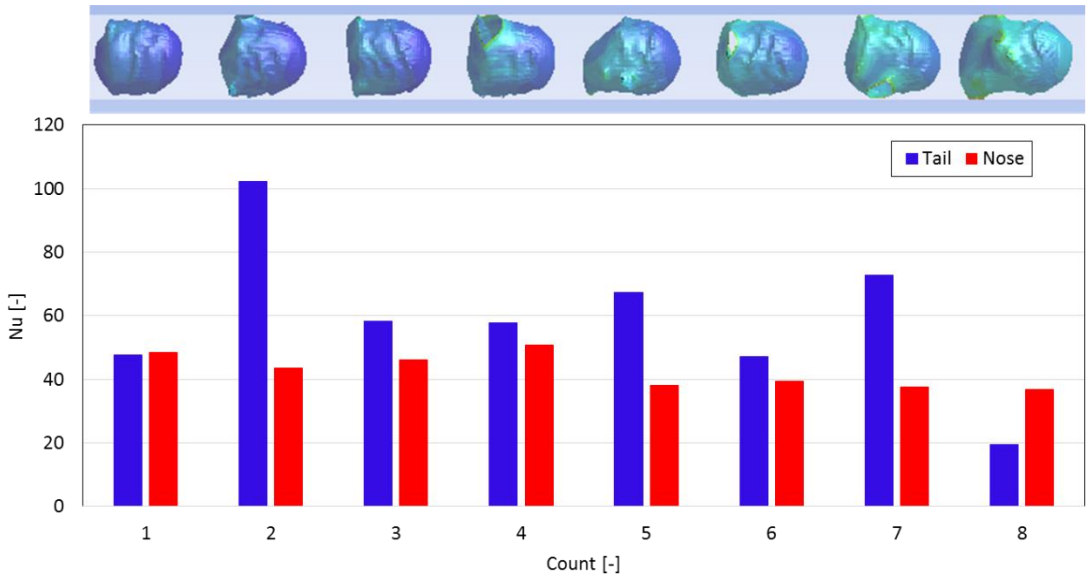

Figure 5-30 : Nusselt number at single location on tail and nose of the bubble slug.

5.4 Effect on superficial velocity on hydrodynamic and heat transfer on two phase flow patterns

The heat transfer rate is strongly dependent on the bubble length and the flow rates of gas and liquid, Kumari *et al*. (2019). In this section, numerical simulations of gas–liquid flow and associated heat transfer without phase change in a 1 mm circular microchannel are carried out. The effect of superficial gas velocity (with constant superficial liquid velocity), the hydrodynamics and the heat transfer of two phase flow based on a unit cell will be discussed in this section. As the mixture velocity increases, the void fraction, β, the capillary number, Ca, and the Reynolds number, Re, are also increasing. The operating conditions employed in this study are summarized in Table 5-3.

Table 5-3 : Summary of operating conditions and corresponding dimensionless numbers.

U_{GS} $[\frac{m}{s}]$	U_{LS} $[\frac{m}{s}]$	U_{TP} $[\frac{m}{s}]$	U_{GS}/U_{LS} $[-]$	β $[-]$	Ca $[-]$	Re $[-]$
0.14	0.13	0.27	1.13	0.52	0.0072	1909.10
0.22	0.13	0.35	1.69	0.63	0.0081	2474.77
0.29	0.13	0.42	2.25	0.69	0.0101	2969.72

5.4.1 Bubbles development

Figure 5-31 shows the developments of the initial bubbles and the variation in the breakup time obtained at three different gas superficial velocity conditions in a 1 mm circular channel with vertical orientation affected by gravity. Generally, the gas bubble size enlarges if the gas flow rate and, thus, the dynamic gas holdup, is increasing irrespectively of the feeding system. Because of the higher flow rate, more gas is fed into the gas bubble while it is still attached at the injector before enough liquid is pumped into the contacting zone affecting the critical detachment force and bubble breakup. As soon as the surface tension forces exceed the inertia forces, the gas jet breaks up to form a single bubble. As noted, the initial bubble departure size in the microtube under liquid co-flow generally depends on the gas superficial velocity. As can be seen in the figure, it increases with increasing gas superficial velocity. Furthermore, at higher superficial gas velocities the time for breakup increases as the instability wave needs to develop a larger amplitude to cause a breakup due to the higher void fraction.

(a)

(b)

(c)

Figure 5-31 : Variation of time of bubble formation at three different superficial gas velocity, $\boldsymbol{U_{GS}}$= (a) 0.14 m/s (b) 0.22 m/s and (c) 0.29 m/s.

Changes in the bubble shape were found to be occur for different superficial gas velocities. At lower superficial gas velocity, ($U_{GS} = 0.14\ m/s$) the front and rear of the bubble slug show a hemispherical cap shape which is consistent for all bubble slugs along the channel. Similar results were observed by Chen et al. (2009a) in their numerical work. However, as the superficial gas velocity increases, ($U_{GS} = 0.22\ m/s$) the front of bubble still shows a hemispherical cap shape, but the rear of the bubble becomes unstable resulting in an inconsistent shape. At the highest superficial gas velocity tested in this study, ($U_{GS} = 0.29\ m/s$) , the slug bubble shape has a flatter tail and a sharper nose. Similar results were observed by Zhang and Li (2016) and Chaoqun *et al*. (2013), who attributed this phenomenon to the increasing inertia force (as Re increases), leading to a Taylor bubble with flatter tail, sharper nose and longer bubble length.

In order to investigate the hydrodynamics and the heat transfer at the different superficial velocities tested in this study, a unit bubble cell was chosen. Figure 5-32 shows such a unit cell which has been selected for different superficial velocities at advanced time. As illustrated in that figure, the selected bubble was at a similar location in the channel. It is worth mentioning here that the occurrence of a dry-out patch on the wall was only observed for the highest superficial gas velocity ($U_{GS} = 0.29\ m/s$).

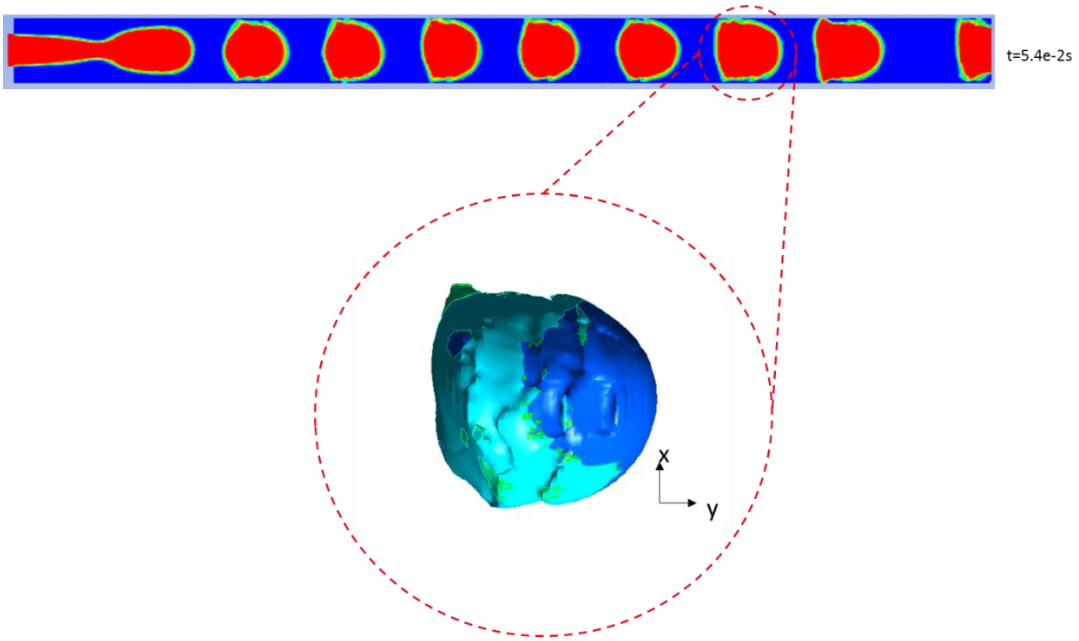

(a)

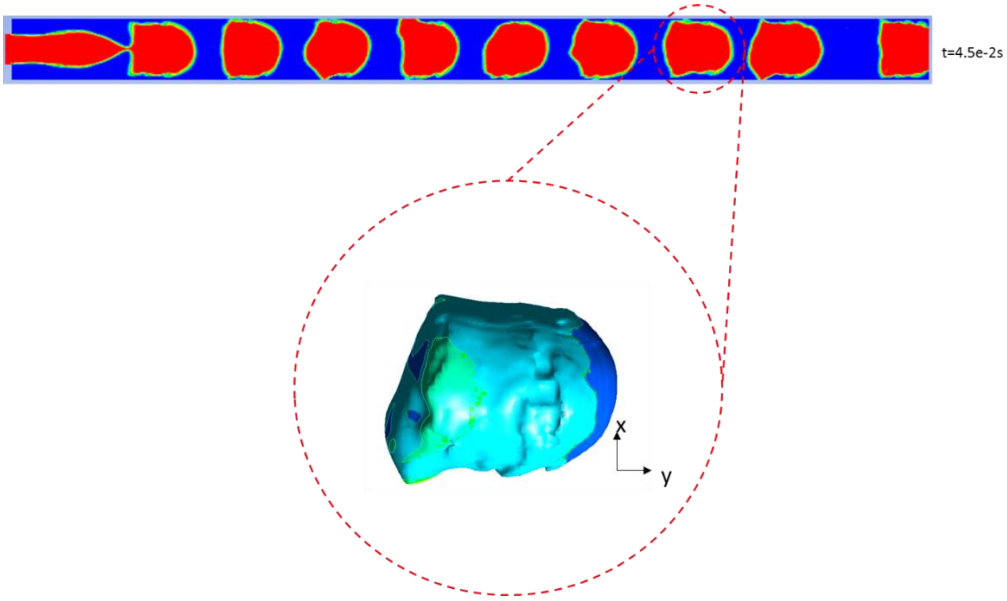

(b)

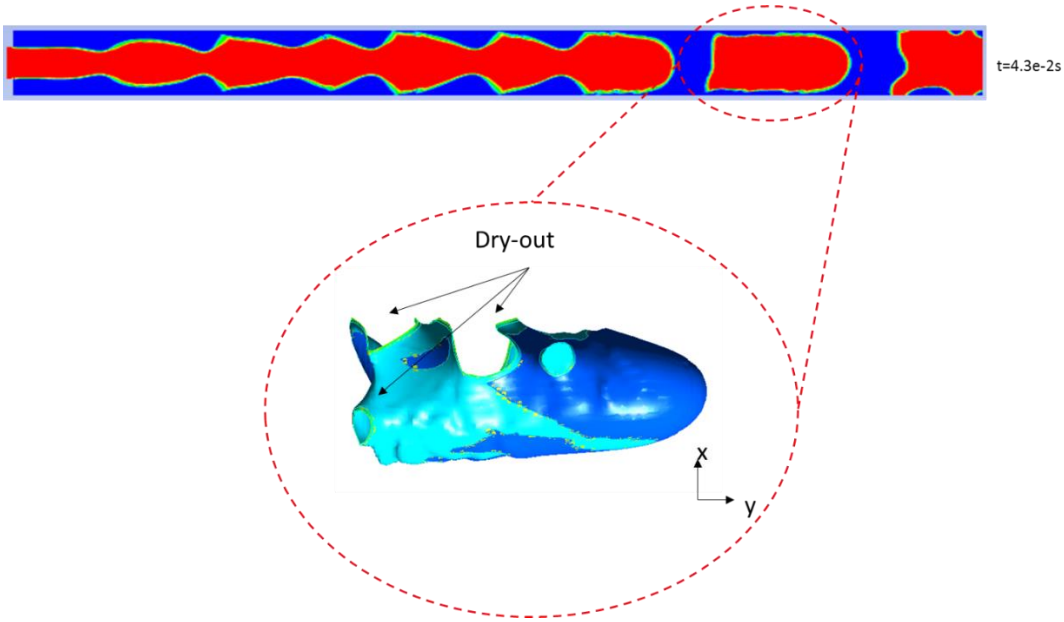

(c)

Figure 5-32 : Gas superficial velocity effect on the development of the two phase flow pattern; $\boldsymbol{U_{GS}} =$ (a) 0.14 m/s (b) 0.22 m/s and (c) 0.29 m/s.

5.4.2 Bubble length

Besides the changes in bubble shape at different operating conditions, the length of bubble is one of important parameters to consider. The bubbles length was obtained by measuring the axial distance between the front and the rear of the bubble. As shown in Table 5-4 the length of the bubble increases with increasing gas superficial velocity. As the U_{GS} increases from 0.14 m/s to 0.29 m/s, the amount of gas entering increases as does the initial bubble size attached to the nozzle. In the end, this causes the length of the bubble to increase from 0.870 mm to 2.174 mm. The increase in bubble length is due to the combination of a slight increase in the value of β combined with an increased value of Ca. Several correlations were found in the open literature that can be used to predict the length of the bubbles. As discussed in the previous section, the length of the bubbles obtained in the simulations is generally under estimated compared to all correlations, except for the correlation of Garstecki *et*

al. (2006). Therefore, in this section the numerically obtained bubble length is compared with the predicted bubble length according to Garstecki *et al*. (2006), and the results are summarized in Table 5-4. The simulated bubble slug length was found to be in agreement with Garstecki *et al*. (2006) only for $U_{GS} < 0.22\ m/s$, however the value is over predicted for $U_{GS} = 0.29\ m/s$ by about 51.4%. The predicted model provided by Garstecki *et al*. (2006) was developed particularly for low Ca, which might be the reason for the over prediction of the bubble length for the highest superficial velocity tested in this study.

Table 5-4 : Simulated bubble length under different gas superficial velocities.

U_{GS} $[\frac{m}{s}]$	Ca $[-]$	L_B $[mm]$	Garstecki *et al*. (2006) $[\pm\%]$
0.14	0.0072	0.870	15.79
0.22	0.0081	1.003	3.79
0.29	0.0101	2.174	51.4

5.4.3 Velocity and thermal profile

The behaviour of the fluid and thermal flow for a unit bubble cell at different superficial velocities are shown in Figure 5-33 till Figure 5-35. Generally, as the gas superficial velocity increased, the bubble length was also found to increase. At the lowest superficial velocity (Ugs=0.14 m/s), the shortest bubble length of 0.870 mm was found to be shorter than the diameter of the channel. The thin liquid film surrounding the bubble slug was found to gradually become thinner from nose to tail.

As shown in Figure 5-33(a), a recirculation zone was observed in the liquid film near the tail of bubble slug, which lead to a higher temperature in that region. As shown in Figure 5-33 (b), the heat is easier to transfer from the wall to the liquid film region. The hot fluid, which was previously in contact with the wall, is brought to the centre of the tube. Furthermore, the temperature gradients present in the bubble slug indicate that the bubble slug transfers heat to the adjacent liquid slugs in the axial direction. As show in the temperature contour plot, the temperature in a bubble slug is higher than in the adjacent liquid slugs, especially near the tail of bubble slugs. As explained before, this is due to the lower heat capacity of the gas in the bubble. As discussed in the previous section, a 'jet-like' thermal behaviour was observed.

Similar analyses of the velocity and temperature profiles for a liquid slug and a bubble slug in previous section, were also conducted in this section, where profiles at seven different locations covering one unit cell are shown in Figure 5-33(c) and Figure 5-33 (d). As in the previous sections, y1 and y7 represent a velocity and a temperature profile of the medium liquid slug located at the front and the rear of the bubble, respectively, where the velocity of the flow was found to be minimum at the centre of the channel for both locations. However, at other locations, that cross bubble region, the velocity profiles were showing a maximum velocity in the middle of the channel. Note that the y2 location is at the rear of the bubble and y6 is at the front of the bubble.

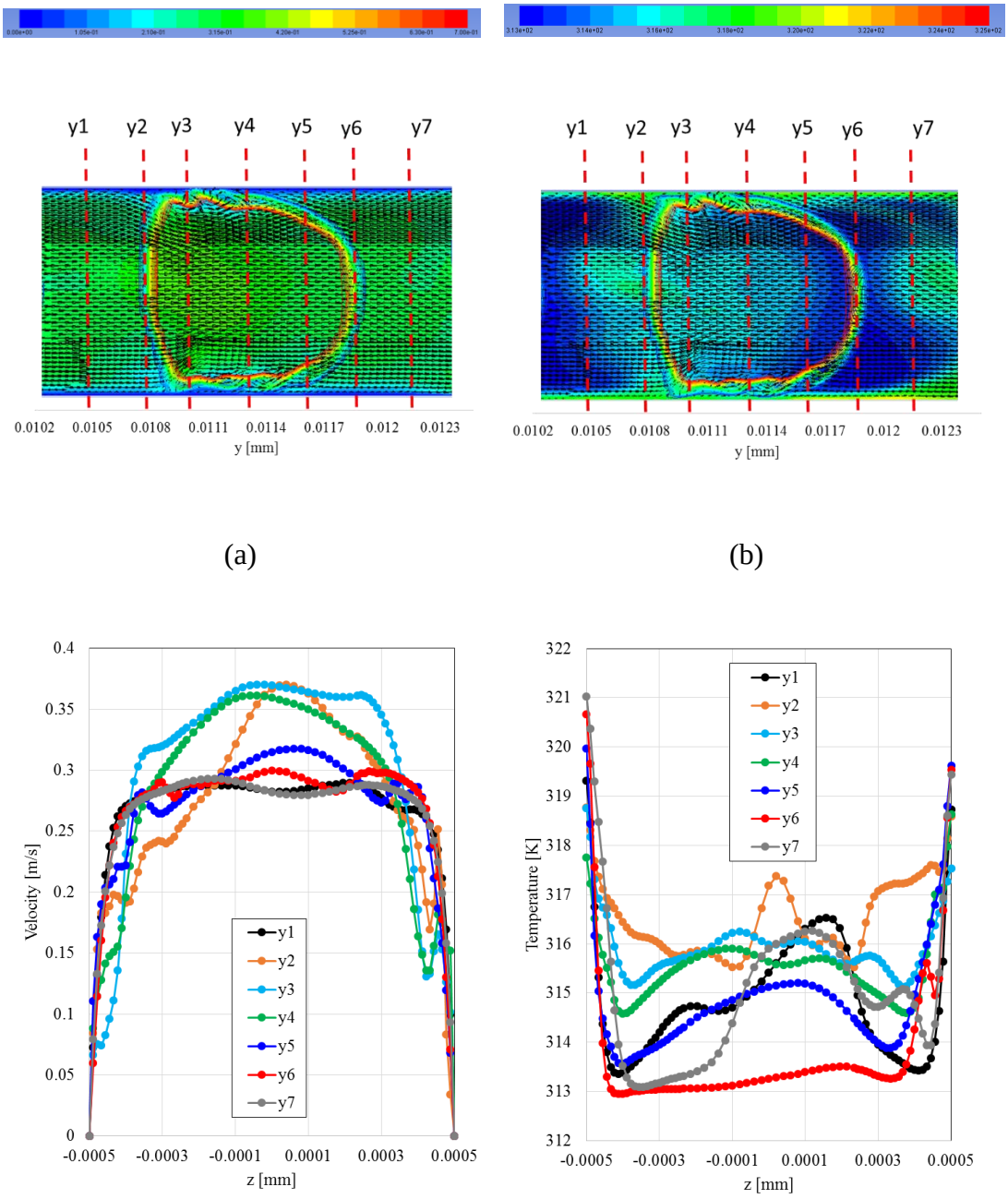

Figure 5-33 : (a) Velocity vector and (b) temperature contour of a unit cell of $U_{GS} = 0.14\ m/s$; (c) velocity profile and (d) temperature profile of selected location on a unit cell for $U_{GS} = 0.14\ m/s$. The boundaries of the cells are identified by colours lines; Red (gas phase), Blue (liquid phase), Yellow-green (gas-liquid interface).

For $U_{GS} = 0.22\, m/s,$ the length of the bubble is 1.01 mm, which is approximately similar to the diameter of the channel tested in this study (see Figure 5-34). The shape of the shown bubble was found to be similar to the bubble obtained at $U_{GS} = 0.14\, m/s$. Also, a recirculation zone was spotted in the liquid film surrounding the bubble for this condition. However, the velocity profiles for this case were found to differ and a non-symmetrical shape was obtained for y1 to y4. A reduction in velocity was observed after $z = 0.003$ mm due to the strong recirculation observed at the rear of the bubble. This phenomenon leads to higher temperature at the bubble tail near to the wall. Besides this, a 'jet-like" thermal shape was also observed for this case.

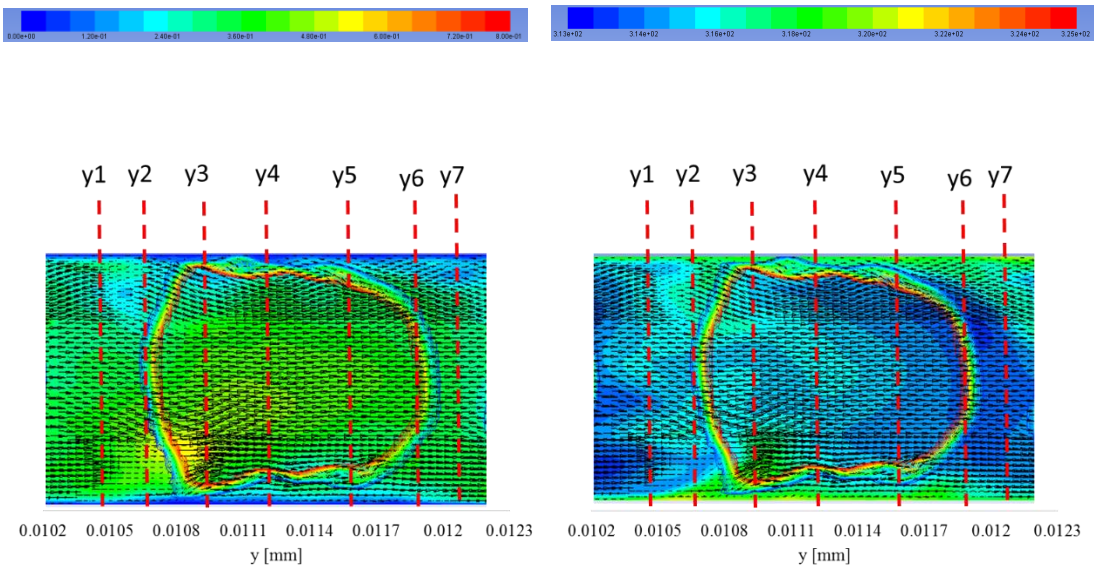

(a) (b)

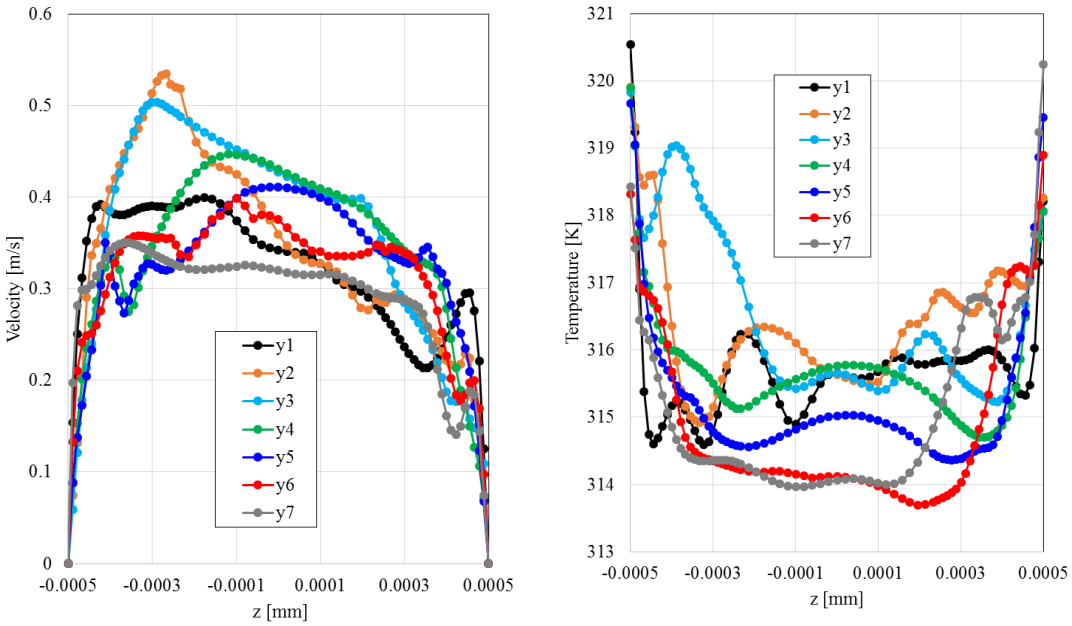

(c) (d)

Figure 5-34 : (a) Velocity vector and (b) temperature contour of a unit cell of $U_{GS} = 0.22\ m/s$; (c) velocity profile and (d) temperature profile of selected location on a unit cell for $U_{GS} = 0.22\ m/s$. The boundaries of the cells are identified by colours lines; Red(gas phase) , Blue (liquid phase), Yellow-green (gas-liquid interface).

Upon increasing the superficial gas velocity, the bubble length increases further, such that at $U_{GS} = 0.29\ m/s$, (see Figure 5-35 c(i)) a bubble slug length of 2.01 mm is obtained, while also the recirculation zone area is bigger compared to the other cases. The velocity profiles at this condition were showing a similar trend as for $U_{GS} = 0.14\ m/s$, where, at y3 to y5 (velocity profile inside the bubble) a maximum value at the centre of channel was obtained. However, the velocity profiles in the liquid slug (y1 and y7) and the velocity at the front (y2) and the rear of the bubble (y6) were found to be nearly flat at the centre of the channel. Furthermore, as mentioned earlier, a 'jet-like' thermal behaviour was not observed this this condition. Therefore,

the temperature profile for this case is more stable than in the other cases, where the temperature profiles are flat at the centre of channel except at the rear of the bubble (y2 and y3) where there are some fluctuations in the temperature due to the recirculation flow.

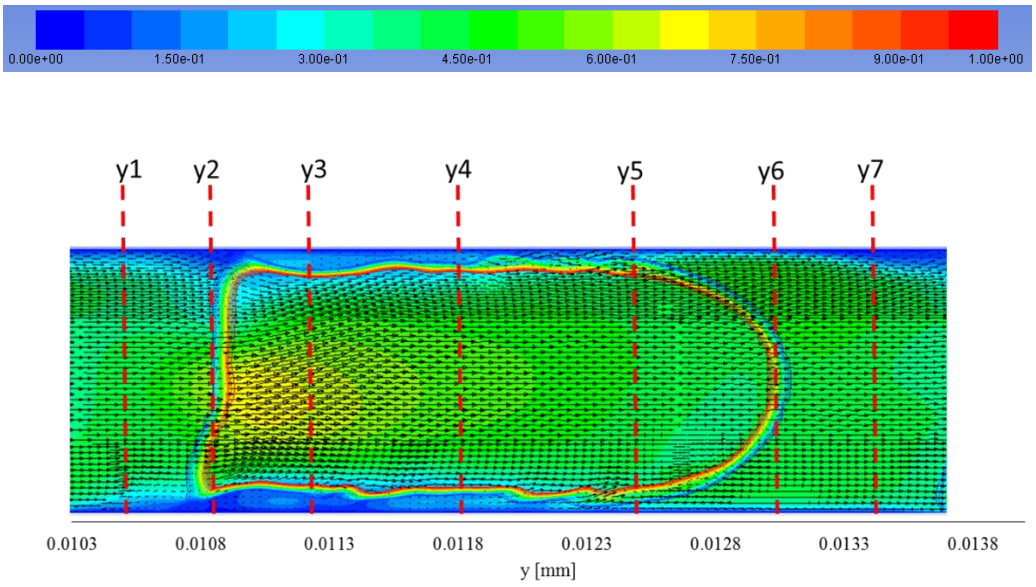

(a)

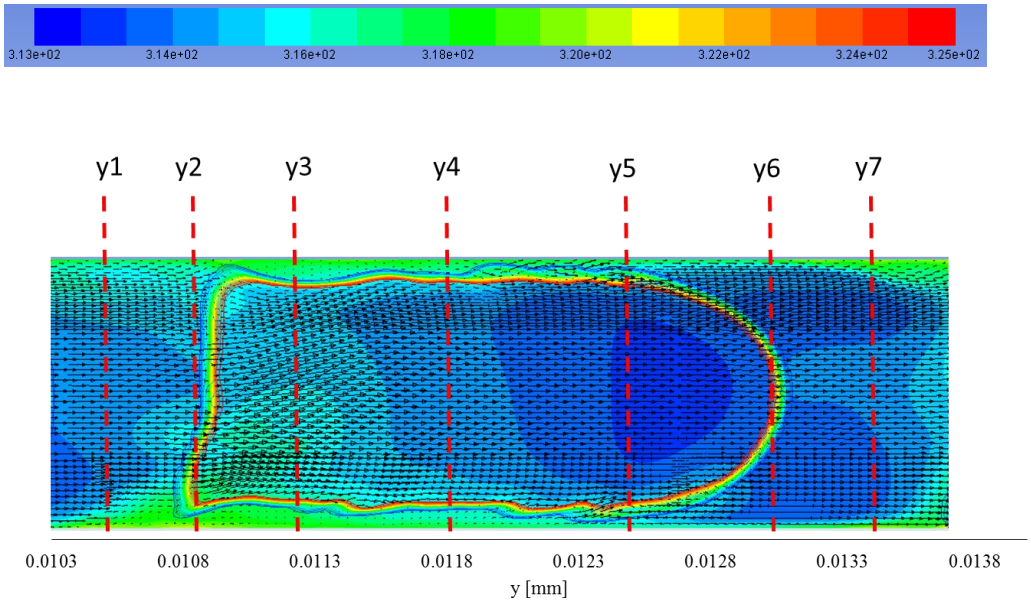

(b)

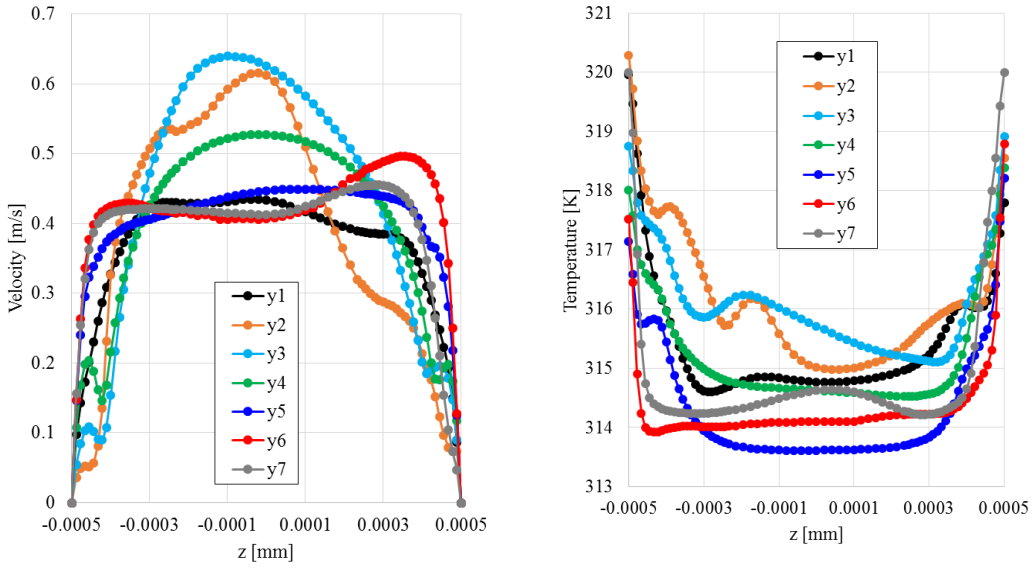

(c) (d)

Figure 5-35 : (a) Velocity vector and (b) temperature contour of a unit cell of $U_{GS} = 0.29\ m/s$; (c) velocity profile and (d) temperature profile of selected location on a unit cell for $U_{GS} = 0.29\ m/s$. The boundaries of the cells are identified by colours lines; Red (gas phase), Blue (liquid phase), Yellow-green (gas-liquid interface).

The ratio of the simulated bubble velocity, U_{Bubble}, and the sum of the gas and the liquid superficial velocity,U_{TP} are summarized in Table 5-5, showing that the value is very close to those obtained for the two-phase superficial velocity. This is in contradiction to Fairbrother and Stubbs (1935) and Lui *et al*. (2005), who observed that the bubble velocity was greater than the average liquid velocity. This phenomenon is due to the fact that the liquid ahead of the bubble gets left behind on a stagnant liquid film and becomes part of the liquid at the back of the bubble. Data of Liu *et al*. (2005) who derived the bubble velocity correlation based on their experimental data, were used to compare with presented study. According to the percentage differences between the presented results and predicted correlations by Lui *et al*. (2005), as shown in Table 5-5, was within $\pm 17\%$.

Table 5-5 : Percentage difference between simulation $\boldsymbol{U_B/U_{TP}}$ value with existing correlations.

U_{GS} $[\frac{m}{s}]$	U_B/U_{TP} $[-]$	Lui *et al*. (2005) [±%]
0.14	1.10	3.38
0.22	0.95	16.81
0.29	1.0	13.72

The quantitative information of hydrodynamics and thermal profiles in the liquid slug between two bubbles were further analysed by comparing the normalized velocity and temperature profiles at three different superficial velocities. The normalized velocity and temperatures are defined by

Normalized velocity :

$$V_x/U_{TP} \tag{5.9}$$

where $U_{TP} = U_{GS} + U_{LS}$

Normalized temperature :

$$T_x - T_w/T_w - T_{ave} \tag{5.10}$$

According to Figure 5-36 (a), none of the tested conditions reached a laminar, single phase and fully developed flow profile (parabolic profile) and similar results were also report by Gupta *et al*. (2010a) in their numerical work. The normalized velocity profiles for all cases are showing similar profiles, where the velocity profiles are virtually flat at the centre and the velocity of the liquid slug is very close to U_{TP}. In contrast, for case $U_{GS} = 0.22\, m/s$, the velocity was reduced in the z-direction (z/D =0.4 to z/D=1), which may due to the occurrence of secondary flow near the rear of the gas bubble, as shown in Figure 5-34 (a).

For the temperature profile, the higher superficial gas velocity ($U_{GS} = 0.29\, m/s$) was found to be more stable than other cases, where the temperature fluctuated at the centre of the channel. As discussed before, this is might be due to a 'jet-like' thermal behaviour that only occurred for the bubble slug with a bubble slug length less than or approximately equal to the diameter of the channel.

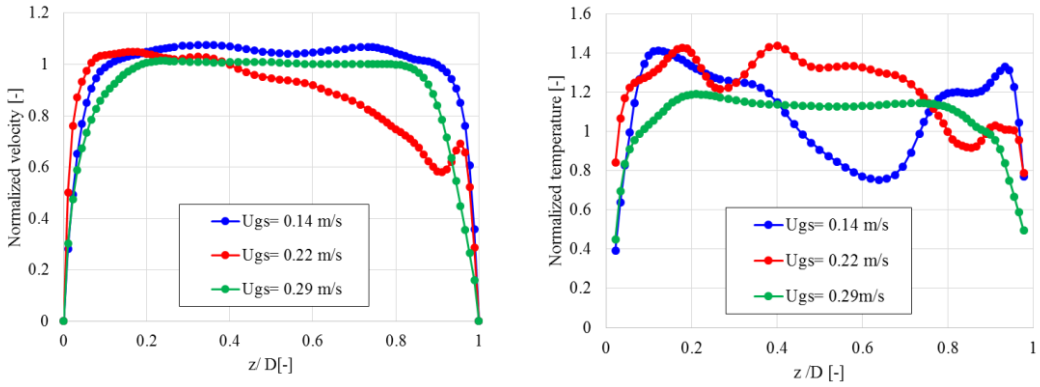

(a) (b)

Figure 5-36 : Comparison of normalized (a) velocity profile and (b) temperature profile of liquid slug at different superficial velocity.

5.4.4 Void fraction

Another commonly-used parameter to characterize slug flow is the relation of the void fraction, α and the homogeneous void fraction, β. In the present study, the void fraction of a unit cell volume, ε_g, was obtained using the expression

$$\frac{\varepsilon_g}{\beta} = \frac{U_{TP}}{U_B} \tag{5.11}$$

where the mixture velocity, U_{TP} and homogenous void fraction, β are already known (as seen in Table 5-3) and the bubble velocity was obtained from the simulations. Table 5-6 shows the value of the void fraction as calculated by using Eq. (6.4.3) as well as the ratio of the void fraction and the homogenous void fraction. The percentage difference between the existing correlations in the open literature with the present results for the void fraction was less than 10%.

Table 5-6 : Percentage difference between simulation void fraction value with existing correlations.

U_{GS} $[\frac{m}{s}]$	U_B $[\frac{m}{s}]$	ε_G $[-]$	ε_G/β $[-]$	Homogenous correlation $[\pm\%]$	Armand's correlation $[\pm\%]$	Liu *et al.* (2005) $[\pm\%]$
0.14	0.296	0.472	0.911	9.7	9.4	3.38
0.22	0.332	0.662	1.053	5	26.4	16.81
0.29	0.419	0.693	1.004	0.4	20.5	13.72

5.4.5 Film thickness

It is well known that the thin liquid film formed between the tube wall and the gas bubble plays an important role in micro tube heat transfer. As mentioned before, the film thickness varies significantly along the bubble, however even though there are small variations in film thickness, the simulated film thicknesses in the present study are only measured at the middle of the slug bubble for all tested cases. The simulation results for the film thickness,δ, and the percentage difference with existing correlations found in literature are tabulated in Table 5-7. The simulated liquid film was found to be thicker for short bubbles. The liquid film thickness is decreases with increasing U_{GS} , which also leads to increases in the capillary value. Similar results were reported in the experimental work conducted by Han and Shikazono (2009). They studied the effect of slug and liquid length on the liquid film of air-water in a 1.3 mm circular microchannel. They stated that that the liquid film thickness in a short bubble becomes thicker because the bubble tail also affects the liquid film thickness. An empirical correlation based on Ca, Re and We, proposed by them was compared in this study for Re>2000. The percentage difference between the simulated film thickness and the correlation proposed by them is in good agreement with the presented results with differences no larger than 15.2%.

Another correlation of the film thickness found in literature was developed by Patel *et al*. (2017), using their own data. This correlation was based on the importance of viscosity and surface tension effects. In the experimental work conducted by them, the effect of operating conditions and channel size on adiabatic air-water flows within slug flow regime was studied. The simulated thickness was observed to be in reasonable agreement with the empirical correlation proposed by Patel *et al*. (2017) with a percentage difference of less than 30%. However, the Patel *et al*. (2017) correlation over predicted δ / D by about 40% for the highest superficial gas velocity.

Table 5-7 : Percentage difference between simulation film thickness value with existing correlations.

U_{GS} $[\frac{m}{s}]$	Ca $[-]$	$\delta/_D$ $[-]$	Han and Shikazono (2009) $[\pm\%]$	Patel *et al*. (2017) $[\pm\%]$
0.14	0.0072	0.133	2.34	20
0.22	0.0081	0.117	4.54	29
0.29	0.0101	0.094	15.2	40.7

5.4.6 Pressure drop

The change in bubble length is interrelated to the change in the flow field, in particular to the change in pressure drop. Figure 5-37 shows the pressure distribution in a single unit cell for different superficial gas velocities at selected locations as noted in the previous section. Based on this figure, it can be concluded that the bubble slug is larger than the liquid slug in all cases and after an initial increase in the pressure increase in the axial direction, it subsequently starts to decrease when approaching the nose of the bubble. It is interesting to note that, for the higher superficial gas velocities in this study, a drop in pressure at y3 was observed. This drop may be related to the dry-out patch as seen in Figure 5-32 (c).

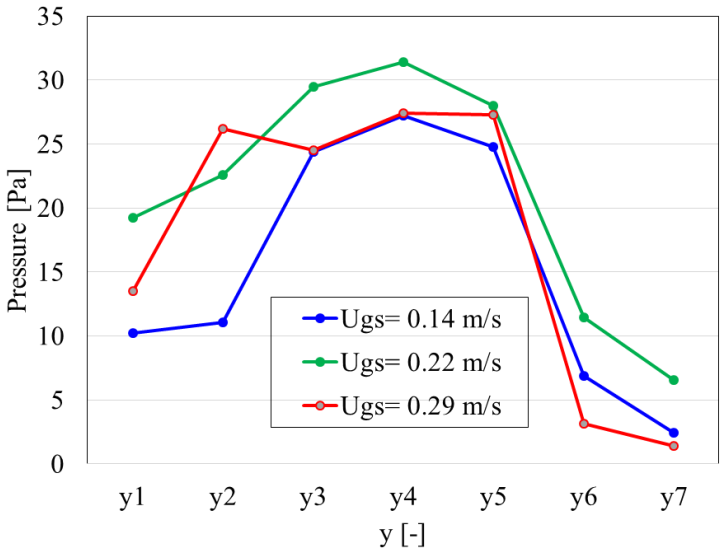

Figure 5-37 : Pressure distribution of unit cell at certain location.

The pressure drop over a single bubble, ΔP_b was calculated simply by taking the difference in pressures at the front and the back of the bubble in the presence of a constant liquid film thickness. According to the simulation, the pressure drop over a single bubble increased with increasing liquid and gas phase velocities and a similar observation was also reported by Choi *et al*. (2010). The simulated pressure drops obtained here were compared with existing correlations provided by Bretherton (1961) and Cherukumudi *et al*. (2015). Bretherton presented an expression for the pressure drop over a single Taylor gas bubble moving through a liquid-filled channel with a circular cross-section. The Laplace pressure from the surface tension and the curvature were taken into account and viscous forces were neglected when $Ca < 0.1$. Based on the percentage difference with the simulated pressure drop over the unit cell, a reasonable agreement with Bretherton's expression was obtained. Recently, Cherukumudi *et al*. (2015) developed an analytical expression for the pressure drop across long bubbles flowing in circular tubes based on a combination of lubrication theory and capillary effects. Even though the effects of inertial and gravity forces were neglected in this analytical expression, the prediction was found to be in good agreement with the pressure drop obtained in the simulations.

Table 5-8 : Percentage difference between simulation pressure drop across single bubble value with existing correlations.

U_{GS} $[\frac{m}{s}]$	ΔP_b $[Pa]$	Bretherton (1961) $[\pm\%]$	Cherukumudi *et al*. (2015) $[\pm\%]$
0.14	3.1522	36.50	13.24
0.22	4.0289	24.84	2.69
0.29	4.6832	25.06	2.39

5.4.7 Heat transfer

Figure 5-38 shows the comparison of the wall and fluid temperatures and the Nusselt number of a unit cell bubble slug for all cases. i.e; (a) $U_{GS} = 0.14\ m/s$ (b) $U_{GS} = 0.22\ m/s$ and (c) $U_{GS} = 0.29\ m/s$. Generally, for all cases, in the liquid region the wall temperature was found to increase in the axis direction to reach its maximum at the rear of gas bubble. As clearly shown in Figure 5-38(a) and (b), in the bubble slug region, both wall and fluid temperatures decrease in the y-direction due to the lower heat capacity of the gas compared to the liquid slug (as discussed in the previous section). However, for the largest superficial gas velocity high wall temperatures were obtained due to dry-out near the rear of the gas bubble. Both wall and fluid temperature decrease with y-axis in bubble slug region due to lower heat capacity compared to liquid slug as discussed in previous section and it clearly shown in Figure 5-38 (a) and (b). However, for a higher tested superficial velocity gas, showing high wall temperature due to dry-out near the rear of bubble gas. (see Figure 5-38 (c)).

It is also intended that simulated Nusselt number at selected location is higher at rear of slug bubble where the film thickness is thin and the Nusselt value decreases as the film thickness increases at front of the bubble. Furthermore, as mentioned earlier, due to occurrence of the dry-out patch on the wall of the channel for higher tested superficial gas velocity lead to high local wall temperature thereby lower heat transfer coefficient. Furthermore, as seen in this figure, $Ugs = 0.22\ m/s$ was showing a greater heat transfer rate compared to other cases. This is due to bigger recirculation occurred near rear of bubble gas (as shown in Figure 5-34 (a)) which lead to increase the thermal heat performance as stated by Kumari *et al*. (2019).

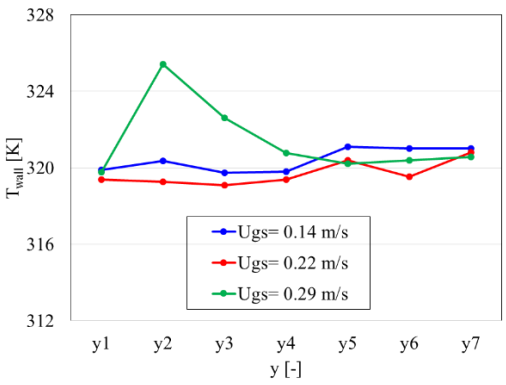

(a)

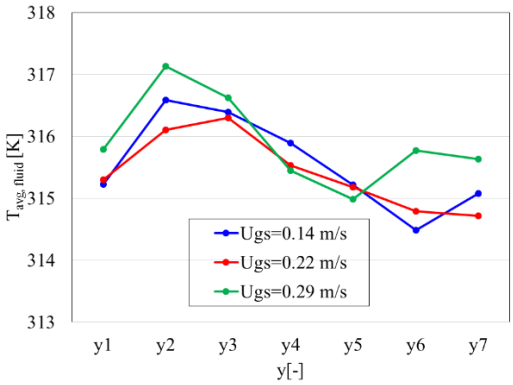

(b)

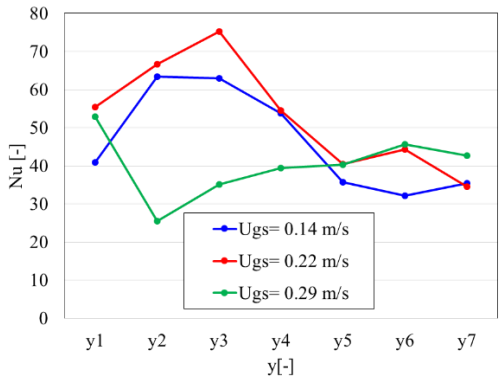

(c)

Figure 5-38 : Comparison of (a) Wall temperature (T_w), (b) fluid temperature (T_f), and Nusselt number (Nu) at y_k location of unit cell for all cases i.e; $U_{GS} = 0.14\ m/s$, $U_{GS} = 0.22\ m/s$, $U_{GS} = 0.29\ m/s$.

5.5 Summary

The numerical simulations of R134a vapour-liquid in 1 mm circular microchannel with a vertical orientation was developed in this chapter. In the first part of this study, a numerical flow regime map was produced by performing simulations for 82 different sets of flow conditions in order to identify the slug flow boundaries. In these simulations two dimensional, axi-symmetry was assumed in order to save computational time and effort. The present results were verified through comparison with the visualization results reported in the experiments of Chen *et al*. (2006) and were shown to agree well. In addition, flow patterns maps generated from the numerical results was also compared with other flow regime transition maps found in the open literature.

In the second part, the topology of the hydrodynamic flow and heat transfer distribution of slug flow was using the annular (concentric) nozzles configuration studied. In this study, a three-dimensional computational domain was used. A non-identical shape of slug cells was observed, where a slug cell with a dry zone and irregular shapes were obtained in the present 3-D numerical work. Therefore, several individual cells with different behaviours and shapes were carefully selected in order to understand the characteristics of the hydrodynamic and thermal behaviour. Furthermore, the effect of superficial gas velocity (with constant superficial liquid velocity) on two phase slug flow was studied. Three different superficial gas velocities were employed in this study. As the mixture velocity increases, the void fraction, β, the capillary number, Ca, and the Reynolds number, Re, are also increasing. In addition, changes in bubble shape, bubble length, liquid film thickness, velocity and temperature profile, pressure drop and heat transfer at different operations were discussed.

6 CONCLUSIONS AND RECOMMENDATIONS

6.1 Conclusions

A numerical study of fluid flow and heat transfer in single and two phase in microchannels was conducted using the computational software package, ANSYS Fluent. The geometry construction and mesh generation was performed in ICEM and for all cases and the hexa mashing grid scheme was used for meshing. In single phase flow, two different configurations were studied, single channel and multichannel configurations. Rectangular microchannel was used in both systems. The effect of axial conduction and geometrical parameters, i.e. aspect ratio and hydraulic diameter, on fluid flow and heat transfer were investigated in the single rectangular channel. The flow distribution inside the channels including the effect of conjugate heat transfer were studied in the multichannel system. Furthermore, the effect of various parameters such as, inlet/outlet area manifold, inlet/outlet flow arrangement and number of channels on flow distribution inside channels were examined. A newly designed of inlet manifold was proposed in this study.

In the two phase study, a 1 mm circular microchannel was used and the design of numerical work pursued two purposes. The first aim was to develop numerical flow regime maps in order to identify the slug flow boundaries and the dependence on annular nozzle configuration and on liquid properties. In this work, the flow field was calculated using a two dimensional, axisymmetric geometry to save computational time and effort. Secondly, to examine the topology of hydrodynamic flow and heat transfer distribution of slug flow. Furthermore, to related these to the operational condition, i.e. gas superficial velocity. In this part, three dimensional work was carried out.

6.1.1 CFD Modelling of Single Phase Fluid Flow in a Rectangular Single Microchannel

A numerical study was carried out to investigate single phase heat transfer and fluid flow in a rectangular microchannel using water as a working fluid. Four models were investigated namely 2D, 3D thin-wall (one side heated), 3D thin-wall (three side heated) and 3D fully conjugated heat transfer model in a single channel system to consider the conjugate effect on heat transfer. The main conclusions are summarized as below:

1. The experimental and numerical results demonstrated that transition from laminar to turbulent occurs at Re=1600–2000.

2. The 3D fully conjugate model showed a significant deviation compared to the experimental data indicating significant conjugate effects. The model predicted that the heat flux is not uniformly distributed along the channel. The deviation was attributed to the assumption of uniform heat flux in the experimental data reduction. In order to consider the effect of non-uniform heat flux in the experimental data reduction, the local heat flux should be measured accurately, which is very difficult in microchannels. Thus, most researchers assumed uniform heat flux as an approximation. The 3D full conjugate simulation can help in determining how much is the error due to the assumption of uniform heat flux boundary condition. For the geometry examined in the present study this error was found to be more than 50% on average.

3. The excellent agreement between the 3D thin-wall model and the experimental data in this study is only due to the fact that they were based on the assumption of uniform heat flux boundary condition, which does not hold true as discussed above. In other words, this agreement does not mean that the simplified 3D thin-wall model is more accurate than the 3D full conjugate model.

4. The predicted friction factor was significantly lower than the prediction by the conventional theory in both laminar and turbulent regions. However, it was found to be in very good agreement with existing experimental results in the laminar region.

Numerical simulations were carried out to investigate the effect of hydraulic diameter and aspect ratio on fluid flow and heat transfer in single rectangular microchannels. In the simulations, a constant heat flux boundary condition was applied on three walls, while the fourth top wall was adiabatic. In the first set of simulations, the range of hydraulic diameters was varied from 0.1 to1 mm and the aspect ratio was fixed at 1. In the second set of simulations, the aspect ratio was varied between 0.39 and 10 while the hydraulic diameter was kept constant at 0.56 mm. The simulations were conducted for a range of Reynolds number from 100 to 2000 (laminar flow) and water was used as the working fluid. Entrance and exit effects were considered by including inlet/outlet plenums in the study. The following conclusions can be drawn:

1. The dimensionless hydrodynamic entrance length does not depend on aspect ratio and hydraulic diameter. The correlations given by Ahmad and Hassan, (2010) and Galvis *et al*. (2012) can predict reasonably the hydrodynamic entry length.

2. The friction factor was found to decrease slightly with increasing aspect ratio (AR) until $AR > 2$ after which it increases continuously with aspect ratio. Thus, based on friction factor data only, an aspect ratio between 1 and 2 may be recommended or designed in order to achieve low pressure drop. However, including heat transfer and using the thermal performance index as an evaluation criterion, channels with AR= 0.39 gave the best performance.

3. Increasing the aspect ratio beyond 2 resulted in a significant effect on the velocity profile. It changed from a nearly parabolic shape at low aspect ratio to

a flattened shape with a large slope at high aspect ratio. This may explain why the friction factor increases with aspect ratio.

4. The aspect ratio has an insignificant effect on the heat transfer rate.

5. The friction factor and average Nusselt number increases with increasing hydraulic diameter for simultaneously thermally and hydrodynamically developing flow.

6. The effect of the hydraulic diameter on friction factor and heat transfer is more important compared to the effect of aspect ratio.

7. The correlations of Shah and London (1978) for predictions of friction factor and heat transfer rates are still applicable at microscale with a reasonable accuracy. This agrees with the conclusion given by Rosa *et al*. (2009) who reported that macro scale theory and correlations are valid at micro scale if measurement uncertainty and scaling effects were carefully considered.

8. The thermal performance index should be taken into consideration in the analysis of thermal-hydraulic performance of microchannels heat exchangers.

6.1.2 CFD Modelling of Single Phase Fluid Flow in a Rectangular Micro Multichannel Microchannel

A numerical study was carried out to investigate single phase heat transfer and fluid flow in a rectangular multichannel microchannel using R134a as a working fluid. The conjugate effect was taken into account. The main conclusions were summarized below:

1. The inlet manifold with a gradual reduction in flow area exhibited very reasonable performance and uniform flow distribution among the channels.

2. The inlet/outlet manifold area has a significant influence on the flow behaviour inside the channels.

3. Multichannel configurations with having a ratio of inlet and outlet area greater than 1 showing the worst flow distributions.

4. Inlet and outlet manifolds with large area gave a better flow distribution for all tested flow arrangements (U-I-Z type).

5. Z-type flow arrangement for both Type D-1 and Type D-2 resulted in higher maldistribution parameters.

6. Firstly, the maldistribution value was found to increase as the number of channels increases when the number of channels is less than twenty. In contrast, if the number of channels exceeds twenty, the maldistribution value reduces with increasing number of channels.

7. A newly design of inlet manifold has been proposed. The sharp edges at the inlet manifold was replaced with curve edges to reduce the occurrence of flow recirculation, which also lead to improve the flow distribution inside channel.

6.1.3 Two phase flow in 1 mm circular microchannel

A numerical flow patterns map within a vertical circular microchannel with diameter of 1 mm under adiabatic conditions were simulated here for 82 different sets of flow conditions. The microchannel is modelled as a two dimensional axisymmetric domain of diameter D to save computational time and effort. The effect of gravity has been accounted. The superficial gas velocity ranges from 0.01 to 2 m/s, and the envelope of superficial liquid velocity varied from 0.01 to 6 m/s. The two-phase flow of R134a in the channel is assumed to be incompressible, adiabatic with constant thermophysical properties. The main conclusions are summarized below:

1. There are four basic flow patterns of R134a two-phase flow, including bubbly flow, slug flow, slug-annular, annular flow, in a circular microchannel. In general, when the liquid superficial velocity is constant and the gas superficial velocity increases, the flow patterns were evolved in sequence from bubbly flow, slug, slug-annular and annular flow.

2. Two different shape of bubbles was observed; spherical (U_{LS} <0.06), and bubble with cap shape in this study. The spherical like shape of the bubbles were flowing in the center tube with diameters smaller than the channel size suggests the dominance of the surface tension force, which always tends to minimize the surface free energy by reducing the surface area; the shape of bubbles and length between each bubbles along the channel is regular. However, different behaviour of bubble flow at U_{LS} >0.07 was observed. In this case, bubbles with cap bubbly head were observed. Furthermore, at this condition, the size and the shape of the bubbles are varied.

3. The comparison of visualization results and flow pattern map of Chen *et al*. (2006) predicted well the numerical data except the transition from bubbly-slug and slug churn flow regime. Also, it is worth noting that, instead of churn flow, the slug-annular flow pattern was observed in the churn flow region as assigned in Chen *et al*. (2006),

4. The flow pattern maps of Hassan *et al*. (2005) and Wei *et al*. (2017) reasonably predicted the experimental flow pattern data.

5. The study also shows that CFD method is a feasible way to draw the two-phase flow patterns map.

A two-phase gas-liquid flow in a cylindrical pipe with a diameter of 1 mm was considered in this study. In the present work, slug formation by an annular (concentric) nozzles configuration, as conducted by Shao *et al*. (2008), has been studied. As shown in the schematic in Figure 5-16, the gas enters in the centre of the channel via a nozzle while the liquid flows around the nozzle as an annulus. The flow field has been

calculated using a three-dimensional geometry so that the effect of gravity could be taken into account.

1. A non-identical shape of the gas bubble slugs was observed, where cells with a dry zone and irregular shapes were obtained in the present 3-D numerical work.

2. A high pressure was observed in the upstream channel due the necking process, where gas flow accelerates leading to a large pressure drop across the neck.

3. The higher value of Nu_x is obtained at the tail of bubble slug and the lower one at the nose of the gas bubble.

4. Dry-out that occurred at the tail of the bubble slug minimizes the heat transfer rate.

5. The shape of bubble gas was observed to change at different superficial gas velocity. For the for lower tested superficial velocity gas, ($U_{GS} = 0.14\ m/s$) a hemispherical cap shape was observed at the front and rear of the bubble slug. As the superficial gas velocity increases, ($U_{GS} = 0.22\ m/s$) the front of bubble was showing similar shape, but the rear of the bubble become unstable and an irregular shape was observed. However, for the highest superficial gas velocity tested in this study, ($U_{GS} = 0.29\ m/s$) slug bubble at this conditions was having flatter tail and sharper nose.

6. The 'jet-like" thermal shape was only observed for a unit cell length of bubble slug , $L_B < 1.00$ mm

7. None of the tested conditions reached a laminar, single phase and fully developed flow profile (parabolic profile). Similar results were also report by Gupta *et al*. (2010a) in their numerical work.

8. The normalized velocity profiles for all cases are showing similar profile, where the velocity profile is flattened like at the center and the velocity of liquid slug is almost close to U_{TP}.

9. The simulated liquid film is thicker for short bubbles. The value of liquid film thickness is decreasing as U_{GS} and Ca number increases.

10. The pressure of a unit cell of bubble gas was increases in axial direction and it is start decrease when approaching nose of the bubble.

11. The pressure drop of single bubble increased with increasing gas phase velocities. Similar observation was also reported by Choi *et al*. (2010). The simulated pressure drop was in agreement with that predicted by the correlation developed by Cherukumudi *et al*. (2015).

12. The bigger recirculation occurred near rear of bubble gas lead to increase the thermal heat performance.

6.2 Recommendations

Based on the results of the present thesis, there are still many open questions and discussions on fluid flow and heat transfer in single and two phase flows in microchannel. The followings are the most important ones which could be considered and addressed in future studies:

1. Single phase flow in microchannel

- The shape and size of channel can affect the flow distribution in multichannel heat sinks, therefore, further investigation on significant impact of these factors is still needed.

- Most previous past reports concerned research work on predicting characteristic of single phase fluid flow and heat transfer in single

microchannel. However, there is lack of available work related to theoretical models for predicting flow and heat transfer in multichannel.

2. Two phase flow in microchannel

- The flow regime maps developed in this project provide some guidance on the occurrence of interfacial phenomena in similar system and using similar fluids. However, more generalised flow pattern maps which can potentially be applied for different channel geometries and fluids are in need.

REFERENCES

Aussillous, P. & Quéré, D., 2000. Quick deposition of a fluid on the wall of a tube. *Physics of Fluids* , 12(10), pp. 2367-2371.

Tibiriçá, C. . B., Nascimento, F. J. d. & Ribatski , G., 2010. Film thickness measurement techniques applied to micro-scale two-phase flow systems. *Experimental Thermal and Fluid Science,* Volume 34, p. 463–473.

Zhang, J., Fletcher, D. F. & Li, W., 2016. Heat transfer and pressure drop characteristics of gas–liquid Taylor flow in mini ducts of square and rectangular cross-sections. *International Journal of Heat and Mass Transfer 103 (2016) 45–56,* Volume 103, p. 45–56.

Abadie, T., Aubin, J., Legendre, D. & Xuereb, C., 2012. Hydrodynamics of gas–liquid Taylor flow in rectangular microchannels. *Microfluid Nanofluid,* Volume 12, p. 355–369.

Abdollahi, A., Norris, S. & Sharma, R. N., 2019. Heat transfer measurement techniques in microchannels for single and two-phase Taylor flow. *Applied Thermal Engineering* , Volume 162, pp. 1-11.

Adam, T., Abdul Khalik, S., Jeter, S. & Qureshi, Z., 1998. An experimental investigation of single-phase forced convection in microchannels. *Int. J. Heat Mass Transfer,* Volume 41, pp. 851-857.

Agostini, B., Bontemps, A. & Thonon, B., 2006. Effect of Geometrical and Thermophysical Parameters on Heat Transfer Measurements in Small Diameter Channels. *Heat Transfer Engineering,* 27(1), pp. 14-24.

Ahmad , T. & Hassan, I., 2010. Experimental analysis of microchannel entrance lenght charcteristics using microparticle image velocimetry. *Journal of Fluid Engineering,* Volume 132, pp. 1-13.

Amiri, E. O., 2019. Numerical investigation of uniformity of flow distribution in parallel micro-channels with different manifolds and working fluids. *Microsystem Technologies* , Volume 25, p. 937–943.

Anbumeenakshi, C. & Thansekhar, M., 2016. Experimental investogation of header shape and inlet configuration on flow maldsitribution in microchannel. *Experimental Thermal anf Fluid Science,* Volume 75, pp. 156-161.

Angeli, P. & Gavriilidis, A., 2008. Hydrodynamics of Taylor flow in small channels: A review. *Proceedings of the Institution of Mechanical Engineers, Part C: Journal of Mechanical Engineering Science, ,* 222(5), pp. 737-751.

Anon., n.d. *ANSYS FLUENT 12.0, User's Guide.* [Online].

Asadi, M., Xie, G. & Sunden, B., 2014. A review of heat transfer and pressure drop characteristics of single and two-phase microchannels. *International Journal of Heat and Mass Transfer ,* Volume 79, pp. 34-53.

Asadolahi, A. N., Gupta, R., Fletcher, D. F. & Haynes, B. S., 2011. CFD approaches for the simulation of hydrodynamics and heat transfer in Taylor flow. *Chemical Engineering Science,* 66(22), pp. 5575-5584.

Asadolahi, A. N. et al., 2012. VAlidation of CFD model of Taylor flow hydrodynammics and heat transfer. *Chemical Engineering Science,* Volume 69, pp. 541-552.

Aussillous, P. & Quéré, . D., 2000. Quick deposition of a fluid on the wall of a tube. *Physics of fluids ,* Volume 12, pp. 2367-2371.

B., X., O. K., W. N. & C. W., 2000. Experimental Investigation of Flow Friction for Liquid Flow in Microchannels. *Int. Comm. Heat Transfer,* 27(8), pp. 1165-1176.

Balaji, S. & Lakshminarayanan, S., 2006. Improved design of microchannel plate geometry for uniform flow distribution. *The Canadian Jounal of Chemical Engineering,* Volume 84, pp. 715-721.

Bandara, T., Nguyen, N.-T. & Rosengarten, G., 2015. Slug flow heat transfer without phase change in microchannels : A review. *Chemical Engineering Science ,* Volume 126, pp. 283-295.

Bao, Z. Y., Fletcher, D. F. & Haynes, B. S., 2000. An experiment study of gas and liquid flow in a narrow conduit. *International Journal of Heat and Mass Transfer,* Volume 43, pp. 2313-2324.

Barajas, A. M. & Panton, R. L., 1993. The effects of contact angle on two-phase flow in capillary tubes. *International Journal of Multiphase Flow,* 19(2), pp. 337-346.

Baviere, R., Favre-Marinet, M. & Person, S. L., 2006. Bias effect on heta transfer measurements in microchannel flows. *International Journal of Heat and Mass Tranfer ,* Volume 49, pp. 3325-3337.

Bayareh, M., Esfahany, M. N., Afshar, N. & Bastegani, M., 2020. Numerical study of slug flow heat transfer in microchannels. *International Journal of Thermal Sciences ,* Volume 147, pp. 1-12.

Beavers, G., Sparrow, E. & Magnuson, R., 1970. Experiments on hydrodynamically developing flow in rectangular ducts of arbitrary aspect ratio. *International Journal of Heat and Mass Transfer,* 13(4), pp. 689-701.

Bejan, A., 2004. *Convection Heat Transfer.* New Jersey: John Wiley & Son, Inc.

Biswal, L., Chakraborty, S. & Som, S., 2009. Design and optimization of single phase liquid cooled microchannel heat sink. *IEEE Transaction on Components and Packing Technologies,* Volume 32, pp. 876-886.

Blasius, H., 1913. *Ähnlichkeitsgesetz bei Reibungsvorgängen in Flüssigkeiten.* Berlin, s.n.

Bordbar, A., Taassob, A., Zarnaghsh, A. & Kamali, R., 2018. Slug flow in microchannels : Numerical simualtion and application. *Journal of Industrial and Engineerign Chemistry,* Volume 62, pp. 26-39.

Brackbill, J., Kothe, D. & Zemach, C., 1992. A Continuum Method for Modeling Surface Tension. *Journal of Compuational Physics,* Volume 100, pp. 335-354.

Bretherton, F., 1961. The motion of long bubbles in tubes. *Journal of Fluid Mechanics,* 10(2), pp. 166-188.

Camilleri, R., Howey, D. & McCulloch, M., 2015. Predicting the flow distribution in compact parallel flow heat exchangers. *Applied Thermal Engineering,* Volume 90, pp. 551-558.

Camilleri, R., Howey, D. & McCulloch, M., 2015. Predicting the flow distrinution in compact parallel flow heat exchangers. *Applied Thermal Engineering,* Volume 90, pp. 551-558.

Celata, G. P., Cumo, M., Gugliemi, M. & Zummo, G., 2002. Experimental Investigation in Hydraulic and Single-Phase Heat Transfer in 0.130mm Capillary Tube. *Microscale Thermphysical Engineering,* Volume 6, pp. 85-97.

Chalgeri, V. S. & Jeong, J. H., 2019. Flow patterns of vertically upward and downward air-water two-phase flow in a narrow rectangular channel. *International Journal of Heat and Mass Transfer,* Volume 128, p. 934–953.

Chandrupatla, A. R. & Sastri, V., 1977. LAMINAR FORCED CONVECTION HEAT TRANSFER OF A NON-NEWTONIAN FLUID IN A SQUARE DUCT. *Int. J. Heat Mass Transfer,* Volume 20, pp. 1315-1324.

Chaoqun, Y. et al., 2013. Characteristics of slug flow with inertial effects in a rectangular microchannel. *Chemical Engineering Science ,* Volume 95, p. 246–256.

Chein, R. & Chen, J., 2009. Numerical study of inlet/outlet arrangement effect on microchannel heat sink performance. *International Journal of Thermal Sciences ,* Volume 48, pp. 1627-1638.

Chen, L., Tian, Y. S. & Karayiannis, T. G., 2006. The effect of tube diameter on vertical two-phase flow regimes in small tubes. *International Journal of Heat and Mass Transfer ,* Volume 49, p. 4220–4230.

Chen, Y., Kulenovic, R. & Mertz, R., 2009a. Numerical study on the formation of Taylor bubbles in capillary tubes. *Internationa Journal of Thermal Sciences,* Volume 48, pp. 234-242.

Cherukumudi, A., Klaseboer, E., Khan, S. A. & Manica, R., 2015. Prediction of the shape and pressure drop of Taylor bubble in circular tubes. *Microfluid Nanofluid,* Volume 19, pp. 1221-1233.

Chinnov, E., Ron'shin, F. & Kabov, O., 2016. Two-phase flow patterns in short horizontal rectangular microchannels. *International Journal of Multiphase Flow ,* Volume 80, p. 57–68.

Choi , C., Yu, D. & Kim, M., 2010. Adiabatic two-phase flow in rectangular microchannels with different aspect ratios: Part II – bubble behaviors and pressure drop in single bubble. *International Journal of Heat and Mass Transfer ,* Volume 53, p. 5242–5249.

Choi, C. W., Yu, D. I. & Kim, M. H., 2011. Adiabaic two-phase flow in rectangular microchannels with different aspect ratios: Part I- Flow pattern, pressure drop and void fraction. *International Journal of Heat and Mass Transfer,* Volume 54, pp. 616-624.

Choi, C., Yu, D. & Kim, M., 2010. Adiabatic two-phase flow in rectangular microchannel with different aspect ratio: Part II-bubbe behaviors and pressure drop in single bubble. *Internatinal Journal of Heat and Mass Transfer,* Volume 53, pp. 5242-5249.

Choi, S., Barron, R. & Warrington , R., 1991. Fluid flow and heat transfer in microtubes. *Micromechanical Sensors, Actuators, and Systems, ASME,* Volume 32, pp. 123-133.

Choi, S. H., Shin, S. & Cho, Y. I., 1993. The effect od area ratio on the flow distribution un liquid cooling module manifolds for electronic packaging. *Int. Comm. Heat Mass Transfer,* Volume 20, pp. 221-234.

Choi, S. H., Shin, S. & Cho, Y. I., 1993. The effect of the reynolds number and width ratio on flow distribution in manifolds of liquid cooling modules for electronic packaging. *Int. Comm. Heat Mass Transfer,* Volume 20, pp. 607-617.

Choo, K. & Kim, S. J., 2011. Heat Transfer and Fluid Flow Characteristics of Nonboiling Two-Phase Flow in Microchannels. *Journal of Heat Transfer,* Volume 133, pp. 1-7.

Chung, P.-Y. & Kawaji, M., 2004. The effect of channel diameter on adibatic two-phase flow characteristics in microchannels. *International Journal of Multiphase Flow,* Volume 30, pp. 735-761.

Cole, K. D. & Cetin, B., 2011. The effect of axial conduction on heat transfer in a liquid microchannel flow. *International Journal of Heat and Mass Transfer,* Volume 54, pp. 2542-2549.

Coleman, J. W. & Garimella, S., 1999. Characterization of two-phase flow patterns in small diameter round and rectangular tubes. *International Journal of Heat and Mass Transfer,* 42(15), pp. 2869-2881.

Commenge, J., Falk, L., Corriou, P. & Matlosz, M., 2002. Optimal design for flow uniformity in microchannel reactors. *AIChE Journal,* Volume 48, pp. 345-358.

Cubaud, T. & Ho, C.-M., 2004. Transport of bubbles in square microchannels. *PHYSICS OF FLUIDS,* 16(12), pp. 4575-4585.

Dai, B. et al., 2014. Investigation on convective heat transfer characteristics of single phase liquid flow in multi-port micro-channel tubes. *International Journal of Heat and Mass Transfer,* Volume 70, pp. 114-118.

Dai, L., Cai, W. & Xin, F., 2009. Numerical Study on Bubble Formation of a Gas-Liquid Flow in a T-Junction Microchannel. *Chem. Eng. Technol.,* 32(12), p. 1984–1991.

Datta, A. & Majumdar, A., 1980. Flow distribution in parallel and reverse flow manifolds. *Int. J. Heat and Fluid Flow,* 2(4), pp. 253-262.

Dharaiya , V. & Kandlikar, S., 2012. Numerical investigation of Heat Transfer in Rectangular Microchannels Under H2 Boundary Condition During Developing and Fully Developed Laminar Flow. *Journal of Heat Transfer,* Volume 134, pp. 1-10.

Dixit, T. & Ghosh, I., 2015. Review of micro- and mini-channel heat sinks and heat exchangers for single phase fluids. *Renewable and Sustainable Energy Reviews ,* Volume 41, pp. 1298-1311.

Dziubinski, M., Fidos, H. & Sosno, M., 2004. The flow pattern map of a two-phase non-Newtonian liquid–gas flow in the vertical pipe. *International Journal of Multiphase Flow,* Volume 30, p. 551–563.

Ergu, O. B., Sara, O. N., Yapici, S. & Arzutug, M. E., 2009. Pressure drop and point mass transfer in rectangular microchannel. *International Communications in Heat and Mass Transfer,* Volume 36, pp. 618-623.

Fayyadh, E. M., Mahmoud, M. M. & Karayiannis, T. G., 2015. *Flow Boiling Heat Transfer of R134a in Multi Micro Channels.* Barcelona, Spain, Proceedings of the World Congress on Mechanical, Chemical, and Material Engineering (MCM 2015).

Fedorov, A. G. & Viskanta, R., 2000. Three-dimensional Conjugate Heat Transfer in The Microchannel Heat Sink for Electronic Packaging. *International Journal of Heat and Mass Transfer ,* Volume 43, pp. 399-415.

Fukagata, K., Kasagi, N., Ua-arayporn, P. & Himeno, T., 2007. Numerical simulation of gas-liquid two-phase flow and convective heat transfer in a microtube. *International Journal of Heat and Fluid Flow,* Volume 28, pp. 72-82.

Fukano, T. & Kariyasaki, A., 1993. Characteristics of gas-liquid two-phase flow in a capillary tube. *Nuclear Engineering and Design,* 141(1-2), pp. 59-68.

Galvis, E., Yarusevych, S. & Culham, J., 2012. Incompresiible laminar developing flow in microchannels. *Journal of Fluids Engineering,* Volume 134, pp. 1-4.

Gamrat , G., Favre-Marinet, M. & Asendrych, D., 2005. Conduction and entrance effects on laminar liquid flow and heat transfer in rectangular microchannels. *International Journal of Heat and Mass Transfer ,* Volume 48, pp. 2943-2954.

Gao, P., Person, S. L. & Favre-Marinet, M., 2002. Scale-effects on hydrodynamics and heat transfer in two-dimensional mini and microchannels. *International Journal of Thermal Sciences,* Volume 41, pp. 1017-1027.

Garstecki, P., Fuerstman, M. J., Stone, H. A. & Whitesides, G. M., 2006. Formation of droplets and bubbles in a microfluidic T-junction—scaling and mechanism of break-up. *Lab on Chip,* pp. 437-446.

Ghani, I. A. et al., 2017. The effect of manifold zone parameters on hydrothermal performance of microchannel heat sink : A review. *International Journal of Heat and Mass Trasnfer,* Volume 109, pp. 1143-1161.

Gunnasegaran, P., Mohammed, H., Shuaib, N. & Saidur, R., 2010. The effect of geometrical parameter on heat transfer characteristics of microchannels heat sink with different shapes. *International Communications in Heat and Mass Transfer ,* Volume 37, pp. 1078-1086.

Guo, F. & Chen, B., 2009. Numerical Study on Taylor Bubble Formation in a Micro-channel T-Junction Using VOF Method. *Microgravity Sci. Technol ,* Volume 21, pp. 51-58.

Guo, Z.-Y. & Li, Z.-X., 2003. Size effect on microscale single-phase flow and heat transfer. *International Journal of Heat and Mass Transfer,* Volume 46, pp. 149-159.

Gupta, R., Fletcher , D. & Haynes, B., 2010. Taylor Flow in Microchannels: A Review of Experimental and Computational Work. *The Journal of Computational Multiphase Flows,* 2(1), pp. 1-31.

Gupta, R., Fletcher, D. F. & Haynes, B. S., 2009. On the CFD modelling of Taylor flow in microchannels. *Chemical Engineering Science,* Volume 64, pp. 2941-2950.

Gupta, R., Fletcher, D. F. & Haynes, B. S., 2010. CFD modelling of flow and heat transfer in the Taylor flow regime. *Chemical Engineering Science* , Volume 65, pp. 2094-2107.

Gupta, R., Fletcher, D. & Haynes, B., 2010. Taylor Flow in Microchannels: A Review of Experimental and Computational Work. *The Journal of Computational Multiphase Flows,* 2(1), pp. 1-31.

Haase, S., 2016. Characterisation of gas-liquid two-phase flow in minichannels with co-flowing fluid injection side the channel, part I: unified mapping of flow regimes. *International Journal of Multiphase Flow,* Volume 87, pp. 197-211.

Haase, S., 2017. Characterisation of gas-liquid two-phase flow in minichanenls with co-flowing fluid injection inside the channel, part II: gas bubble and liquid slug lengths, film thickness, and void frcation within Taylor flow. *International Journal of Multiphase Flow,* Volume 88, pp. 251-269.

Han, D. H. & Kedzierski, M. A., 2008. Micro effects for single phase pressure drop in microchannels. *Int. J. Trans. Phenomena,* Volume 10, pp. 103-112.

Han, Y. & Shikazono, . N., 2009. Measurement of the liquid film thickness in micro tube slug flow. *International Journal of Heat and Fluid Flow,* Volume 30, pp. 842-853.

Harms, T. M., Kazmierczak, M. J. & Gerner, F. M., 1999. Developing Convective Heat Transfer in Deep Rectangular Microchannels. *International Journal of Heat and Fluid Flow,* Volume 20, pp. 149-157.

Hasan, M. I., Rageb, A. M. A. & Yaghoubi, M., 2012. Investigation of a counter flow microchannel heat exchanger performance witth nanofluid as a coolant. *Journal of Electronics Cooling and Thermal Control,* Volume 2, pp. 35-43.

Hassan, I., Vaillancourt, M. & Pehlivan, K., 2005. Two-Phase Flow Regime Transitions in Microchannels: A Comparative Experimental Study. *Microscale Thermophysical Engineering,* Volume 9, p. 165–182.

Hassan, M. I., Hasan, H. M. & Abid, G. A., 2014. Study of axial conduction in parallel flow microchannel heat exchanger. *Journal of King Saud University-Engineering Science,* Volume 26, pp. 122-131.

Haverkamp, V. et al., 2006. Hydrodynamics and Mixer-Induced Bubble Formation in Micro Bubble Columns with Single and Multiple-Channels. *Chem. Eng. Technology,* 29(9), p. 1015–1026.

Heil, M., 2001. Finite Reynolds number effects in the Bretherton. *PHYSICS OF FLUIDS,* 13(9), pp. 2517-2521.

He, Q., Hasegawa, Y. & Kasagi, N., 2010. Heat transfer modelling of gas-liquid slug flow without phase change in micro tube. *International Journal of Heat and Fluid Flow,* Volume 31, pp. 126-136.

Iaccarinno , G., Ooi, A., Durbin, P. & Behnia, M., 2002. Conjugate heat transfer predictions in two-dimensional ribbed passages. *International Journal of Heat and Fluid Flow,* Volume 23, pp. 340-345.

Irandoust, S. & Anderson, B., 1989. Liquid Film in Taylor Flow trough a Capillary. *Ind. Eng. Chem. Res.,* Volume 28, pp. 1684-1688.

Jang, J.-Y., Huang , Y.-X. & Cheng , C.-H., 2010. The effect of geometric and operating conditions on the hydrogen production performance of a micro-methanol steam reformer. *Chemical Engineering Science,* Volume 65, pp. 5495-5506.

Jones, B. J., Lee, P.-S. & Garimella, S. V., 2008. Infrared micro-particle velocity measurements and predictions of flow distribution in microchannel heat sink. *International Journal of Heat and Mass ,* Volume 51, pp. 1877-1887.

Judy, J., Maynes, D. & Webb, B., 2002. Characterization of frictional pressure drop for liquid flows through microchannels. *International Journal of Heat and Mass Transfer ,* Volume 45, pp. 3477-3489.

Kadam, S. T. & Kumar, R., 2014. Twenty first century cooling solution: Microchannel heat sink. *International Journal of Thermal Sciences,* Volume 85, pp. 73-92.

Kandlikar , S. G. et al., 2013. Heat Transfer in Microchannels-2012 Status and Research Needs. *Journal of Heat Transfer,* Volume 135, pp. 1-18.

Kandlikar, S. et al., 2005. *Heat transfer and fluid flow in minichannels and microchannels.* s.l.:Elsevier.

Kandlikar, S. et al., 2009. Measurement of flow maldistribution in parallel channels and its application to ex-situ and in-situ experiements in PEMFC water management studies. *International Journal of Heat and Mass Transfer,* Volume 52, pp. 1741-1752.

Kashaninejad, N., Chan, W. K. & Nguyen, N.-T., 2012. *Analytical and numerical investigations of the effects of microchannel aspect ratio on velocity profile and friction factor*. Gold Coast, Australia, International Conference on Computational Methods.

Kawahara, A., Chung, P. -Y. & Kawaji, M., 2002. Investigation of two-phase flow pattern, void fraction and pressure drop in a microchannel. *International Journal of Multiphase Flow,* 28(9), pp. 1411-1435.

Kim , D., Yu, C.-H., Yoon, S. H. & Choi, J. S., 2011. Effect of manifold geometries on flow distribution to parallel microchannels. *Journal of Mechanical Science and Technology,* 25(12), pp. 3069-3074.

Kim, B., 2016. An experimental study on fully developed laminar flow and heat transfer in rectangular microchannels. *International Journal of Heat and Fluid Flow,* Volume 62, pp. 224-232.

Kim, J., Shin, J. H., Sohn, S. & Yoon, S. H., 2019. Analysis of non-uniform flow distribution in parallel micro-channels. *Journal of Mechanical Science and Technology* , Volume 33 , p. 3859~3864.

Kim, S., Choi, E. & Cho, Y. I., 1995. The effect of header shapes on the flow distribution in a manifold for electronic packing applications. *International Communications in Heat and Mass Transfer,* 22(3), pp. 329-341.

Kishor, K. et al., 2017. Numerical Study on Bubble Dynamics and Two-Phase Frictional Pressure Drop of Slug Flow Regime in Adiabatic T-junction Square Microchannel. *Chem. Biochem. Eng. Q.,* 31(3), p. 275–291.

Klaseboer, E., Gupta, R. & Manica, R., 2014. An extended Bretherton model for long Taylor bubbles at moderate capillary numbers. *Physics of Fluids,* Volume 26, pp. 1-8.

Klaseboer, E., Gupta, R. & Manica, R., 2014. An extended Bretherton model for long Taylor bubbles at moderate capillary numbers. *Physics of Fluids* , Volume 26, pp. 1-8.

Kou, H.-S., Lee, J.-J. & Chen, C.-W., 2008. Optimum thermal performance of microchannel heat sink by adjusting channel wiidth and height. *International Communications in Heat and Mass Transfer,* Volume 35, pp. 577-582.

Kreutzer, M. T. et al., 2005. Inertial and interfacial effects on pressure drop of Taylor flow in capillaries. *AIChE Journal,* 51(9), pp. 2428-2440.

Kumaraguruparan, G., Kumaran, R. M., Sornakumar, T. & Sundararajan, T., 2011. A numerical and experimental investigation of flow maldistribution in a micro-channel heat sink. *International Communication in Heat and Mass Transfer,* Volume 38, pp. 1349-1353.

Kumaran, R. M., Kumaraguruparan, G. & Sornakumar, T., 2013. Experimental and numerical studies of header design and inlet/outlet configuration on flow mal-distribution in parallel microchannels. *Applied Thermal Engineering,* Volume 58, pp. 205-216.

Kumari, S., Kumar, N. & Gupta, R., 2019. Flow and heat transfer in slug flow in microchannels: Effect of bubble. *International Journal of Heat and Mass Transfer 129 (2019) 812–826,* Volume 129, p. 812–826.

Kumari, S., Kumar, N. & Gupta, R., 2019. Flow and heat transfer in slug flow in microchannels: Effect of bubble. *International Journal of Heat and Mass Transfer,* Volume 129, p. 812–826.

Kumar, S. & Singh, P. K., 2019. Effects of flow inlet angle on flow maldistribution and thermal performance of water cooled mini-channel heat sink. *International Journal of Thermal Sciences* , Volume 138, pp. 504-511.

Kurimoto, R., Hayashi, K., Minagawa, H. & Tomiyama, A., 2018. Numerical investigation of bubble shape and flow field of gas-liquid slug flow in circular microchannels. *International Journal of Heat and Fluid Flow,* Volume 74, pp. 28-35.

Laborie, S., Cabassud, C., Durand-Bourlier, L. & Laine, J., 1999. Characterisation of gas}liquid two-phase #ow inside capillaries. *Chemical Engineering Science* , Volume 54, pp. 5723-5735.

Lakehal, D., Larrignon, G. & Narayanan, C., 2008. Computational heat transfer and two-phase flow topology in miniature tubes. *Microfluid Nanofluid,* Volume 4, pp. 261-271.

Lalot, S., Florent, P., Lang, S. & Bergles, A., 1999. Flow maldistribution in heat exchangers. *Applied Thermal Engineering,* Volume 19, pp. 847-863.

Lee, M., Yi-Kuan, L. & Zohar, Y., 2012. Single-phase liquid flow forced convection under a nearly uniform heat flux boundary condition in microchannels. *Journal of Micromechanics and Microengineering* , pp. 1-10.

Lee, P.-S. & Garimella, V. S., 2006. Thermally developing flow and heat transfer in rectangular microchannels of different aspect ratios. *International Journal of Heat and Mass Transfer* , Volume 49, pp. 3060-3067.

Lee, P.-S., Suresh, G. V. & Liu, D., 2005. Investigation of heat transfer in rectangular microchannels. *International Journal of Heat and Mass Transfer,* Volume 45, pp. 1688-1704.

Lee, P.-S., Suresh, G. V. & Liu, D., 2005. Investigation of heat transfer in rectangular microchannels. *International Journal of Heat and Mass Transfer*, Volume 45, pp. 1688-1704.

Lelea, D., Nishio, S. & Takano, K., 2004. The experimental research on microtube heat transfer and fluid flow of distilled water. *International Journal of Heat and Mass Transfer*, Volume 47, pp. 2817-2830.

Leung, S. S., Gupta, R., Fletcher, D. F. & Haynes, B. S., 2012. Gravitational effect on Taylor flow in horizontal microchannels. *Chemical Engineering Science,* Volume 69, p. 553–564.

Leung, S. S., Liu, Y., Fletcher , D. F. & Haynes, B. S., 2010. Heat transfer in well-characterised Taylor flow. *Chemical Engineering Science ,* Volume 65, p. 6379–6388.

Li, H. & Hrnjak, P., 2019. Flow patterns and plug/slug flow characteristic of R134a in a 0.643 mm microchannel tube. *International Journal of Heat and Mass Transfer,* Volume 132, p. 1062–1073.

Li, H.-W.et al., 2014. Flow pattern map and time–frequency spectrum characteristics of nitrogen–water two-phase flow in small vertical upward noncircular channels. *Experimental Thermal and Fluid Science,* Volume 54, p. 47–60.

Li, J. & Peterson, G., 2007. 3-Dimensional numerical optimization of silicon based high performance parallel microchannel heat sink with liquid flow. *International Journal of Heat and Mass Transfer ,* Volume 50, pp. 2895-2904.

Lim, Y. S. & Yu, S., 2014. Numerical simulations of heat transfer characteristics of gas-liquid two phase flow in microtubes. *International Journal of Thermal Scienes,* Volume 86, pp. 115-124.

Lim, Y. s., Yu, S. & Nguyen, N. T., 2013. Flow visualization and heat transfer characteristics of gas–liquid two-phase flow in microtube under constant heat flux at wall. *International Journal of Heat and Mass Transfer,* Volume 56, p. 350–359.

Lim, Y., Yu, S. & Nguyen, N., 2013. Flow visualization and heat transfer characteristics of gas–liquid two-phase flow in microtube under constant heat flux at wall. *International Journal of Heat and Mass Transfer ,* Volume 56, p. 350–359.

Li, S. et al., 2019. A state-of-the-art overview on the developing trend of heat transfer enhancement by single-phase flow at micro scale. *International Journal of Heat and Mass Transfer ,* Volume 143, pp. 1-34.

Liu, D. et al., 2019. Experimental and numerical analysis on heat transfer performance of. *International Journal of Heat and Mass Transfer*, pp. 1-14.

Liu, J.-T., Peng, X.-F. & Yan, W.-M., 2007. Numerical study of fluid flow and heat transfer in microchannel cooling passages. *International Journal of Heat and Mass Transfer ,* Volume 50, pp. 1855-1864.

Liu, X. & Yu, J., 2016. Numerical study on performance of mini-channel heat sinks with non-uniform inlets. *Applied Thermal Engineering,* Volume 93, pp. 856-864.

Li, Z., He, Y.-L., Tang, G.-H. & Tao, W.-Q., 2007. Experiemntal and numerical studies of liquid flow and heat transfer in microtubes. *International Journal of Heat and Mass Transfer,* Volume 50, pp. 3447-3460.

Lui, H., Vandu, C. O. & Krishna , R., 2005. Hydrodynamics of Taylor Flow in Vertical Capillaries: Flow Regimes, Bubble Rise Velocity, Liquid Slug Length, and Pressure Drop. *Ind. Eng. Chem. Res.,* Volume 44, pp. 4884-4897.

Lu, M.-C. & Wang, C.-C., 2006. Effect of the Inlet Location on the Performance of Parallel Channel Cold-Plate. *IEEE Transaction on Component and Packing Technologies*, 29(1), pp. 30-38.

Magnini, M. & Thome, J. R., 2016. A CFD study of the parameters influencing heat transfer in microchannel slug flow boiling. *International Journal of Thermal Sciences,* Volume 110, pp. 119-136.

Mala, G. M. & Li, D., 1999. Flow characteristics of water in microtubes. *International Journal of Heat and Fluid Flow,* Volume 20, pp. 142-148.

Mansoor, M. M., Wong, K.-C. & Siddique, M., 2012. Numerical investigation of fluid flow and heat transfer under high heat flux using rectangular micro-channels.. *International Communications in Heat and Mass Transfer,* Volume 39, pp. 291-297.

Maranzana, G., Perry, I. & Maillet, D., 2004. Mini- and microchannel: influence of axial conduction in the walls. *International Journal of Heat and Mass Transfer,* Volume 47, pp. 3993-4004.

Mathew, B., John, T. & Hegab, H., 2009. *Effect of manifold design on flow distribution in multichanneled microfluidic devices.* Vail, Colorado, USA, Proceeding of the ASME 2009 Fluids Engineeering Division Summer Meeting.

McQuillan , K. W. & Whalley, P. B., 1985. Flow patterns in vertical two-phase flow. *Int. J, Multiphase Flow,* 11(2), pp. 161-175.

Mehta, H. B. & Banerjee, J., 2014. An investigation of flow orientation on air–water two-phase flow in circular minichannel. *Heat and Mass Transfer,* 50(10), p. 1353–1364.

Mirmanto, Kenning, D. B. R., Karayiannis, T. G. & Lewis, J. S., 2012. *Pressure drop and heat transfer characteristics for single phase developing flow of water in rectangular microchannels.* s.l., s.n.

Moharana , M. K. & Khandekar, S., 2012. Effect of aspect ratio of rectangular microchannels on the axial back conduction in its solid substrate. *International Journal of Microscale and Nanoscale Thermal and Fluid Transport Phenomena,* Volume 4, pp. 211-229.

Moharana, M. K., Singh, P. K. & Khandekar, S., 2012. Optimum Nusselt number for simultaneously developing internal flow under conjugate conditions in a square microchannel. *Journal of Heat Transfer,* Volume 134, pp. 1-10.

Mokrani, O., Bourouga, B., Castelain , C. & Peerhossaini, H., 2009. Fluid flow and convective heat transfer in flat microchannels. *International Journal of Heat and Mass Transfer,* Volume 52, pp. 1337-1352.

Morini, G. L., 2004. Single-phase convective heat transfer in microchannels: a review of experimental results.. *International Jounal of Themal Sciences,* Volume 43, pp. 631-651.

Mudawar, I., 2011. Two-Phase Microchannel Heat Sinks: Theory, Applications and Limitations. *Journal of Electronic Packaging,* Volume 133, pp. 1-31.

Munson, B. R., Young, D., Okiishi, T. & Huebsch, W. W., 2009. *Fundamentals of Fluid Mechanics.* 6th ed. s.l.:John Willey and Sons Inc..

Narayanan, C. & Lakehal, D., 2008. Two-phase Convective Heat Transfer in Miniature Pipes Under Normal and Microgravity Condition. *Journal of Heat Transfer,* Volume 130, pp. 1-5.

Owhaib, W. & Palm, B., 2004. Experimental investigation of single phase convective heat transfer in circular microchannels.. *Experimetal Thermal and Fluid Science ,* Volume 28, pp. 105-110.

Pan, M., Shao, X. & Liang , L., 2013. Analysis of Velocity Uniformity in Single Microchannel Plate with Rectangular Manifolds at Different Entrance Velocities. *Chemical Engineering & Technology,* 36(6), pp. 1067-1074.

Pan, M., Tang, Y., Pan , L. & Lu, L., 2008. Optimal Design of Complex Manifold Geometries for Uniform Flow Distribution between Microchannels. *Chemical Engineering Journal,* Volume 137, pp. 339-346.

Papautsky, I. et al., 1999. *Effects of rectangular microchannel aspect ratio on laminar friction constant.* s.l., Proceedings of SPIE - The International Society for Optical Engineering 3877.

Park, H. S. & Punch, J., 2008. Friction factor and heat transfer in multiple microchannels with uniform flow distribution. *International Journal of Heat and Mass Transfer,* Volume 51, pp. 4535-4543.

Patankar, V. S., 1980. *Numerical Heat Transfer and Fluid Flow.* Washington, DC: Hemisphere Publishing Corp.

Patel, R. S., Weibel, J. A. & Garimella, S. V., 2017. Characterization of liquid film thickness in slug-regime microchannel flows. *International Journal of Heat and Mass Transfer*, Volume 115, pp. 1137-1143.

Pattamatta, A., Sielaff, A. & Stephan, . P., 2015. A numerical study on the hydrodynamic and heat transfer characteristics of oscillating Taylor bubble in a capillary tube. *Applied Thermal Engineering 89 (2015)* , Volume 89, pp. 628-639.

Peng, X. & Peterson, G., 1995. The effect of thermofluid and geometrical parameters on convection of liquids through rectangular microchannels.. *Int. J. Heat Mass Transfer,* Volume 38, pp. 755-758.

Peng, X. & Peterson, G., 1996. Convection heat transfer and flow friction for water flow in microchannel structures. *Int. J. Heat Mass Transfer,* 39(12), pp. 2599-2608.

Peng, X., Peterson, G. & Wang, B., 1995. Frictional flow characteristics of water flowing through rectangular microchannels. *Experimental Heat Transfer* , pp. 249-264.

Peng, X., Wang, B., Peterson, G. & Ma, H., 1995. Experimental investigation of heat transfer in flat plates with rectangular microchannel. *Int.J.Heat Mass Transfer,* Volume 38, pp. 127-137.

Perkins, K., Schade, K. & McEligot, D., 1973. HEATED LAMINARIZING GAS FLOW IN A SQUARE DUCT. *Int. J. Heat Mass Transfer,* Volume 16, pp. 897-916.

Pfund, D. et al., 2000. Pressure drop Measurements in Microchannel. *AIChE Journal*, 46(8), pp. 1496-1507.

Phillips, R. J., 1987. MS Thesis Department of Mechanical Engineering. In: *Forced-convection, liquid-cooled, microchannel heat sinks.* Cambridge : s.n., p. 70.

Pistoresi, C., Fan, Y. & Luo, L., 2015. Numerical study on the improvement of flow distribution uniformity among parallel mini-channels. *Chemical Engineering and Process: Process Intensification,* pp. 63-71.

Qian, D. & Lawal, A., 2006. Numerical study on gas and liquid slugs for Taylor flow in a T-junction microchannel. *Chemical Engineering Science* , Volume 61, p. 7609 – 7625.

Qu, W., Mala, G. M. & Li, D., 2000. Heat transfer for water flow in trapezoidal silicon. *International Journal of Heat and Mass Transfer*, Volume 43, pp. 3925-3936.

Qu, W. & Mudawar, I., 2002. Experimental and Numerical Study of Pressure Drop and Heat Transfer in A Single-Phase Microchannel Heat Sink. *International Journal of Heat and Mass Transfer* , Volume 45, pp. 2549-2565.

Qu, W. & Mudawar, I., 2003. Thermal design methodology for high-heat-flux single-phase and two-phase microchannel heat sinks. *Components and Packaging Technologies, IEEE Transactions* , 26(3), pp. 347-356.

Qu, W., Mudawar, I., Lee, S.-Y. & Wereley, S., 2006. Experiemntal and computational investigation of flow development and pressure drop in rectangular micro-channel.. *Journal of Electronic Packaging* , Volume 128, pp. 1-9.

Rahman , M. M. & Gui, F., 1993. Experimental measurements of fluid flow and heat transfer in microchannel cooling passages in a chip substrate. *Advances in electronic Packaging* , Volume 2, pp. 685-692.

Rahman, M. M., 2000. Measurements of heat transfer in microchannel heat sinks. *Int. Comm. Heat Mass Transfer*, 27(4), pp. 495-506.

Ranganatakulu, C., Seetharamu, K. & Seevatsan, K., 1997. The effect of inlet fluid flow nonuniformity on thermal performance and pressure drops in crossflow plate fin compact heat exchangers. *Int. J. Heat Mass Transfer*, Volume 40, pp. 27-38.

Rao, B. P. & Das, S. K., 2004. Effect of flow distribution to the channel on thermal performance of multipass plate heat exchanger. *Heat Transfer Engineering*, Volume 25, pp. 48-59.

Rao, B. P., Kumar, P. K. & Das, S. K., 2002. Effect of flow distribution to the channels on thermal performance of a plate heat exchanger. *Chemical Engineering and Processing,* Volume 41, pp. 49-58.

Rebrov, E. V., 2010. Two Phase Flow Regimes in Microchannels. *Theoretical Foundations of Chemical Engineering,* Volume 44, p. 355–367.

Rosa, P., Karayiannis , T. & Collins, M., 2009. Single-phase Heat Transfer in Microchannels: The Important of Scalling Effects. *Applied Thermal Engineering ,* Volume 29, pp. 3447-3468.

Ryck, A. d., 2002. The effect of weak inertia on the emptying of a tube. *Physics of Fluids,* 14(7), pp. 2102-2108.

Ryu, J., Choi, D. & Kim, S., 2003. Three-dimensional numerical optimzation of manifold microchannel heat sink. *International Journal of Heat and Mass Transfer,* Volume 46, pp. 1553-1562.

Saisorn, S., Kuaseng, P. & Wongwises, S., 2014. Heat transfer characteristics of gas-liquid flow in horizontal rectangular microchannels. *Experimental Thermal and Fluid Science,* Volume 55, pp. 54-61.

Saisorn, S. & Wongwises , S., 2008. Flow pattern, void fraction and pressure drop of two-phase air–water flow in a horizontal circular micro-channel. *Experimental Thermal and Fluid Science ,* Volume 32, p. 748–760.

Saisorn, S. & Wongwises, S., 2008. A review of two-phase gas–liquid adiabatic flow characteristics in micro-channels. *Renewable and Sustainable Energy Reviews,* Volume 12, p. 824–838.

Saisorn, S. & Wongwises, S., 2015. Adiabatic two-phase gas–liquid flow behaviors during upward flow in a vertical circular micro-channel. *Experimental Thermal and Fluid Science 69 (2015) 158–168,* Volume 69 , p. 158–168.

Sardeshpande, M. V. & Ranade, V. V., 2013. Two-phase flow boiling in small channels: A brief review. *Sadhana,* 38(6), pp. 1083-1126.

Scammell, A. & Kim, J., 2015. Heat transfer and flow characteristics of rising Taylor bubbles. *International Journal of Heat and Mass Transfer* , Volume 89, p. 379–389.

Sehgal, S., Murugesan, K. & Mohapatra, S., 2012. Effect of channel and plenum aspect ratios on performance of microchannel heat sink under different flow arrangement. *Journal of Mechanical Science and Technology* , 26(9), pp. 2985-2994.

Serizawa, A., Feng, Z. & Kawara, Z., 2002. Two-phase flow in microchannels. *Experimental Thermal and Fluid Science,* 26(6-7), pp. 703-714.

Shah, R. K. & London, A., 1978. *Laminar flow forced convection in ducts. In Adavnces in Heat Transfer (Suppl. 1).* New York: Irvine TF, Hartnett JP (eds).Academic Press.

Shah, R. K. & London, A., 1978. *Laminar flow forced convection in ducts. In Advances in Heat Transfer (Suppl. 1).* New York: Irvine TF, Hartnett JP (eds).Academic Press.

Shah, R. & Sekulic, D., 2003. *Fundamentals of Heat Exchanger Design.* s.l.:John Wiley and Sons, Inc..

Shao, N., Gavriilidis, A. & Angeli, P., 2009. Flow regimes for adiabatic gas–liquid flow in microchannels. *Chemical Engineering Science,* 64(11), pp. 2749-2761.

Shao, N., Gavriilidis, A. & Angeli, P., 2011. Effect of Inlet Conditions on Taylor Bubble Length in Microchannels. *Heat Transfer Engineering,* Volume 32, p. 1117–1125.

Shao, N., Salman, W., Gavriilidis, A. & Angeli, P., 2008. CFD simulations of the effect of inlet conditions on Taylor flow formation. *International Journal of Heat and Fluid Flow* , Volume 29, p. 1603–1611.

Shen, S., Xu, J., Zhou, J. & Chen, Y., 2006. Flow and heat transfer in microchannels with rough wall surface. *Energy Conversion and Management* , Volume 47, pp. 1311-1325.

Siddique, A. et al., 2017. Design of a collector shape for uniform flow disribution in microchannels. *Journal of Micromechanics and Microengineering,* 27(7).

Silverio, V. & Moreira, A. L., 2008. *Friction losses and heat transfer in laminar microchannel single-phase liquid flow*. Darmstadt, Germany, Procedding of the 6th Internatioanl ASME Conference on Nanochannels, Microchannels and Minichannels.

Siva V, M., Pattamatta, A. & Das, S. K., 2013. A Numerical Study of Flow and Temperature Maldistribution in a Parallel Microchannel System for Heat Removal in Microelectronic Devices. *Journal of Themal Science and Engineering Applications*, Volume 5, pp. 1-9.

Siva V, M., Pattamatta, A. & Das, S. K., 2013. Investigation on Flow Maldistribution in Parallel Microchannel System for Intergrated Microelectronic Device Cooling. *IEEE Transactions on Components, Packaging and Manufacturing Technology,* pp. 2156-3950.

Siva, M. V., Pattamatta, A. & Das, S. K., 2014. Investigation on flow maldsitributio in parallel microchannel system for intergrated microelectronic device cooling. *IEEE Transaction on Components, Packaging and Manufacturing Technology,* 4(3), pp. 438-450.

Sobhan, C. B. & Garimella, S. V., 2001. A comparative analysis of studies on heat transfer and fluid flow in microchannels. *Microscale Thermophysical Engineering,* Volume 5, pp. 293-311.

Solovitz, S. A. & Mainka, J., 2011. Manifold design for micro-channel cooling with uniform flow distribution. *Journal of Fluid Engineering,* Volume 133, pp. 1-11.

Suo, M. & Griffith, P., 1964. Two-phase flow in capillary tubes. *Journal of Fluids Engineering, Transactions of the ASME,* 86(3), pp. 576-582.

Sur, A. & Liu, D., 2012. Adiabatic air-water two phase flow in circular microchannels. *International Journal of Thermal Sciences,* Volume 53, pp. 18-34.

Taha, T. & Cui, Z. F., 2004. Hydrodynamics of slug flow inside capillaries. *Chemical Engineering Science,* Volume 59, p. 1181 – 1190.

Taha, T. & Cui, Z. F., 2006. CFD modelling of slug flow in vertical tubes. *Chemical Engineering Science 61 (2006) 676 – 687,* Volume 61, p. 676 – 687.

Talimi, V., Muzychka, Y. & Kocabiyik , S., 2012. A review on numercial studies of slug flow hydrodynamics and heat transfer in microtubes and microchannels. *International Journal of Multiphase Flow,* Volume 39, pp. 88-104.

Tang, S., Zhao, Y., Diao, Y. & Quan, Z., 2018. Effects of various inlet/outlet positions and header forms on flow distribution and thermal performance in microchannel heat sink. *Microsystem Technologies ,* Volume 24, p. (2018) 24:2485–2497.

Tiselj, I. et al., 2004. Effect of Axial Conduction on The Heat Transfer in Microchannels.. *International Journal of Heat and Mass Transfer,* Volume 47, pp. 2551-2565.

Tong, J. C., Sparrow, E. M. & Abraham, J. P., 2009. Geometric strategies for attainment of identical outflow through all of the exit ports of a dsitribution manifold in a manifold system. *Applied Thermal Engineering,* Volume 29, pp. 3552-3560.

Tonomura, O. et al., 2004. CFD-Based Optimal Design of Manifold in Plate-fin Microdevices. *Chemical Engineering Journal ,* Volume 101, pp. 397-402.

Triplett, K. A., Ghiaasiaan, S. M., Abdel-Khalik , S. I. & Sadowski, D. L., 1999. Gas-liquid two phase flow in microchannels; Part I: two-phase flow patterns. *International Journal of Multiphase Flow ,* Volume 25, pp. 377-394.

Tullius, J. F., Vajtai, R. & Bayazitoglu, Y., 2011. A Review of Cooling in Microchannels. *Heat Transfer Engineering,* 32(7-8), pp. 527-541.

Turkakar, G. & Okutucu-Ozyurt, T., 2012. Dimensional optimization of microchannel heat sinks with multiple heat sources. *International Journal of Thermal Sciences,* Volume 62, pp. 85-92.

van Steijn, V., Kleijn, C. R. & Kreutzer, M. T., 2010. Predictive model for the size of bubbles and droplets created in microfluidic T-junctions. *Lab Chip,* Issue 19, pp. 2513-2518 .

Walsh, E. et al., 2009. Pressure drop in two phase slug/bubble flows in mini scale capillaries. *International Journal of Multiphase Flow,* Volume 35, pp. 879-884.

Walsh, P. A., Walsh, E. J. J. & Muzychka, Y. S., 2010. Heat transfer model for gas–liquid slug flows under constant flux. *International Journal of Heat and Mass Transfer,* Volume 53, pp. 3193-3201.

Wang, B. & Peng, X., 1994. Experimental investigation on liquid forced convection heat transfer through microchannel. *Int. J. Heat Mass Transfer,* Volume 37, pp. 73-82.

Wang, C.-C., Yang, K.-S., Tsai, J.-S. & Chen, I. Y., 2011. Characteristics of flow distribution in compact parallel flow heat exchangers part II : Modified inlet header. *Applied Thermal Engineering* , Volume 31, pp. 3235-3242.

Wang, C.-C., Yang, K.-S., Tsai, J.-S. & Chen, I. Y., 2011. Characteristics of flow distribution in compact parallel flow heat exchangers, part I: Typical inlet header. *Applied Thermal Engineering,* Volume 31, pp. 3226-3234.

Wang, H., Chen, Z. & Gao, J., 2016. Influence of geometric parameters on flow and heat transfer performance of micro-channel heat sinks. *Applied Thermal Engineering,* Volume 107, pp. 870-879.

Warnier, M. J. F., Croon, M. H. J. M. d., Rebrov, E. V. & Schouten, J. C., 2010. Pressure drop of gas–liquid Taylor flow in round micro-capillaries for low to intermediate Reynolds numbers. *Microfluid Nanofluid* , Volume 8, pp. 33-45.

Webb, R. L., 2003. *Effect of manifold design on flow dsitribution in parallel micro-channels.* Hawaii, USA, International Electronic Packaging Techanical Conference and Exhibition .

Wei, L. et al., 2017. Numerical study of adiabatic two-phase flow patterns in vertical rectangular narrow channels. *Applied Thermal Engineering,* Volume 110, p. 1101–1110.

Wong, H., Radke, C. J. & Morris, S., 1995. The motion of long bubbles in polygonal capillaries. Part 2. Drag, fluid pressure and fluid flow. *Journal of Fluid Mechanics,* Volume 292, pp. 95-110.

Wong, H., Radke, C. J. & Morris, S., 1995. The motion of long bubbles in polygonal capillaries. Part 2. Drag, fluid pressure and fluid flow. *Journal of Fluid Mechanics,* Volume 292, pp. 95-110.

Wu, H. & Cheng, P., 2003. An experimental study of convective heat transfer in silicon microchannels with different surface conditions. *International Journal of Heat and Mass Transfer,* Volume 46, pp. 2547-2556.

Xia , G. D. et al., 2015. Effect of different geometric structures on fluid flow snd hest transfer performance in microchannel heat sinks. *nternational Journal of Heat and Mass Transfer,* Volume 80, pp. 439-447.

Xing, D., Yan, C., Wang, C. & Sun, L., 2013. A theoretical analysis about the effect of aspect ratio on single-phase laminar flow in rectangular ducts. *Progress in Nuclear Energy,* Volume 65, pp. 1-7.

Xu, B., O. K., C. W. & W. N., 2000. Experimental Investigation of Flow Friction for Liquid Flow in Microchannels. *Int. Comm. Heat Transfer,* 27(8), pp. 1165-1176.

Xu, B., Ooti, K., Wong, N. & Choi, W., 2000. Experimental investigation of flow friction for liquid flow in microchannels. *International Communications in Heat and Mass Transfer,* 27(8), pp. 1165-1176.

Yang, C.-Y. & Lin, T.-Y., 2007. Heat transfer characteristics of water flow in microtubes. *Experimental Thermal and Fluid Science,* Volume 32, pp. 432-439.

Yang, C.-Y. & Shieh, C.-C., 2001. Flow pattern of air–water and two-phase R-134a in small circular tubes. *International Journal of Multiphase Flow,* 27(7), pp. 1163-1177.

Yao, C. et al., 2019. Characteristics of gas-liquid Taylor flow with different liquid viscosities in a rectangular microchannel. *Chemical Engineering Journal,* Volume 373, pp. 437-445.

Yao, C. et al., 2019. Characteristics of gas-liquid Taylor flow with different liquid viscosities in a rectangular microchannel. *Chemical Engineering Journal* , Volume 373, p. 437–445.

Yu, D., W., R. & T., 1995. *An Experimental and theoritical investigation of fluid flow and heat transfer in microtubes.* Hawaii, ASME /JSME Thermal Engineering Conference.

Yue, J. et al., 2008. An experimental investigation of gas–liquid two-phase flow in single microchannel contactors. *Chemical Engineering Science* , Volume 63, pp. 4189 - 4202.

Yue, J. et al., 2008. An experimental investigation of gas–liquid two-phase flow in single microchannel contactors. *Chemical Engineering Science,* 63(16), pp. 4189-4202.

Zaloha, P. et al., 2012. Characteristics of liquid slugs in gas-liquid Taylor flow in microchannels. *Chemical Engineering Science,* Volume 68, pp. 640-649.

Zhai , Y., Xia, G., Li, Z. & Wang, H., 2017. Experimental investigation and empirical correlations of single and laminar convective heat transfer in microchannel heat sinks. *Experimental Thermal and Fluid Science 83 (2017) ,* Volume 83, p. 207–214.

Zhai, Y., Xia, G., Li, Z. & Wang, H., 2017. Experimental investigation and empirical correlations of single laminar convectie heat transfer in microchannel heat sinks. *Experimental Thermal and Fluid Science* , pp. 207-214.

Zhang , J. & Li, W., 2018. Thermal and Flow Characteristics of Water–Nitrogen Taylor Flow Inside Vertical Circular Tubes. *Journal of Heat Transfer,* Volume 140, pp. 1-10.

Zhang , T. et al., 2011. Gas–liquid flow in circular microchannel. Part I: Influence of liquid physical properties and channel diameter on flow patterns. *Chemical Engineering Science* , Volume 66 , p. 5791–5803.

Zhang, J., Diao, Y., Zhao, Y. & Zhang, Y., 2014. An experimental study of the characteristics of fluid flow and heat transfer in the multiport microchannel flat tube. *Applied Thermal Engineering,* Volume 65, pp. 209-218.

Zhang, J. & Li, W., 2016. Investigation of hydrodynamic and heat transfer characteristics of gas– liquid Taylor flow in vertical capillaries. *International Communications in Heat and Mass Transfer* , Volume 74, pp. 1-10.

Zhang, J. & Li, W., 2016. Investigation of hydrodynamic and heat transfer characteristics of gas–liquid Taylor flow in vertical capillaries. *International Communications in Heat and Mass Transfer,* Volume 74, pp. 1-10.

Zhang, P. & Fu, X., 2009. Two-phase flow characteristics of liquid nitrogen in vertically upward 0.5 and 1.0 mm micro-tubes: Visualization studies. *Cryogenics,* Volume 49, p. 565–575.

Zhao, C. & Lu, T., 2002. Analysis of microchannel heat sinks for electronics cooling. *International Journal of Heat and Mass Transfer,* Volume 45, pp. 4857-4869.

Zhao, T. & Bi, Q. C., 2001. Co-current air–water two-phase flow patterns in vertical triangular microchannels. *International Journal of Multiphase Flow*, 27(5), pp. 765-782.

Zheng, D., He, X. & Che, D., 2007. CFD simulations of hydrodynamic characteristics in a gas–liquid vertical upward slug flow. *International Journal of Heat and Mass Transfer,* Volume 50, p. 4151–4165.

PUBLICATIONS

A. Conference

1- **Sahar, A.M**., Ozdemir, M.R., Mahmoud, M. M., Wissink, J. and Karayiannis, T.G. Single-phase flow pressure drop and heat transfer in a rectangular metallic micro channel. 4 th Micro and and Nano Flows Conference, London, 2014.

2- **Sahar, A.M**., Wissink, J., Mahmoud, M. M. and Karayiannis, T.G. Effect of hydraulic diameter and aspect ratio on single phase flow and heat transfer in a rectangular microchannel. 14th UK Heat Transfer Conference, Edinburgh, 2015.

B. Journal

1- **Sahar, A.M.**, Ozdemir, M.R., Mahmoud, M. M., Wissink, J. and Karayiannis, T.G. Single-phase flow pressure drop and heat transfer in rectangular metallic microchannels. Applied Thermal Engineering, 93:1324-1336, 2016.

2- **Sahar, A.M**., Wissink, J., Mahmoud, M. M., Karayiannis, T.G, and Mohamad S. A. Ishak. Effect of hydraulic diameter and aspect ratio on single phase flow and heat transfer in a rectangular microchannel. Applied Thermal Engineering, 115: 793-814, 2017.